Prototyping of a Surface-integrated Mechano-optical Microsensor System for 3D Traction Force Measurements

by Dipl.chem. Hendrikje M. Neumann

Institute for Materials Science
Faculty of Engineering
Christian-Albrechts University of Kiel

tf

Prototyping of a Surface-integrated Mechano-optical Microsensor System for 3D Traction Force Measurements by DHM/DIC

by

Hendrikje M. Neumann

submitted in fulfillment of the requirements for the degree of Doctor of Engineering Sciences (Dr.-Ing.) to the
Faculty of Engineering at the Christian-Albrechts-University of Kiel

June 17, 2019

Declaration

I, Hendrikje Marie Neumann, hereby declare that I wrote this dissertation entirely by myself without improper external assistance besides the advice of my supervisor and to the best of my knowledge and belief. I furthermore declare that my treatise was not yet presented fully or in parts in any other examination procedures besides in the course of this corresponding procedure. Finally, I declare that I have identified all quotations of other authors and used none but the indicated sources to keep the rules of good scientific practice defined by the German Research Society (DFG).

Hendrikje M. Neumann,   Faculty of Engineering

Department of Materials Science   Christian-Albrechts University of Kiel

Kiel, 09/10/2019

_____

Place/Date   Signature

Reviewers   **Examination Committee**

Prof.Dr. Christine Selhuber-Unkel   Prof.Dr. Christine Selhuber-Unkel

Prof.Dr.-Ing. Eckhard Quandt   Prof.Dr.-Ing. Eckhard Quandt

                                         Prof.Dr.-Ing. Jeffrey McCord

Examination Committee Chairman: Prof.Dr.Franz Faupel

Date of the oral exam: 09/06/2019

Dedicated to my parents
who taught me to fight and never give up

~

In special honor of my dad Dipl.Des. Michael Roger Neumann

(∗ 12.06.1947 - † 10.04.2019)

~

In memory of Sabine Neumann

(∗ 03.10.1952 - † 30.01.2019)

~

and Marianne Müller-Mohnssen

(∗ 03.06.1935 - † 12.02.2019)

Abstract

In times of a rapid development and growing market in robotics with special regard to humanoids, high-tech protheses and the personalization of medicine, biomimicking natural materials like artificial tissue are of central interest within research and industry. To fully understand the structure-function relations within living systems, comprehensive knowledge about the smallest living block, the cell, and its biomechanics are a central topic in world-wide research. However, there is so far no comprehensive technique established that can measure 3D cell forces quantitatively e.g. during migration processes.

In this project, a novel surface-integrated mechano-optical microsensor system has been conceptualized, designed, prototyped and tested, which allows for the record of pico- to micronewton traction forces in three dimensions pseudo simultaneously including a continuous screening of the sensor element condition during the measurement. Here, the displacement of a sensor element with a well-defined structure is directly correlated to a distinct force by determining the element spring constant for each spatial direction.

Within this prototyping, first adequate sensor elements were designed via topology optimization and linear static finite element analysis. Here, a free-standing element consisting of four spring-arms with three slopes, symmetrically arranged, attached to a frame and connected in the centre via a centre plate showed the best performance for in-and out-of-plane displacements in the nanometer range. These design results were fabricated by established micromachining processes of biocompatible thin films of nickel-titanium (NiTi) and amorphous silicon (a-Si). A minimum sensor element diameter of 45 μm at a device material thickness of 200 nm and a minimum feature size of 1 μm was achieved. Furthermore, a plasma etching process was developed to fabricate fully biocompatible, gold-coated polydimethylsiloxane (PDMS) structures in membranes. This sets the starting point for the fabrication of attractive cost-efficient sensor arrays with easily tunable spring constants by

variation of the polymeric composition.

For future accurate and quantitative traction force measurements, atomic force microscopic cantilever based calibrations of the out-of-plane and in-plane sensor element spring constants were established. For lateral spring constants, a diamagnetic levitation force calibrator (D-LFC) was used for the first time as an adequate calibration method for sensor elements with a high accuracy of 1 %. The axial spring constant of the 45 μm sized a-Si sensor elements were determined to about 0.012 N/m and lateral to 4.66 N/m, while those of the NiTi elements with 170 μm edge length are as low as 0.004 N/m out-of-plane and 0.087 N/m in-plane.

For the cost-efficient, simple, compact, comprehensively modifiable and sensitive mechano-optical readout of the force induced sensor element displacements, a setting based on the combination of digital holographic microscopy (DHM) and digital image correlation (DIC) was conceptualized and tested. This readout system allows for displacement resolutions as small as 200 nm. Using the NiTi sensor element, traction forces in the pico- to nanonewton range out-of-plane and in the nano-to miconewton range in-plane can now be quantitatively sensed.

To control adhesion sites of the samples to the centre of the sensor elements, a technique has been conceptualized and run based on the fusion of ink-jet printing with the established gold-nanodot patterning method of diblock-copolymer micelle nanolithography. Here, fast, accurate, simultaneous micro-and nanogold dot printings of smooth, sensitive device surfaces like the sensor elements with user-defined microstructures including quasi hexagonal gold nanoparticle patterns were succesfully achieved. By this method, the distinct adhesion and the control of the amount of adhesion sites for future precise 3D cell force distribution measurements is ensured.

Zusammenfassung

In Zeiten schneller Entwicklung und wachsender Märkte im Bereich der Robotik, mit einem besonderen Augenmerk auf humanoide Roboter, der high-tech Prothetik und der personalisierten Medizin ist die Biomimetik natürlicher Materialien wie beispielsweise inform künstlicher Haut zentrales Interesse in Forschung und Industrie. Um die Struktur-Funktions-Beziehungen in lebenden Systemen umfassend zu verstehen ist die umfangreiche Wissenserweiterung in Bezug auf den kleinsten lebenden Baustein, die Zelle, und seine Biomechanik Gegenstand weltweit laufender Forschungsprojekte. Dennoch gab es bis jetzt keine umfassende etablierte Methode, die 3D Zellkräfte zum Beispiel während des Zellwanderungsprozesses quantitativ messen kann.

In diesem Projekt wurde ein neuartiges, oberflächen-integriertes, mechano-optisches Mikrosensorsystem konzeptioniert, gestaltet, prototypisiert und getestet, das die Messung piko-bis mikronewton kleiner Zugkräfte gleichzeitig in drei Dimensionen ermöglicht. In diesem System wird die Verschiebung eines Sensorelementes mit wohl definierter Struktur direkt mit einer bestimmten Kraft korreliert, indem zuvor die Kraftkonstanten für jede Raumrichtung ermittelt werden. Der Zustand der Sensorelemente wird während der Messung dabei kontinuierlich mit aufgenommen.

In dieser Erstentwicklung eines Systemmusters wurden zunächst geeignete Sensorelemente mittels Topologieoptimierung und linear statischer Finite Elementanalyse konzipiert. Hier zeigten freistehende Sensorelemente, die aus vier Federarmen mit jeweils drei Schlaufen aufgebaut, symmetrisch angeordnet, in einem Rahmen angebracht und im Zentrum des Elementes mit einer Mittelplatte verbunden sind, die besten Eigenschaften bei lateralen und axialen Verschiebungen im Nanometerbereich. Diese Designergebnisse wurden mittels etablierter Mikromaterialbearbeitungsprozesse aus biokompatiblen Nickel-Titan (NiTi) und amorphen Silizium (a-Si)-Dünnschschichten hergestellt. Ein minimaler Sensorelement Durchmesser von 45 μm bei einer Schichtdicke von 200 nm und einer Struk-

turgröße von 1 μm wurde erreicht. Desweiteren wurde ein Prozess entwickelt, um vollständig biokom-patible, Gold beschichtete Polydimethylsiloxan (PDMS) Mikrostrukturen in Membranen herzustellen. Dies legt den Ausgangspunkt für die Herstellung attraktiver, günstiger Sensorelement-Arrays mit ein-fach variierbaren Federkonstanten durch Variation der Polymerkomponenten.

Für zukünftige genaue und quantitative Zugkraftmessungen wurden Atomkraftmikroskopie-Cantile-ver basierte Kalibrierungen der axialen und lateralen Sensorelement-Kraftkonsten etabliert. Zum ersten Mal wurde dabei ein diamagnetischer Levitationskraftkalibrator (D-LFC) als geeignete Kalib-rierungsmethode für die Sensorelemente genutzt, dessen Genauigkeit 1% beträgt. Die damit bes-timmten Federkonsten des 45 μm kleinen a-Si Sensorleementes betragen 0,012 N/m aus der Ebene und 4,66 N/m in der Ebene, während die Federkonstanten des 170 μm großen NiTi Sensorelemente mit 0,004 N/m axial und 0,087 N/m lateral kleinstmöglich sind.

Für eine günstige, einfache, kompakte, umfassend veränderbare und empfindliche mechano-opti-sche Datenauslesung wurde ein Aufbau konzeptioniert und getestet, der auf einer Kombination digi-taler holografischer Mikroskopie (DHM) und digitaler Bildkorrelation (DIC) basiert. Diese Auslesemeth-ode ermöglicht die kleinstmögliche Auflösung von Verschiebungen von 200 nm. Bei Einsatz der NiTi Sensorelemente können so axiale Zugkräfte im Piko- und Nanometerbereich und lateral im Nano-bis Mikronewton Bereich quantitativ gemessen werden.

Um die Adhäsionspunkte der Proben auf der Sensorelement-Mittelplatte zu kontrollieren wurde schließlich eine Technik konzeptioniert und durchgeführt, in der Ink-Jet Drucken mit der etablierten Methode der Diblock-Copolymer Mizellen Nanolithographie (BCML) kombiniert wurde. Damit wurden schnel-le, genaue, simultane Mikro-und Nanogoldpunkt Drucke auf glatten, empfindlichen Bauelementoberflächen wie den Sensorelementen mit Nutzer-definierten Mikrostrukturen realisiert, die quasi hexagonale Gold Nanopartikel Muster enthalten. Durch diese Methode wird die gezielte Ad-häsion und die Kontrolle der Anzahl von Adhäsionsstellen für zukünftige 3D Zellkraftverteilungsmes-sungen ermöglicht.

Résumé

A une époque de développement rapide et de croissance du marché dans les domaines de la robotique et plus particulièrement des robots humanoïdes, des prothèses de haute technologie et de la médecine personnalisée, la biomimétique des materieaux naturels comme par example la peau artificielle présentent un intérêt central pour la recherche et l'industrie. Pour bien comprendre les rélations structure-fonction dans les systèmes vivants, l'élargissement significatif des connaissances concernant des plus petites unités vivantes, les cellules, et leurs bioméchaniques sont les sujets des recherches actuelles internationales. Cependant, il n'y a pas jusqu'ici de technique compréhensive qui puisse mesurer simultanément les forces cellulaires en trois diréctions comme pendant les migrations des cellules.

Au cours de ce projet, un noveau système à microcapteur mécano-optique intégré à la surface a été conceptualisé, conçu et testé, ce qui permet l'enregistrement simultané des forces de traction de pico- à nanonewton en trois diréctions et le dépistage continu de la condition de l'élément capteur pendant les mesures. Dans ce système, le déplacement d'un élément capteur d'une strutcure bien defénie est corrélé directement à une certaine force grâce à la détermination des constantes de ressort en trois diréctions pour l'élément capteur.

Dans ce procédé prototype, les éléments capteurs appropriés ont été conçus d'abord par une fonction d'optimisation topologique et l'analyse par éléments finis linéaire-statique. Un élément autoportant qui consiste en quatre bras de plume avec trois méandres, disposés symétriquement, attachés à un cadre et connectés par un panneau central dans le centre de l'élément possède les meilleures propriétés concernant les déplacements latéraux et axiaux à l'échelle nanométrique. Le design de ces éléments a été fabriqué en utilisant les procédures établiées du microtraitement des matériaux avec des couches minces de nickel-titane (NiTi) et de silicium amorphe (a-Si). Un diamètre

minimum des éléments capteurs de 45 μm avec une épaisseur du matériau de 200 nm et une taille structurelle de 1 μm a été réalisé. En outre, un procédé de gravure par plasma a été développé pour fabriquer des structures de polydiméthylsiloxane (PDMS) biocompatibles et revêtus d'or dans des membranes. Celui-ci marque le point initial de la fabrication des réseaux d'éléments capteurs attractifs avec des constantes de ressort bien réglables par la variation des compositions de polymères.

Pour les mesures des forces de traction précises à l'avenir, les procédés de calibrage des constantes de ressort axiales et latérales ont été établies en se basant sur les cantilevers de la microscopie à force atomique. A cet égard, la méthode de calibrateur de forces de lévitation diamagnétique (D-LFC) a été utilisée pour la première fois comme technique de calibrage appropriée pour les éléments capteurs avec une précision de 1%. Les constantes de ressort des éléments capteurs a-Si était de 0,012 N/m pour des déplacements axiaux et de 4.66 N/m pour des déplacements latéraux, tandis que le constante de ressort axial des éléments capteurs NiTi d'une longueur d'arête de 170 μm était de 0,004 N/m et latéral de 0.087 N/m.

La construction qui se base sur la combinaison de la microscopie de holographie numérique (DHM) et de la corrélation d'images digitales (DIC) a été conceptualisée et testée pour l'enregistrement mécano-optique, rentable, simple, compact, trés modifiable et sensible des déplacements d'éléments capteurs occasionnées par des forces de traction. Ce système d'enregistrement possède une capacité de résolution des déplacements de 200 nm. En utilisant les éléments capteurs NiTi, des forces de traction axiales du domaine du pico- à nanonewton et latérales du domaine du nano- à micronewton sont quantitativement mesurables.

Pour le contrôle des sites d'adhésion des prélèvements au centre des éléments capteurs, on a conceptualisé et testé une technique qui combine le jet d'encre avec la nanolithographie micelles des copolymères dibloc (BCML). Des micro- et nanostructures rapides, personnalisées et précises ont été réalisées simultanément avec succès sur des surfaces lisses des éléments sensibles avec des matrices de 4 x 4 de microgouttes micellaires contenant des dessins quasi hexagonals des nanoparticules d'or. Cette méthode permettra l'adhésion ciblée et le contrôle du nombre de sites d'adhésion pour les mesures futures en trois déménsions de la distribution des forces cellulaires.

Preface

Ce qui était impossible hier, sera possible demain.

| Luise Weiss, French 'European politician of the first hour' and Suffragette, 1893-1983 |

Since the publications by the Organisation for Economic Co-operation and Development (OECD) in the 1970s, the intense work of researchers in different disciplines finding a common communication base for scientific exchange and trouble shooting has grown importance. In those times, the problems within the society should be solved by interdisciplinary science overcoming the scientific tradition of disciplinarity summed up in the slogan:"Communities have problems, universities departments".[1] A new scientific trend was born, that today lead to large scale research programs funded by the Deutsche Forschungsgesellschaft, or grants by the European Research Council that are popular methods to settle pools for academic interdisciplinary work.

Moreover, the European Commission today defines the so-called "Great Challenges" of our European societies such as health, energy, climate and by this, strongly influence the scientific landscape. To find solutions to those complex tasks, interdisciplinarity is therefore desired to flatten the most suitable and efficient path.

The believe in this idea of interdisciplinarity "(...) as the most productive and interesting way to advance knowledge" (Klein et al., 1990) and as a central instrument for an efficient solution to a complex scientific problem by creating bridges between a diversity of different research fields[2], already

---

[1] Arnold, V. Gaube, B. Wieser, *Interdisziplinär forschen*, 2014 in G. Dressel, W. Berger, K. Heimerl und V. Winiwarter, *Interdisziplinär und transdisziplinaär forschen. Praktiken und Methoden,* transkript Verlag: 105-119, Bielefeld.

[2] J. T. Klein, *Interdisciplinarity: history, theory, and practice,* Wayne State Press, 1990, 331 pages

influenced my personal studies during my school time. Here, I had to cope with natural scientific questions that needed an interdisciplinary approach such as insights into chemical procedures like the Mallet reaction where physics are needed to understand chemical processes. Over the years, my interest in disciplines that follow ways over limits became more and more dominant. In consequence, my decision was to first create and organize the intradisciplinary communication seminar "train your brain" to overcome the communication borders of chemists from different disciplines during my diploma time.

To further broaden my scientific horizons and deepen my understanding of scientific interconnections and differences in the scientific views on certain tasks, I additionally studied physics apart from chemistry. Following the iridescent paths of great physico-chemists like Otto Hahn, my combination of disciplines was then concentrated to challenging, isolated fundamental research as a scientific coworker in physical chemistry combining the fields of chemistry, physics and engineering tasks. Even though the work offered me insight into a two-dimensional research direction, it poked my intention for a more fruitful interference by off-topics or interdisciplinary cross relations.

Accompanying to my regular chemistry study time, I therefore studied the rather more theoretical sports law, a very interdisciplinary and young research field combining sports science, the three pillars of judiciary and social aspects. By this, it opened an entirely new view on interconnections and the creation of interconnections in science to me. Regarding more applicative complex tasks solved in groups, intense applicative team work as a designer, engineer and constructor in a formula student team followed to construct a formula racecar, pointing out the challenges of communication in interdisciplinary teams that have to find efficient, precise and reliable technical solutions under high time pressure.

The acquired knowledge out of these projects was transferred to work as a spokesperson in an interdisciplinary team for the research project "SFB677- Function by Switching" after having been an active researcher in this project years before. Here, my team and I established a basis to communication between doctoral candidates of various disciplines like materials science, chemistry, pedagogics, biology and physics as well as a sense of belonging of these young researchers to work more efficient as a team.

Having experienced these different interdisciplinary surroundings, I strived the combination of

research and application in an interdisciplinary challenging project that offered the chance of free scientific work with a technical and socially relevant background.

The result of this pursuit has been finally found in the interdisciplinary subject materials science and was distilled in the course of this PhD thesis. Here, the combination of the disciplines of physics, biology, chemistry, optical engineering and materials science was intended to dare steps across limits to create a novel technological approach to measure cell adhesion forces in 3D by means of light.

The challenge was the incorporation into this versatile thematic area and the productive and efficient cooperation as well as communication with other scientists all over Germany from totally different scientific fields. The success in these interdisciplinary tasks meant the success of this PhD project:

A challenging, sometimes exhausting, but always exciting path close to the edge, partly passing the limits supported by the unbreakable will to take the risk, contributing to something outstanding.

Hendrikje M. Neumann

Kiel, 28th of March 2019

Contents

1 Introduction

In times of a rapid development and growing market in robotics[1][2] with special regard to humanoids,[3] high-tech protheses[4][5] and the personalization of medicine,[6][7] biomimicking natural materials like artificial tissue are of central interest within research,[8] industry[9] and health care.[10]

To mimick the self healing mechanisms in tissue repair or wound healing requires profound knowledge enhancements regarding the biochemistry of intra- and extracellular signaling, but also on the biomechanical interaction between cells and their surrounding,[11] which is a central subject of ongoing world-wide research.[12][13][14]

The macroscopically observable phenomena such as self-healing are caused by cells creating defined forces to migrate, proliferate, adhere, divide or differentiate. The characterization and research of forces opened the entirely new discipline of mechanobiology used as basis for pursuing biophysical and bioengineering tasks. Today, the hot topic of cellular force sensing offers a broad and still growing spectrum of methods and technologies to enlighten the precise understanding of the mechanical cell behavior.

In the course of the introduction, the central interest of this PhD work is motivated introducing the cell, cell adhesion with a special focus on mechanotransduction and established cell force sensing methods. Finally, an overview on the central project tasks is given.

1.1 Cells

The smallest building blocks of all living organisms are cells that are distinguished between prokaryotic and eukaryotic cells.[15] Prokaryotic cells are unicellular systems that consist of a capsule enclosing a cell plasma membrane, DNA, ribosomes and cytoplasm, and move forward via a long tail the so-called flagellum. They are found especially in bacteria and make the majority regarding the overall

amount of cells.[16] While eukaryotic cells are most relevant for animal organisms like human beings and are of major relevance for this project regarding the future mimicking of phenomena like wound healing processes.

A spread living eukaryotic cell of a rat embryonic connective tissue, which is surrounded by other cells, is shown in figure 1.1 **A**. Here, the central difference to prokaryotic cells can be observed very well, which is the nucleus embedded in the cell membrane that contains the entire genetic information. Moreover, the diameter of eukaryotic cells is in average 100 times bigger than prokaryotes and range between 1 to 100 μm.[17] Here, the diameter of an adhered cell of this cell type is about 150 to 200 μm. A schematic overview about the most important components of this cell is depicted in figure 1.1 **B**. In general, the cell nucleus is embedded in the cytoplasm, which includes all material inside the cell membrane and outside cell nucleus.
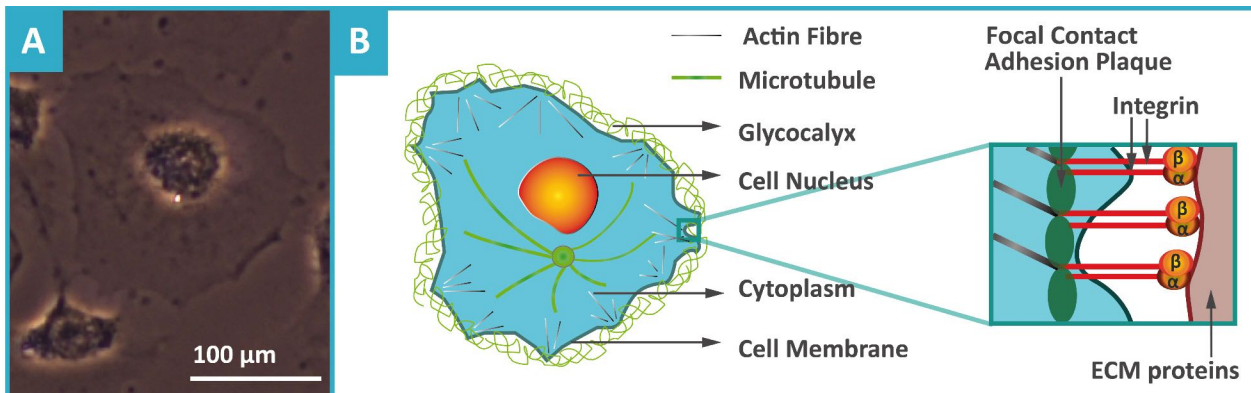
Figure 1.1: **A** Image of a rat embryotic fibroblast cell, which is adhered to a nickel-titanium surface. **B** Schematic description of the cell shown in A. An eukaryotic cell consists of a cell nucleus, which is embedded in the cytoplasm and stabilized by the cytoskeleton, which consists of filaments such as microtubule and actin fibre. The entire cell is stabilized in its shape by a cell membrane, which is covered by the glycocalix. Cell adhesion to the extracellulaire matrix (ECM) is ensured by the interaction and corresponding proteins on the surface of the ECM as shown in the inset box (modified from Albers et al., ref.[18] and Selhuber, ref.[19]).

The component with highest volume within the cell is cytosol, a liquid to gelly material which consists of organelles and inclusions like stored nutrients. There are different types of organelles such as mitochondria, which are essential for cell energy supply, but also for signaling, cell differentiation, cell growth or even cell death.[20] Cytosol therefore has multiple functions within cell processes such

as signal transduction between the cell sites and the nucleus, [21] the control of the cell division process via the so-called cytokinesis [22] or the transportation of the metabolites within the cell. [23]

The shape, the resistance against outer impacts and the migration of a cell is ensured by the cytoskeleton, which is an interconnected network of different filaments based on three different polymerized protein subunits and regulatory proteins. Its essential elements are: microtubuli, actin-filaments and intermediate filaments. [24] Microtubuli are the stiffest protein filaments with an average diameter of 20 to 30 nm growing around the centrosome, a small spherical element near the nucleus. They create complex networks with tracks of the length of an entire animal cell and are able to quickly rearrange, which is of central importance during mitosis. Here, the microtubuli generate a DNA segregating motor called mitotic spindle that finds and aligns chromosomes.

Actin based filaments are less stiff than microtubuli and of about 6 nm diameter [25]. They can transfer force via their fast growing end of the filament when pushing against the cell membrane, which is important for the leading of a migrating cell [26] and responsible for muscle contractions, cytokinesis, intracellular transport and cell mobility. [24]

Finally, the intermediate filaments are the least stiffest of all cytoskeletal filaments with a diameter of 10 nm. [27] They act as integrating device for the cytoskeleton cytosol and as a mechanical stress absorber.

The entire outer cell membrane surface is covered by the glycocalix, which consists of polysaccharides covalently bond to the cell membrane proteins. Here, the composition of the polymeric matrix makes cell recognition possible. So the organism is e.g. able to differentiate between healthy and deseased cells or transplanted tissue. [28]

The cell properties vary between the different cell types according to their function. The above presented fibroblast cells are large, flat, and spindle-shaped when they are elongated, have an oval, flat nucleus, are very agile and can migrate in three dimensional surroundings. [29] For that reason, they are perfectly adapted to the tissue and rapid tissue repair. A hot topic in skeletal tissue engineering regarding muscle reconstruction after injuries is the comprehensive understanding of muscle cells. They are found in muscle tissue, have a long tubular shape, are very smooth, consequently behave as satellite cells and consist of contractile material. In that way, the cells can fastly move throughout the tissue to support total muscle recovery from deseases or injuries, but also ensure the contraction

of the muscles in case of outer force impacts or self-driven movement. [30] [31]

Cell Adhesion   The migration and tissue development are the results of defined cell-matrix and cell-cell interactions on a molecular level. Here, cell receptors bind to the corresponding acceptors at the extracellular matrix (ECM), in a first step. Then, adhesion clusters are generated by the arrangement of various proteins to distinct binding sites called cell adhesion. The five relevant groups of cell adhesion molecules (CAMs) in this process are: cadherins, immunoglobulins, mucins, selectins and integrins. [18]

Integrins are a group of 24 different glycoproteins consisting of two non-covalent bound chains and are composed by eighteen alpha and eight beta subunits (see inset box in figure 1.1 **B**). [18] The beta subunit promotes the binding to actin filaments within the cell cortex. While the cells are spreading or migrating, integrins cluster to so-called focal adhesion clusters to amplify the adhesion effect. [18] Their adhesion force ranges between 500 pN and 100 nN. [32]

In consequence, integrins act as a transmembrane linker and cause the interaction between the cellular cytoskeleton and the ECM as well as the cell regulation and signal transduction. [33]

Mechanotransduction   In the 1990s, Wang et al. proved that integrins, and associated intracellular proteins of focal adhesions, mediate the mechanical force transmission to the cytoskeleton. [34] Furthermore, it could be shown that mechanical stimulation of cells by external forces cause an increase in focal adhesion clusters. Hence, a mechanical signal is transferred into a biochemical signal within the cell, which is the basis for macroscopically observable phenomena like wound or fracture healing based on bone or connective tissue growth. [35] Here, the mechanical load cause the production of new ECM. [36] This signal translation is known as mechanotransduction and essential for senses and physiological processes in the body. [37] [38]

Experiments even indicated, that there is a direct correlation between the pertubation of mechanotransduction and pathologies ending up in various diseases like cancer or cardiovascular disorders. [39] [40]

Regarding connective tissue cells, three different reactions to mechanical stress can be distinguished, which are: compression, e.g in cartilage, [35] tensile stress, [41] which occurs during the

entire movement sequences within the various tendons, and shearing e.g. in blood vessels. [42]

With regard to focal adhesion clusters, there are various approaches to fully explain the cluster growth due to mechanical stress. Geiger et al. offered an explanation via a mechanobiochemical feedback loop, in which a force causes signaling within the hydrolase enzymes and the stimulation of a force generation in the cytoskeleton. [43] De Rio et al. suggested that mechanical stretching of focal adhesion clusters cause a conformational change within the integrin-fibronectin bond, a glycoprotein directly connected to the integrins, and talin bonds, a high weight cytoskeletal protein, which connects integrin to the cytoplasmic plaque. [44]

In conclusion, a comprehensive understanding of the processes in focal adhesion mechanotransduction, cell adhesion regulation as well as cell sensing are essential to mimic or optimize macroscopic phenomena such as wound healing. For that reason, a variety of different techniques have been developed by various research groups in the last years and hence, selected established methods are presented in the following.

1.2 Cell Force Sensing

Due to the significant importance of cell force sensing, various traction force measurement methods have been developed within the last decades summarized, described and compared in numerous review articles. [45] [46] [47] [48] [49] [50] [51] Established techniques for force sensing are based on piezoelectric, piezoresistive, capacitive, optical and microelectro-mechanical (MEMS) sensing systems with a broad range of structural solutions as concisely compiled in figure 1.1. [52]

For a fast, short, but comprehensive overview on established techniques for cell force measurements a modified and enhanced list based on the publication of Polachek et al. is given in table 1.1 to 1.3. It includes established methods and their corresponding force resolutions, dimensions to be measurable, the number of measurable cells per experiment, the strengths and limitations for each method. [48]

For the sake of comprehensibility and rigor, the terms sensor element, sensor and sensor system will be used according to the definitions offered by Madou, in the following. [53] A sensor element is defined as "a device that converts one form of energy into another [...]," (Madou, 2011). By
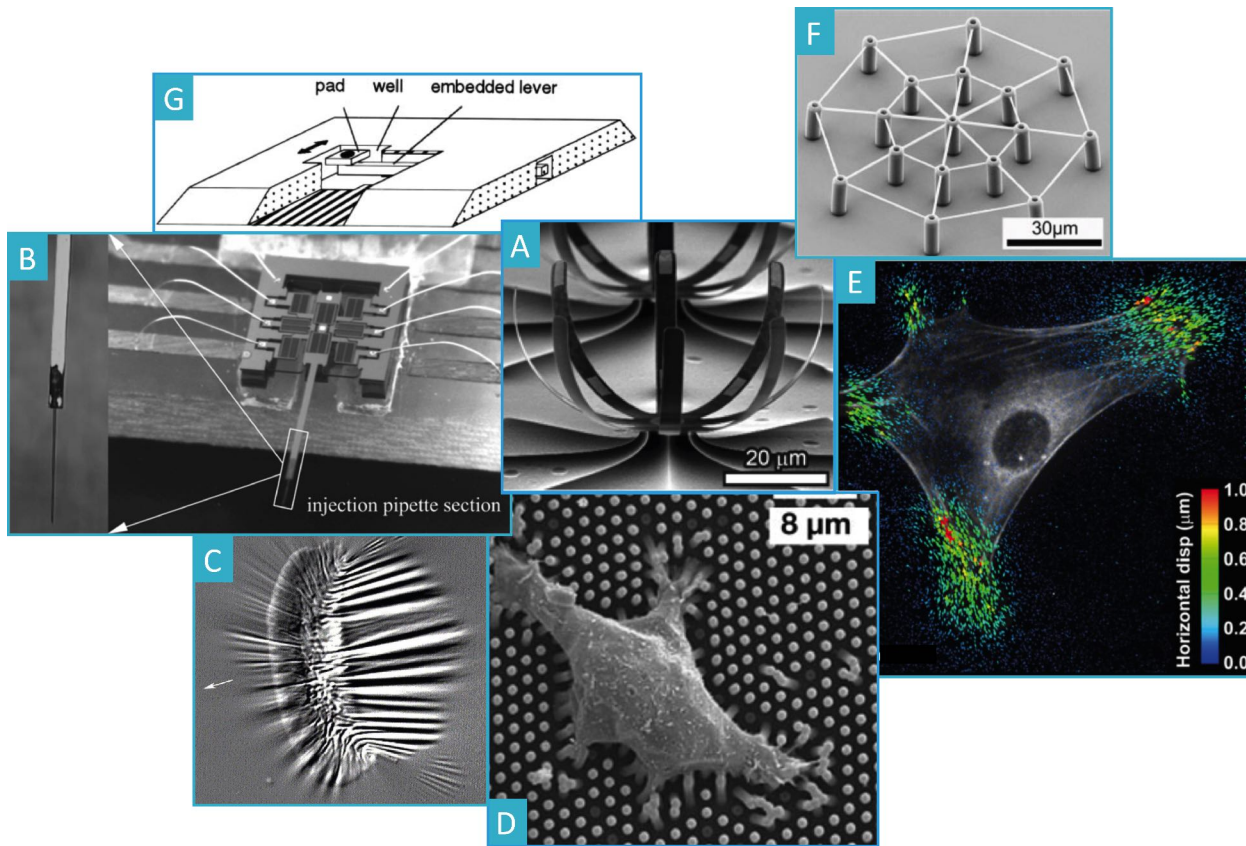
Figure 1.2: **A** Cantilever based mechanical three dimensional sensor element for cell adhesion measurements called μ-flower designed by Marelli et al. (reproduced from Ref.[54] with permission from The Royal Society of Chemistry). **B** MEMS capacitive force sensor with an injection pipette for biomechanical and cell force measurements developed by Sun et al. (reproduced from Ref.[45], Biomedical Materials by IOP Publishing. Reproduced with permission of IOP Publishing in the format Thesis/Dissertation via Copyright Clearance Center), **C** Silicon membrane shrinkage cell measurements by Burton et al. (reprinted from ref.[55], page 80, with permission from © 2001 Elsevier). **D** SEM images of an adhered cell on a micropillar array by du Roure et al. (reproduced from ref.[56] with permission from © 2005 National Academy of Sciences). **E** Traction force microscopic image by Legant et al. with computationally calculated shear and normal components of bead displacements, which are color-coded by magnitude (reproduced from ref.[57] with permission from © (2012) National Academy of Sciences). **F** String-connected micropillars for cell studies in an 3D environment by Klein et al. (reproduced by permission from John Wiley and Sons: Advanced Materials, *Elastic Fully Three-dimensional Microstructure Scaffolds for Cell Force Measurements*, F. Klein, et al., © 2010 WILEY-VCH Verlag GmbH Co. KGaA, Weinheim). **G** Micromachined mechanical sensor for in-plane cell traction force measurements by Galbraith et al. (reproduced from ref.[58] with permission from © 1997 National Academy of Sciences).

this, a specific input is transferred into a measurable output such as radiation, chemical, mechanical, magnetic or electric signals. A sensor is the combination of a sensor element or element array with a physical packaging and external electrical or optical connections. Finally, the sensor system then is the ensemble of the sensor element or array and the signal detection and processing system.

As indicated within table 1.1 to 1.3, all established sensor systems possess advantages and limitations regarding their force range, their precision, their complexity, their stability or their spatial resolution.

By means of tissue pillars, which are vertical cantilevers of known stiffness used to measure tissue contractile forces by displacement analysis of the cantilever, micropillar arrays (see figure 1.2 **D**), atomic force microscopy (AFM) or MEMS (see figure 1.2 **B**), a broad force range can be covered. But, while tissue pillars just offer qualitative data in-plane, AFM results suffer from high standard deviations due to the corresponding calibration methods, a high sensitivity against outer influences like noise corrupting the quality of the force curves, are reduced to 1D to 2D measurements and just measure overall global cell forces. Micropillar array based cell force sensing is an indirect measurement method based on the deformation of pillars according to cellular force impact. For small deformations below 200 nm reference measurements are needed and it is only suitable for in-plane force detection, while the sensitivity to normal forces is very low. [59] [60]

MEMS, as those developed by Sun et al. (see figure 1.2 **B**), can e.g. sense mechanical impacts like cell forces by small sensor deflections, which are first transduced into detectable capacitance changes and afterwards converted into a voltage variation. [45] This type of force sensor systems appear to be the best solution for convenient results as there is no optical setting needed and they are stable against outer influences. However, the minimum structure size is limited due to the present established microfabrication technologies and moreover, measurements with high precision are just possible in two dimensions at once. For a three dimensional measurement solution, two physical phenomena like piezoresistivety and capacity would need to be combined to realize a direct 3D force information. However, this would lead to a more complex fabrication process and a bigger overall size.

A promising two to three dimensional measurement technique is traction force microscopy (TFM) based on the microscopic tracking of fluorescent particle displacements in polymeric substrates like

Table 1.1: Overview of established cell force measurement methods adapted by permission from Springer Nature Customer Service Centre GmbH: Springer Nature, Nature Methods, *Measuring cell-generated forces: a guide to the available tools*, W.J. Polacheck, C.S. Chen, © 2016 Nature America, Inc. (1.-6.) and additional methods (7.-10). [51]

Method	Force Range	Cells per measurement	Spatial Resolution	Special Requirements	Strengths	Major Limitations	References
1. Collagen gel	N/A	1x10^4 to 1x10^6	N/A	None	Ease of implementation	- Qualitative - Cannot determine forces from single cells	[61] [62]
2. Tissue pillars	1 μN to 0.5 mN	100 to 2x10^6	4 mm	Tissues <10 mm require microfabrication	High through-put Ease of computation	- Cannot determine forces generated by single cells, - 2D	[63] [64] [65] [66] [67]
3. TFM	2-120 nN	1 to 1x10^3	2 μm	Hydrogel or PDMS synthesis and functionalization - Microparticle tracking algorithms	Uses standard lab equipment and fluorescence microscopy	- 2D substrates - Synthetic substrates with limited biological relevance - Computationally expensive - Requires cell lysis or manipulation	[68] [69] [70] [71] [72] [73] [74] [55] [57]
4. Micropillars	50 pN-100 nN	1-10	0.1-1 μm	Microfabrication PDMS functionalization suitable Calibration	Ease of implementation and computation	Forces are independent for posts Fabrication, 2D, Low spatial resolution	[59] [75] [76] [56] [77] [78]

Method	Force Range	Cells per measurement	Spatial Resolution	Special Requirements	Strengths	Major Limitations	References
5. 3D TFM	Not characterized	1	5 μm	- Confocal microscopy - 3D mesh editing and finite element software - 3D, MMP-cleavable synthetic hydrogels	Fully resolved 3D tractions in physiologic 3D environments	- Currently limited to single cells - Computationally expensive	[79][71]
6. DNA hairpin	4.7 pN-2 nN	1	0.2 μm	DNA hairpin synthesis	High resolution with standard fluorescence microscopy	- 2D - Currently limited to glass substrates - Long sample-prep time	[80][81]
7. Silicon membrane shrinkage	(10 nN-1.2 μm)	11-2	depends on used objetive magnification	- Fabrication of homogenous polymer membranes - Phase-contrast microscope	Ease of implementation	- 2D, complex non-linear method - Variation of Young's modulus within membrane - Qualitative results	[82][83][84][85]
8. Piezoresistive Piezoelectric Capacivitive MEMS	12 nN-1 mN (piezoresistive) 1-500 μN (capacitive)	1-2	0.02 μm-5 μm	Microscope Micromachining	Large force and displacement range Tunable spring constant	- 2D - Measurement in one direction at once - Minimum size limited by micromachining	[86][87][88][58][89][90][91][92][93][45][54]

Method	Force Range	Cells per measurement	Spatial Resolution	Special Requirements	Strengths	Major Limitations	References
9. AFM	>10 pN- 1 μm	1-2	5 nm	AFM setting with inverse microscope	- Broad force range - High sensitivity	- 1D Measurements in **or** out-of-plane - High deviation due to calibration methods (>25%) - Sensitive to external noise	[94] [95] [96] [97] [98] [99] [100] [101] [102] [103]
10. Biosensors	1-100 pN $\geqq$ 1		nm- μm range, no specific values available	Fluorescence microscope Surface biofunctionalization	- High resolution technqiue on molecular scale - Molecular sensor with high selectivity	Limited force range No directional resolution Elaborate calibration method	[104] [105] [106] [107] [108] [51]

polydimethylsiloxane (PDMS) and hydrogels. The method strongly depends on homogenous polymer membranes with comparable Young's moduli all over the substrate surface, which is a challenging goal. To sense very small forces, extremely soft hydrogels have to be used. However, soft hydrogels change the cell behavior, which corrupts the force measurement results. Furthermore the data processing is highly time- and cost-intense.

A recently published three dimensional approach developed by Kronenberg and Gather et al. is elastic resonator interference stress microscopy (ERISM) allowing for force measurements in the piconewton range.[109][110] This method is based on interference measurements sensing the cell force induced thickness changes of a coated ultrasoft siloxane membrane, the so-called cavity. Here, every dark fringe of the interference pattern, which is a local minimum in the reflectance spectrum, corresponds to a position where resonant modes of the cavity are created by the coupling of the illuminating light. These minima are then used to calculate the cavity thickness. Based on stiffness maps of the cavity surface, the thickness then is correlated to certain external forces. This technique is extremely sensitive to thickness inhomogenities of the membrane, membrane reflection as well as transmittance. Additionally, homogenous material behavior all over the surface is a challenging task using polysiloxanes. Moreover, the cavity thickness has to be linked to a well-defined set of local minima in the reflectance spectrum and correlated forces collected in special databases to ensure precise force measurements. Besides a well-defined material property data set for the non-linear simulations of polysiloxanes and intense image as well as algorithmic data processing are necessary.

Furthermore, biosensors cover a broad field of established cell force measurements in the piconewton region where molecular recognition of a target analyte is converted into a measurable signal via a transducer. The measureable forces are then single-molecular forces within a cell or between the cell matrix surface and the substrate surfaces or another cell.[111][112] Here, Förster resonance energy transfer (FRET), photo-quenching, loss of fluorescence or changes in fluorophore emission properties are used to record more insights into mechanotransduction on the molecular level inside and outside cells in two and three dimensions.[105][106][112][113] Apart from this broad range of available and partly established techniques, there is currently no method available that offers the possibility of measuring cell traction forces in three dimensions in the nanonewton force range at once, generating reliable direct and quantitative data results as well as cost- and time-efficient settings all in one.

1.3 Concept

In the course of this project, a novel approach to measure forces quantitatively in three dimensions (3D) at once in the pico- to nanonewton range was persuaded. This setting shall allow for 3D cell traction force sensing of focal adhesion clusters in future applications. By combination with atomic force microscopy (AFM) which does not allow for local force sensing, the cells are stimulated externally in terms of mechanotransduction and additionally, global forces during cell rupture processes can be recorded. The approach for this new tool is shown in figure 1.3. Here, the different measurement steps (**1.-4.**) regarding an entire cell are presented in the left column and the corresponding microscopic events for one cell binding site on one sensor element are shown in a zoom-in in the right column.

First, a cell adheres to a force sensor element array. The array consists of a thin film of a biocompatible material that is structured via micromachining and consists of a regular pattern of sensor elements. Here, the cell only interconnects to the centre of each sensor element. On top of the cell, a biofunctionalized cantilever of an AFM is adhered to this cell. The position of the centre of the sensor element is recorded via an optical setup schematically depicted by a light source, a read beam and a detector.

In the second step, the cantilever is retracted and by this, the cell is stretched and only keeps contact to the sensor element contact plates. In consequence, the elements are displaced in- and out-of-plane due to the cell traction forces. This displacement is detected via the optical readout.

In dependence on the strength of the interaction forces of the cell with each sensor element, the cell loses its adhesion to the element centre plates when further retracted (see step **3.**). Other elements might be displaced out-of-plane (z-direction) or in-plane to a maximum. Finally, the cell binding sites entirely rupture and all sensor elements jump back to their original position (see step **4.**).

In this approach, the three dimensional element displacement is directly correlated to a distinct force in x-, y-, and z-direction on one local point of the cell matrix surface.

By use of an element array, several matrix points are recorded regarding their local force development and by this, the quantitative description of the cell force distribution during a rupture event

can be recorded. At the same time, the AFM cantilever measures the global force development during this rupture process. In consequence, a comprehensive data set of global and local cell forces will be available by just one experiment.

The central challenges of this project were the development of surface-integrated sensor elements based on established fabrication technologies for biocompatible materials that suite the dimensions
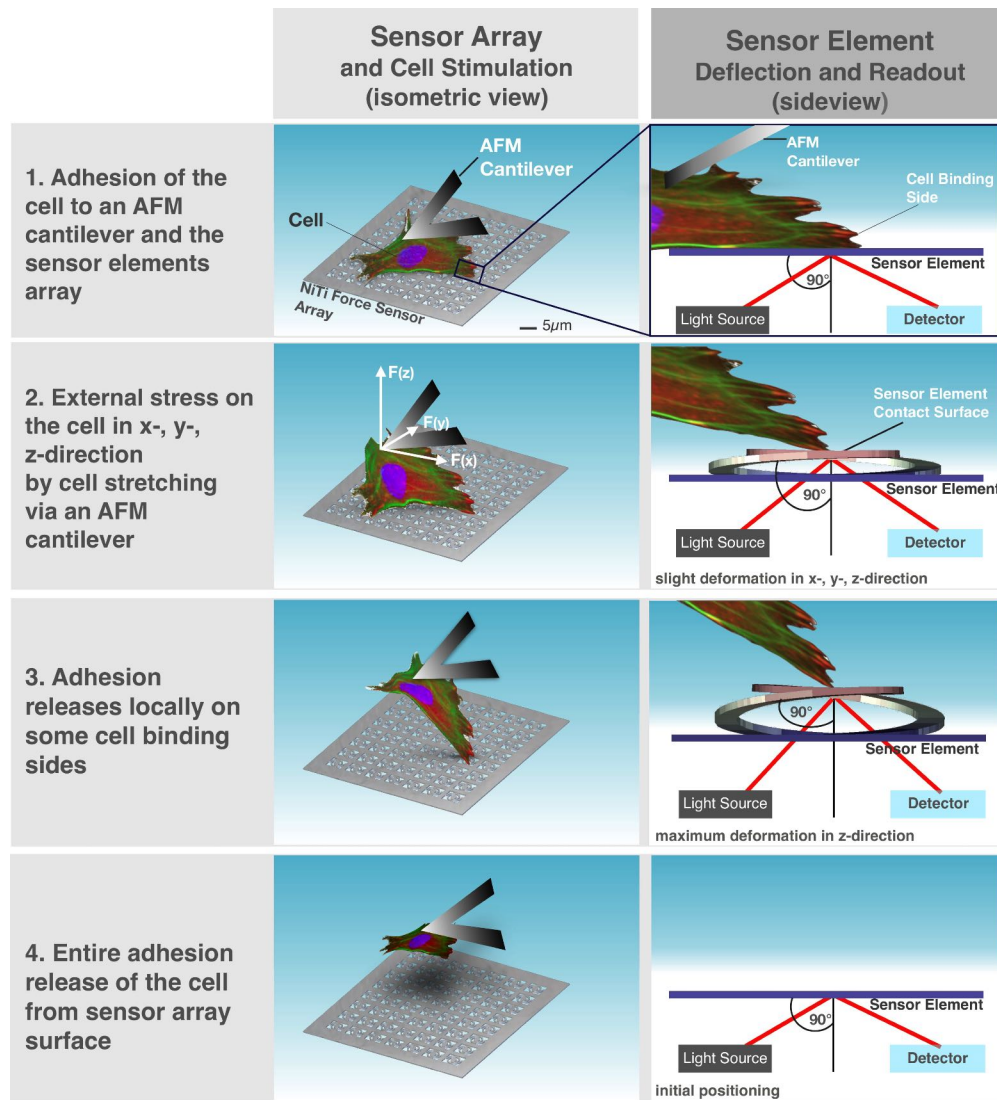

Figure 1.3: Schematic presentation of the concept for the mechano-optical readout in a combined local and global cell traction force measurement. In the images on the left, the overall process on top of the sensor array is shown, while on the right, the corresponding process on one single sensor element is depicted in sideview.

of an adhered cell, so that a maximum of local cell force data can be recorded per experiment. Here, the higher the density of sensor elements, the more comprehensive the depicted force distribution. Furthermore, the finally chosen technology and material should not only offer minimum structure dimensions, but most preferably also be cost-efficient and reproducible to fabricate affordable one-way sensor element arrays for future customer applications.

Moreover, a suitable design of the sensor element structures was important to create comparable force sensitivities in all three dimensions and support optical readout based on interference measurements. The most complex part was the choice of an appropriate optical method to record the deformations of the sensors in real time, in a way that even very small displacements down to the nanometer range corresponding to cell forces in the nanonewton region were accessible in 3D. In this product development, the setting should be preferably easy to handle and cost-efficient with regard to future use by random customers. The overall list of design requirements is presented in chapter 2.

Based on the above described goals, five different sub-projects have been defined and lead in the course of this central PhD project (see figure 1.4). These were:

1. Sensor Element Design and Optimization,

2. Sensor Element Fabrication and Characterization,

3. Sensor Element Calibration, the development of an approach for

4. Optical Readout and

5. Sensor Surface Functionalization.

The order of the different chapters was adapted to the different prototyping steps starting from scratch with the computer added design and optimization of an appropriate sensor element. Based on the definition of the sensor element design, the fabrication and characterization of the corresponding sensor element arrays out of three different materials was established. Afterwards, the most reliable calibration techniques chosen and used for these sensor arrays were tested and established. The fourth chapter includes the central part of the sensor prototyping, which was the choice and implementation of an appropriate three dimensional optical readout. The last sub-project consisted of the development of a high-throughput functionalization of these free-standing elements by means of ink-jet printing.

Each chapter includes a theoretical background, materials and methods as well as the presentation of the results and their discussion.

Finally, the results are compiled in chapter 7 giving an outlook on the next steps within this project the final product maturity, possible improvements and future applications of the presented sensor system prototype.
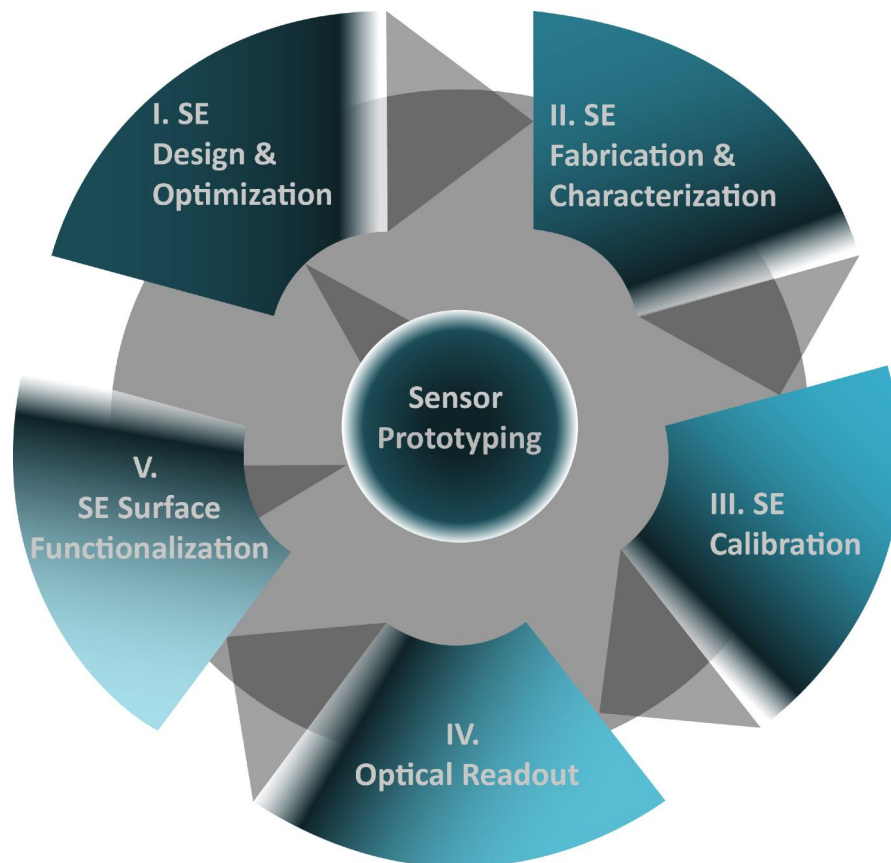

Figure 1.4: Sensor system prototyping was run implementing five different sub-projects, which are presented within this thesis: Starting from I. the sensor element (SE) design and optimization (chapter 2), the chosen SE designs were then fabricated according to the descriptions in II. SE Fabrication and Characterization (chapter 3). The fabricated SEs were afterwards calibrated as presented in III. SE Calibration (chapter 4). The mechano-optical readout system has been conceptualized and tested in sub-project IV. Optical Readout (chapter 5) and finally, a possibility for a distinct adhesion control on the sensor element array is presented in V. Sensor Surface Functionalization (chapter 6).

2 SE Design and Optimization

The prototyping of a sensor from scratch according to well-defined micro-sensor features is a challenging and rather complex task. After the first step of having defined the sensor requirements including aspects like a high mechanical sensitivity to forces in the pico- to nanonewton range or a force readout to measure forces in three dimensions at once, additional tools are needed to define the starting point to useful sensor shapes, but also to validate the most appropriate design for further fabrication. For that purpose, the so-called finite element method and topology optimization have been chosen within this project as well established theoretical methods in prototyping. These are presented theoretically in the following chapter as well as the sensor requirement list. In this way, the entire design and optimization procedure in this sensor system prototyping should to be reduced to a minimum of material, time and cost.

In a next step, different sensor shapes according to the requirements list were developed and analyzed by means of the simulation tools. Ten of the most promising designs are introduced and discussed in this chapter, followed by a determination of the most sufficient sensor structure.

2.1 Finite Element Analysis

2.1.1 A mathematical insight

Finite Element Method (FEM) is a numerical simulation method based on the approximation of the real complex solution by means of discretization via numerical model equations. The use of FEM to analyze a phenomenon such as material deformations or heat transfer under defined boundary conditions is then called finite element analysis (FEA). In the following, the fundamental mathematical background is exemplified for a 1D problem by the so-called direct stiffness method based on the pub-

lications of Logan et al. and Chen et al. [114] [115] This method is one of the structural analysis meth-
ods, also known as matrix stiffness method, and best suited for the algorithm-based computational
analysis of more complex problems. [116] A spring as shown in figure 2.1., with a length L in relaxed
state and a spring constant k, is constrained in point
1, ends in point 2 and is displaced in x-direction by a
force F. The points are equal to so-called nodes which
are coordinate locations in space where the degrees
of freedom (DoFs) are defined. Here, the DoF is one
displacement $u(x)$. The displacement function is then
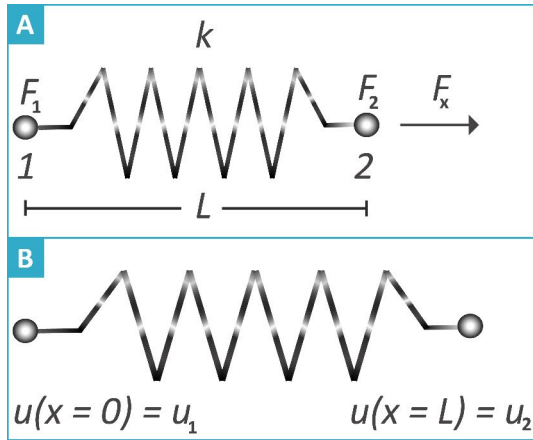defined as: [114] [115]

Figure 2.1: Schematic presentation of the elongation u_2 (B) of a spring with spring constant k, of length L constrained in point 1 and effected by a force F in point 2 in x-direction (A).

$$u(x) = a_1 + a_2 \cdot x = [1x] \begin{pmatrix} a_1 \\ a_2 \end{pmatrix} \qquad (2.1)$$

The amount of coefficients a_i depend on the
amount of DoFs. With $u(x = 0) = u_1 = a_1$ and

$$u(x = L) = u_2 = a_2 \cdot L + a_1 \implies a_2 = \frac{u_2 - a_1}{L}:$$

$$u(x) = u_1 + \frac{u_2 - u_1}{L} x = (1 - \frac{x}{L}) \cdot u_1 + \frac{x}{L} \cdot u_2 = [(1 - \frac{x}{L}) \cdot \frac{x}{L}] \begin{pmatrix} u_1 \\ u_2 \end{pmatrix} \qquad (2.2)$$

Introducing the so-called interpolation functions N_i, which describe the variation of the displace-
ments over the element with $N_1 = 1 - \frac{x}{L}$ and $N_2 = \frac{x}{L}$ for this spring:

$$u(x) = [N_2 N_1] \begin{pmatrix} u_1 \\ u_2 \end{pmatrix} \qquad (2.3)$$

Based on Hook's Law:

$$F = k \cdot \delta \qquad (2.4)$$

with: $F = \begin{pmatrix} F_1 \\ F_2 \end{pmatrix}$, $F_1 = k \cdot (u_1 - u_2)$, $F_2 = k \cdot (-u_1 + u_2)$ and $\delta = u_2 - u_1$, it is:[114] [115]

$$\begin{pmatrix} F_1 \\ F_2 \end{pmatrix} = \begin{bmatrix} k & -k \\ -k & k \end{bmatrix} \begin{pmatrix} u_1 \\ u_2 \end{pmatrix} \tag{2.5}$$

Here: k equals $\frac{E \cdot A}{L}$. The matrix includes the entire material and structure information by means of the Young's modulus E, the cross-sectional area A and the length of the spring. It is also known as the local or element stiffness matrix $\Bbbk$. Regarding this example, an analytical solution can be found easily. But describing an entire, more complex object over all finite elements e, the global stiffness matrix is then defined as:

$$K = \sum_1^e \Bbbk_e = [K] \tag{2.6}$$

With: $F = \sum_1^e F_e = \{F\}$, the master stiffness equation of structural analysis then is:

$$\{F\} = [K]\{u\} \tag{2.7}$$

Based on equation 2.7, more dimensional and complex structural problems can be solved numerically by first defining the elements of the stiffness matrix. Then the structure is analyzed with regard to the force effecting the structure or the displacement induced by the load. Here, different analysis methods can be utilized such as linear static or dynamic analysis as presented in subchapter 2.1.2.

Within this work, pico- to nanonewton forces are assumed to induce small deformations of the sensor elements. In this deformation range, the stress within the materials is assumed to remain in the linear-elastic region, where stress is direct proportional to strain as presented exemplarily in figure 2.2. Here, a stress-strain-diagram of an arbitrary metal is presented with a linear region at low stress values. Within this range, linear static analysis can be run, in which the amount of sensor element deformation is direct proportional to the effecting force according to Hook's Law. In this region, the structure returns to its original shape after unloading. Furthermore, the boundary conditions including the constraints as well as the magnitude and direction of the loading are time-independent.
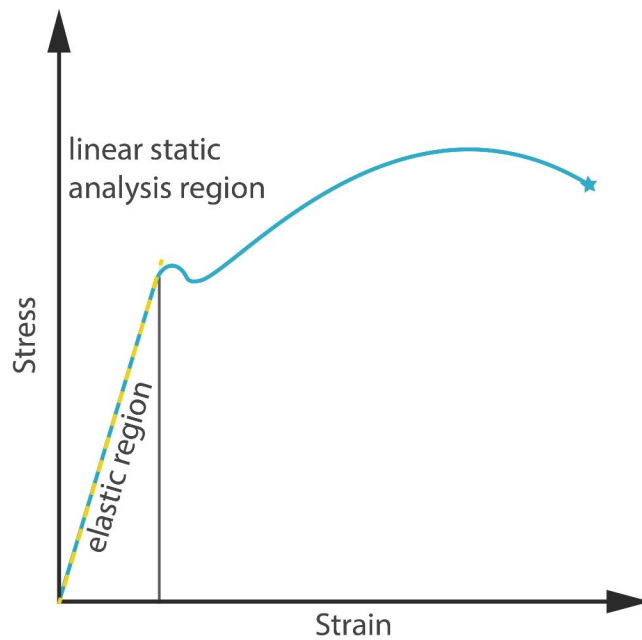
Figure 2.2: Exemplary schematic stress-strain diagram of an arbitrary metal. At low strains, stress and strain are direct proportional defining elastic material behavior, which is well described by linear static FEA procedures and were used within this project.

The forces develop slowly and gradually to their peak value and by this, induce negligible accelerations and velocities. So, inertial and damping properties are ignored. In this case, the structure's stiffness matrix is constant and therefore, the linear static simulations run very fast compared to non-linear problems.

2.1.2 Practical insights and relevance

The first published structural analysis in the design of aircraft wings within the aerospace industry in 1956 by Turner and Clough at Boeing set the beginning of a new era in industrial prototyping and product development. Ten years after this publication, Clough's terminology for their numerical simulation method was accepted among specialists and the finite element method (FEM) was born. [117] [118] [119]

In 1969, Zimmer and his group at Daimler AG then set a milestone based on Turner's and Clough's work using their self-written software ESEM (Elasto-static Element Method) for the first time to design the entire bodywork and frame of a new car model (Mercedes-Benz 220D). In consequence of

their success and the invention of the computer technology, fast growing and cost-effective industries like the automotive sector soon integrated comparable simulation methods within their daily routines to reduce design and service costs. [120]

Today, FEM is a well established tool not only in the everyday work of industrial product and development engineers, but also in natural sciences, geophysics or medical technologies [121] in and outside academia. [122]

The modern simulation procedures provide several significant benefits such as efficient and less expensive design cycles, enhanced design and early evaluation of critical design parameters, analysis of arbitrary geometries, an increase in accuracy or the reduction of research and development costs. [123] [124] [125]

Due to the broad range of applications, a diversity of different FEM programs were developed to simulate phenomena like heat transfer in dynamics, velocities in flow analysis, buckling or bending in stability analysis, sound propagation in acoustics or the field distribution in transistors in one, two or three dimensions. In the course of this project, structural analysis were used to analyze linear static deformation behavior of sensor elements in three dimensions. [125]

Currently, several dozens of open-source and licence-based FEM packages are available of which NASTRAN®, SolidWorks®, ABAQUS®, ANSYS®, Pam-Crash®, LS-DYNA® and HyperWorks® are the most widespread once, especially in industry. [126] In the course of this work, the different software suites were validated and compared regarding their prizing and solutions packages of which HyperWorks® was chosen due to its comprehensive range of applications and as it is a low-price FEM full-package. This software offers the most powerful meshing tool HyperMesh® on the current pre-processor market (2019). Moreover, it includes different solvers i.e. OptiStruct® for linear FEM problems like in this project and Radioss® as one of the fastest solvers for non-linear tasks that will be solved in future projects for non-linear material behavior as for polymeric substrates.

The different analysis steps are summed up in figure 2 as exemplified for Altair HyperWorks®. The pre-processing starts with the importing or developing of a geometry of the prototype by use of a computer aided design (CAD) software or in HyperMesh® directly (figure 2.1, **1**). Afterwards, the dimensions are chosen accurately by the user as the solver code solves the problem dimensionless. Then the analysis type such as static, dynamic, buckling, and the definition of the material parameters
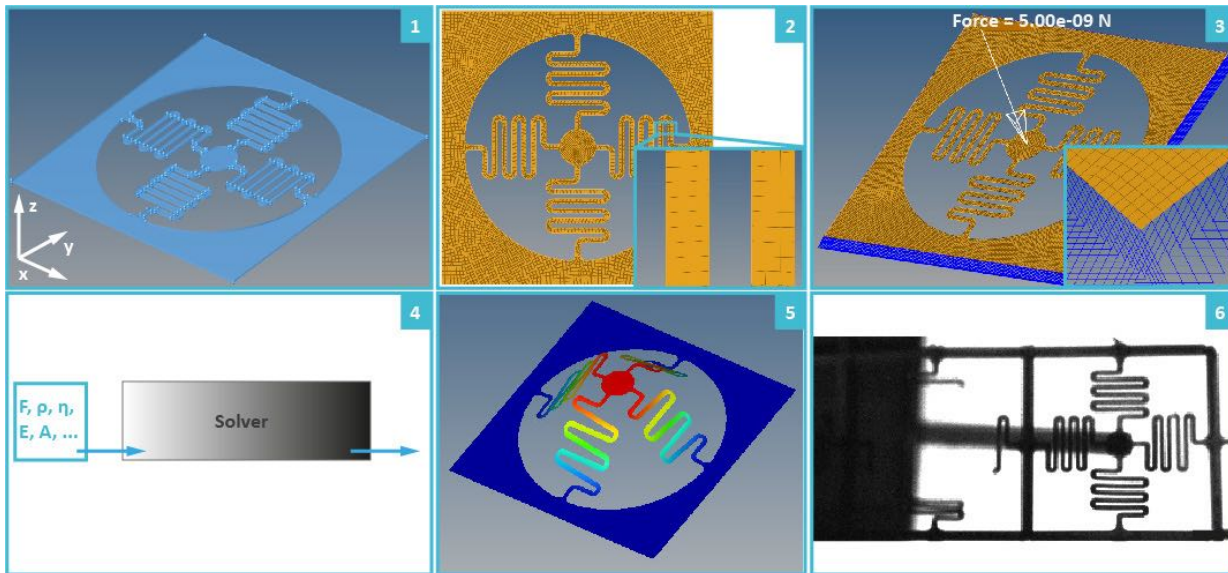
Figure 2.3: Schematic presentation of the different FEA process steps based on the software suite HyperWorks[®] and implemented for the exemplary sensor element structure investigated within this thesis. **1** Design of the structure in a computer aided design software and exported as a step (Standard for the Exchange of Product Data) file. **2** Import of the design in a pre-processor to create a sufficient grid of nodes by meshing and definition of the material properties, the analysis type as well as the dimension of the structure. The zoom presents the mesh in more detail. **3** Definition of the boundary conditions: the blue triangles (see zoom in) at the edges of the sensor element represent the constraints, while the white arrow marks the normal force of 5 nN affecting the central node on the sensor contact plate. **4** Running of a linear static analysis by means of the solver OptiStruct[®] based on the material input data such as force, density, Poisson ratio, Young's modulus, etc. **5** Analysis of the simulation results by use of a post-processor (here HyperView[®]) in a three dimensional animation where the displacement is additionally outlined by a color height scale with red representing regions of high deformation and blue showing regions of no deformation. To highlighten the out-of-plane displacement, the original displacement is amplified by a factor of 500. **6** The FEM results are then evaluated in macroscopic test settings and rerun in case of a variation between theoretical and real data. Here, an axial atomic force spectroscopic setting is presented testing the sensor element centre plate via a rectanguar cantilever in z-direction.

are chosen and the entire object is discretized into finite elements creating a grid, the so-called mesh (figure 2.1, **2**). An appropriate choice of the element type is of major importance for the final quality of the mesh and the accuracy of the solver process. In general, the quality of a mesh strongly depends on the task and the geometry to be simulated and includes several aspects like

no or a minimum amount of distorted elements or sufficient element size and shape for the given purpose. Within the FEM software, the interpolation error is correlated to the element-based mesh quality metrics that analyzes the asymptotic behavior of bounds for minimum error. Hence, a convergence of the finite element method is proved for each simulation. [127] In general, truss and beam elements are used within 1D FEM problems, quadratic and triangular membranes, shells and plates for two dimensions like thin film simulations, and solids like tetrahedral, brick or combined shapes for simulations in three dimensions. In this project, the deformation of a sensor element thin film was treated as a 2D problem using shell elements as the thickness of the element was much smaller than its edge lengths.

On the contact points (1D), lines (2D) or areas (3D) of the elements, the software sets the nodes. The type and the amount of DOFs per node depend on the analysis type and therefore can take a lot of different forms. In a static analysis, for instance, the DOFs are displacements in three directions while in fluid dynamics, it is pressure that effects in three directions and a time-component. Finally, the boundary conditions are defined, setting the constraints of the geometry as well as the loads such as forces that effect the geometry (figure 2.1, **3**).

Having completed the pre-processing, the problem is then solved by the solver OptiStruct® (figure 2.1, **4**) and the results can be analyzed in post-processors like HyperView® as contour plots, diagrams or animations (figure 2.1, **5**). After testing the results in real experiments (figure 2.1.6), this routine might be repeated iteratively until the most sufficient prototype result is achieved (restart at a modified version of figure 2.1, **1**). Differences between the FEA and the experimental results can be caused by various reasons like an unappropriate choice in software, in which the simulation algorithms do not suite the numerical problem, an unsufficient abstraction of the problem itself or a wrong choice in meshing parameters like boundary conditions, element size, type or shape, just to mention the most relevant aspects. [128]

2.2 Topology Optimization

With the invention of the FEA, the design process was reduced to an iterative process of application of design variables, simulation by given boundary conditions and analysis of the results based on the

defined requirements. In the 1980s, this numerical procedure was mathematically enhanced by the introduction of objective functions such as object weight or stiffness. By this, the so-called structural optimization problem was defined as "the reverse problem of structural mechanics". Here, structural variables are determined for a defined structural behavior instead of setting these parameters to obtain a structural object response achieved by FEA. [129] [130]

Today, a variety of different optimization methods are known, of which three central optimization types are representatively mentioned here: 1. Topography Optimization, which is the optimization of the geometrical object surface to enhance the object reinforcement within the design space. 2. The size optimization supports optimizing the properties of designable elements such as bars or plates for two dimensional structures. And 3. the topology optimization, which is used to achieve an optimum component geometry by optimizing the material distribution in a defined design space. [129] [130]

Within this project, the latter was used to determine the most appropriate sensor structure for further analysis and optimization. For a deeper insight into this simulation process, the fundamental mathematical background is therefore discussed in more detail based on the publications of Bendsøe and Beckers. [129] [131] [132] [133]

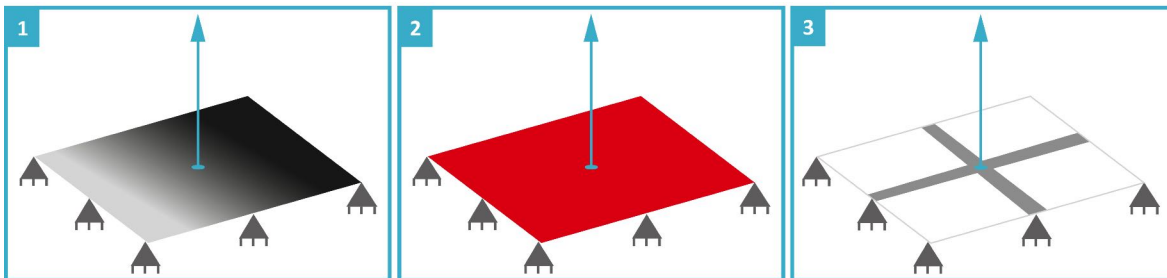### 2.2.1 Mathematical Fundamentals

Figure 2.4: Schematic presentation of the different process steps within the topology optimization exemplified for a two-dimensional problem: a membrane that is constrained on all four edges and with a force (blue arrow) affecting the membrane centre. **1** Definition of the constraints (grey triangles) and loads (blue arrow) effecting the geometry, here: a membrane. **2** Definition of the design space Ω (red area), **3** Optimization procedure for maximum stiffness and minimum weight with presentation of the partial space Ω_{opt} with (grey stripes) and without material (white area).

A design space Ω and its boundary conditions are defined for a membrane (grey square in figure 2.3.1) as shown in figure 2.3. By means of topology optimization, a subspace Ω_{opt} of a certain material distribution is achieved fulfilling the required criteria (see the red membrane in figure 2.3. 2.). To determine the filled (grey) and unfilled material (white) space (see figure 2.3. 3.), the design space is then discretized by finite elements. Introducing the density function $i(x)$, with x being the spatial position of one point in the design space, the filled and unfilled areas are defined as: [129] [131]

$$
i(x) = \begin{cases} 0 \;, if \; x \; \epsilon \; \Omega/\Omega_{\text{opt}} \\ 1 \;, if \; x \; \epsilon \; \Omega_{\text{opt}} \end{cases}
\tag{2.8}
$$

with 0 for no material and 1 for space with material. The volume integral of the sub design space Ω_{opt} for any function $g(x)$ can also be written as:

$$
\int\limits_{\Omega_{\text{opt}}} g(x) \; d\Omega = \int\limits_{\Omega} g(x) \cdot i(x) \; d\Omega
\tag{2.9}
$$

For a homogeneous, isotropic material, a linear elastic analysis type is supposed. In case of single load effecting the design space, the standard approximation is the definition of the maximized global stiffness of the structure. Based on the equivalence between a maximum global stiffness and a minimum work of the external load, the so-called compliance function $c(u)$ can be defined as follows: [129] [131]

$$
c(u) = \int\limits_{\Omega_{\text{opt}}} f^{\mathsf{T}} \cdot u \; d\Omega + \int\limits_{\Gamma_{\text{t}}} t^{\mathsf{T}} \; d\Gamma_{\text{t}} = \int\limits_{\Omega} f^{\mathsf{T}} \cdot u \cdot i(x) \; d\Omega + \int\limits_{\Gamma_{\text{t}}} t^{\mathsf{T}} \cdot u \; d\Gamma_{\text{t}}
\tag{2.10}
$$

with f - loads, u - displacements that need to fullfill equilibrium, compatibility and constitutive equations, t - boundary conditions, Γ_{t} - part of the boundary, where the boundary conditions are imposed. The overall object volume for a homogeneous distribution of the boundary conditions

imposed on the displacements is then defined by:

$$V = \int\limits_{\Omega_{\text{opt}}} d\Omega = \int\limits_{\Omega} i(x)\, d\Omega \tag{2.11}$$

To minimize the compliance $c(u)$ in equation 2.3 and find the optimum volume, the problem is then solved by discretization of the design space and an algorithm implemented iterative process following the boundary conditions. Here, so-called Multiple Objective Optimization (MOO) algorithms such as the well established Strength Pareto Evolutionary Algorithm (SPEA) are used, but differ between the various FEM suites.[134][135] The interested reader might consult further literature for more detailed information that are not presented here for reasons of significance for this work.

In this project HyperWorks solidThinking Inspire® 2017 was used for topology optimiziation. Here, the object is meshed by a combination of HyperMesh® and Simlab® and analyzed by background algorithms via the solver OptiStruct®.

Based on the mathematical Ansatz of Bendsøe, the density function (see term 2.8) can have continuous values between 0 and 1, which includes not only a differentiation between material or no material (see figure 2.4.3), but also average densities. These intermediate values cannot be realized in actual fabrications and therefore need to be converted into discrete values. For this purpose, so-called filters are used that include penalization factors to exclude values between 0 and 1.[136][137]

2.2.2 Design Requirements

In the course of the prototyping, the development of the new sensor system is started by defining the central requirements based on the field of its application as a biocompatible mechano-optical pico-to nanonewton 3D force sensor system. These requirements are listed in the following table. The second step is the design process, in which the suitable sensor element design is determined regarding the proper choice of the device material, its dimensions, sensitivity and torsion stability for precise optical readout. These aspects might interfere with other limitations for the entire sensor system like finances or producability that were not predictable from the beginning. For a rapid and comprehensive overview on the diverse project constraints, the following list includes all of the requirements in the design, fabrication and handling of the novel sensor system.

Requirements	Ansatz
biocompatibility and high deformability	chosen sensor materials with low Young's moduli: • nickel-titanium (NiTi) • amorphous silicon (a-Si) • polydimethylsiloxane (PDMS)
surface-integrated device	• flat 3D-deformable sensor design • free-standing
sensitivity	• comparable force sensitivity in x-, y- and z-direction: measurement of normal and shear forces at once • force sensitive in a range of 500 pN to 50 nN • thin film sensor fabrication
high spatial force-resolution (for cell testing)	• compact sensor design, • sensor miniaturization according to the fabrication limits • decoupling of the sensors by rigid frames
force distribution measurements	arrangement of sensors in arrays
optical readout for 3D-measurements in combination with AFM	• interference-based deformation measurements • high sensor surface reflectivity • torsion-stable sensor design • flexible installation setting: direct combination with AFM setup needs to be possible
easy to handle and cost-efficient setup for high-throughput measurements	cost and handling analysis of interference settings
control of the cell adhesion sites to the sensor element surface	local biofunctionalization of the sensor element contact plate based on a combination of a block-copolymer gold-micelle solution and a non-contact printing method

2.3 Nickel-titanium and a-Si based Sensor Elements

Simulations of different sensor element designs were carried out based on the material parameters of nickel-titanium and amorphous silicon. The fundamentals of these two materials are therefore briefly introduced within the following sections. More detailed information can be found in the cited literature, when needed.

2.3.1 Fundamentals: Nickel-Titanium (NiTi)

With their comprehensive report and patent in 1965, Bühler et al. gave the initial point in the application of Nickel-titanium (NiTi), a representative of alloys, later known as smart materials, possessing two special functional properties: the shape memory effect and superelasticity. [138] [139] The shape memory effect describes the deformation of the alloy at low temperatures and the reversal of this deformation to its original shape at high temperatures. The effect was first described by Greninger and Mooradian in 1938 for Cu-based alloys and is caused by the unique crystallographic transformation within the material. [140] [139] Regarding NiTi, the shape memory is observable for Ni percentages between 49.3 to 51 at%. [141] [142] Here, the stretched monoclinic crystal B19' structure of the low temperature NiTi phase (martensite) is transformed via a temperature increase into a body centered cubic symmetric B2, high temperature phase (austenite) and vice versa. [139] Superelasticity or pseudoelasticity describes the recovery of materials after large stress above 8% and corresponding stress-strain hysteresis in load-unload procedures. [143] This reversible elastic respons to mechanical stress upon the austenite finish temperature and within a very small temperature range is caused by a reversible phase transformation from austenite to martensite via stress induced boundary movements within NiTi. Elongation of the tensile stress is achieved by the material deformation. When removing the stress, the corresponding strain returns to its initial value in the austenite phase. [144] [145] Hence, the material can be loaded and unloaded periodically. Moreover, it is known for its corrosion resistance and fatigue properties [146] making it an interesting alloy for longterm applications like actuators or cryo connectors and hydraulic couplings in aerospace applications, [147] [148] [149] [150], but also as "[...] fasteners, electrical connectors, [...] sensors, release mechanisms, triggering devices, fuel injection or ventilation control [...]," according to Bhaumik et al.. [139] In combination

with its biocompatibility[151] and bioactivity[152][153] as well as its good ductility of more than 20%
in the austenite phase and 50% in the martensite phase,[148][139] NiTi has gained significant impor-
tance in the biomedical field.[147][154] It is used for protheses like bone binding implants[152],[155] in
orthopaedics,[156] for medical instruments,[157] or endovascular stents,[158][159][160]

In this project, NiTi has been chosen due to its 1. superelastic behavior, 2. its low Young's modu-
lus of 75 GPa for the austenite phase[161][139], 3. its biocompatibility and 4. corrosion resistance
for future cell experiments as well as 5. the accessibility of established micromachining processes
for the fabrication of fully biocompatible microsensor elements with a high resistance against outer
mechanical impact and good material deformability.

2.3.2 Fundamentals: amorphous Silicon (a-Si)

Silicon is the second most abundant element on earth, which makes about 26 % of the earth's crust in
weight, a tetravalent metalloid and semiconductor in its crystalline form.[162] In times of automation
and digitalization, this element and its modifications have gained central significance in every day life
in terms of transistors,[163][164] microchips,[165][166] solar cells[167] or materials for construction,[168]
automotive,[169] textile,[170] medical,[171][172] coatings and color,[173][174] paper,[175] rubber,[176]
cosmetics[177] or polymer industry.[178][179]

In 1808, Louis Jacques Thénard and Joseph Louis Gay-Lussac (Paris) as well as Sir Humphry
Davy (London) first described the formation of brown silicon when heating potassium in dry "gaz
fluorique" (SiF4).[180][181] By this, the non-crystalline form of silicon, amorphous silicon (a-Si), has
been synthesized for the first time. In this formation, the long-range interactions between silicon
atoms forming tetrahedral structures within the crystalline lattice of silicon are replaced by short
range interactions creating a random network of silicon atoms. Here, the fourfold coordination of
each atom is corrupted and hence, there are atoms with free valences, so-called dangling bonds,
which cause an anomalous electric behavior of the material.[182][178]

Little is known about the mechanical properties of a-Si, but it is well-known for its biocompatiblity
and its manifacturability. Today, the fabrication of a-Si thin films is the most well developed of
the thin film technologies being on the market since the 1960s. These thin films are much more
uniform over large areas than mono- or polycrystalline silicon, can easily be fabricated in a variety

of shapes and sizes and possess a higher resistance to heat and outer impacts than crystalline silicon layers. By passivating a-Si with hydrogen to a-Si:H, the reduction of the electronic defect density and hence, an improvement of its seminconductor properties due to the saturation of the dangling bonds by hydrogen can be achieved. [183] [53] Due to 1. its electrical properties, 2. its low-cost and simple thin film producability, 3. its environmentally friendly properties lacking heavy metal doping like cadmium, as well as 4. the possibility of depositing large areas of ultrathin, homogenous a-Si:H layers on inexpensive materials such as glass, stainless steel or plastic, [184] it is major application is within the photovoltaic industry as solar cells [185] [53] in pocket calculators or solar panels, [186] in microelectro-mechnical systems (MEMS), [187] as well as in thin-film-transistor liquid-crystal display (TFT-LCD) technology. [188] [189] Due to its low temperature deposition, it can be deposited on flexible substrates and in roll-to-roll manufacturing techniques, which makes it an interesting candidate for wearable electronics and flexible solar panels. [190] Furthermore, a-Si is sensitive to visible light within a wavelength range of 400 nm to 800 nm, for which reason it is used within light sensors such as photodiodes. [191] [192] In the course of this project, amorphous silicon has been chosen due to its biocompatibility, [193] its low Young's modulus of 80 GPa [194] ranging in the region of austenitic NiTi and its fabrication accessibility for homogenous thin films. [184]

2.3.3 Materials and Methods

The topology optimization was run in Altair SolidThinking Inspire®. Due to the software based lower limits regarding the object dimensions in μm range, a membrane of minimum edge length 1 x 1 mm and 4 μm thickness was first drawn based on the thickness to edge length ratio of the real sensor and constrained on all four edges. A force of 1,25 μN was applied to the centre of the membrane in x-,y-, and z-direction. The topology optimization of the membrane was then run to create a design of minimum stiffness and 15% of the total membrane mass, by which the suitable shape of the element was still distinguishable and physically reasonable. Based on the results of the topology optimization, different sensor element designs were created with one, two, three and four sensor arms and compared via finite element analysis. For better comparison, the sensor arm length of each design was set to 20 μm.

FEM analysis was run in Altair HyperWorks®. Due to the small sensor thickness compared to

the sensor edge length and to reduce the computational time, the 3D CAD model of each sensor was first reduced to a mid-surface 2D model. Within the pre-process, a finite element mesh was generated automatically by use of the HyperWorks® included preprocessor HyperMesh® using a mixed mesh type of squares and triangles. The mesh density was iteratively optimized to a minimum of elements in order to ensure an accurate result and minimum computational time.

Each sensor model was constrained at its inner egdes of the frame. A force of 5 nN was applied to the centre node of the sensor plate. Linear-static analysis based on an isotropic material behavior was then run in x-, y- and z-direction using the solver OptiStruct®. The material parameters and values for Nickel-Titanium (Ni:51%, Ti:49%) and amorphous Silicon (a-Si) are listed in table 2.1.

Material	Nickel-Titanium (austenite)[161]	amorphous Silicon
Youngs Modulus / [MPa]	75 000	80 000[194]
Poisson's Ratio	0.3	0.22[194]
Mass Density / [g/cm]	6.34	2.33[195]
Thermal Expansion Coefficient / [K^{-1}]	$1.1 \cdot 10^{-5}$	$0.42 \cdot 10^{-5}$[196]
Device Thickness / [nm]	50, 100, 200, 300, 400	100, 200, 300, 400
Material Behavior	isotropic	isotropic

Table 2.1: FEM relevant material parameters of austenite nickel-titanium (NiTi) and amorphous silicon (a-Si).

2.3.4 Results and Discussion

The results of the topology optimization for deformations of a membrane in x- (1), y- (2) and z-direction are presented in figure 2.5.

The membrane was constrained on its edges as indicated by the red dots in figure 2.5.2. With forces effecting the membrane centre in-plane (1, 2), material (blueish colored area) is needed along the effective direction. Consequently, sensor element shapes similar to bending beams are most suitable. Here, the centre of the element seems to be irrelevant with regard to the force transfer and hence, is reduced to a string.

In figure 2.5.3., the most promising topology for an out-of-plane force application is shown. A cross like shape with material enhancements in the transfer region between the frame and the sensor element as well as in the sensor centre support the force transfer in z-direction. The wave-like edges
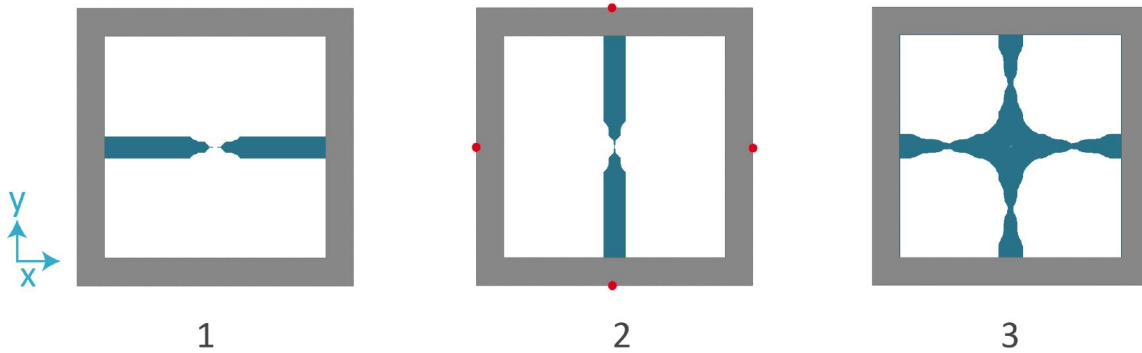
Figure 2.5: The design starting point was a topology analysis of a membrane as shown in figure 2.2 affected by a force impacting the membrane centre in **1** x-, **2** y- and **3** z-direction. The gray colored areas represent the constrained frame, while the blue parts show the maintained device material for a structure with minimum mass.

of these designs are due to the algorithm implemented penalty factors creating the mathematically most suitable design. In consequence, it is up to the engineer to translate this shape into a design that can be fabricated easily. Each element is included in a grey frame, which was set at the beginning of the optimization process and corresponds to the rigid frame as defined in the requirements list to decouple the different sensor element in one array.

Comparing the topology of 1, 2, and 3, the combination of the sensor element shape for in-plane deformations appear to be implemented in the third topology. In consequence, sensor designs consisting of four sensor arms and a centered contact plate were taken as a basis for the most suitable sensor element prototypes.

Regarding the development of a sensor element of high force sensitivities in all three-dimensions, the stiffness of the sensor design has to be minimized additionally. Here, the Young's modulus of the material, the material thickness, the sensor arm design and the width of the sensor arm were taken into consideration. The material could not be chosen randomly and just based on its elasticity value, but its choice was as well related to its biocompatibility, the access to established fabrication technologies and its producibility in micrometer dimensions. For that reason, the stiffness of the sensor material could not be tuned and was set to $75\,000$ MPa for austenite NiTi[161] and $80\,000$ MPa[194] for a-Si.

On the other hand, the material thickness could be manipulated, but was determined by the need

of an easy handling and stability against outer influences like mechanical impacts as well as the limits of the fabrication procedure (see chapter 3). In general, the spring constant of the sensor element is inversely proportional to the cube of the material thickness. Therefore, the thinner the sensor element material is the higher the mechanical deformability. In figure 2.6, the dependence of the out-of-plane deformation behavior of a NiTi cantilever on the material thickness h is exemplified for six different h values. To evaluate the FEA results (see figure 2.6 **B**, dark blue line with dots) for a thickness of 50 nm, 100 nm, 200 nm, 300 nm, 400 nm and 500 nm, an analytical calculation was additionally run based on the model of the one-sided clamped cantilever for a constant force impact **F** of 5 nN as shown in figure 2.6 **A** (turquoise line with squares).

The displacement s was then calculated by:

$$s = \frac{l^3}{3EI}F \tag{2.12}$$

with: $I = \frac{Ah^3}{12}$. As can be observed in figure 2.5 **B**, the analytical results overestimate the displacement for each thickness compared to the results of the FEA by constantly 23 %. This is due to the idealization within the beam theory, on the one hand and the discretization of the model by shells within the FEM, on the other. [128]

Regarding the consistency of the result differences and since, the displacements are in the same range, the FEA values are in good agreement with the analytical results and hence, the simulated data are reliable. Regarding the FEM data, material thicknesses bigger than 200 nm allowed maximum displacements in the lower nanometer region. So, 300 nm of NiTi cause an out-of-plane displacement of about 30 nm, 400 nm of 13 nm and 500 nm of 6.7 nm. While smaller thicknesses than 200 nm would allow for displacements in the upper nanometer and lower micrometer range, but would be difficult to fabricate and handle without destruction. So for a 100 nm layer, the deformation range is 1 μm and 6.6 μm for 50 nm of NiTi. Due to the concept of an optical readout based on interference measurements, resulting displacements in the upper nanometer region were preferred as the resolution of the optical system would be limited by the wavelength that is used. Consequently, out-of-plane movements down to 150 nm to 200 nm would be possible, if UV emitting light sources were chosen. Displacements in the μm region could cause measurements out of focus,and hence, appropriate
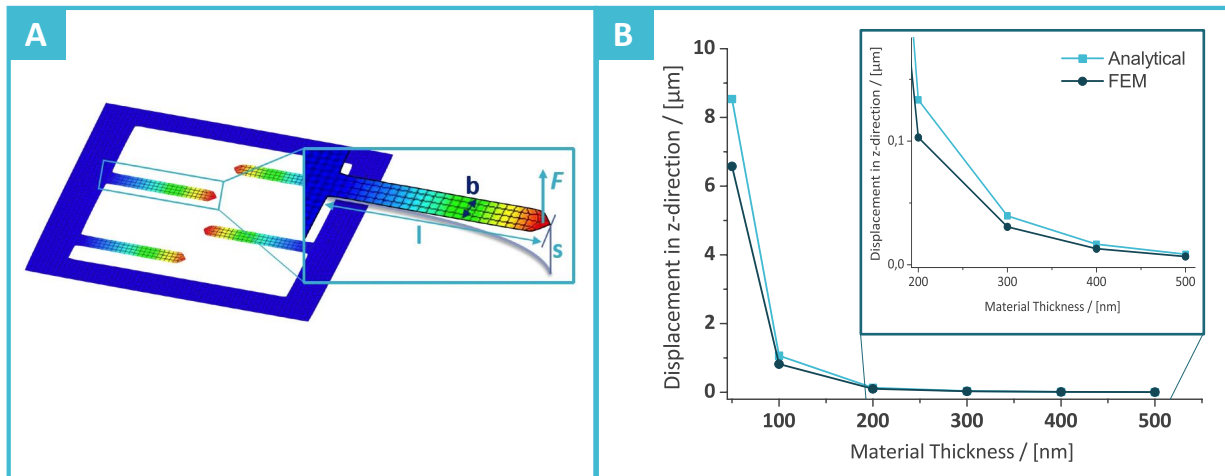
Figure 2.6: **A** Meshed reference cantilever to evaluate the quality of the FEA result in comparison to an analytical solution based on the model of an one-sided clamped bending beam. The cantilever length l was set to 20 μm, the beam width b was 2 μm, the thickness h and the load F was 5 nN. s indicates the displacement in z-direction. **B** FEA and analytical results regarding the dependence of the sensor element deformability in z-direction on the material thickness h for a cantilever design shown in **A**. Here, a thickness of 50 nm leads to a maximum deformation of 6.6 μm, 100 nm to 820 nm and 200 nm to about 100 nm. In the inset box, a material thickness between 200 nm and 500 nm is shown which result in displacements $\leq$ 40 nm.

optical auto-refocus procedures would be necessary. More detailed information is provided in chapter 5. Based on these restrictions, an sensor element material thickness of 200 nm had been selected. Therefore, the material thickness of all designs was set to 200 nm within this linear static FEA of the different sensor element designs.

Another possibility to increase the deformability of the sensor is the reduction of the sensor arm width as can be supposed by equation 2.12. Regarding FEA, there are no limitations, so very narrow arms could be taken into consideration. However, the used fabrication processes (see chapter 3) did not allow for smaller structures than 1 μm with a-Si and 2 μm for NiTi.

Finally, the design of the sensor arms has a strong impact on the stiffness of the sensor element: The longer the arms, the higher the deformability. As the design had to be compact to ensure maximum force resolution in all three dimensions and at the same time, and surface-integrated, the arms of the final designs were meander springs. Here, the amount of coils within the meander control

the lengthening of the sensor in the distinct direction.

In the following two tables, the ten most promising sensor element designs and their corresponding linear static FEA results regarding their in-plane (x,y-direction) and out-of-plane (z-direction) displacements in case of an applied external force of 5 nN to the sensor element centre plate (according to figure 2.3) are presented for a-Si and NiTi. Additionally, the tilt of the central sensor element plate has been simulated for each design to analyze the impact of an uncentered normal force of 5 nN applied to the edge of the sensor centre plate. For interference measurements, a tilt of the sensor plate can cause interfering signals by additional interferences via scattered light, which would finally reduce the precision of the measured forces. To reduce this effect, the design should be stable against tilts or at least show only small displacements compared to the displacements in the main directions. The sensor designs were later on fabricated in the course of four different evolutional design and fabrication process optimized steps, which are listed for the sake of the data completeness in the rightmost column of these tables. The designs are subdivided into four different groups: sensor elements with one, two, three and four arms. The directions of the in-plane displacements are indicated by the axis inscribed at the centre plate of each sensor design in the added FEA images. Here, the images of the different sensor element designs include a color code, in which reddish areas correspond to maximum displacements out-of-plane, while the blueish areas mark sensor element parts, which are not displaced. The sensor element type designations are based on the initial letters of significant design characteristics named in German, which were worked out and developed throughout the years of this project and shall not be object of further detailed descriptions in the interests of the readability. The initial letters of the most important designs are explicitly presented towards the end of this chapter.

The first design group consists of sensor types named CWT and SES. CWT is a 2x2 arrangement of classical rectangular shaped cantilevers of 2 μm width. The most straightforward shape of sensors elements based on a rectangular design is used as a reference for comparison between an established (CWT) and the newly developed designs. As supposed, there is a neglectable tilt and displacement in the picometer range along the cantilever, and about 1.4 nm along the y-axis. A significant displacement is achieved when deforming out-of-plane. Here, about 170 nm for NiTi sensor elements and 150 nm for a-Si based devices are determined. These sensor features are not congruent with the
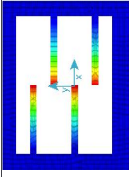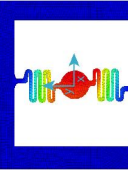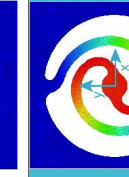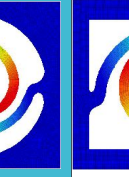
sensor requirements regarding the needed minimum deformation behavior and comparable sensitivity in all three dimensions, for which reason this design type is not suitable for the purposes of this work. Regarding the overall results for all simulations, the determined displacements for a-Si sensor elements are constantly lower within a range of 10% to the ones of NiTi due to the above listed material parameters (see table 2.1) with the difference in Young's Moduli, in particular. In consequence, the simulation results for NiTi are analyzed and discussed in more detail, but are transferable to the results for a-Si.
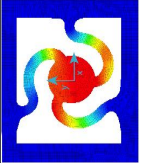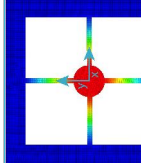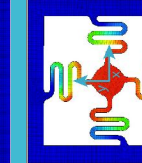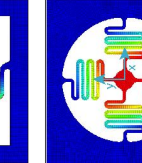
SES was the first sensor design approach based on previous work of Selhuber-Unkel et al. [197] [198] It is an one-sided clamped spiral shaped sensor element, which possesses comparable deformation behavior like CWT. In addition to these inappropriate features, the sensor element shows a strong tilt of about 41 nm, which is 22 % of its overall out-of-plane displacement and was therefore not chosen for further investigations.

The second group of sensor types is consisting of ZFE, DSR and DSBE. The two sensor arms are arranged along the y-axis and vary in their sensor arm design and centre plate. ZFE consists of two meander like flat spirals with three coils each which are clamped to the frame and a small centre plate of 9 μm diameter. Its in-plane displacement behavior is comparable to SES and in the subnanometer range, while its out-of-plane deformability is less then one third of CWT and SES. Furthermore, this design shows a tilt of 101 nm compared to displacements beyond 1 nm in-plane and of about 47 nm out-of-plane. Hence, it is very vulnerable for tilts and has the highest sensitivity of all designs regarding uncentered force transmissions.

DSR and DSBE are both designed based on two merging spirals connected by the centre plate. But while DSBE is the first evolution step for that sensor type with a big centre plate of 12 μm diameter, a sensor arm width of 2 μm in a rectangular frame, DSR is the optimized version of DSBE with a decreased arm width of 3 μm, a small sensor plate of 7 μm and a circular frame shape. The circular frame has been chosen due to the fabrication process requirements according to the producer of the sensor element samples (Fraunhofer ISIT). Hence, all of the designs having an edged frame were fabricated by wet chemistry processes within the first fabrication evolution steps (mask 1.0 to mask 3.0), while the circular frames correspond to sensor elements fabricated by dry-etching (mask.4.0), where the etching processes is especially convenient for round shapes. The slight changes in sensor

Table 2.2: Overview on the FEA results of the most appropriate sensor element designs including: 1. their element type designation, 2. the maximum displacement in x-, y-, and z-direction as well as the maximum tilt of each sensor element centre plate in case of normal force impacts on the centre plate edge given in nm for NiTi (left columns 2.-4) and a-Si (right columns 7.-10.) sensor elements, 3. FEM images of the element sensor designs including a color code to mark element parts with maximum displacement (red) and no displacement (blue). The coordinate system inscribed at the sensor element centre plate marks the lateral displacement directions x and y. 4. For the sake of completeness of the data, the prototype evolution step of the fabrication is listed in the rightmost column. Here, mask 1.0 to 3.0 summarize sensor elements fabricated by wet chemistry processes (NiTi) using chromium masks with designs 1.0 to 3.0, while mask 4.0 corresponds to the last evolution step. Here, the sensor elements were fabricated by dry etching of the a-Si device material.

Design Name	max. Displacement (NiTi)/[nm]				Design	max. Displacement (a-Si)/[nm]				Evolution Step
	x-axis	y-axis	z-axis	Tilt		x-axis	y-axis	z-axis	max.Tilt	
CWT	0.0163	1.47	163	non		0.0154	1.38	152	neglictible	mask 4.0
SES	0.667	0.836	186	40.8		0.628	0.784	170	37.6	mask 1.0
ZFE	0.66	0.714	46.8	101		0.669	0.618	42.8	92.9	mask 2.0
DSR	0.609	0.372	130	35		0.571	0.349	117	31.6	mask 4.0
DSBE	0.52	0.3	118	73.3		0.487	0.282	105	34	mask 3.0

Design Name	max. Displacement (NiTi)/[nm]				Design	max. Displacement (a-Si)/[nm]				Evolution Step
	x-axis	y-axis	z-axis	Tilt		x-axis	y-axis	z-axis	Tilt	
3-FS	0.0124	0.0128	16.2	14.2		0.0118	0.0121	14.6	8.59	mask 1.0
3-FL	0.0223	0.0241	20.1	0.00113		0.0208	0.0224	18.6	6.96	mask 1.0
3-AR	1.49	1.43	90.5	24.3		1.4	1.35	82.3	22.1	mask 3.0
4-AP	0.00239	0.00238	8.39	3.27		0.00221	0.00223	7.91	3.05	2.0
4-FE	0.207	0.2	17.6	7.37		0.191	0.187	16.2	6.74	mask 2.0
4-FR	1.11	1.11	43.2	2.77		1.04	1.04	39.6	2.53	mask 4.0

element design cause an improvement with regard to the sensor displacement of 15 % in x-direction, 20 % in y-direction and 10 % from 118 to 130 nm in z-direction. The tilt could be reduced by 48 % from about 73 to 35 nm, but still is 27 % of the maximum out-of-plane displacement. So, due to the extensive tilt and a sensitivity variation by a factor of 350 between the in-plane and out-of-plane displacements, the entire sensor type group is not satisfying the requested requirements. In sensor group three, sensor elements 3-FS, 3-FL and 3-AR were tested via FEA. The first two designs are just different in the diameter of their centre plates and consist of three meander springs with one coil, uniformly connected to the centre plate. Here, the reduction of the plate diameter from 16 μm to 10 μm induces a tilt reduction by a factor of 10^{-4}. In general, this design can be fabricated with very small edge lengths (about 35 μm). However, the in-plane displacement is in the lower picometer region, which corresponds to a high lateral spring constant of this design and the sensitivity in z-direction is about 1000 times higher than in x- and y-direction. Therefore, these two designs were not favorized for this project. To increase the elasticity of the sensor, two coils were added to each spring to create 3-AR. This design is already established in micromedical devices[199] and provides insights into the impact of more coils to a three-armed design. The sensor arms were regularly arranged around the centre plate. Additionally, a circular frame has been introduced here, which is beneficial in the fabrication processes presented in chapter 3. This design modification was accompanied with a deformation increase in-plane by a factor of 64 from 22 pm to 1.5 nm, while in z-direction an increase of 70 nm to a maximum deformation of 90 nm were achieved. However, this improvement included an increase of the centre plate tilt to 24 nm, which again is 27 % of the out-of-plane deformation. Due to this instability and although the sensitivity in all three directions is adequate for the envisaged applications, this design was also discarded for this project.

Finally, sensor group four included design type 4-AP ("4-Arm Primitiv"), 4-FE ("4-Feder Eckig")and 4-FR ("4-Feder Rund"). 4-AP is the prototype of this group, directly extracted from the results of the topology optimization. It consists of four cantilever-like arms arranged symmetrically in a 90 degree angle one to another and fixed to the centre plate. This shape should be rather stiff, as there are no springs or meanders implemented. Indeed, the results of the FEA support this assumption and therefore, this design is the stiffest design solution within this analysis. By in-plane displacements of 2 pm, out-of-plane displacements of 8 nm and a tilt of 3 nm, neither the amount of displacement,

nor the sensitivity distribution or tilt to out-of-plane displacement ratio are in any way fullfilling the defined requirements. In consequence, once again additional coils were induced in the sensor arm design. As an overall compact sensor design should ensure a maximum force resolution, the amount of coils per arm were increased to two in the first step. This caused a doubling of the tilt and the displacement in z-direction as well as an increase of the in-plane displacement by a factor of 100. As the tilt to z-displacement ratio is 38 % and the in-plane displacement is in subnanometer region, more coils had to be added.

By this, the final sensor type 4-FR was designed consisting of four meander springs with three coils in a symmetric arrangement around the centre plate within a circular frame. The in-plane displacements are in the lower nanometer range, the out-of-plane deformation is 43 nm, i.e. fourty times higher than in-plane and the design is stable with regard to tilts by uncentered force applications, which is 6 % of the out-of-plane displacement. Hence, this design shows the most comparable and highest sensitivity in-and out-of-plane as well as high stability regarding force impacts beyond the centre of the sensor element plate in comparison to the nine other presented design concepts. Moreover, this design can be manufactured due to its structure dimensions and the diameter of the inner frame edge can be kept as low as 45 μm to support the need of a minimum sized, compact sensor design.

Considering the defined requirements (see subchapter 2.2.2), the sensor element design 4-FR and 4-FE were in consequence succesfully designed, defined and determined for this project purpose and were therefore set as basis for the following fabrication, characterization, calibration and readout procedures, which are presented in the next chapters 3 to 6.

3 SE Fabrication and Characterization

The fabrication of the designs presented in chapter 2 is the limiting prototyping step regarding the miniaturization of the sensor elements. Due to the low diameter of a spread cell of up to 200 μm, the sensor diameter should be in the lower micrometer region to create a maximum sensor density. Well established processing techniques in this size range are bulk and surface micromachining as part of microsystem technologies. As the producible structure size varies for each material in a given fabrication procedure, the most suitable processing technologies have to be chosen to generate minimum dimensions for stable structures.

To analyze mechanotransduction and traction force distributions of cells properly, the device material has to be well chosen. Here, biocompatibility is of major importance for a universal measurement result. Representatives of three different material types were used to fabricate the novel sensor device based on their biocompatible and mechanical properties as well as their processability. These were: 1. nickel-titanium (NiTi) as a representative of superelastic metallic alloys and smart materials (see section 2.3.1), 2. amorphous silicon (a-Si), a semiconductor material, which is well established regarding its processability and use for micromechanical systems (see section 2.3.2) and 3. polydimethylsiloxane (PDMS) belonging to the group of polymers and frequently used in biological experiments (see section 3.5.3).

In this chapter, a short theoretical insight into micromachining and the utilized characterization technologies, which were laser scanning microscopy and biocompatibility testing are presented. The different fabrication techniques and steps apart from material description for NiTi based sensors, a-Si sensor elements and the process development for the PDMS based sensor membranes are separately presented in subsections 3.5.1 to 3.5.3.

3.1 Bulk and Surface Micromachining

In times of a fast-growing semiconductor industry facing mega trends like autonomous driving and mobile infotainment, the miniaturization of devices such as sensors, actuators or microchips with cheap production steps and high output is of central industrial interest. [200] Here, microsystem technology (MST) has gained profound importance since its development in the 1950s. [201] It is synonymously known as microfabrication, micromachining or micro electromechanical systems (MEMS) technology and sums up all fabrication methods of devices with one or more dimensions in the micron range. [202] Throughout the years, further disciplines like biology, medicine or chemistry developed an increasing interest in MST and in consequence, today disposes of a variety of different methods and settings. [203]

Two fundamental processes in MST are bulk and surface micromachining are shortly presented and compared in the following. [204] [205]

The principle of bulk micromachining is subtractive and based on the etching into or the removal of parts of a substrate to define structures. [199] The wafer thickness therefore defines the device height and for that reason, this method is especially used for fabricating thick films. The lateral structural dimensions that can be fabricated by this technique range from 3 to 5 mm, the vertical from 100 to 500 μm. The corresponding substrates can be processed from top and bottom side. [206]

Regarding the etching procedures, two general types of etching can be distinguished: wet (liquid phase) and dry (plasma) etching. [207] Wet etching in bulks is used to etch sacrificial layers between two structural layers to release a structure. For this purpose, etchants like ethylene diamine pyrocathechol (EDP), tetramethyl ammonum hydroxide (TMAH), sodium hydroxide (NaOH) or hydrazine are used. The corresponding etchant is chosen regarding safety aspects, process compatibility, material to be etched and the corresponding etch rate, etch ratio between the different crystal planes, costs and target surface roughness.

On the other hand, dry etching is mainly chosen to structure layers with higher resolution than for wet etching. Here, the substrates are etched via:

1. vapour etchants such as sulphur hexafluoride (SF6), oxygene, tetrafluormethane or hydrogen bromide in a plasma environment via chemical reactions with the substrate,

2. a bombardment with high energy particles based on physical removal by momentum transfer or 3. a combination of 1 and 2.[208] [209]

In general, this etching method is more 1. expensive than wet etching due to the equipment needed, 2. takes more space within the laboratory and 3. although just small amounts of etchants are required for each process, the vapours or etching products can be very harmful for which reason filters and neutralization procedures are necessary.

Both etching types can create so-called isotropic and anisotropic etching profiles as presented in figure 3.1. Isotropic etching profiles (see figure 3.1.**A**) show a concave shape of the sacrificial layer and an underetching of the structural layer, which is therefore not supported anymore. This is due to a non-directed etching process, in which the type of etchant and the material to be processed
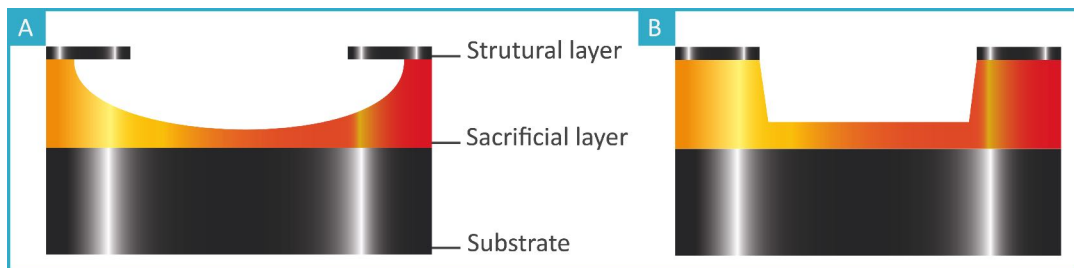

Figure 3.1: Schematic presentation of cross sectional etching profiles: **A** In isotropic etching, the sacrificial layer is etched in all directions at once creating a concave profile shape. By this, the structural layer is underetched and not supported anymore. **B** The anisotropic etching profile shows side-walls at an angle to the substrate surface, which can also be vertical. One preferred etching direction can be observed, which can depend on the crystal orientation of the sacrificial layer.

influence the etching rate. In anisotropic etching processes (see figure 3.1 **B**), the sacrificial layer is etched along a certain direction and in crystalline materials, this direction depends on the crystal (plane) orientation. In that way, vertical side-walls or walls at an angle are created. As the etching rate of the different planes vary, it is possible to control the etching shape to v-shaped trenches or pyramidal holes.[207]

Surface micromachining is based on a layer by layer technique on one surface of a substrate. Here, the surface properties in the plane are defined by dry etching, whilst wet etching of the sacrificial layer is for undercutting. The deposition processes limits the maximum height of the surface machined

devices and is therefore especially used for thin film fabrication. In general, surface micromachining offers high resolution with smaller feature sizes than by bulk micromachining. In dependence of the chosen processing technologies and materials, the minimum achievable feature sizes are smaller than 100 nm.[210] [211] Within this project, a lateral structure size of 2 μm for wet etching processes and of 1 μm for dry etching were achieved (see subsections 3.5.2 NiTi based sensor elements and 3.5.2 a-Si sensor elements).

One disadvantage of surface micromachining is the sticking of suspended structures or stiction due to capillary forces in wet processes for releasing structural elements from a substrate.[199] [205] [212] Moreover, the different batches in production lines can have different mechanical and electrical properties. Hence, the reproducibility of the samples is not given and needs to be controlled constantly.

In the course of this project, reactive ion etching as one representative for dry etching processes will be introduced in more detail in the next paragraph.

3.2 Reactive Ion Etching

Reactive Ion etching (RIE) is a representative of dry etching technologies based on glow discharge apart from plasma etching (PE), high plasma density (HPD) such as sputter etching and combines physical and chemical etching processes.[199] [213] Here, a radio frequency (RF signal) is applied between two electrodes and vertical to the sample surface stimulating the oscillation of free electrons. These excited electrons collide with the chosen gaseous etchant producing a plasma. The electrons collide with further etchant molecules and highly reactive ions, neutral reactive radicals as well as inert ions are generated that bombard the surface of the sample to be etched. Basis for this is the acceleration of the ions by an acceleration voltage towards the sample surface. By this and the ion kinetic energy, the chemical bonds of the surface atoms are loosened or entirely damaged, initiating an improved reaction of the reactive ion gas and the substrate surface. In consequence, cavities and trenches are etched into the sample surface. Throughout the procedure, ions collide with the bottom of these trenches and far less with the side walls. In consequence, the RIE process is anisotropic, but can also be run for isotropic etching. This anisotropy can technically be optimized by back-side cooling of the sample down to -120°C inhibiting side reactions. The reaction products are in general

directly removed by evacuation in high vacuum.

The etching characteristics of RIE processes - including etch rates, etch profiles, homogeneity or selectivity - can be controlled easily compared to wet etching methods by RF, the applied voltage, the gaseous etchants and its density as well as the corresponding chamber pressure. By this, even structure sizes below 100 nm can still be well fabricated.[213] For that reason, RIE today is a well-established etching technology in micro- and nanosystem technology for anisotropic processing of silicon, organic and inorganic dielectrics, metallic buffer layers, or polymers for electronic and opto-electronic applications.[213][214]

In the mid 1990s, the so-called Bosch process was first used for the development of the deep reactive ion etching (DRIE) process to overcome the limitations of RIE in high-aspect ratio micro-machining.[199]

3.3 Confocal 3D Scanning Microscopy

In 1957, Marvin Minsky, a cognitive scientist and one of the epinomes of the artifical intelligence, patented his optical measurement principle following his goal to record 3D images of nerve cells in unstained preparations of living brains as a "wiring diagram".[215] This patent marks the starting point of confocal scanning microscopy, a milestone in optical microscopy.[216][217][218][219] It took another thirty years and the invention of the computer and the laser till the first commercial confocal laser scanning microscope (CLSM) was launched in 1987 by Bio-Rad.[220]

Conventional widefield microscopy suffers from scattered light outside the focus plane that cause a significant blur. In confocal microscopy, spatial filtering is used to block light outside the focus plane and by this, high quality images with high signal-to-noise ratios and contrast can be recorded.[219]

The resolution of confocal microscopy is based on its capacity to distinguish between two points in close proximity in axial and lateral direction during the scanning process. For a simple mathematical description of the axial and lateral resolution, the Rayleigh criterion finally leads to:[221][222][223]

$$Lateral\ resolution = \frac{0.51 \cdot \lambda}{NA} \tag{3.1}$$

$$Axial\ resolution = \frac{0.88 \cdot \lambda}{n - \sqrt{n^2 - NA^2}} \tag{3.2}$$

with: λ - wavelength of the illuminating source, NA - numerical aperture of the objective lens and n - refractive index of the immersion liquid. These equations just slightly differ from those of conventional microscopy (see [222]). The significant gain in resolution in confocal measurements is based on the direct proportionality of the resolution to the wavelength of the light source and not to the wavelength of the reflected or emitted light like in conventional microscopy. Hence, the shorter the chosen illuminating wavelength, the higher the resolution. Using light in the UV range, resolutions in the lower nanometer range can be achieved. [215]

The principle of a confocal microscope is presented in figure 3.2. A point light created via a pinhole hits a dichromatic mirror and is then deflected on the objective lens. For better understanding, the light cone here is represented by three bundles of rays of the same beam cone in brownish, violet and greenish color. They pass the lens and are focused on the sample surface. Here, they hit different focal planes (1, 2, 3) in dependence of their focal length. The greenish ray is reflected from the 2nd plane of the surface, while the violet and brownish rays are reflected from a higher that is to say lower plane. The reflected light then passes the lens and the dichroic mirror. Just reflected rays from one focal plane, here the greenish bundle of rays, can pass the second pinhole and are recorded on a light detector. The detector needs to be both sensitive to low light intensities and also to possess a high spatial resolution. For that purpose, complementary-metal-oxide-semiconductor (CMOS) or charge-coupled device (CCD) chips are today used as fast area detectors in confocal microscopy. [224]

In case of fluorescent samples, the incoming light excites the sample surface and the fluorescence is then selected by a combination of a pinhole and a filter before being detected. One specific feature of confocal microscopy is the possibility of a stepwise scanning of the different focal planes by relatively moving either the sample towards the objective or the lens towards the sample. By a software based z-stacking of the images, a three dimensional surface mapping is carried out and the topography of the sample can be analyzed regarding roughness or line profiles. [222]

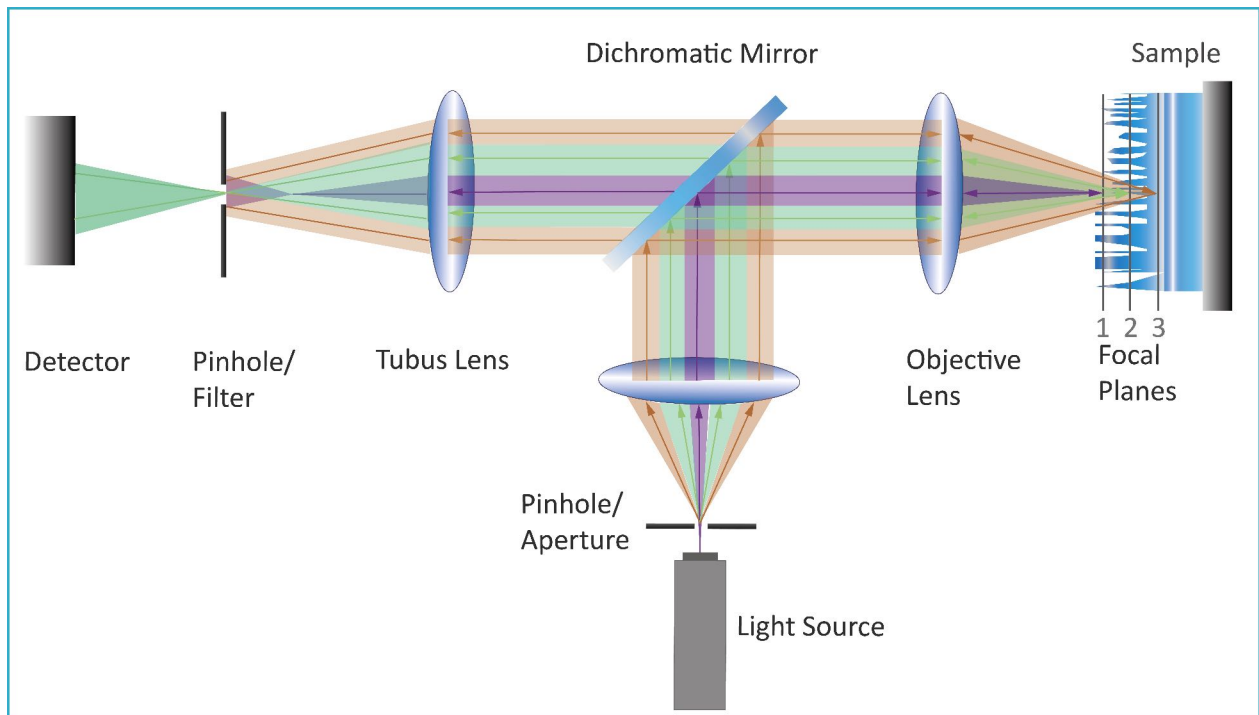There are various methods for the object-to-image transformation. One technique used within

Figure 3.2: Schematic presentation of the beam path within a confocal microscope: Light emitted by a xenon lamp (white light confocal microscopy) or a laser (CLSM) passes through a pinhole and is collimated by a lens. For better understanding, three arbitrary bundles of rays (in brownish, violet and greenish color) of the same beam cone are presented. The rays are deflected via a dichromatic mirror on the objective through which the light is focused on the sample surface. The bundles of rays are slightly different focused and hit different focal planes of the surface. If fluorescence can be stimulated in the sample by means of the chosen light source, light is emitted that passes the objective lens and the dichroic mirror. In case of non-fluorescent samples, the light is just reflected by the surface. Depending on the focal plane, the rays are afterwards blocked by a pinhole after passing a tubus lens. In case of fluorescence measurements, an additional filter is installed. Here, only rays from one focal plane (here, plane 2) pass the second pinhole and are then detected by a light detector such as a CMOS chip.

CLSM is a point-wise scanning of the surface and a point-to-point recording, which is a time intense process. The spinning disk confocal microscopy is based on a disk implemented between the objective and dichromatic mirror, consisting of spirals of pinholes like the common Nipkow disk. [225] Here, the disk rotates at high speed and the object is scanned within one round in real time. By the disk spinning, a static image of the surface can be realized. In line scanning confocal microscopy, the sample surface is excited and detected in all points in an one-dimensional line, which is especially

used in medical applications and in vivo experiments. [226] [227]

Another differentiation of types of confocal microscopy is based on the chosen light source. White light that is e.g. emitted by a xenon lamp, is used for confocal white light microscopy (CWLM), which is used for highly reflective surfaces like metals. Due to the broad spectrum of wavelengths, the overall resolution of the CWLM is limited to the micrometer range. In general, this method is used in industrial quality control like in the marine, automotive or aviation industry as well as in industrial and scientific materials testing. [228] [229]

In confocal fluorecscence microscopy (CFM) and CLSM, coherent light i.e. a laser is used as an illuminating source. [230] For CFM, the specimen itself is fluorescent or marked by fluorescent particles before being scanned. This is very useful in cell experiments, wherefore this technique is the most used in dermatology to analyze *ex vivo* and *in vitro* samples, [231] in neuroscience and physiology to image neuronal cells, [232] such as in biology and biomedical sciences to image fixed or living tissues and cell cultures. [233] [215] For non-fluorescent surfaces, CLSM is used to characterize materials like polymers, ceramics, wood, bones, teeth and any other solid or liquid materials [234] and was combined with methods like Raman to e.g. analyze the morphology of polymeric multiphase solid-state samples [235] or the distribution of glassfibers in polymeric composites. [236]

Due to its high resolution, a pseudo-infinite depth-of-field imaging, the possibility to measure in air without additional coatings, or other sample preparations, and to record 3D images, laser scanning confocal microscopy is a powerful tool for quantitative and qualitative measurements and therefore, an adequate alternative to scanning electron microscopy. [237] [238] [239] Furthermore, it is serving as a fast, non-tactile optical 3D method for topography analysis overcoming the problems of tactile methods like conventional profilometry or atomic force microscopy, where sensitive samples surfaces can be damaged or scanning procedures are highly time intense. [237] In consequence, the popularity of confocal microscopy has increased dramatically since its first use in the quality control business of the silicon chip industry. Within this time, the equipments have been improved significantly according to Paddock et al. regarding 1. bright and stable laser light sources, 2. efficiently reflecting mirrors and more precise filters, 3. improved methods of scanning and electronics for data capture, 4. high quantum efficiency low noise photodetectors, 5. improved methods of specimen preparation, 6. fast computers with image processing capabilities, 7. elegant software solutions for analyzing the images

and 8. high-resolution digital displays and color printers. [215]

Today, it is a widespread technique covering a spectrum from all disciplines in life sciences to physical sciences and gaining importance in materials science. [237] [222] [223] [221] [240]

Within this project, the sensor element array topography could not be characterized via a tactile method due to their sensitivity to external forces and impacts. For that reason, CLSM has been chosen to characterize the sensor elements in three dimensions with regard to their degree of release after fabrication.

3.4 Biocompatibility

One of the central requirements of this project was the fabrication of biocompatible sensor elements to ensure the viability and adhesion of cells on the surface of this novel device. For that reason, the devices were tested regarding their biocompatibility in this work. In the following, some insights into biocompatibility and biocompatibility testing are given.

In 1986, biocompatibility was first defined more precisely by Williams as "the ability of a material to perform with an appropriate host response in a specific application". [241] [242] However, the science of biomaterials has changed throughout the years, which is why Williams gave a more clinical definition in 2008. Here, the requirement of biocompatibility is "that the material shall do no harm to those tissues [the tissues of the human body; the author], achieved through chemical and biological inertness". [243] In 2013, Ratner supposed a new definition of biocompatibility in a rather bio-engineering context as "[...] the ability of materials to locally trigger and guide normal wound healing, reconstruction, and tissue integration." [244] [245] In consequence, all other materials that were succesfully used *in vivo* so far should be defined as "bio-tolerable".

These rather philosophical examples of attempts at the definition of biocompatibility outline the importance of a rather practicable standardized approach, which is today realized via the qualification of biocompatibility by ISO standard 10993. Here, standard biocompatible testing requirements are defined in twenty different sections regarding the biological safety or risk of medical materials. [246] Standardized tests for toxic effects like systematic toxicity, cytotoxicity, gen toxicity, carcinogenity, sensitization, reproductive toxicity as well as chemical, physical and mechanical characterization and

validation techniques are described.

One of the cytotoxicity tests according to ISO 10993-5 is the MTT (3-(4,5-dimethylthiazol-2-yl)-2,5-diphenyl tetrazolium bromide) assay test,[247][248] which was used in this project to bio-charaterize the fabricated sensor element plates. In general, cells are cultured with the extraction of the sample to be characterized. Then, the yellow cell membrane active MTT dye is added as a salt, which is reduced by vital cells to blue-violet formazan crystals. These are not membrane active and are collected in proliferating cells. The reaction is induced by mitochondrial dehydrogenises of the living cells. The incubation time of the cell toxic MTT assay is rather long (4h). After lyses of the cells and dissolution of the crystals, the concentration of the dye can be detected via colorimetry and is then compared to a control sample. By this, the optical density value can be adapted to the amount of vital cells and so, defines the cell viability for this test sample.

3.5 Fabrication of NiTi, a-Si and PDMS sensor element arrays

Based on their biocompatible and mechanical behavior, NiTi, a-Si and PDMS were chosen as sensor materials. In this section, the general materials and methods for the characterization of all materials, are generated followed by a presentation of the fabrication processes and the corresponding materials and methods for NiTi and a-Si sensors as well as the process development of the PDMS sensor membrane fabrication are outlined.

3.5.1 NiTi Sensor Elements

3.5.1.1 Materials and Methods

Patterned NiTi thin films on borosilicate glass wafer Patterned NiTi thin film samples were fabricated in a cooperation with Aquandas® GmbH based on a well-established process developed by Dr.-Ing. R. Lima de Miranda et al.[159][160] according to my masks designed in CAD. A schematic overview of the different fabrication steps is given in figure 3.3. A 4 μm thick film of copper (Cu) was sputtered on 2" borosilicate wafers (SCHOTT BORO-FLOAT® 33 Borosilicatglas) of 100 μm and 400 μm thickness. Then, a 200 nm thick film of NiTi was deposited by means of magnetron sputtering with an Alcatel 450 sputtering device (figure 3.1.**1**).
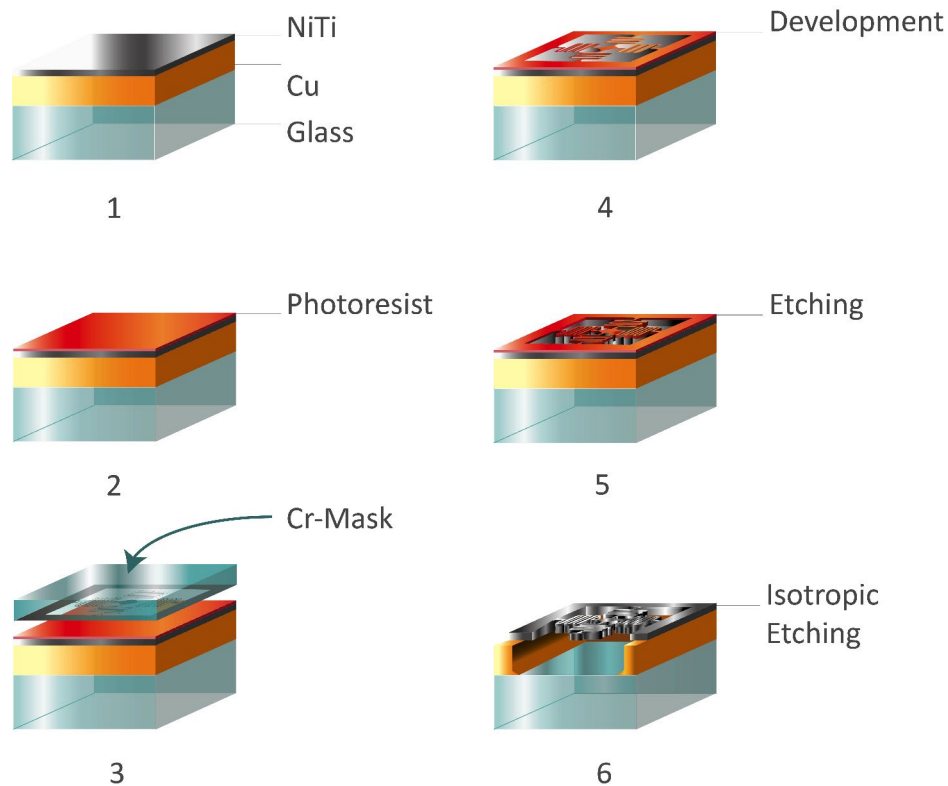
Figure 3.3: Schematic presentation of the fabrication steps to produce NiTi MEMS Structures on glass: **1** Sputtering of 4 μm of copper and 200 nm of NiTi on a borosilicate glass wafer. **2** Spin coating of photo resist on the NiTi layer. **3** and **4** Photolithographic processing: Aligning of the chromium mask on the wafer and structuring of the photoresist by UV treatment. **5** Wet etching of the NiTi thin film. 6 After Isotropic etching of the sacrificial copper layer and removing of the photoresist, the released sensor element structure is achieved. For better insight into the structure, a free cross section is shown.

Sputtering was carried out at a base pressure below $1 \cdot 10^{-7}$ mbar, an Argon flow of 20 sccm and a sputtering pressure of $2 \cdot 10^{-3}$ mbar. The magnetron sputtered films had a composition of Ni50.8Ti49.2 atom-%. The NiTi patterning was attained by spin-coating of positive photoresist (figure 3.1.**2**), aligning of a chromium coated sodalime mask (bvm.maskshop A. + V. Mulch GbR) on the sample (figure 3.1.**3**), followed by UV-treatment on a mask aligner (SUSS MicroTec MJB4) (figure 3.1.**4**) and wet etching (figure 3.1.**5**). Afterwards, the sacrificial Cu layer was isotropically wet etched to generate free-standing NiTi structures and the photoresist was dissolved in acetone (figure 3.1.**6**). Finally, the wafers were temperature treated at $650°$C to transform amorphous NiTi

to its austenitic state.

Free-standing NiTi films Free-standing NiTi structures on thick film frames were fabricated in a cooperation with Acquandas® GmbH according to my masks designed in CAD. A detailed description of the fabrication process was published by Lima de Miranda et al. [160] and is shown schematically in figure 3.4.
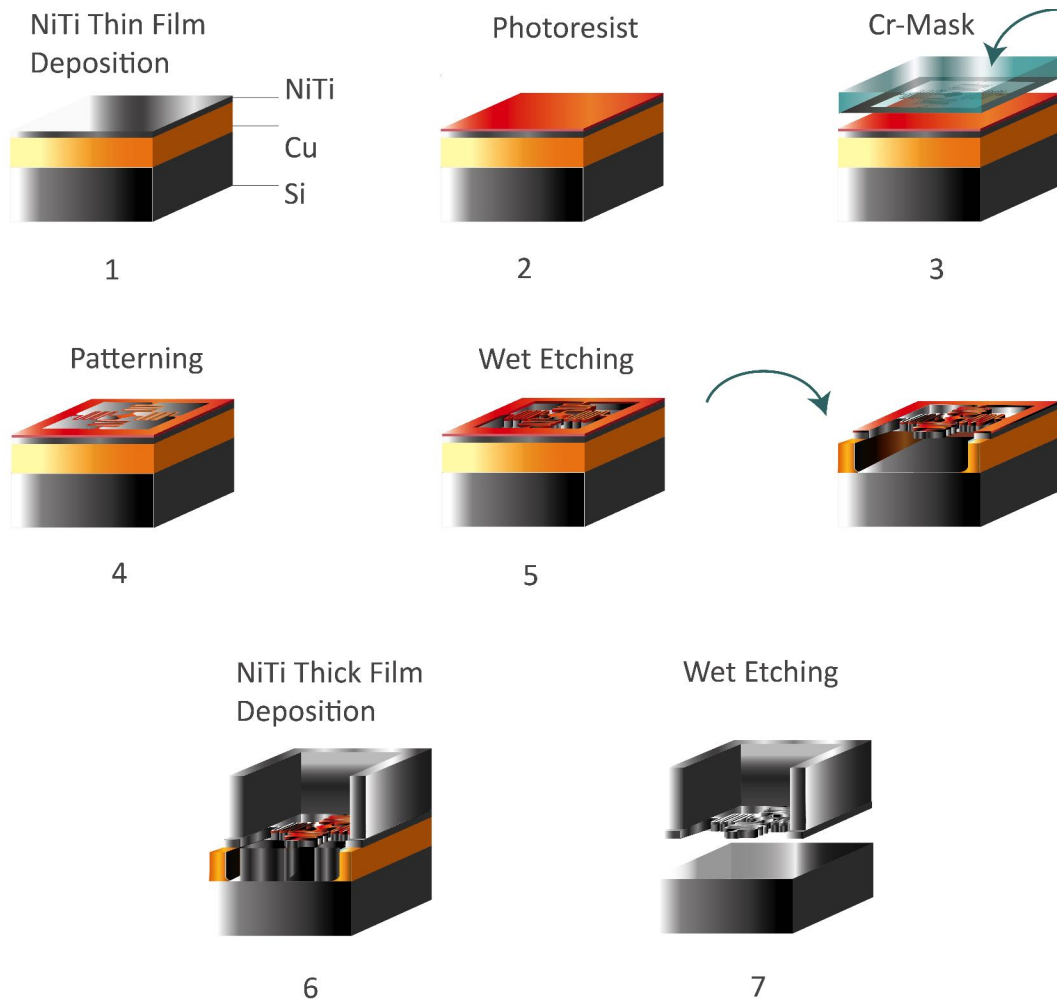

Figure 3.4: Fabrication scheme of the sensor elements in a 50 μm thick NiTi foil: **1** Sputtering of 4 μm of copper and 200 nm of NiTi on a silicon wafer. Step **2** to **5** are in accordance with the processing steps shown in figure 3.3; here a cross section of the isotropically etched element is shown. **6** Deposition of a 50 μm thick NiTi layer on. **7** By wet etching of the sacrificial layer, the patterned NiTi foil is lifted off the Si substrate.

The deposition of thin films was carried out as described in the previous paragraph. A sacrificial layer of Cu was pre-sputtered on a silicon substrate (see figure 3.2.**1**-3.2.**5**). Afterwards, a 50 μm thick film of NiTi was deposited on top of the structured NiTi thin film (figure 3.2.**6**). Finally, the copper layer is entirely wet etched. By this procedure, 1 x 1 mm sized NiTi foils with 200 nm thick sensors were fabricated (figure 3.2.**7**) and fixed in a home-built aluminium frame for further characterization and testing.

Confocal 3D Laser-Scanning Microscopy Surface topography was determined by confocal 3D-laser-scanning microscopy (KEYENCE$^{\circledR}$ VK-250X) using 5x, 10x, 20x, 50x (50x Plan Apo Epi, Nikon$^{\circledR)}$) and 150x (150x CF Plan, WD 0.2, Nikon^{TM}) objectives in dependence of the sensor size. According to Keyence the following in-plane and out-of plane resolutions could be achieved:

Objective	x-y Resolution / [μm]	z Resolution / [nm]
CF IC EPI Plan 10x	1.318	0.5
CF IC EPI Plan 20x	0.659	0.5
CF IC EPI Plan Apo 50x	0.264	0.5
CF IC EPI Plan Apo 150x	0.088	0.5

For each sensor design and sensor material, white light images were first recorded. Afterwards, the setup was switched to confocal mode and the scan range between the upper and lower focus was defined automatically. The scan was then run in surface topography mode with maximum resolution and minimum step size. The images were finally processed using the KEYENCE$^{\circledR}$ MultiFileanalyzer software. The image tilt was corrected automatically for each 3D image.

Scanning Electron Microscopy (SEM) SEM (Supra 55VP, Zeiss$^{\circledR}$, Germany and SEM with FIB, FEI$^{\circledR}$ Dualbeam Helios NanoLab) imaging was carried out at 5 kV using the in-lens detector at a working distance of 5 mm. The deformation behavior of the amorphous silicon sensor structures was shown by attacking the sensor centre plate with a tungsten needle of a micromanipulator (Kleindiek$^{\circledR}$ MM3E). The deformation process was recorded in movie mode implemented in the SEM software.

MTT testing Material cytotoxicity was tested for NiTi sensor systems on a 50.8 mm in diamater borosilicate glass substrate and 50 x 50 mm^2 sensor plate of a 200 nm thick a-Si device layer according

to the ISO 10993 norm. First, each sample was autoclaved for 1,5 h at $135°$C. In correspondance to the sample surface, the NiTi sample was incubated in 3 mL that is to say the a-Si sample in 2.2 mL of Dulbeccos Modified Eagles Medium (DMEM supplemented with 10 % FBS and 1 % Penilicin; Biochrom$^®$, Berlin, Germany) at $37°$C and 5 %- CO_2 for 72 h. 10 000 cells were cultured in a 96 well-plate with 100 μL DMEM for 24 h each sample. The medium was then exchanged by 100 μL of extraction medium. DMEM was added to produce concentrations of 0 %, 16 %, 32 %, 64 % and 100 % extract and incubated for another 24h at $37°$C and 5 %- CO_2. 50 μL of (3-(4, 5-dimethylthiazolyl-2)-2, 5-diphenyltetrazolium bromide (MTT, Sigma Aldrich$^®$, Darmstadt, Germany) were added to each well plate in order to mark the vital cells. After 2 h of incubation, the absorbance of the solutions was measured with a micro-platereader (μQuant Biotek$^®$ Instruments GmbH, Winooski, USA) at 570 nm. DMEM containing isopropanole was used as positive control and fresh, untreated medium as negative. The test results were normalized to the absorbance of the control samples.

5.1.1.2 Results and Discussion

The fabricated patterned NiTi thin films on borosilicate glass wafers are presented in figure 3.5 **A**. Four highly-reflective NiTi squares with four different designs are shown, of which the upper right square contains 340 sensor elements of type 4-FR, which is analyzed in the following. In figure 3.5 **B** and **C**, the smallest designed elements considering the fabrication limits have an edge length of 135 μm (**B**) that is to say 170 μm (**C**). The sensor arm springs of **B** are sticking together. Obviously, the distance of 1 μm was not sufficient in this case. In **C**, the spring slopes of the sensor arms had a distance of 2.5 μm. By this, the overall size of the sensor element is bigger than **B**, but the manufacturable minimum size limit of this processing technique.
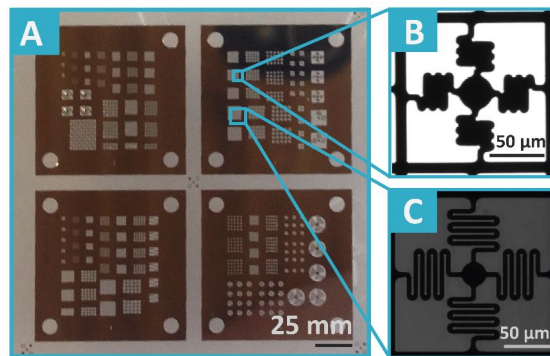
Figure 3.5: White light microscope images of the bulk micromachining process fabrication results of a 200 nm thick NiTi film on a 4 μm thick Cu layer and a 400 μm glass substrate. **A** White light microscope image of the four different NiTi sensor design boxes. In the upper right box, 5x5 sensor arrays of 4-FR sensor elements and single elements in different size are contained that are shown in B and C in more detail. **B** The sensor arm springs of a 4-FR sensor element with an edge length of 135 μm are not developed, while **in C** the same sensor type with an edge length of 170 μm is fully developed.

To control whether the highly sensitive structures are entirely released without damaging them, CLSM was carried out. In figure 3.6, the results of CLSM are exemplarily shown for the designs presented above in figure 3.5 **B** and **C**. In the laser microscope top-view images 3.6 **B** and **C**, excerpts of the sensor element arrays indicating six different element areas of interest by colored fields (green, red and yellow) are presented. Here, F_L stands for left-sided sensor element frame, SA_L for left sensor arm spring, CP for centre plate of the element, and F_R and SA_R for right frame
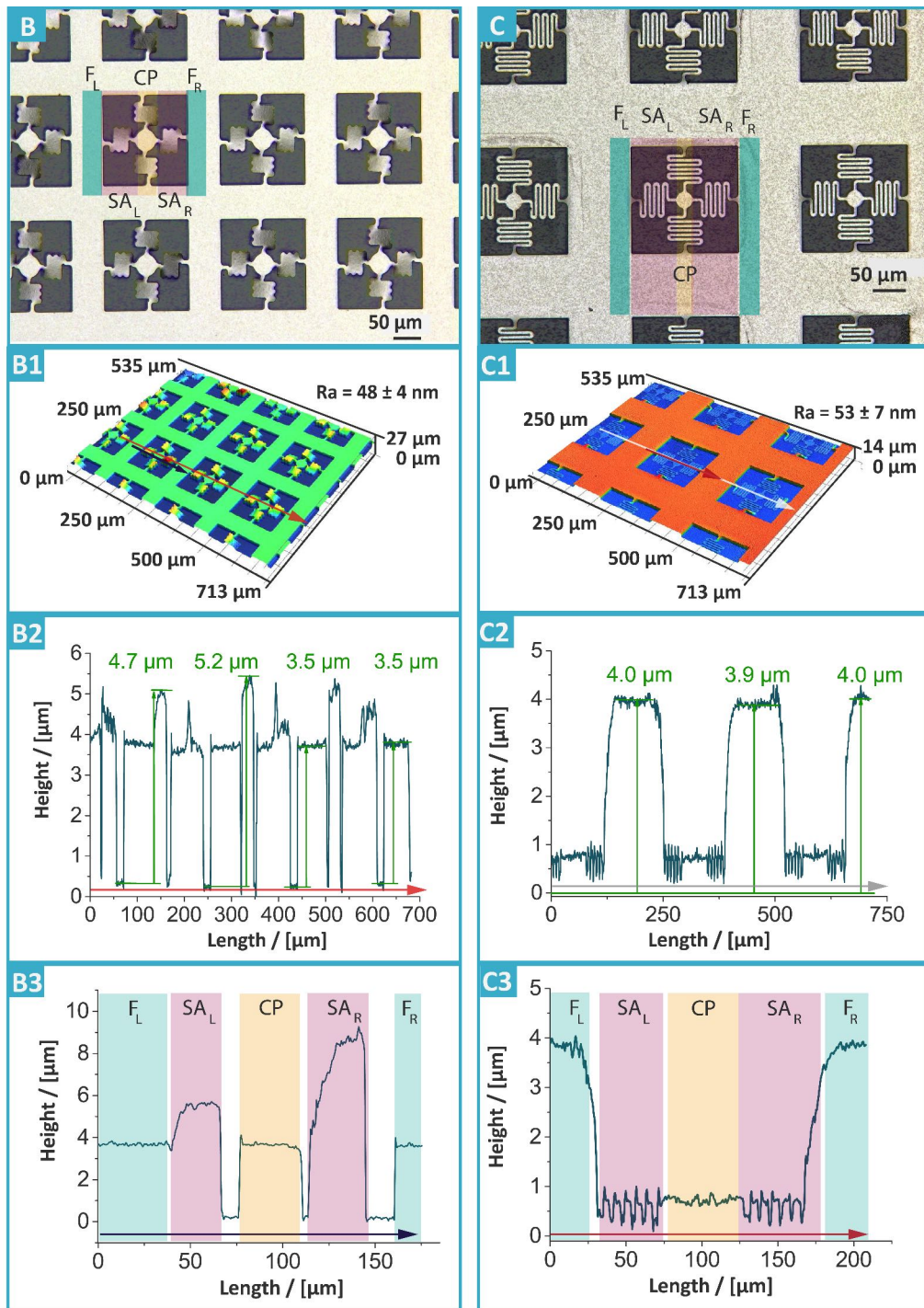
Figure 3.6: CLSM results of the processed NiTi samples shown in figure 3.5 **B** and **C**. **B** and **C** Laser microscope images of array parts of the sensor elements. The marked color regions represent areas of interest, with: F_L - Frame, left side, SA_L - Sensor arm, left side, CP - Centre plate of the sensor element, SA_R - Sensor arm, right side and F_R - Frame, right side. **B1** and **C1** Isometric presentation of the 3D CLSM records. The surface topography is color-coded. Therefore, red areas represent higher regions, while

dark blue areas are bottom parts. The vectors indicate the path of the profiles shown in the following. Here, the sensor elements of **B2** are on the same height level like the frame (both are green colored), while in **C2**, the frame is the highest area of the array and the sensors (blue colored) are attached to the substrate surface. **B2** Line Profile of the sensor element array surface along the red vector.
The prominent columns of 4.7 and 5.2 μm correspond to sensor arms that are deformed out of plane. **C2** Line surface profile along the white vector in **C1**. Here, the prominent columns represent the frame parts. The alternating structures between the frame columns correspond to the sensor arm spring coils, that can be identified more precisely in **C3**. In **B3** and **C3**, the line profile along the black (**B3**) that is to say the red **C3** vector of a single sensor element is presented including the corresponding areas of interest (compare **B** and **C**).

and spring sensor arm. The elements of the arrays are homogenous, indicating a well reproducible process. In (**B1**) and (**C1**), isometric illustrations of the confocal records give an overview on the surface topographies. Based on a color-coding, the red areas represent elevations, while blue areas indicate valleys. In **B1**, the frame and the sensor elements have a greenish color and in consequence, have the same height level. The outer parts of the sensor arms are The outer parts of the sensor element arms are yellow to red, which is due to a tilt of the arms out-of-plane. In contrast, the area of the frame is red and the sensor elements are blue in figure **C1**. Here, the structures are sticking to the substrate surface.

To further clarify the condition of release of these elements, line profiles were recorded along the vectors as marked in **B1** and **C1**. The profile along the red vector is shown in **B2** and gives an overview on the general height levels in a row of sensor elements. Here, the columns of 4.7 to 5.2 μm height are tilted SAs as already described above, while areas of about 4 μm height correspond to the frame and the centre plate CP. This is outlined in more detail in the profil **B3** for a single element along the black vector. The dominant out-of-plane tilt of the SAs of up to 6 μm is caused by internal stress due to the sticked meander structures. Buckling due to material stress is a well known challenge in micromachining.[199] This problem has been solved for the second sensor element as shown in **C2** and **C3**. Here, the alternating small structures between the frame column of 4 μm height and the sensor centre plate correspond to the five sensor arm slopes. The spikes that can be observed at the edges of the coils are known phenomenons within CLSM and caused by interferences

along sharp edges.[249] These spikes are in general smoothed by adequate software filters causing a slight change in height resolution. To keep the highest possible resolution in z-direction, the author forwent these filters.[250] The sticking of the sensor element to the substrate surface is another well-known phenomenon in micromaching and is caused by capillary forces.[199] In figure 3.7, the process of releasing a NiTi sensor element is exemplarily shown in sideview. The sacrificial Cu layer is wet etched (see figure 3.1 **B**). By the evaporation of the etching liquid and the corresponding interaction of the fluid and the sensor element surface, the centre plate of the sensor is gradually lowered (see figure 3.1 **C**). Finally, a thin fluid film is left possessing two menisci caused by capillary forces bet-
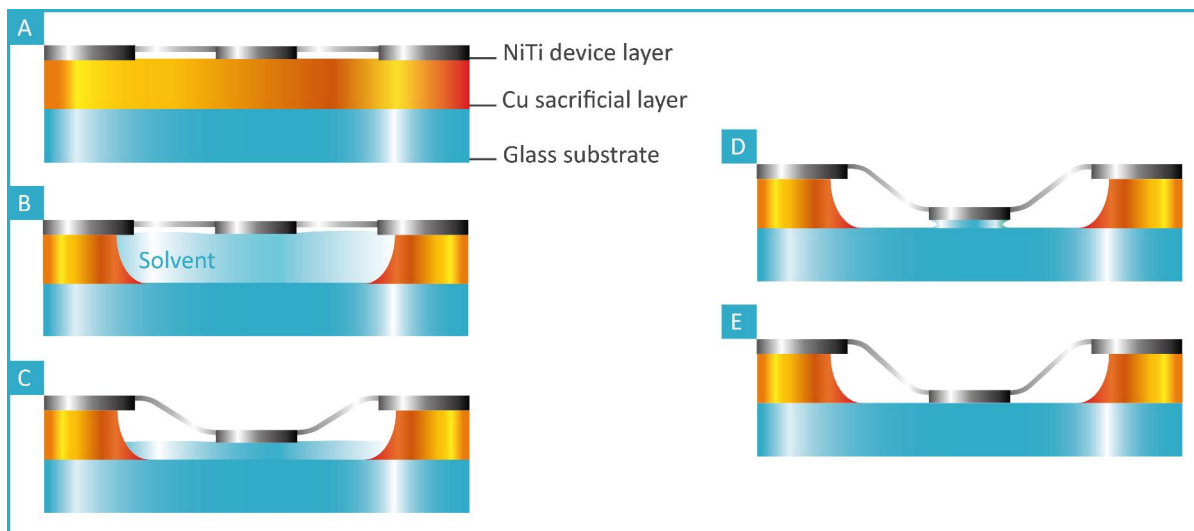
Figure 3.7: Sideview of the stiction process after wet etching the sacrificial Cu layer of a NiTi sensor element. **A** NiTi sensor element on Cu layer before wet etching. **B** The sacrificial layer is isotropically wet etched by a well-chosen solvent that interacts with the NiTi contact plate. **C** The evaporation of the solvent during the drying procedure has started and causes a lowering of the interacting contact plate. **D** Progressive evaporation of the fluid leads to the formation of a liquid meniscus between the substrate surface and the bottom part of the centre plate. The dominating capillary forces induce an additional approach of the centre plate to the substrate surface. **E** The fluid is entirely evaporated and by this, the contact plate of the sensor element sticks to the glass substrate.

ween the solids and the fluid. This additionally approaches the centre plate to the substrate surface (see figure 3.1 **D**). The above described interactions and the entire evaporation of the liquid cause a sticking of the sensor to the substrate (see figure 3.7 **E**), which causes a function failing of the sensor

element. When controlling sensor elements of bigger size or other sensor samples, the same result has been observed. To overcome these capillary forces, the sacrificial layer thickness could have been theoretically increased. By this means, the maximum elongation of the sensor arm springs due to capillary forces during the evaporation process needs to be overcome by its restoring force. This would lead to Cu layer thicknesses higher than 10 μm. However, the thicker the buffer layer the bigger the size of a producible sensor element considering the wet chemistry fabrication process. In consequence, a different fabrication technique was then applied.

Figure 3.8: Fabrication result of NiTi sensor elements in 10x10 mm NiTi foils (**A**) of 50 μm thickness. **B** Laser microscopic image of 4-FR sensor as already presented in figure 3.5 **C**. Sensor elements of 170 μm edge length were the only fully developed structures that were stable against impacts by handling.

10 x 10 mm free NiTi foils of 50 μm thickness including 200 nm thick sensor element arrays were fabricated as described above. The fabrication results are shown in figure 3.8 **A**. In contrast to the element arrays on a glass substrate, the release of the sensor elements was directly ensured by the lift off process at the end of the fabrication procedure. However, these membrane like foils (see figure 3.8 **A**) had to be handled sensitively as slight impacts caused the destruction of sensor elements bigger than 170 μm (see figure 3.8 **B**). Moreover, internal stresses within the membrane caused torsions of the sensor elements which were higher the bigger the sensor element size. In figure 3.9, SEM images of the same sensor as presented in figure 3.8 indicate a slight torsion within the element, which is due to stress within the foil and the less rigid frame compared to the fully fixed frame structure of the glass substrate based sensor array approach. These sensor elements were used throughout the mechanical characterization of 4-FR NiTi elements and proved to be longterm resistant to outer impacts in the everyday laboratory routine. To achieve smaller NiTi element sizes for future applications, the fabrication could be changed to a gas phase etching process, which is e.g. based on a CO/NH3 plasma treatment of the structural NiTi layer.[251] Besides the
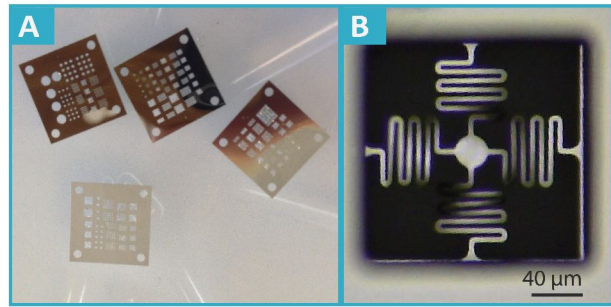
characterization of the mechanical be-
havior of the sensor element arrays, the
used samples needed to be biocompat-
ible.

Regarding the biocompatibility of the
NiTi foils, the viability of cells on this
material has already been shown else-
where.[154] [252]

Figure 3.9: SEM images of one 170 μm sized 4–FR sensor element from top- (**A**) and sideview (**B**). The whole in the middle of the sensor element centre plate has been shot via an ion beam and was needed for further mechanical testing as presented in chapter 4.

On the contrary, the glass substrate based sensor element arrays were not characterized with regard to their cell viability before. In consequence, an MTT test based on ISO10993-5 was carried out. The result is presented in figure 3.10. Here, samples of pure DMEM were used as control samples with a viability of the cells of 100 %. Samples with a concentration of the pure NiTi array extraction of 16 % and 32 % show a viability above 100 %. In consequence, this environment has a proliferative effect on the cells. With regard to higher extraction concentrations of 64 % and 100 %, the viability drops to 80 % that to say 50 %. Here, the last NiTi sample is categorized as cell toxic according to ISO 10993-5:2018, in which all samples with cell viabilities below 70 % are defined as non-biocompatible.[246]

The reason for these results is the remaining copper layer between the NiTi device layer and the glass substrate. In general, copper is a heavy metal, which has an antibacterial effect and is toxic in high concentrations. However, it is an important trace element and hence is an essential component within various enzymes. Human beings therefore need a daily dosis of up to 1.5 mg.[253] Obviously, the concentration limit of copper ions was exceeded in the last extraction, for which reason the cell viability was reduced and the material behaved toxic. Within the MTT test, the DMEM was exposed to the sensor element wafer for 24h according to the ISO standard. In first real time experiments for 3D cell traction force testing, the overall exposure of the cells to this extraction is a few hours
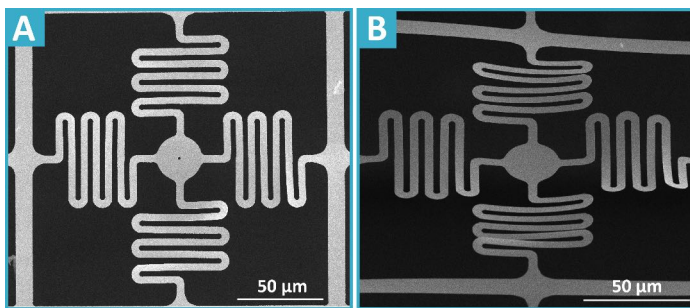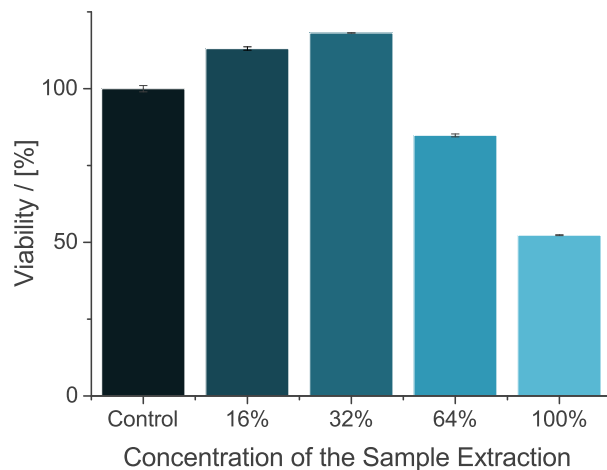
Figure 3.10: MTT test[1] result for NiTi sensor element arrays fabricated on glass substrates with a sacrificial copper layer. Pure DMEM was set as a control with a cell viability of 100 %. Concentrations of the NiTi array liquid extraction of 16 % and 32 % have a proliferative effect on the cells, wherefor the viability is higher than in the positive control sample. Extraction concentrations of 64 % correspond to viabilities of about 80 %. On the contrary, 100 % of the extraction cause the death of 50 % of the cells. For shorter exposure times than 24h, as set in this project, the cells survive. The toxicity of the samples at high extractions concentrations are due to Cu ions dissolved by the buffer solution over time. The error bars correspond to standard deviations for five measurements per concentration, which are: for the control, for 16 %, for 32 %, for 64 % and for 100 %. Hence, the deviations are neglectable.

only. So, the cell viability throughout the experiment is given although the sensor plate would not be classified as biocompatible according to the ISO norm.

As a result, NiTi foil based sensor elements are suitable regarding the defined requirements (see section 2.2.2) and were chosen for further experiments.

3.5.2 a-Si Sensor Arrays

To reduce the overall sensor size and produce arrays of elements which are mechanically decoupled by means of rigid frame structures, a-Si based sensor elements were fabricated by dry etching surface micromachining on glass substrates. The established fabrication procedure and the results are presented in the following as well as the results of cell shearing tests on the sensor element surface and biocompatibility testing.

3.5.2.1 Materials and Methods

a-Si Surface Micromachining Amorphous Silicon sensor arrays were kindly fabricated in a cooperation by the group of Prof.Dr. B. Wagner at Fraunhofer ISIT Itzehoe according to my masks designed in CAD. The process flow is shown in fig. 3.11.

Here, 400 μm thick 8 " borosilicate glass wafers were coated with 20 nm of aluminum to protect the backside glass surface from etching by hydrogen fluoride (HF). 4 μm of silicon dioxide were then deposited by plasma-enhanced physical vapor deposition, followed by thin layers of amorphous silicon with 100 nm, 200 nm, 300 nm and 400 nm thickness (figure 3.11.**1**). The wafers were spin coated with photoresist and then patterned by UV-lithography (figure 3.11.**2-4**). 50 x 50 mm plates of sensor arrays were then cutted with a wafer dicing saw for better handling. Afterwards, the a-Si layer was structured by dry etching with HF. The photoresist was ashed (Gasonics$^{®}$ L3510) and the aluminum was wet etched. Free-standing a-Si structures were created by gas-phase etching of the sacrificial silicon dioxide layer by hydrofluoric acid with treatment times of 750 s, 1000 s and 1250 s.

Characterization The a-Si sensor arrays were characterized according to the methods used for NiTi (see subsection 3.5.1 Materials and Methods).

Cell shearing Rat embryonic fibroblast wild type 52 cells (ref52 wt) were first transferred to phosphate buffered saline (PBS, Sigma-Aldrich$^{®}$, P5493) and washed for three times. A 50 x 50 mm^2 sensor plate with a 200 nm thick a-Si layer was washed with ethanol for three times, then with PBS and a frame of biocompatible glue was set around one sensor square. The cells were then pipetted on the sensor surface and incubated in DMEM$^{®}$ (supplemented with 10 % FBS and 1 % Penilicin;
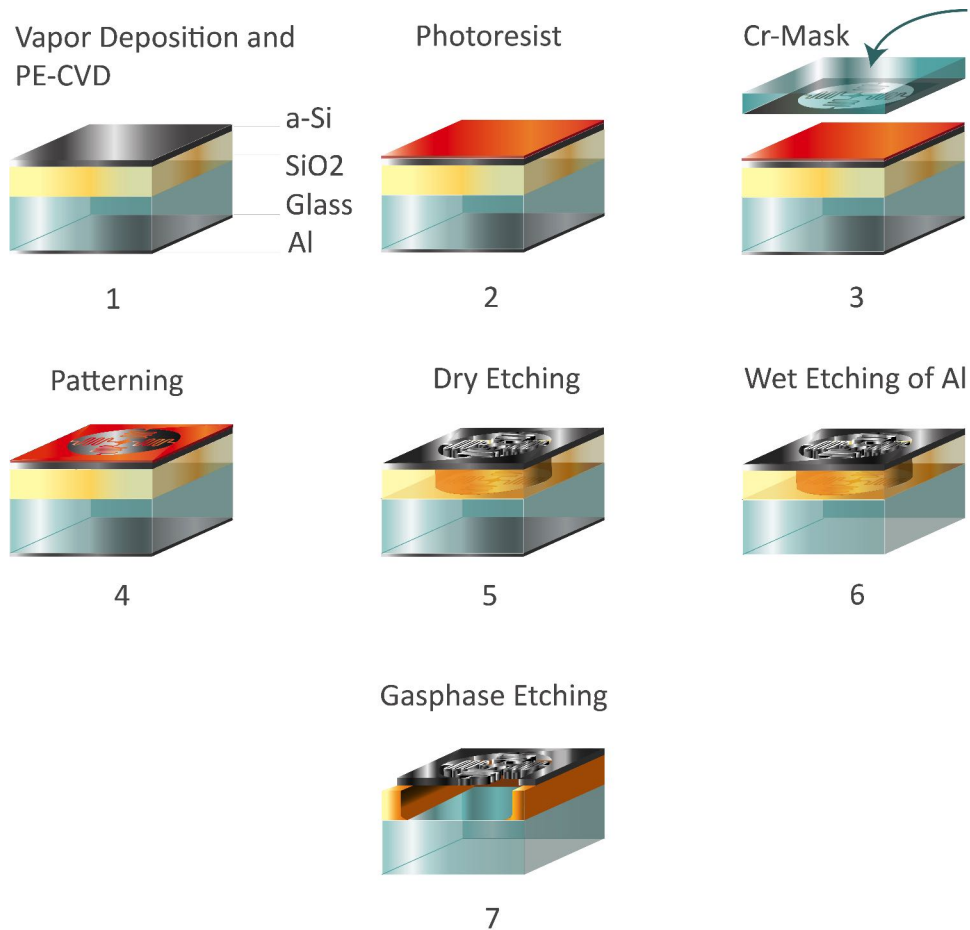
Figure 3.11: Schematic illustration of the surface micromachining process to fabricate a-Si sensor elements: **1** Vapour deposition of an aluminium thin layer on the backside of the 400 μm thick glass wafer to protect the glass against the dry etching process. On the front-side, a 4 μm thick sacrificial silicon dioxide layer and a 200 nm thin a-Si layer were deposited by means of PECVD. **2** Spin coating of photoesist on top of the device layer. **3** and **4** UV lithographical patterning of the photoresist. **5** Dry etching of the a-Si layer by SF_6. **6** Removal of the aluminium protection layer by wet etching. **7** Release of the a-Si structure by gasphase etching of the sacrificial layer by HF. To indicate the isotropic etching of the buffer layer, a cross sectional illustration of the released sensor structure has been chosen.

Biochrom®, Berlin, Germany) at $37°$C and 5% CO_2 for 24 h. Afterwards, the sensor plate was installed on an inverted microscope (Olympus® IX 81, Shinjuku, Japan) and 4-FR a-Si sensor elements (sensor diameter: 45 μm, sensor thickness: 200 nm) were set in focus using a 40x magnification

objective (Olympus® LCAch Nm 40x/0.55 PHP). A glass microneedle was positioned via a microma-

nipulator as shown in figure 5.3 **B**. Here, the micrometer z-translational stage (1) (PI® M501.1PD:

$\delta(z) = 12.50$ mm, resolution: 0.024 μm; controller C-863 Mercury Servo Controller) and the x-, y-,

z-piezo nanopositioner (2) (PI® 517.3CL: $\delta(x,y)_{max} = 100$ μm; $\delta(z) = 20$ μm, resolution: x,y: 1 nm,

z: 0.1 nm and controller E-517) were electronically driven by the PI software. By this, the needle

was injected in a cell adhered on top of the sensor structure without harming the nucleus. Then,

the needle was first translated in 5 μm steps to 50 μm in-plane displacement from the starting point

and then moved out-of-plane in 5 μm steps, while the deformation process was recorded via the

microscope software.

3.5.2.2 Results and Discussion

Four different a-Si structural layers were deposited and patterned to find the most suitable layer

thickness regarding 1. minimum layer thickness for maximum deformability, 2. release of the struc-

tures overcoming the problem of surface sticking and 3. minimum under-etching of the frame to

ensure a well-defined deformation behavior.

CLSM images of the fabrication results for 100 nm, 200 nm, 300 nm and 400 nm thick layers after

1000 s of gas phase etching as well as line profiles along the indicated black vectors are shown in

figure 3.11. For better comparison 4-FR sensor elements (shown in **A** to **D**) of the same edge length

of 45 μm and a sensor arm width of 1 μm have been chosen. All structures are well developed. The

difference in material surface color is caused by the difference of the a-Si layer thickness ranging in

nanometer region.

In **A1** to **D1**, surface topographies in isometric view of the corresponding sensor element arrays

are presented. Here, the arrays of 200 nm, 300 nm and 400 nm thickness possess a homogenous

topography without material elevations. For 100 nm thick layers, dark red columns between the

different sensors are observable. Out-of-plane material deformations are caused by under-etching

and stress within the a-Si layer along the sensor arm axis.

To validate the topography of the sensors more precisely, line profiles are presented in **A2** to **D2**.

As already introduced for the profiles of NiTi sensor arrays, the broad columns represent the frame

structures between the sensor elements. The thinner column in the middle of the frame structures
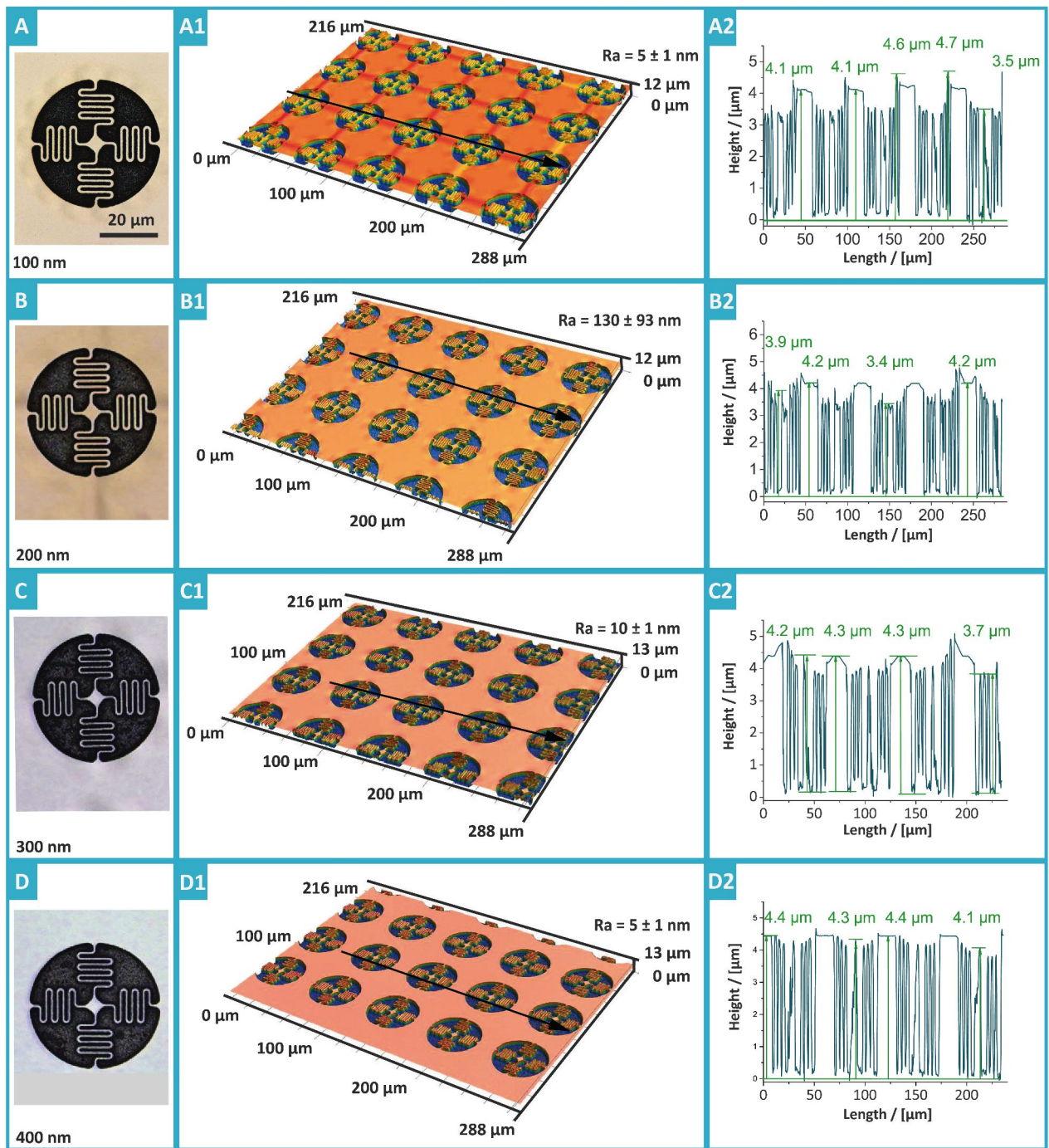
Figure 3.12: **A** to **D**: CLSM images of 4-FR sensor elements with a diameter of 45 μm after an etching treatment of 1000 s and different layer thicknesses: **A** 100 nm, **B** 200 nm, **C** 300 nm, **D** 400 nm. All structures are well developed. The difference in color is due to the change of the structural layer thickness. **A1** to **D1** Surface topographies of the corresponding sensor element arrays. In **A1**, red colored columns along the axis of the

element sensor arms indicate out-of-plane deformations of the 100 nm thick structural layer due to structural stress within the elements. The topography of **B1** to **D1** appears to be in one plane indicated by a homogenous reddish color. **A2** to **D2** Line profiles along the indicated black vectors. Here, the broad columns correspond to the frame structure, the thin columns in the middle between of two frame structures are the sensor contact plates and the alternating structures between the frame and the centre plate represent the sensor arm spring coils. In **A2**, the difference between the frame height (4.1 μm) and the centre plates (3.5 μm) are caused by a slacking of the element due to its dead weight. Elevations of up to 4.7 μm are caused by internal stress of the element, which causes an out-of-plane deformations of the sensor arm root at the frame. Slight deformations can be observed for 400 nm thick layers (**D2**).

corresponds to the element centre plate and the alternating structures between the frame columns and the centre plate are the sensor arm spring coils. For 100 nm thick structures, the lowest regions are the centre plates with a height of 3.5 μm. The alternating columns representing the sensor arms increase gradually in height from the centre plate to the frame from 3.5 μm to 4.1 μm. The highest points are 4.6 to 4.7 μm and correspond to an out-of-plane deformation of the sensor arm root at the frame due to the dead weight based slack of the element structure. A comparable slacking can also be observed for 200 nm thick a-Si sensor elements with a variation of the centre plate height and the frame structures of about 600 nm. However, no elevations or under-etching are observable. Regarding 300 nm thick layers, the overall frame height is 4.3 μm. The height of the sensor centre plate varies between 4.3 and 3.7 μm and the sensor arm spring coils even show a strong bending out-of-plane of up to 4.8 μm. In comparison to the out-of-plane deformations of 100 nm thick structures, there is no homogenous increase in hight from the centre plate to the frame. So obviously, there is internal stress within the structures wherefore, they are slightly tilted. Finally, a height difference of only 200 nm maximum between the element centre and the frame is observable in case of 400 nm thick a-Si layers. These structures are not tilted and slightly slack, but they are stiffer than the 200 nm thick elements. Hence, layers of 200 nm thickness were chosen for further experiments. The optimum release of the structures is based on an adequate etching time. For this reason, 200 nm thick a-Si samples were also etched for 750 s and 1250 s.

The results are shown in figure 3.13. In general, the etching result after an HF treatment for 750 s

is comparable to the results of a treatment for 1000 s. The elements slack wherefore the frame height and the centre plate differ by up to 800 nm. Moreover, the sensor arms springs slopes cannot be distinguished and single peaks are only observable. Hence, the etching time was not sufficient to remove the supporting material entirely.
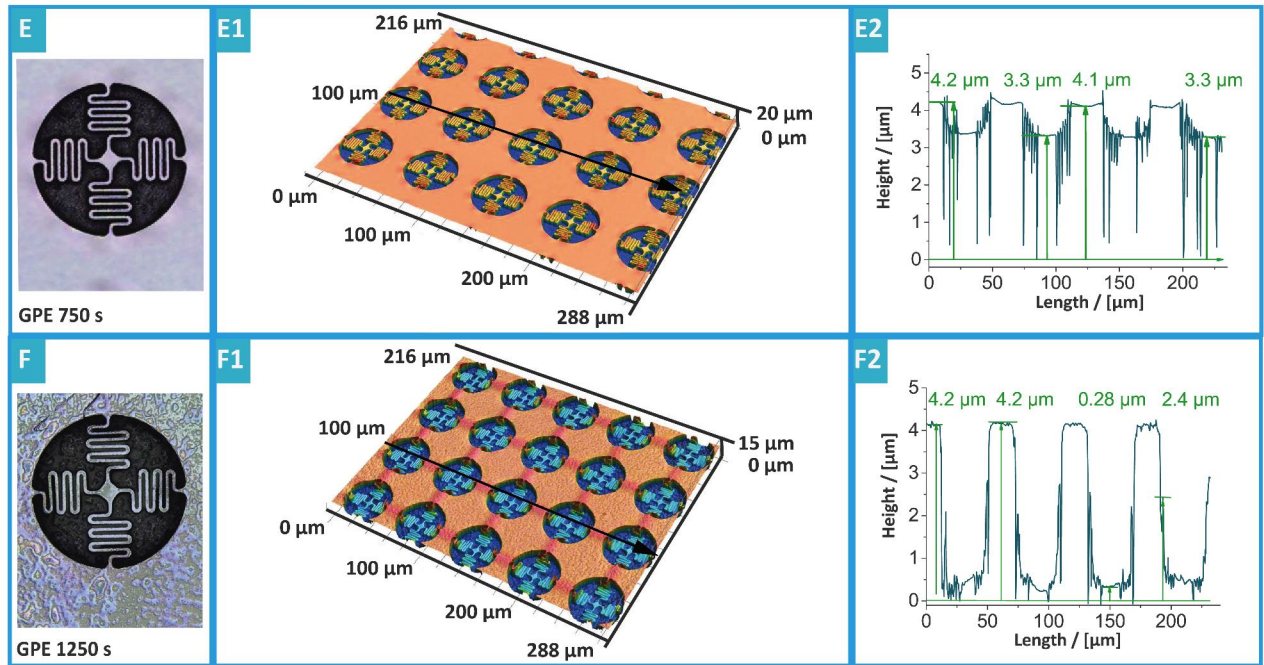

Figure 3.13: CLSM images of 45 μm sized 4-FR sensor element arrays of 200 nm thickness after HF gas phase treatment for **E** 750 s and **F** 1250 s. **E1** to **F1**: Surface topography of the two samples. After 750 s **E1**, the structures are already under-etched and the sensor arms are slightly deformed out-of-plane as can be seen by the reddish color of the element roots. In **F1**, the sensors stick to the substrate surface. **E2** to **F2**: Line profiles of the two sensor arrays along the indicated black vector.

So, the structures appeared to have left-over silicon dioxide that sticks between the coils. After 1250 s of HF treatment, the structures were under-etched as can be seen by the red-colored elevated frame material along the prolonged sensor-arm axis as already observed for 100 nm thick layers (see figure 3.12 **A**).

The frame columns have a height of 4.2 μm, while the centre plate is at around 0.28 μm. The sensor arms cannot be properly detected, which might be due to the grained silicon dioxide buffer layer that was left over on the substrate surface. With regard to the topography record (**F1**) and

the line profile (**F2**), all of the elements stick to the substrate surface. Based on these results, an a-Si layer of 200 nm thickness that was treated with HF for 1000 s has been chosen.

To find the minimum producible sensor element size, different element sizes were fabricated as shown in figure 3.14. Here, the 4-FR sensor element type 1 differs from the 4-FR sensor element type 2 by the distance between the spring coils. In design **1A**, the distance is 500 nm and in **2A**, it is 1 μm, for which reason design **1A** is 24 % smaller than **2A**.

However, the spring coils of **1A** stick to each other as already observed in the fabrication of the small NiTi sensor elements and hence, this sensor element was ignored within the following experiments. Elements of type 1 with a diameter of 38 μm to 114 μm (see **1B** to **1E**) are well developed. Here, SEM images **1A** and **1E** indicate strong loading effects on the surface as indicated by the blurred black parts within the images even after intense optimization of the SEM setting parameters and deposition of additional 10 nm of gold coating.

This is due to the silicon dioxide sacrificial layer which left grains after etching as seen as white deposit between the a-Si structures in all images. Regarding 4-FR type 2 sensor elements, all sizes ranging from 45 μm (**2a**) to 136 μm (**2E**) could be fabricated. As a result, 200 nm thick a-Si sensor element arrays, which were HF treated for 1000 s with an edge length of 45 μm and a minimum sensor arm width of 1 μm were the most promising sensor elements used within further experiments.

Compared to the well-known superelastic behavior of austenitic NiTi regarding deformations in the micrometer region, little was known about the mechanical behavior of a-Si structures in this layer thickness region and the deformation in the micrometer range. Hence, the centre plate of the above defined 4-FR a-Si sensor elements was micromanipulated by a tungsten needle in an SEM surrounding as shown in figure 3.15. First, the tip was approached to the left edge of the centre plate (**0 s**), then the element was carefully displaced in z-direction (**5 s** and **14 s**) to a first maximum deformation of about 6 μm (**22 s**). The sensor was afterwards retracted to its original position (**25 s** and **28 s**). At 40 s, the tip was lifted by about 5 μm and the a-Si element was displaced out-of-plane. Finally, the element was displaced for a second time in z-direction by a maximum displacement of about 20 μm (**65 s**), followed by an entire relaxation to its original position at 80 s. By this, it was shown that an a-Si structure of 200 nm thickness can be repeatedly displaced up to 200 % of their sensor arm length without being damaged and hence possess a well-suited elastic behavior for the
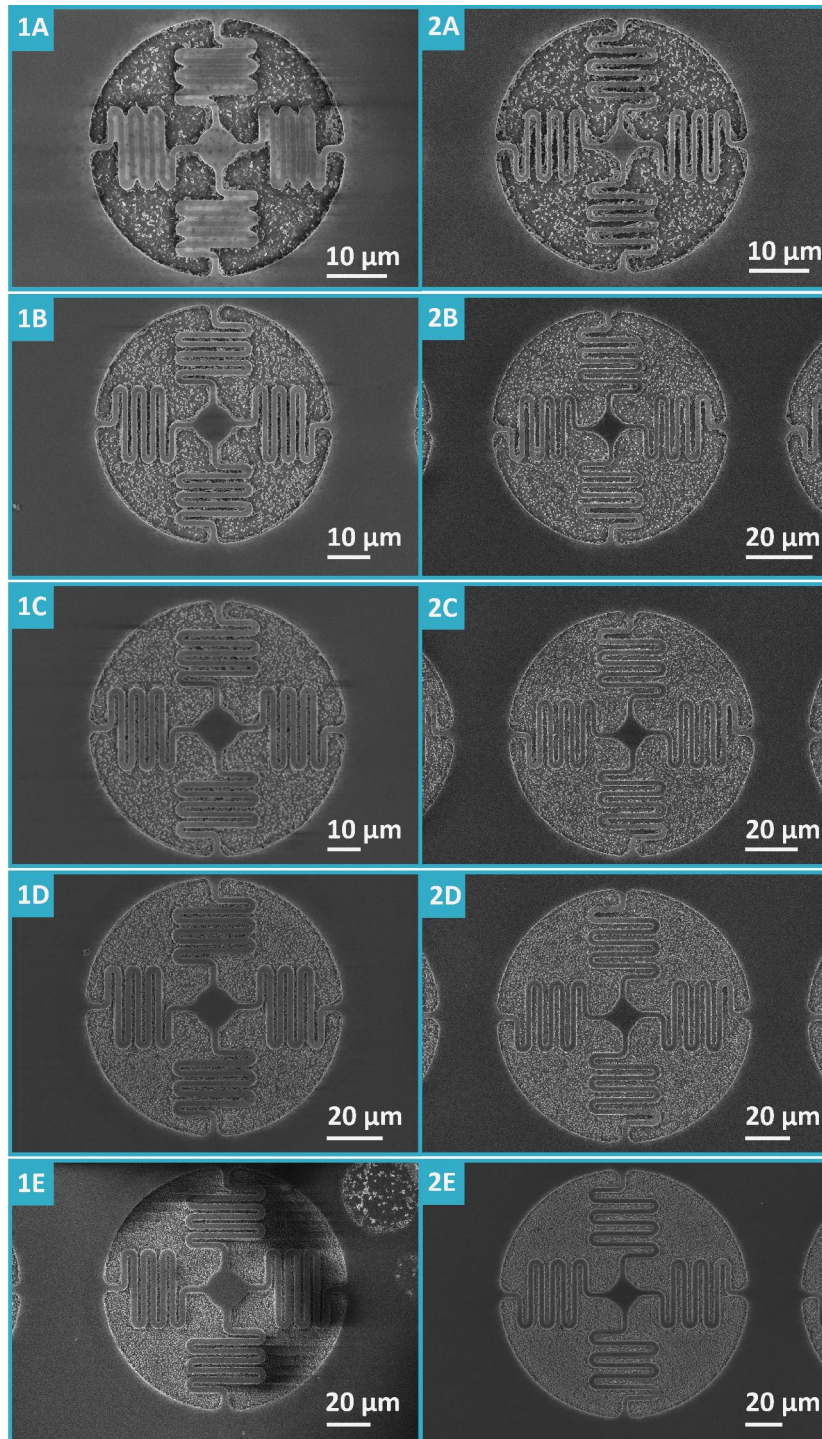
Figure 3.14: SEM images of 200 nm thick 4-FR sensor elements of different size (**A**-**E**): **1A** The element has a diameter of 38 μm and a sensor arm width of 1 μm. The distance between the spring coils was set to 500 nm. However, the coils are sticking together.

The diameter in a row of sensor type 1 are: **1B** - 57 μm, **1C** - 76 μm, **1D** - 95 μm, **1E** - 114 μm. **2A** Sensor element with a diameter of 45 μm, a sensor arm width of 1 μm and a distance between the spring slopes of 1 μm: this is the minimum sized a-Si sensor element of type 4-FR, which was used throughout this project. The diameters of the other elements of type 2 are: **2B** - 68 μm, **2C** - 91 μm, **2D** - 113 μm , **2E** - 136 μm.

purpose of this project (see section 2.2.2, chapter 2). Due to the change from a wet chemistry based process to a dry etching fabrication, the sensor element size could be reduced by 70% to a more compact size. As shown in figure 3.16, the smallest 4-FR element in 50 μm thick NiTi foil (**A-A2**) has an edge length of 170 μm and a theoretical spring constant based on FEA of 0.066 N/m. The size optimized 4-FE NiTi based design (**B-B2**) fabricated on a glass substrate has an edge length of only 70 μm, with a theoretical spring constant of 0.25 N/m.

However, this design suffers from sticking to the glass substrate as described above. The compact 4-FR design fabricated by dry etching surface micromachining of a-Si (**C-C2**) has a minimum element size of 45 μm at a theoretical spring constant of 0.15 N/m. In figure 3.16 **A2** to **C2**, the corresponding 5x5 sensor element arrays are compared regarding their overall size that range from 890 μm for the NiTi based structures **A2** to an optimum of 265 μm for the a-Si sensor elements. In consequence, **A** is the ultimate sensor element regarding the geometrical project requirements of solid state based element structures.

Regarding the biological suitability of the 4-FR a-Si sensor element array, its biocompatibility was tested by an MTT test as described in section 3.5.1.1. The results of the test are presented in figure 3.17. The control is again pure DMEM, in which a cell viability of 100 % was observed. Extractions of the solution that was exposed to the a-Si surface for 24h were diluted to concentrations of 16 %, 32 % and 64 % . Here, the cell viability is higher the higher the extraction concentration and vary between 80 % and 100 % considering the standard deviations. Pure extractions even seem to support cell proliferation, for which reason the cell viability is higher for extraction concentrations of 100 % than for the positive control samples. When considering the standard deviation, the viability of the
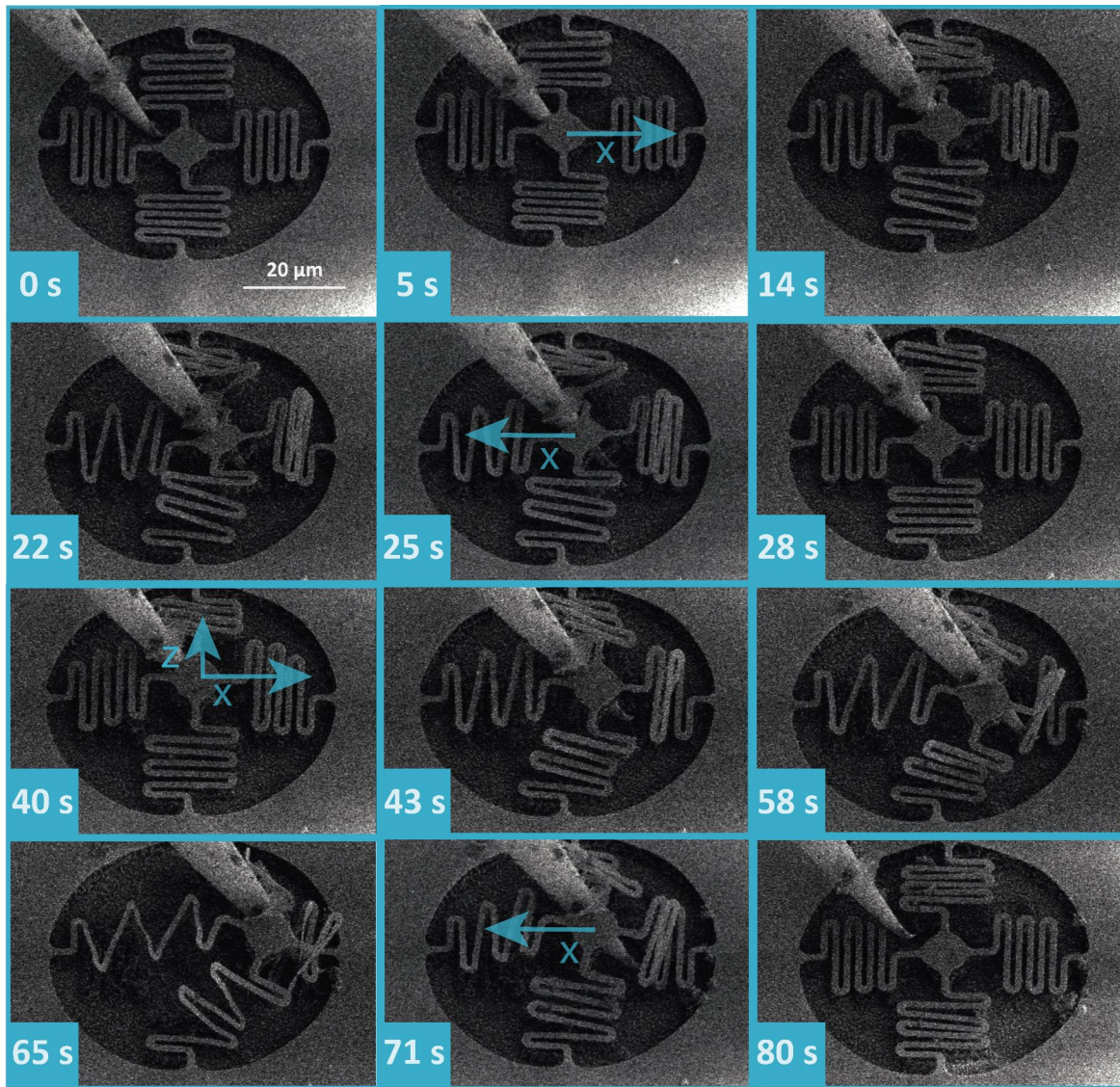
Figure 3.15: SEM images recorded in a time laps during the displacement of a 45 μm sized 4-FR sensor element via a tungsten tip. Here, the sensor contact plate was carefully displaced and relaxed twice. **0 s** Approach of the tungsten tip to the centre plate: starting point. **5 s**-**25 s** first displacement of the sensor plate of up to 12 μm. **28 s** Gradual relaxation of the sensor to its original position. **40 s** Slight displacement of the element in z-direction up to 5 μm. **43 s**-**65 s** Second displacement in z-direction of about 20 μm. Here, the left sensor arm is elongated by 200 % of its original length. **71 s** and **80 s** Relaxation of the sensor element to its starting point. The sensor element was mechanically displaced repeatedly without any damage.
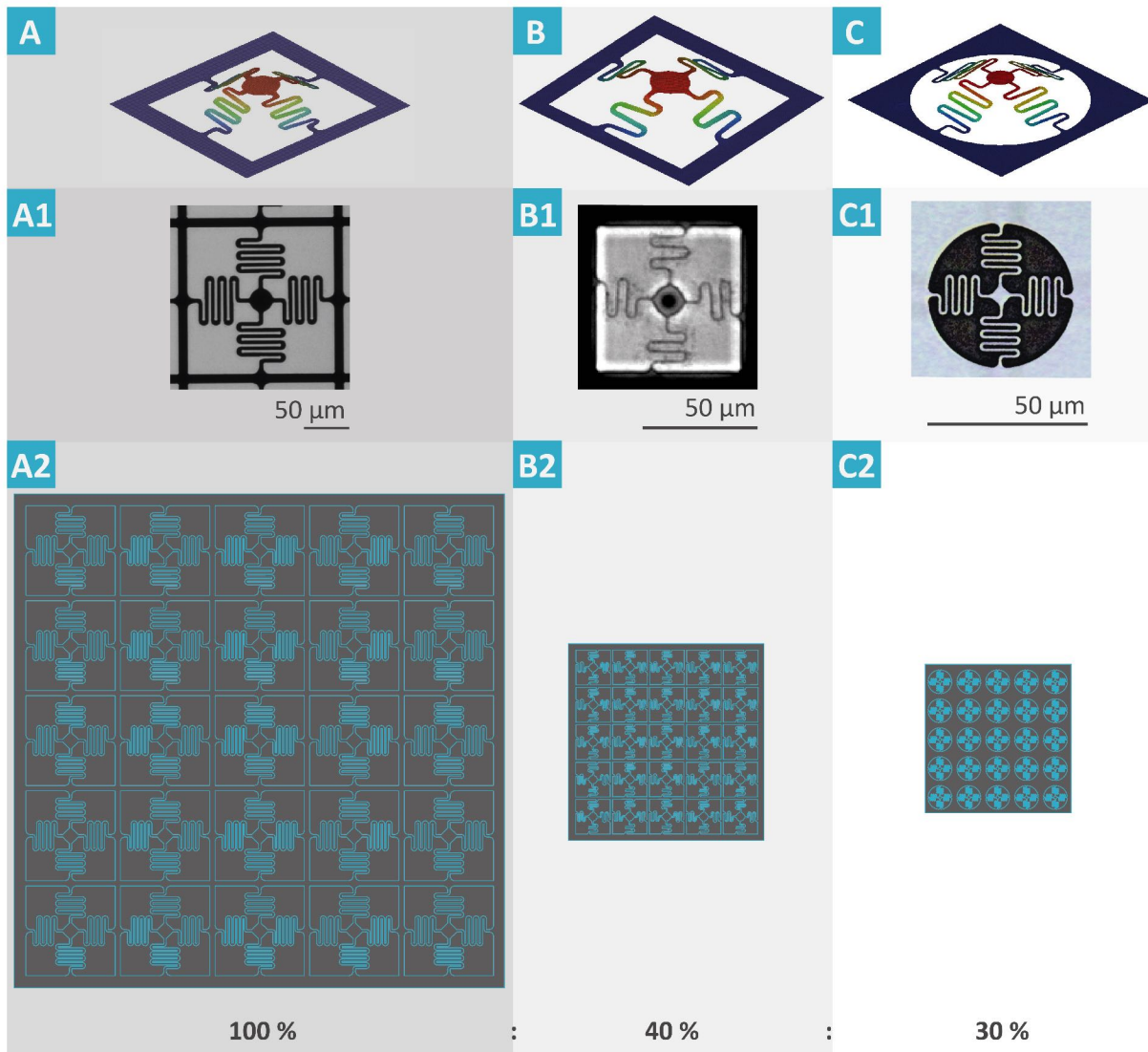
Figure 3.16: Overview on the size reduction of the 4-FR sensor element by means of different fabrication processes: **A** to **C** FEA images of the sensor elements and their the out-of-plane displacement in case of an effective force of 5 nN. For better clarity, the display of the displacement has been enhanced by a factor of 1000. Based on FEA, the spring constant of **A** is 0.0065 N/m at an edge length of 170 μm, of **B** about 0.25 N/m at an edge length of 67 μm and of **C** 0.15 N/m at an edge length of 45 μm. In **A1** to **C1**, white light microscope images of the corresponding fabrication products are shown. **A1** 200 nm thick NiTi structure in a 50 μm thick NiTi foil fabricated by wet chemistry micromachining. **B1** Size optimized NiTi element 4-FE with two spring slopes fabricated on a 400 μm glass substrate by wet chemistry processes. **C1** Smallest a-Si sensor element structure fabricated by gas phase etching surface micromachining. **A2** to **C2**: Comparison of the overall sensor element array size for design **A** to **C** with **A2**: 890 μm array length, **B2** 375 μm length and **C2** 265 μm overall array length. The total array size was reduced by over 70 % from design **A** to design **C**.

control sample and the pure extraction are the same. As has been shown elsewhere, [254] [255] silicon and silicon dioxide particles support the growth and development of plants and are in vitro biocompatible and non-toxic according to ISO10993-5. In consequence, the sensor elements also proofed to be most promising with regard to their fulfillment of the biological project requirement.
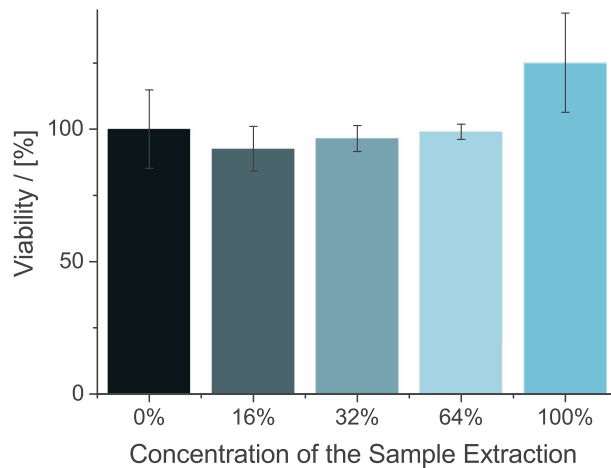

Figure 3.17: MTT test[2] result for a-Si sensor element arrays fabricated on glass substrates with a sacrificial silicon dioxide layer. DMEM was set as a positive control with a cell viability of 100 %. Concentrations of the a-Si array liquid extraction of 16 %, 32 % and 64 % range from 85 % to 95 % viability of the cells. Here, the viability increases with increasing extraction concentrations. Extraction concentrations of 100 % appear to have a proliferative effect on the cells, for which reason the viability is higher than within the control sample. The error bars correspond to standard deviations for five measurements per concentration.

Cell shearing was carried out as shown in figure 3.18. For this purpose, rat embryo fibroblast ref52 cells were incubated for 24h on the a-Si array surface. The adhered cell (indicated by the greenish area **2**) was then sheared by means of a glass microneedle (**1**), which was carefully inserted into the cell matrix without harming the cell nucleus. From this starting point, the microneedle was driven stepwise via a piezo driven translational stage along the y-axis to its maximum travel path position. Within the image, the corresponding displacements of the sensor contact plate are indicated in the blue boxes on the top left of each image.

---

[2]The MTT test was kindly run by our technical assistant A. Duttmann (working group of Prof. Selhuber-Unkel, Department of Biocompatbile Nanomaterials/ Christian-Albrechts University of Kiel).
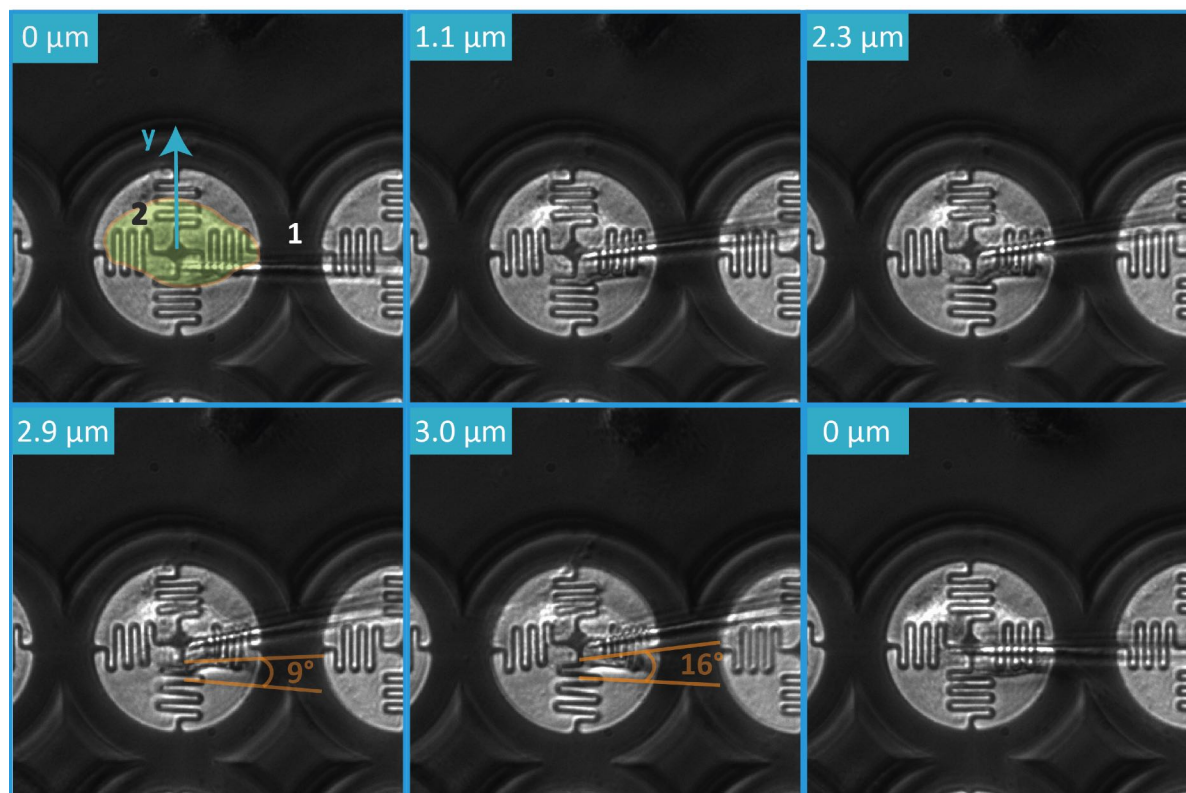
Figure 3.18: Cell shearing[3] of a 45 μm sized 4-FR a-Si sensor element of 200 nm thickness via a cell (greenish area **2** indictated in the first image) that was manipulated by a glass microneedle (**1**). The displacements of the centre plate from its original position are inscribed in the blue boxes on the top left of each image. (**0** μ**m**) The microneedle was inserted into an adhered cell that was positioned in the middle of the sensor element. (**1.1** μ**m**) The microneedle was moved along the z-axis indicated by the blue arrow. This movement induced a displacement of the sensor centre plate of 1.1 μm. By further movement of the microneedle, the plate was gradually displaced up to **3.0** μ**m**. At **2.9** μ**m**, a strong bending of the bottom cell matrix can be observed. Here, the cell is still adhered to one of the sensor arm spring coils, but de-attached on all other parts of this region. The orange lines are extensions of the spring coils to indicate the change of spring deformation from 9° to 15° opening of the spring legs. At 3.0 μm displacement, the cell ruptured from this spring coil and the spring relaxes to its initial position. Here, the microneedle is driven to the maximum travel position of the translational stage (50 μm). Finally, the a-Si sensor element is relocated to its original position (**0** μ**m**).

At a displacement of the centre plate of **2.9** μ**m**, the bottom part of the cell matrix possesses a strong bending due to its adhesion to the sensor arm spring coil, which is ruptured in the following displacement step as can be seen in the next image (**3.0** μ**m**). Here, the spring coil has been relaxed to its original position without an additional force impact by cell traction forces. Finally, the microneedle is driven back to its starting point and the sensor element plate is relocated to its original position (**0** μ**m**). In consequence, cells adhere perfectly to this sensor element surface. Furthermore, the elasticitiy of this sensor element suits the cell shearing forces, wherefore microscopic displacements can be observed. Additionally, the element is usable in liquid surrounding without being damaged. As cell traction forces shall be measured by the displacement of the sensor element plate, cells shall only adhere to the contact plate. For this reason, the cell adhesion sites need to be controlled by biologically inert coating of the frame and the sensor arms in future experiments as already mentioned in the project requirement list (see section 2.2.2, chapter 2). An appropriate solution strategy for this purpose is presented in chapter 6.

Based on the results of the fabrication and characterization of the NiTi and a-Si based sensor element arrays, the 45 μm sized 4-FR a-Si sensor element of 200 nm thickness has shown to be the most promising solid-state sensor element. Its major advantages are 1. its comparably small geometrical dimensions of 45 μm in diameter and 1 μm thick sensor arm width (see figure 3.1.2 and 3.16), 2. its producible free-standing structures (see figure 3.12 and 3.15), 3. its biocomaptibility (see figure 3.17), 4. its mechanical compatibility and stability to liquid environments (see figure 3.15 and 3.18), 5. its suitable surface topography for good cell adhesion (see figure 3.18), 6. its elasticity and mechanical deformability with displacements of the spring coils of up to 200% of their original length (see figure 3.1.5).

The fabrication based on surface micromaching of a-Si is nevertheless rather time- and cost-intensive, wherefore an additional approach was taken into consideration, which is presented in the following section.

3.5.3 Process Development of PDMS based Sensor Elements

The above presented fabrication processes and used materials turned out to be time- and cost intense, while being limited in their mechanical properties due to their composition and minimum geometrical dimensions. When it comes to optimizations such as 1. the reduction of the overall sensor element array fabrication and material costs and time, 2. cheap one-way sensor elements for cell biological experiments, 3. a low Young's modulus for maximum sensitivity to weak forces down to the lower pN region and 4. a tunable Young's modulus to broaden the measurable force range by slight modifications of the same basis material, a different biocompatible material is needed.

A well established material is polydimethylsiloxane (PDMS), which was used in this project to develop a fabrication process for PDMS based sensor elements.

PDMS is a silicon based non-toxic, biocompatible, cost effective and chemically inert cross-linked polymer[256] of tunable elasticity,[257][258] which has a wide range of applications due to its properties. Consequently, it is used as food additive in the conservation of vegetables or marmelades,[259] as antifoaming agent in drugs or drug delivery,[260][261] in cosmectics, as well as basis material for contact lenses,[262] microfluidics[263] and biomedically used microelectromechanical devices.[264]

In the following, the different process steps of the developed fabrication procedure for PDMS based thin structured membranes as well as the characterization of each intermediate product are presented and shortly discussed.

3.5.3.1 Materials and Methods

PDMS Frame Fabrication SYLGARD®-184 base monomer and curing agent (SYLGARD®-184, Dow Corning, Midland, MI) were stirred at wt(monomer):wt(curing agent) = 10:1 in an IKA tube (IKA® VE ST-20 tube with stirring device, Staufen, Germany) for 15 min. After degassing of the prepolymer in high-vacuum, PDMS was poured in self-designed and workshop-built teflon molds (see fig. 3.19 **IV.A**, white box on the left side), degassed once again in high-vacuum, cured for 24 h at 65 °C and finally demolded for further use.

PDMS Sensor Fabrication The microfabrication of PDMS MEMS structures has been developed based on a process published by Chen et al. in 2012.[265] The process flow is presented in figure 3.19.

First, 25 x 25 mm^2 poly-silicon wafer plates (nominal thickness: 525 $\pm$ 25 μm, Siegert$^{\circledR}$ Wafer, Germany) were cleaned in acetone (<99.7 %, Ph.Eur., extra pure, Carl Roth, Germany) in an ultrasonic bath at 25 °C for 15 min. The N$_2$ dried plates were then spin-coated (OPTI spin ST22P, Solar-Semi, Germany) with protective resin of about 2 μm thickness (AZ 520D, AZ Electronic Materials$^{\circledR}$, Branchburg, NJ; level 1: t = 20 s, 3000 rpm, ramp of 120 rpm/s; level 2: t = 30 s, 3000 rpm, ramp of 120s) to facilitate subsequent release of patterned PDMS at the end of the fabrication process and to reduce the preparation time compared to a pre-silanization of the surface (see figure 3.19.**1**). Afterwards, the resin was baked for 5 min at 120 °C. To exclude air within the protective coating, the small plates were evacuated for 15 min in high vacuum. Meanwhile, a mixture of SYLGARD$^{\circledR}$-184 base monomer and curing agent (SYLGARD$^{\circledR}$-184, Dow Corning, Midland, MI) were stirred at wt(monomer):wt(curing agent) = 10:1 in an IKA tube (IKA$^{\circledR}$ VE ST-20 tube with stirring device, Staufen, Germany) for 15 min. The PDMS was then evacuated in high-vacuum until the polymer was degassed. The small silicon plates were spin-coated with PDMS prepolymer based on an established PDMS spin-coating program (level 1: t = 30 s, 1200 rpm, ramp of 90 rpm/s; level 2: t = 60 s, 5000 rpm ramp of 480s, level 3: t = 0 s, 80 rpm, ramp of 60 rpm/s) in order to generate 10 μm thick layers.[4] Afterwards, they were evacuated for 30 min in high vacuum and baked at 125 °C for 20 min. To avoid crack formation due to different thermal coefficients of the protective resin and PDMS, all heating and cooling processes were gently run (see figure 3.19.**1**).

According to Chen et al., the polymeric surface was first O$_2$ plasma treated (SENTECH$^{\circledR}$ SI 100, Berlin, Germany; t = 300 s, 25 Watt, 8 cm^3) and afterwards coated with a 10 nm thin gold layer by vapor deposition in ultra-high vacuum (customized Amocon$^{\circledR}$ FT&T GmbH photovoltaic setup, Burghausen, Germany) (see figure 3.19.**2**). This coating was used to ensure homogenous coating of the PDMS surface with photoresist in the next process step and to generate an appropriate reflectivity of the sensor element for optical readout.

---

[4]HBL-PDMS spin-coating program written by M.Sc. Henrik Block (working group of Prof. Dr. M. Gerken, Institute for Electrical Engineering, Faculty of Engineering, Christian-Albrechts-University of Kiel).
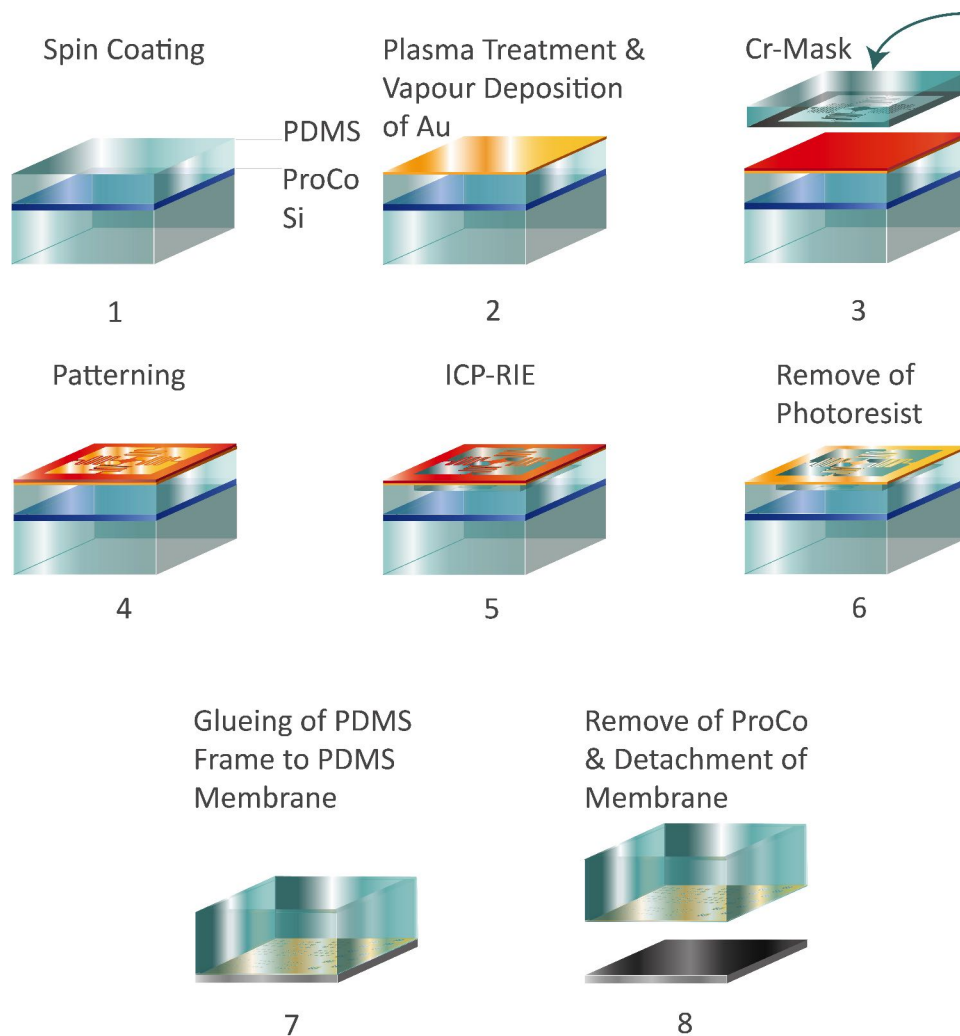
Figure 3.19: Process flow to fabricate structured PDMS membranes. In step **1** to **6**, the process is exemplarily shown in more detail for one sensor element. **1** Spin-coating of protective resin and 10 μm of PDMS on a silicon wafer. **2** After curing, the PDMS layer is plasma treated to improve the PDMS coating properties and coated with a 10 nm thick gold layer via vapour deposition. **3** and **4** Spin-coating of a 8 μm thick positive photoresist layer, soft baking at 110 °C and structuring by UV treatment through a chromium mask. **5** Reactive Ion Etching of the PDMS sample for anisotropic etching results. **6** and **7** Removal of photoresist, glueing of the PDMS frames to the PDMS membranes and curing at 65 °C for 24 h. Here, one PDMS square with about 300 4-FR sensor elements is illustrated. **8** Removal of the PDMS membranes from the silicon substrate by insertion of the samples in warm DMSO till the protective resin is dissolved.

Positive photoresist (AZ9260, AZ Electronic Materials[®], Branchburg, NJ) was spin-coated uniformly on the samples (level 1: t = 30 s, 1200 rpm, ramp of 120 rpm/s; level 2: t = 30 s, 2400 rpm, ramp of 240 s, level 3: t = 0 s, 2400 rpm, ramp of 800 rpm/s) layers of about 8 μm thickness were generated.[4] After soft-baking at $110\ ^\circ$C for 165 s, the small plates were transferred to the mask aligner (Suess MicroTec[®] MA 6/BA 6, Garching, Germany) and structured by UV treatment through a chromium photomask (Compugraphics[®] Jena, Germany) (see figure 3.19 **3**). To avoid sticking of the PDMS surface to the chromium mask, the illumination was run in non contact mode for 59 s with a gap between the samples and the chromium mask of 5 μm. The photoresist was then developed using AZ400k (1:4 dilution, AZ Electronic Materials[®], Branchburg, NJ) (see figure 3.19.**4**) and PDMS was processed with RIE (SENTECH PTSA-ICP Plasma Etch System SI 500 RIE[®], Berlin, Germany) using a gas mixture of 75,00 ccm SF_6 and 25,00 ccm of O_2 for 1200 s (see figure 3.19.**5**).

After that, the PDMS frames were glued via prepolymer PDMS to the different sensor boxes and cured for 24 h at $65\ ^\circ$C in a drying cabinet as presented in fig. 3.10. **IV.A** and **B** (see figure 3.19.**7**). Finally, the remaining photoresist and the protective resin were removed with heated DMSO (80 $^\circ$C)(see figure 3.19.**8**). By this, the PDMS sensor membranes were lifted off the silicon substrate and dried by N_2 gas before characterization.

3.5.3.2 Results and Discussion

The PDMS based structured membranes were fabricated in an eight step process as shown in figure 3.19. The intermediate products are presented and characterized in the following.

First, the cleaned silicon wafers were coated with a protective resin. Chen et al. used a silanization process to increase the sticking of the PDMS to the silicon wafer surface in order to generate an homogenous PDMS layer. Unfortunately, the detachment of the PDMS layer from the silicon surface is not possible for lower layer thickness without damaging the membrane, when using this surface treatment. Consequently, a different method was needed, which finally lead to the use of the low cost protective resin AZ 520D that is stable to a lot of different solvents, but can be removed by warm dimethyl sulfoxide (DMSO).[266][267] By this, the membrane does not need to be peeled and

mechanically deformed later on, but is detached without stress by a layer remover. A 15 μm thick PDMS layer was then spin coated. Here, the layer thickness can be controlled by the spin speed and the viscosity of the PDMS.[265] As was shown by Thangawng et al., adding defined amounts of hexane to PDMS allows for layer thicknesses down to 70 nm.[268] By this means, the elasticity of the PDMS structures can be manipulated for future applications. To increase the sticking property of the PDMS layer, the surface was plasma treated to generate a rougher surface and hence, a bigger contact surface.[269] [270] Afterwards, the sample was coated with a 10 nm thin gold layer.
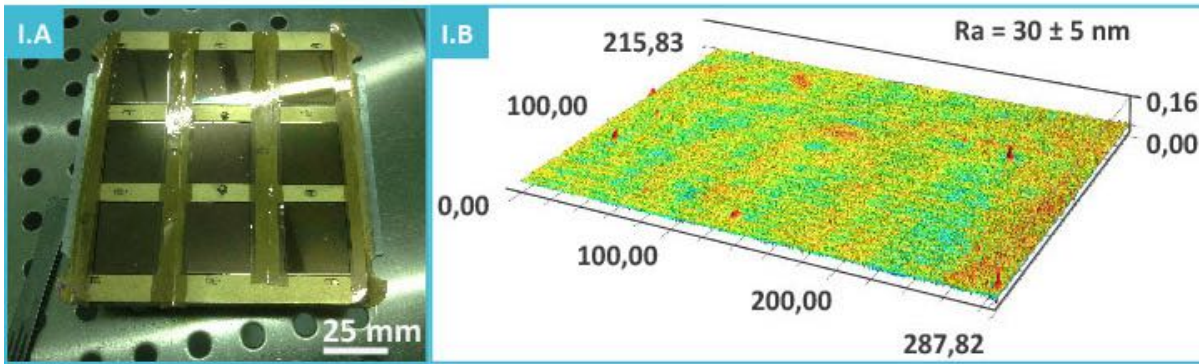
Figure 3.20: First and second fabrication step: **I.A** 3x3 silicon platelets fixed in a sample holder after vapour deposition of a 10 nm thick gold layer on top of the protective resist, a 15 μm thick PDMS layer. To improve the bonding between the gold layer and the PDMS surface, the PDMS was plasma treated before coating. **I.B** Isometric CLSM image of a PDMS surface after gold coating in 50x magnification. The average roughness of the surface was 30 nm.

This layer was used to increase the homogenous coating of the PDMS layer with positive photoresist, which was not possible by simple O_2 plasma treatment. Moreover, a permanently high-reflective surface is needed for the optical readout. For that reason, the metallic layer needed to be inert, available, cost-effective and processable within vapour deposition or sputtering. This made gold the most suitable material for these purposes. Vapour deposition has been chosen, as sputtering would have caused harm on the PDMS surface by pollutant particles or crack generation without extensive process parameter adaptations.[271] The exemplary surface topography of a gold coated PDMS sample is shown in figure 3.20 **I.B**. Here, the average layer roughness is 30 nm and by this, about ten times rougher than the surface of a silicon wafer. Then, positive photoresist was ho-
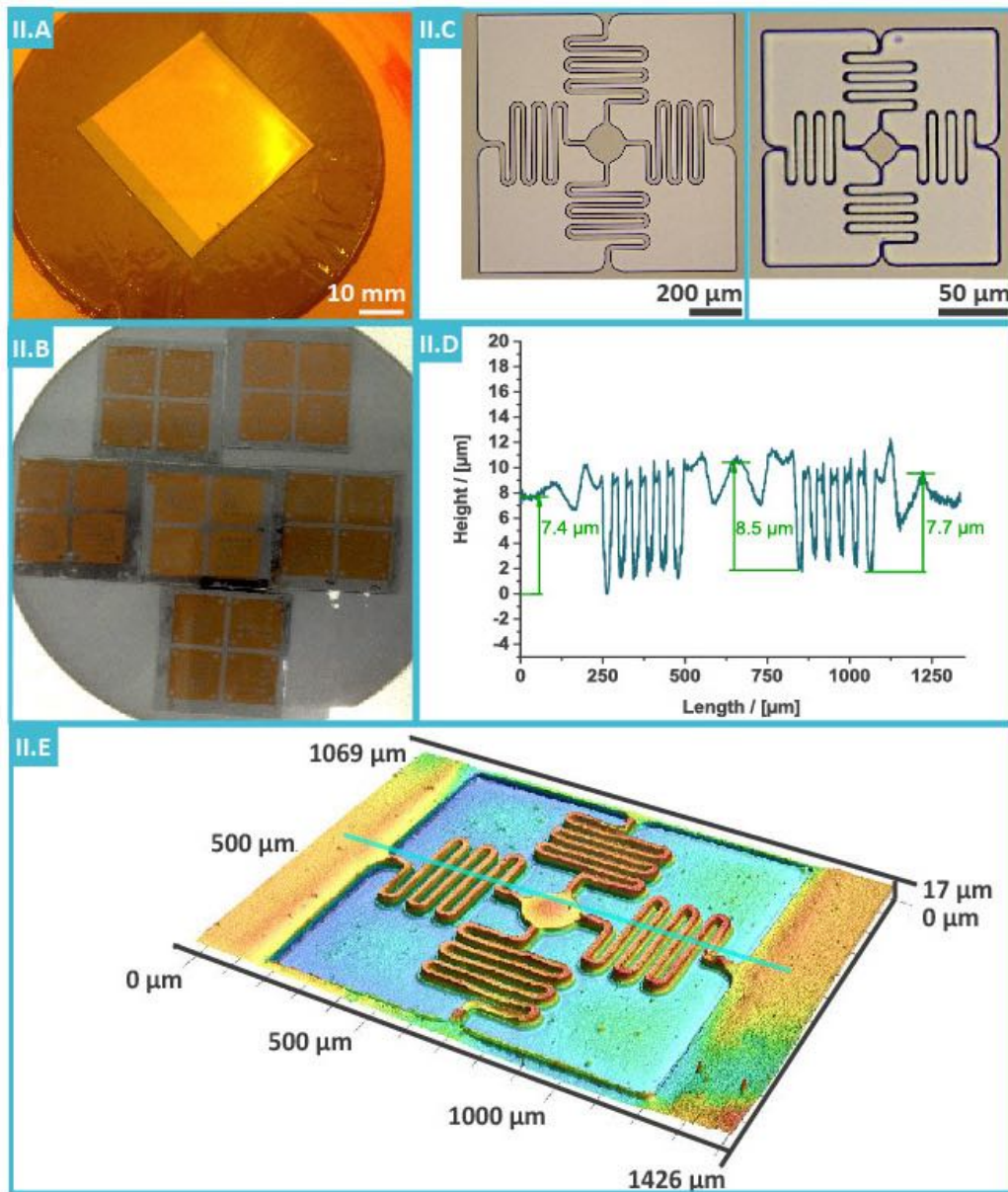
Figure 3.21: Third and fourth fabrication step: **II.A** Gold coated PDMS sample after spin coating of positive photoresist. Due to the additional gold layer, the generation of a homogenous photoresist layer with an average roughness of about 0.35 μm was ensured. **II.B** Six samples arranged for RIE processing after soft baking and patterning of the photoresist by UV treatment through a chromium mask. **II.C** Laser microscope images of the patterned photoresist: the sensor element structure on the left side has an edge length of 1.0 mm, while the edge length of the sensor on the right side is 170 μm. **II.D** Line profile along the blue vector indicated in the big sensor element shown in **II.E**. Here, the height of the photoresist is 7.4 to 7.7 μm within the area of the frame and 8.5 μm on the middle of the centre plate. The alternating structures between the frame and the centre plate correspond to the sensor arm spring coil and are well-developed.

mogenously spin coated on top of the gold layer as shown in figure 3.21 **II.A** and UV treated through a chromium mask. Four 10 x 10 mm squares of sensor elements were depicted in photoresist on each sample as presented in figure 3.21 **II.B**. The patterning results in the resist are shown in **II.C**. The maximum sized element of 1 mm edge length (figure **II.C**, left image) and a sensor element structure of 170 μm edge length (figure **II.C**, right image) are well developed. The second element was the smallest possible structure. Sensor element sizes below this edge length could not be prepared. This might be due to the non-contact mode during the UV treatment, wherefore there was a gap between the chromium mask and the PDMS surface. In consequence, contact of the PDMS surface and the mask would be needed during the UV treatment, which was not possible due to the sticky behavior of the PDMS surface and its high sensitivity to external impacts. As a result, the overall resolution was lower than 2 μm.[199] In **II.D** and **II.E**, the line profile along the indicated green arrow and the 3D surface topography of the 1 mm sized element are presented. The frame columns have a height of about 7.5 μm, while the centre plate is of 8.5 μm height. This variation in height of the photoresist indicates unevenesses within the PDMS, on the one hand, and fluctuations of the resist layer thickness, on the other hand. The alternating structures between the centre plate and the frame correspond to the sensor arm springs, which are well-defined. The spikes at the edges of the coils are well-known artifacts within CLSM and caused by additional interferences by sharp edges as also observed for the NiTi sensor elements.[249]

The gold coated PDMS was then structured via a combination of inductively coupled plasma (ICP) and reactive ion etching (RIE) according to Chen et al. and Green.[265][272] So, the gold layer is a stop layer with regard to RIE treatment with SF6.[199] Hence, the ICP process is needed to first etch the gold surface and afterwards, the PDMS layer can be etched via RIE.

Three different sensor elements of 1 mm size fabricated on two different samples were characterized after ICP-RIE by CLSM as presented in figure 3.22. During the RIE process, parts of the photoresist were entirely removed from the gold layer as can be noticed by the bright areas in image **III.A-III.C** showing the pure gold layer. The brownish parts belong to layer areas still coated with photoresist. All structures are well developed, but appear to have much rougher surfaces compared to the samples before ICP-RIE treatment. When looking at the corresponding isometric 3D topographies in **III.D** to **III.F**, the average roughness varies between 0.74 μm and 1.84 μm, which is due to the variation
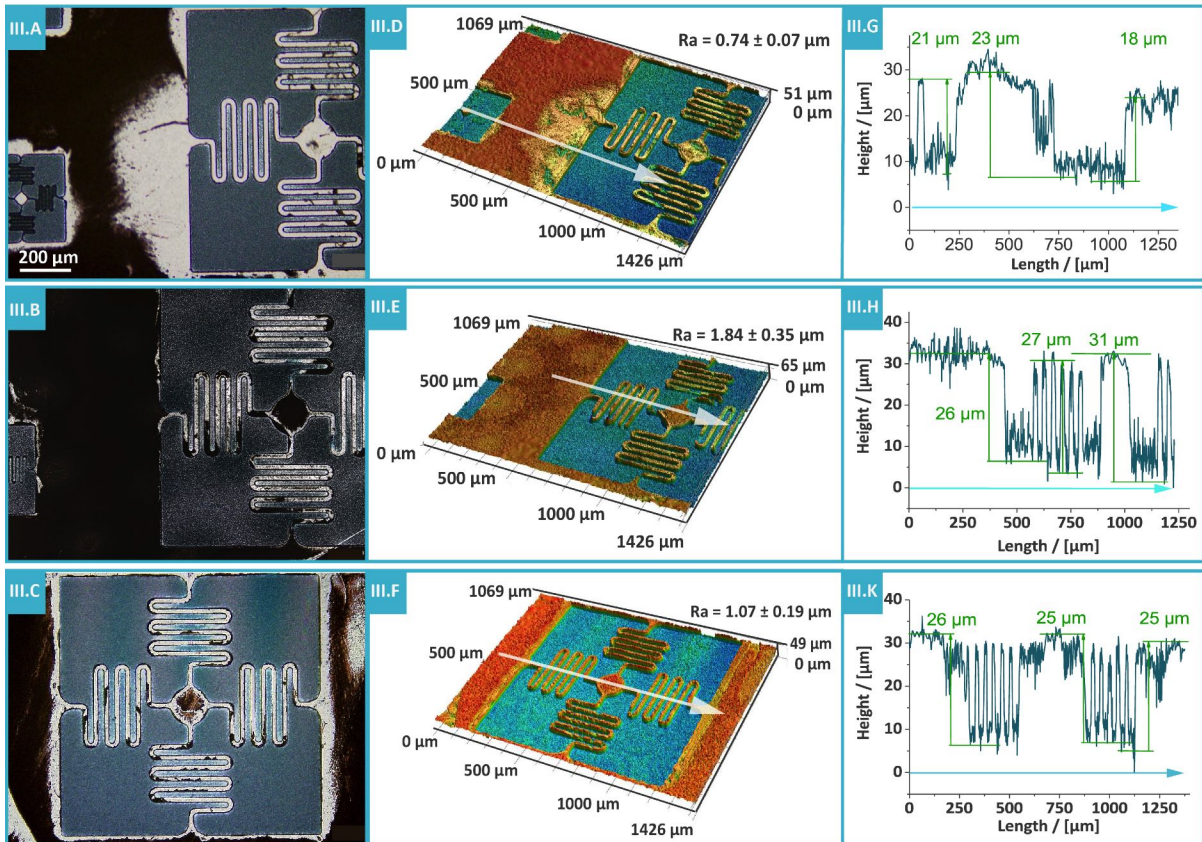
Figure 3.22: Fiffth fabrication step: **III.B** and **III.C** Laser microscopic images of the same sized 4-FR sensor element on two different samples. The brownish parts are areas of processed photoresist, the bright areas correspond to areas of varnish-free gold areas. The element structures are well developed. **III.D** to **III.E** Isometric 3D CLSM images of the surface topography of three 4-Fr sensor elements of two different samples. The structures are all well defined, the surface is rough ranging between 0.74 to 1.84 μm of average roughness. In **III.G** to **III.K**, the corresponding line profiles along the white arrows indicated within the surface topography images are presented. Here, strong fluctuations due to the increased surface roughness are observable. The frames and the centre plates have a height of 23 to 31 μm. In **III.G**, the photoresist is partly removed, for which reason the frame height changes from 23 to 18 μm. In **III.G**, the alternating structures of the spring slopes can still be well observed. Overall, the membrane was etched by about 15 μm.
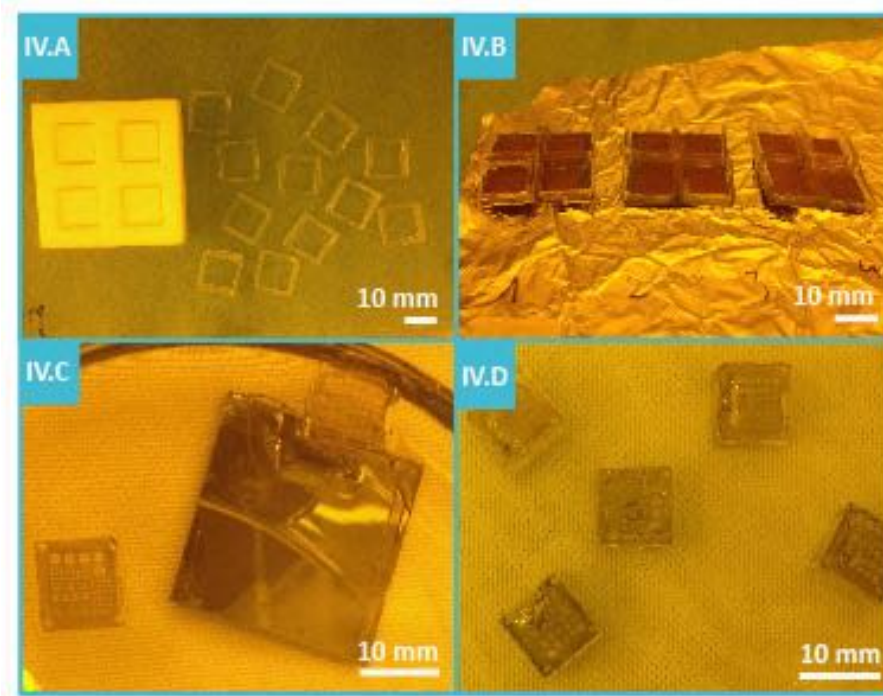
Figure 3.23: Sixth to eigth fabrication step: **IV.A** PDMS frame after moulding in a teflon mold (white box), heat treatment for 24 h at 65°C and unmoulding of the transparent 10x10x5 mm boxes.. **IV.B** PDMS frames glued to PDMS sensor membranes after RIE process before detachment from the Si substrate. **IV.C** Detachment of the final product (bottom left) from the Si wafer in warm DMSO. **IV.D** Sensor boxes: Structured and Au coated PDMS membranes lying on their PDMS frames.

in photoresist thickness as shown above. This roughness is also observable in the line profiles **III.G** to **III.K**, where there are fluctuations of up to 5 μm along areas of one level. Here, the broad columns represent the frame structures, that have a height of about 23 to 26 μm, just like the centre plate and the spring slopes. These roughnesses are due to the remaining photoresist and the necessary long ICP-RIE treatment of the PDMS surface. The significant increase of the polymeric surface roughness by plasma treatment has also been observed by others such as by Cvelbar et al. This group plasma treated a graphite/polymer composite and by this, generated an increase of the surface roughness of up to 15 times to four to five micrometers. [273]

In **III.H**, a smaller structure is included within the line profile at a length of 0 μm to 250 μm, which is shown at the bottom left side in image **III.B**. This structure has an edge length of 500 μm,
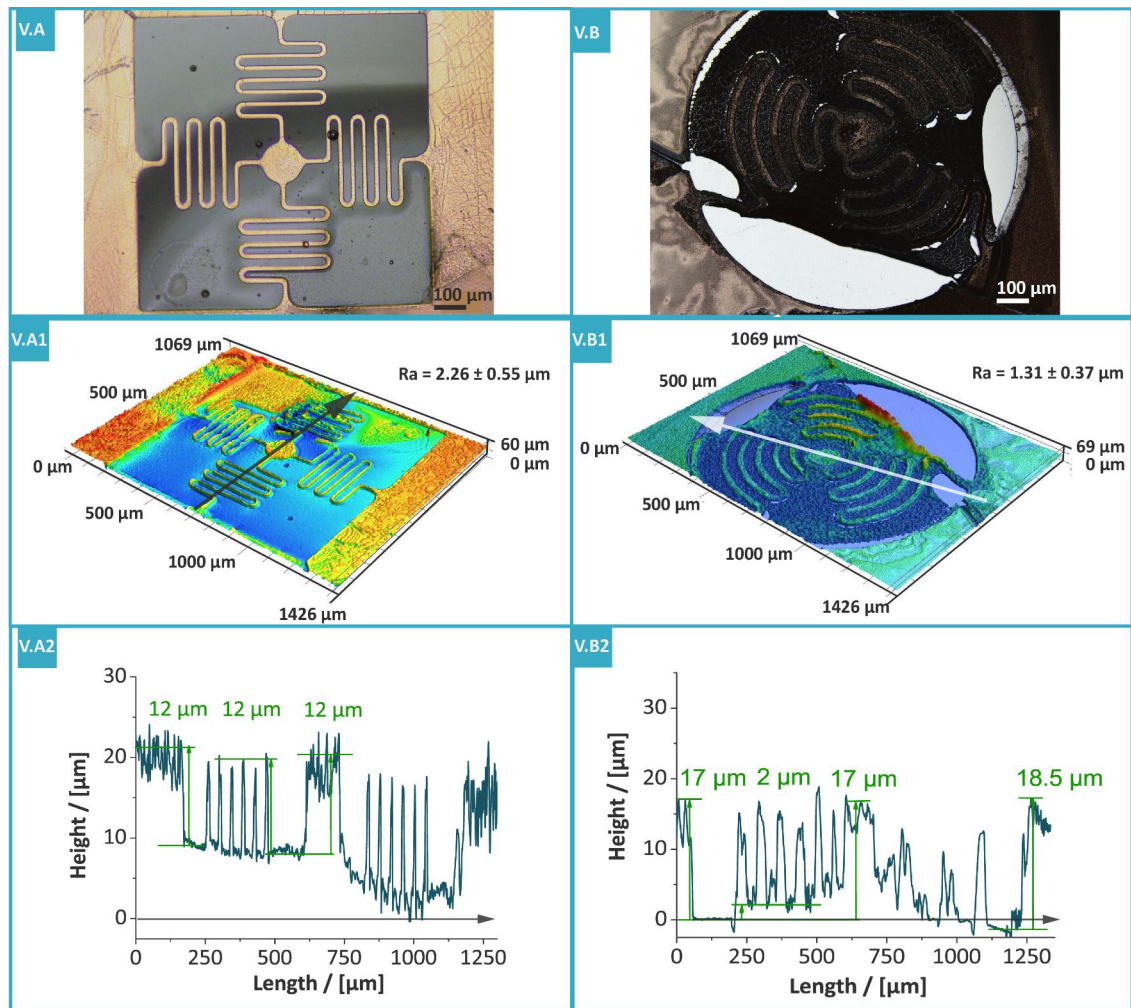
Figure 3.24: Final fabrication products: **V.A** 4-FR sensor element with an edge length of 1.0 mm. The structure is well defined; the dark arc within the structure indicates a deformation of the sensor membrane, which can also be observed within the 3D CLSM image as yellow area in **V.A1**. The roughness of the gold surface of the frame is about 2.3 μm. In **V.A2**, the line profile along the grey arrow is presented. The overall structure height of the final product is 12 μm. The overall material thickness is 20 μm. The curved profile btwenn a length of 750 to 1250 μm is due to the membrane deformation. **V.B**-**V.B2**: Control sample to validate the structured PDMS layer and the etched membrane thickness by means of a damaged sensor element. Here, the membrane is partly ruptured after the lift off process and unsensitive handling. In **V.B2**, the line profile of this sample is shown. The overall height of the frames and the centre plate of this sample are 15 μm. The spring slopes are well-developed, but vary in height between 9 μm to 15 μm.

and the sensor arm spring slopes are not fully developed. In consequence, the contact plate was processed with a final height of 21 μm, but there are no alternating structures observable between the frame and the centre plate. In consequence, the dimensions of this element were not resolvable.

To generate free-hanging membranes, that can be handled without damaging the thin PDMS structures, 10 x10 mm sized frames of PDMS were glued via PDMS to the sensor layer surface as presented in figure 3.23. First, the frames were fabricated by means of teflon molds (**IV.A**) and afterwards fixed to the undetached structured PDMS membranes (**IV.B**). The PDMS glue was cured for 24 h and the final product was then detached from the substrate by removing the protective layer in a bath of warm DMSO (**IV.C**). The cleansed sample was characterized by CLSM as shown in figure 3.24. Here, a 1 mm sized 4-FR sensor element is presented in figure **V.A** having a homogenous gold coating and a well-developed meander structure. The cracks within the frame are well-known within PDMS micromaching. On the one hand, PDMS is sensitive to plasma treatment and shows crack propagation during this process. On the other hand, PDMS and gold have different material expansion coefficients. This causes crack propagations during heat treatment within the curing processes and during solvent treatments. Due to these cracks, the average surface roughness is about 2.3 μm. In accordance to the line profile (**V.A2**), the structure height after anisotropic etching is about 12 μm. The parabolic course of the line profile between a length of 750 to 1250 μm is due to a deformation within the membrane.

To validate the overall thickness of the etched and un-etched PDMS layer, a scrap product was used (see **V.B**). Due to the relative measurements of the structure height via CLSM, the absolute membrane thickness can only be measured by the determination of the distance between the upper membrane surface lying in contact on the reference surface and a reference background, which is set to zero height. In this case, the background corresponds to the sample plate surface positioned on the CLSM. The membrane needs to be damaged to observe the plate surface like the one presented in **V.B**, where the white areas correspond to holes in the membrane through which the plate surface is observable.

The line profile along the white arrow indicated in image **V.B1** was determined (see **V.B2**). The frame columns on the right and the left side of the profile have an absolute height of about 15 μm. The fluctuating peaks between these two columns correspond to the sensor element arms and the

centre plate at a length of around 650 μm. The etched membrane thickness can be determined to about 3 μm. For future application, the PDMS sensor boxes (see figure 3.23 **IV.D**) can be varied in height by choice of appropriate frame molds. Furthermore, additional surface functionalizations of the PDMS on the top of the membranes can be run to control the cell adhesion sites as described above.

The backside is gold coated, which is used for further optical readout (see chapter 5). In figure 3.25, the reflectivity of this surface is shown. Here, the general reflectance was first tested by use of a red-light emitting laser pointer (**1**), which was directed to the backside of the PDMS sensor membrane (**2**). The intense red dot at the wall (**3**) corresponds to the reflected laser light and roughly outlines the adequate reflectance for the purpose of this project.
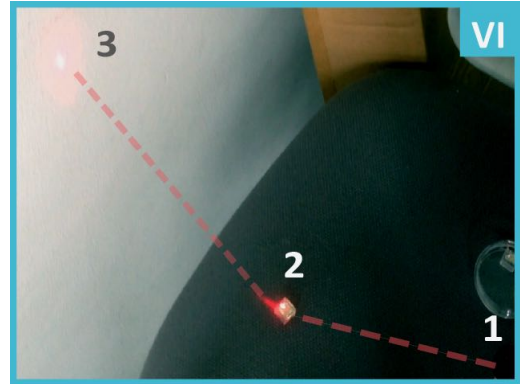

Figure 3.25: Reflectivity testing of the sensor surface: a laser pointer (**1**) was pointed at the surface of the gold coated PDMS membrane (**2**). The light is reflected from the sensor membrane surface to point (**3**).

3.5.4 Conclusion

Three different material fabrications were presented by which means biocompatible NiTi , a-Si and PDMS sensor element arrays were fabricated.

The established process based on wet chemistry surface micromachining of superelastic NiTi allowed for fabricating functional 4-FR sensor elements of 170 μm edge length in a 50 μm thick NiTi foil. The achieved lateral resolution was 2 μm. By dry etching surface micromachining of a-Si on a 400 μm glass substrate, the overall edge length could be reduced by over 70 % to 45 μm due to a minimum lateral resolution of 1 μm. The release of the elements was made sure by a sacrificial silicon dioxide layer.

Besides these solid-state based sensor structures, a first approach for the fabrication of soft material based elements was developed to reduce material and fabrication costs compared to NiTi and a-Si

processes. The procedure is based on dry etching bulk micromachining of 15 μm thick PDMS layers, whereby structures of 1 mm edge length could be fabricated in high quality. The structures are supported by a 3 μm thick PDMS membrane. Based on this first fabrication process attempt, future sensor structures can be reduced to gold coated circles on a thin PDMS membrane instead of the meander based sensor element structures, as the supporting sensor arm springs of the 4-FE design can be replaced by the thin film PDMS membranes. By this, the overall dimension of one PDMS sensor element can be optimized to a few micrometers in diameter of the gold circles.

Furthermore, the use of cross-linked PDMS opens the possibility of tuning the elasticity of the sensor elements by changing the material monomers and cross-linkers as already shown elsewhere.[257] [258]

4 SE Calibration

To improve the sensor performance, the structurally induced deviations from sensor to sensor resulting in individual response in sensor output need to be removed by means of calibration. Here, the structural errors are the difference between the expected and the real measured result such as force or voltage, which repeatedly appear for each measurement. To record reliable and quantitative data of high precision, it is therefore of central importance to find an appropriate calibration method for a distinct sensor application. [274]

In the following chapter, a short insight into established calibration techniques for mechanical force sensors as well as the theoretical background of atomic force microscopic (AFM) calibrations are presented. Moreover, the calibration of the above discussed, fully functional NiTi and a-Si sensor elements is described regarding their lateral (in-plane) and axial (out-of-plane) spring constants. Finally, the results of these calibration methods are presented in comparison to the expected FEA results.

4.1 Calibration Techniques

The calibration of the sensor elements is of crucial importance for the precision of the cell traction force data. The higher the lack of precision of this calibration method, the higher the error of the 3D force data.

In this project, a suitable parameter to determine the traction forces based on the sensor element deformation is the spring constant of the sensor element for each direction in space. Here, the actual spring constant for each element needs to be determined by a well-defined, non-destructive, reproducible and mechanical method that suits the geometrical dimensions and material proper-

ties. Different potential methods were taken into consideration such as vibrometer measurements, indentation and atomic force microscopy (AFM).

Nano-and pico-indentation are today well established techniques in material testing that are based on the early work of Friedrich Mohs in the 19th century. [275] He defined a scale, the Mohs scale, of ten materials with a certain hardness, which were used to validate the hardness of random materials based on their indentation and scratch behavior.

This method was optimized throughout the years and today, indentation is used to measure material properties down to Å resolution. [276] Here, a calibrated tip such as the well established Berkovich tip, a three-sided pyramidal diamond indenter with a tip diameter of down to an atom, approaches the surface of the sample. When the indenter is in contact, the force is increased linearly and the tip indents in the sample surface. After a user-defined dwell time, the indenter is entirely retracted. During this procedure, load-displacement curves are recorded parallel to the contact area of the indented tip. The curves are then basis to the determination of mechanical properties such as hardness, elastic modulus or plastic flow properties. [277]

Ying et al. used a commercial indenter to calibrate the out-of-plane spring constants of rectangular cantilevers. [278] Here, low loads were used, for which reason the diamond tip just deformed the cantilever, but did not indent into the AFM cantilever surface. In that way, the slope of the load-displacement curves corresponds to the spring constant of the cantilever. The uncertainty of the spring constant with this method was determined to less than 10 %.

For that reason, 4-FE NiTi sensor elements (see chapter 2, table 2.2) were tested via nano-and picoindentation by Hysitron/ Bruker in vacuum, in the course of this project. However, the spring constants were too low for nanoindentation suffering from a high noise-level within this method. In picoindentation, the elements were too compliant especially in-plane, so that forces could not exactly be resolved for one element, but was a combination of elements of one array. Hence, this method was not suitable for this project, too.

Another well established technique for the determination of the spring constants and resonance frequency are vibrometer measurements. [279] [280] Here, a laser beam is directed to the back of the cantilever, passing an interferometric system and the vibrational fourier transformed spectrum is measured. The spectrum is then analyzed regarding the resonance frequency and hence, the

stiffness of the cantilever. The accuracy and precision of this technique is limited by the size and shape of most cantilevers with an uncertainty that ranges in ± 5 %.[279] However, this method is just suitable for the calibration of out-of-plane spring constants, on the one hand. And on the other hand, the dimensions of the sensor element arrays fabricated within this project were not suitable to commercially available settings without further severe modifications that could have caused damage of the array plates.

A very powerful and well established analytical method working in small scales and with low loads is atomic force microscopy (AFM). In the course of this project, AFM has proven to be the only possible and currently available method to determine the axial and lateral spring constants of the fabricated sensor elements. For that reason, this method will be presented in more detail in the following.

4.2 AFM

Since its introduction by Binnig, Quate and Gerber in 1986, AFM has grown to a universal tool to image surfaces down to the atomic scale or measuring interacting forces down to sub nanonewton range for versatile analysis in physics, chemistry, biology or engineering.[281] [282] [283] [284] [285]

In general, it consists of three components: 1. a laser diode beam, 2. a cantilever, with or without a tip at the end, which is fixed on a glass block and movable via a piezoelectric stage and 3. a position sensitive quadrupole photodiode (PSPD). The laser beam is reflected from the back end of the cantilever to the PSPD. A voltage signal is detected depending on the deflection of the cantilever or rather the corresponding position of the reflected laser beam on the PSPD. At the beginning of each experiment, the beam is adjusted on an unbent cantilever with 0 V detected by the PSPD.

Two types of AFM Measurements are distinguished: 1. imaging and 2. spectroscopy. In imaging measurements of sample surfaces, the cantilever is deflected by means of unevennesses on the surface, while in spectroscopy, forces between the cantilever and the sample are recorded by force cruves. In both cases, the cantilever is deflected and the beam spot moves on the PSPD. Hence, the voltage signal changes depending on the cantilever deflection. When the spring constant and the sensitivity of the cantilever are known, the electrical signal can directly be correlated with a certain height

(imaging) that is to say a force (spectroscopy).

The accuracy of these measured results strongly depends on the precision of the calibration method of the cantilever spring constant. Various statical and dynamical techniques for the determination of the out-of-plane (k_z) and in-plane ($k_{x,y}$) spring constants were published within the last decades, well described and compared by Palacio et al in 2010. [286] In the course of this project, the lateral and axial calibration methods presented in the following sections were first used to calibrate the spring constants of rectangular reference cantilevers. In a second step, the sensor elements described in chapter 3 were calibrated by use of the calibrated reference cantilevers.

4.2.1 Axial Force Measurements

Regarding nominal spring constants, Senden et al. developed the method of an inverted loaded cantilever, in which a particle is glued to the cantilever end and the resulting deflection of the inverted cantilever is measured. [287] A major drawback is the possibility of braking the cantilever, on the one hand and on the other hand, the cantilever is modified by this procedure. The dynamical pendant of this method was published by Cleveland et al. in 1993. [288] Here, several particles are attached to the cantilever end and set into motion to determine its resonance frequency. In addition to the difficulties described by Senden et al., the method by Cleveland suffers from an uncertainty of the particle positions and sizes on the lever, which cause significant errors.

A rather exotic technique was developed by Butt et al., [289] in which a cantilever tip is pushed against a pendulum and the spring constant is then calculated based on the resulting displacements of the pendulum and the tip. However, there is a high risk of damaging the cantilever by this method and moreover, a suitable pendulum setup as well as its additional calibration is needed. For that reason, this technique has never grown importance.

A more well established and frequency based method was introduced by Sader in 1995 for rectangular cantilevers. [290] [291] In this dynamic calibration procedure, the cantilever is tuned measuring the resonance frequency and the quality factor in vacuum. Knowing the cantilever thickness, density and mass, the spring constant can than be determined. Although this technique is comparably simple, it has to be corrected for liquid environments by considering the Reynolds number as well as the hydrodynamic equation and it suffers from inaccuracies of the geometrical dimensions of the

cantilever.

Today, the most widespread method is the thermal noise method first published by Hutter and Bechhoefer.[292] It is based on the approximation of a cantilever as an ideal spring that follows the equipartition theorem. In consequence, the nominal spring constant is direct proportional to the temperature and the thermal fluctuations are measured to determine the axial spring constant. By means of additional correction factors, the non-harmonic behavior of the cantilever is taken into consideration. In general, this rather simple technique is very accurate for soft cantilevers with an uncertainty ranging between 5 to 10 %.[293] Hence, it was applied in the course of this project to calibrate the reference cantilever used for further calibration of the sensor elements.

Then, the axial spring constant calibration of the sensor elements was run by a classical static calibration method based on the work of Ruan et al.[294] Here, a calibrated reference cantilever is approached to the surface of the sample and afterwards, the probe or the cantilever is moved, so the deflection of the reference cantilever can be detected. A schematic setting for this calibration is
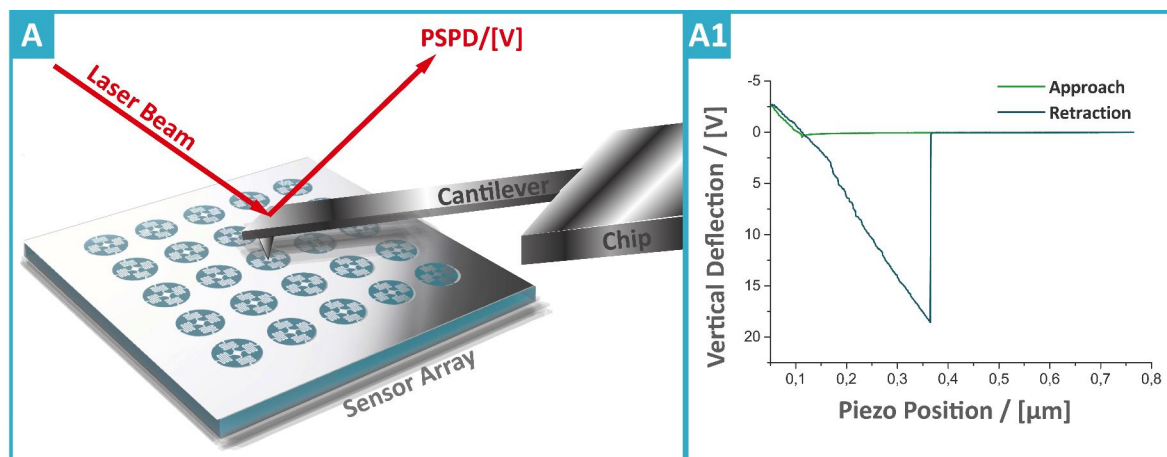
Figure 4.1: Schematic presentation of the axial calibration of the sensor element spring constant (**A**) by AFM measurements. The deflection of the cantilever is sensed by a photodiode laser beam. The displacement of the laser spot on a position-sensitive photodiode (**PSPD**) corresponds to a change in voltage, which is proportional to a force. The resulting AFM measurement is shown in **A1**. Here, the approach of the cantilever to the sample surface is described by the green curve. At 0.12 μm (piezo position), the cantilever jumps into contact with the sensor element surface and is afterwards slightly deflected with further approach of the cantilever towards the sensor element plate. When retracting the cantilever, the sensor-cantilever interaction causes an intense deflection of the cantilever. Consequently, the jump out of contact here is reached at a piezo position of 0.38 μm.

presented in figure 4.1 **A**. Here, a reference cantilever with a tip radius of 10 nm is approached to the centre plate of one 4-FR sensor element with a diameter of 5 μm (see figure 4.1, **A**) within a 5 × 5 sensor array and its deflection is recorded. The resulting raw data are shown in figure 4.1 **A1**. The approach of the cantilever is depicted as a green curve. At a piezo position of 0.12 μm, the cantilever jumps into contact with the sensor element surface. In general, this jump depends on the surface properties of the sample. In this case, the sensor element is free-standing and very soft, wherefore the interactions between the element surface and the cantilever right before the jump into contact can cause an out-of-plane deformation of the element towards the cantilever tip. Hence, the overall deflection of the cantilever in case of the jump into contact appears to be small. Afterwards, the vertical deflection of the reference cantilever increases just slightly. Then, the cantilever is retracted. Due to the high deformability of the sensor element based on its nanometer thickness and low Young's modulus, the interaction between the cantilever and sensor element seem to be stronger than the restoring moment of the sensor element. Hence, the contact between the lever and the element remains up to a piezo position of 375 nm before the cantilever jumps back to its original position.

The lateral spring constant k_z of each sensor element can than easily be determined via the slope of the curve. Here, the positioning of the tip on top of the element centre plate is of central importance regarding the uncertainty of the calibration which was estimated to about 8 to 9 % by Clifford et al.[295] Besides of the fact that the AFM based calibration method is the only available method, the major benefit of this method is its simplicity and simple implementation within the AFM. As a result, this technique is conform with the project aspiration of easy handling, low complexity and cost-efficiency.

4.2.2 Lateral Force Measurements

The determination of the lateral spring constant has grown importance with an increasing interest in molecular level surface frictional behavior for soft and hard material surfaces. Hence, a diversity of techniques were developed to calibrate the levers for advanced friction force measurements, summarized and compared in different review articles.[296] [286] [297]

Regarding dynamical methods for in-plane spring constant calibrations, Green et al. published

two approaches, which are based on the procedures by Sader, Senden and Cleveland et al. for axial spring constants. [298] The first attempt is based on particles that are glued to the cantilever and its resonance frequency is recorded. In the second one, the resonance frequency, quality factor and the dimensions of the cantilever are measured. Besides of the disadvantages already mentioned for the Senden and Cleveland method, the major drawback of these methods is that the lateral spring constant is indirectly determined via the torsional spring constants, wherefore the results suffer from uncertainties.

Static calibration methods are e.g. based on 1. Lorentz force measurements introduced by Jeon et al., [299] 2. the use of electrical nanobalance platforms by Cumpson et al., [300] 3. twist measurements of the cantilever when deflected perpendicular by a reference cantilever with a spherical tip used by Ecke et al., [301] 4. angular deflection measurements of the cantilever when attached to a lever with a sphere and fibre glass by Feiler et al., [302] 5. hysteresis measurements of compliance and tilts of a cantilever with a spherical tip by Stiernstedt et al. [303] and 6. scanning of a micropippette by Anderson et al. [304] or rather via an edge by Gao et al. [305]

Two of the more well established techniques are first, the axial sliding method developed by Ruan and Bhushan. [294] Here, the precise cantilever length and tip height are needed to calculate the spring constant based on the recorded height changes of the piezo during the sliding process of the cantilever over a rigid surface. The second very well-known and widespread technique was first introduced by Ogletree et al. using a wedge as a standard made of $SrTiO_3$ or Si. [306] So, the cantilever is scanned over the standard that possesses two well-defined slopes. By knowing one angle of the wedge and the normal force, the friction force and in-plane spring constant can than be determined. A variation of this method was offered by Varenberg et al. [307] and Wang et al. [308] [297] using a grating instead of a wedge. By this, the friction can be measured on a flat surface for tips with a large radius. However, this method lacks in accuracy due to the dependence on a well-shaped standard, an adequate computational method and pull-off forces during the scanning process that influence the friction force results. In consequence, inaccuracies as high as 10 to 20 % are most probable for optimized settings. [309]

In 2006, Li et al. published a direct calibration method at small length scales based on a diamagnetic levitation spring. [310] The accuracy of this method was reported to be as good as 0.1 % and was

proofed to offer significant advantages compared to the well established wedge technique. [286] [311] Consequently, this technique has been chosen for the calibration of the lateral spring constants of the sensor element.

A schematic illustration of the used diamagnetic lateral force calibrator (D-LFC) according to Li et al. is shown in figure 4.2 **A** in side- (top) and top-view (bottom). Here, a rigid mica platelet is glued to a pyrolytic graphite plate (PGP), which is a sheet of parallel graphite layers. The PGP of mass m is positioned on the top of four NdFeB magnets. In general, the PG is a representative of diamagnetic materials with a strong anisotropic susceptibility, for which reason the out-of-plane susceptibility is much higher than in-plane. This anisotropic behavior is the reason why the gravity force is balanced in the magnetic field of the NdFeB magnetic cubes and the PG floats several millimeters above the magnets. By this, a levitation spring (LS) system is created which has a very
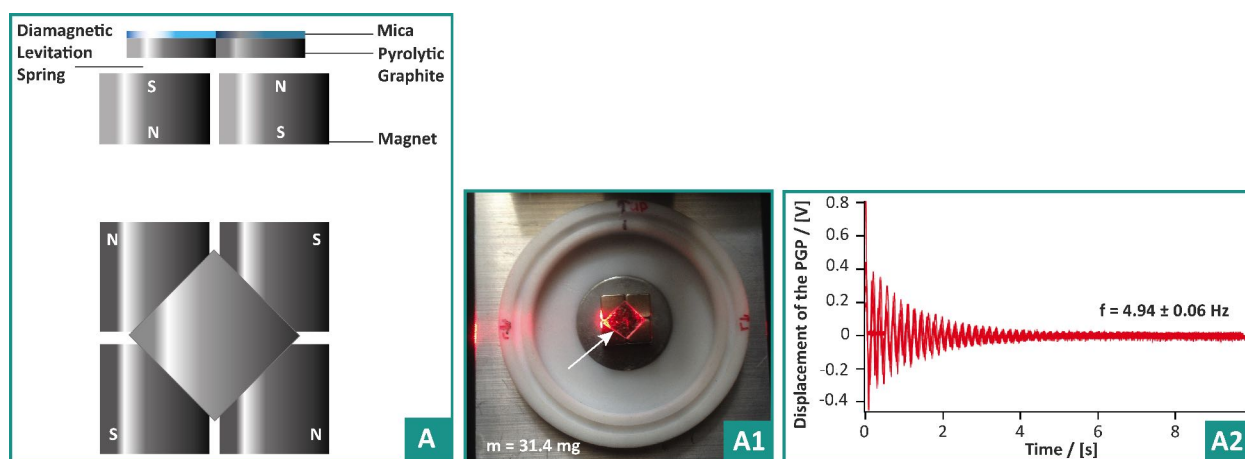
Figure 4.2: Schematic presentation of the D-LFC setting to calibrate the pyrolytic graphite plate (**A**) (modified from Q. Li et al, *Lateral force calibration of an atomic force microscope with a diamagnetic levitation spring system*, Review of Scientific Instruments **77**, 065105 (2006) with the permission of AIP Publishing). A pyrolytic graphite sheet is glued on a mica sheet and positioned on a four-pole magnetic field. The space between the graphite plate (PGP) and the magnets behaves as a diamagnetic leviation spring. **A1** Setting of **A** within the calibration setup for the levitation spring with a mass m of 31.4 mg. A laser diode beam is directed on one edge of the quadratic plate and reflected to a position-sensitive photodiode. **A2** Damped oscillation of the graphite plate moved in direction of the white arrow. Here the frequency of the graphite plate was determined to about 5 Hz.

small spring constant k_{LS}. To calibrate k_{LS}, the PGP is first weighed and then tuned in a laser-displacement-tracer (see figure 4.2 **A1**). Here, a laser diode beam is directed to one edge of the PGP (red light coming from left). Then, the platelet is displaced along the white arrow and set into oscillation. During this damped motion, the part of the laser beam blocked by the PGP changes, which is recorded by a position-sensitive photodiode (PSPD) via the change in intensity. The resulting time-displacement diagram is shown in figure 4.2 **A2**. Fourier transformation finally leads to the resonance frequency ν_{LS} of the spring, which is about 5Hz in this example. Based on the definition of the angular frequency $\omega_{LS} = \frac{\nu_{LS}}{2\pi}$, the spring constant k_{LS} can then be determined by $k_{LS} = \omega_{LS}^2 \cdot m$ (here, it is 19.4 nN/mm). Afterwards, the sensitivity of the cantilever for further characterization of the sensor elements is calibrated as presented schematically in figure 4.3 **B**. The cantilever tip is positioned in the centre of the PGP at a constant normal load and the AFM is run in scanning mode along the same scan line. The real setting is shown in figure 4.3 **B1** indicating the magnets, the levitating spring and the AFM head hosting the cantilever. As presented in figure
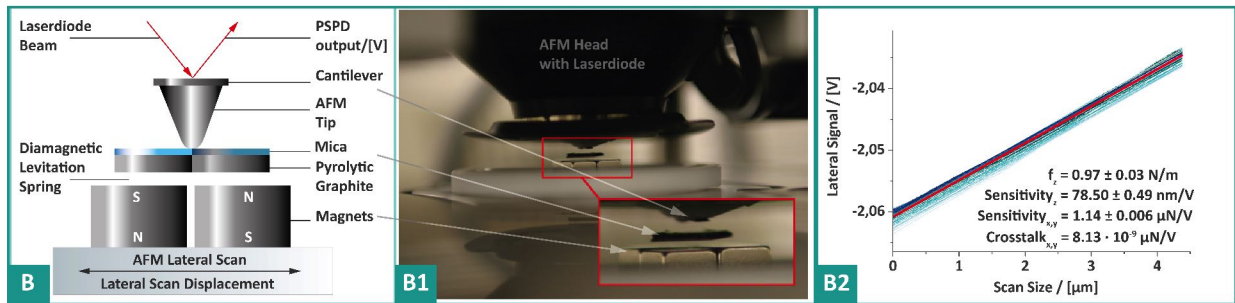
Figure 4.3: Lateral calibration procedure of the reference cantilever in sideview. **B** Schematic illustration of the setting according to Li et al. (see figure 4.2 **A**). A cantilever with an AFM tip is positioned on the centre of the calibrated PGP. A laser diode beam is directed on top of the cantilever and its movement is registered via a position-sensitive quadrupole photodiode (PSPD). The cantilever is moved in scan mode, so that the PGP is laterally displaced in x,y direction from its original position. **B1** Real setting in sideview including the AFM head with a laserdiode on top of the calibration setting. In the inset box, the magnets, the levitating PGP and the cantilever chip are shown (image modified from L. Wiegleb, *Kalibration eines Rasterkraftmikroskops für Reibungsmessnungen*, Bachelorarbeit, TU München, Zentralinstitut für Medizintechnik, July, the 11th, **2011** with kind permission of Prof. Hugel). **B2** Resulting scan curves over 20 scans in plane. Here, the out-of-plane resonance frequency f_z, the sensitivity out-of-plane (z) as well as in-plane (x,y) and the crosstalk in-plane for the reference cantilever are presented. Here, the lateral signal corresponds to the PSPD signal.

4.3 **B2**, the PSPD signal is recorded depending on the scan range, which corresponds to the lateral displacement of the cantilever. Here, 20 scans were run for a more precise result. This displacement is the sum of the displacement of the levitation spring and of the tip. The displacement of the tip is based on its twist, which is in the range of a few nanometer, while the spring displacement Δx_{LS} is in the order of several micrometer. Hence, the tip displacement is negligible. The lateral force can then be calculated by $f_{LF} = k_{LS} \cdot \Delta x_{LS}$.

During this procedure, the friction between the tip and the PGP surface needs to be ensured by the correct choice of the scan distance which corresponds to a linear ratio between the PSPD signal and the displacement. Sliding would cause a severe corruption of the calibration results.

The lateral sensitivity is finally determined by the spring constant and the inverse slope of the scan line:

$$sensitivity_{lateral} = k_{LS} \cdot slope^{-1} \tag{4.1}$$

The lateral crosstalk of this setting caused by a a deformation out-of-plane during the bending process is small compared to its sensitivities as shown in in figure 4.3 **B2** and hence can also be neglected.

Finally, the reference cantilever is used to determine the spring constants of the sensor elements by displacing the centre plate at a constant normal force based on the known sensitivity of the cantilever. The exact procedures are presented in the following.

4.3 Materials and Methods

4.3.1 Axial Spring Constant Calibration

Axial force constant measurements were carried out by means of AFM force spectroscopy (NanoWizard 3, JPK® Instruments AG, Berlin, Deutschland) using a gold-coated cantilever with tetrahedral tip (NT-MDT, CSG 11, k = 0.0143 N/m, sensitivity = 71.59 nm/V). To ensure maximum accuracy, the cantilever was calibrated four times based on the JPK software implemented thermal noise method and the average value of the spring constant and the sensitivity were used within the following force spectroscopic measurements.

Three 4-armed free-standing 4-FE NiTi sensors of the same size (see chapter 2: 170 μm edge length, 200 nm thickness, fabricated by AQUANDAS®, Kiel) as well as three of the smallest (4-FR-1B, 4-FR-2A, DSR-4A, 3-AR-5A) and the biggest (4-FR-1E, 4-FR-2E, DSR-4E, 3-AR-5E) sensors of each a-Si sensor design were analyzed after approaching the cantilever to the surface of each sensor centre. Here, a setpoint of 5 nN has been chosen, for better comparison between the different sensor designs and the FEA results, and 20 force curves were recorded for every sensor. Using the JPK postprocessing software, the force constants were determined by a software implemented sample-to-tip correction, fitting a linear fit to each retract curve and averaging the resulting force constants for each sensor design and material. The averaged results for each sensor element design and size are listed in table 4.1 and 4.2.

4.3.2 Lateral Spring Constant Calibration

The calibration of the reference cantilever by D-LFC and of the sensor elements was performed by me in the course of a cooperation with kind support by MSc Sofia Brander, MSc Joanna Urban and Dr. Doreen Schütze in he laboratories of the group of Prof.Dr. Hugel at the Institute for Physical Chemistry (University of Freiburg).

D-LFC was used to calibrate the lateral force constant of the reference cantilevers for further calibration of the sensor elements listed above. First, a square-shaped graphite platelet was weighed (m = 16.1 mg) and positioned on the centre of four cubic NdFeB magnets as shown in figure 4.2 **A**. The setting of the calibration of the diamagnetic levitation spring is shown in figure 4.4. The laser beam was adjusted to one edge of the platelet, so the shadow of the platelet was set to the middle of the photodiode. After starting the self-written D-LFC LabView program, the graphite sheet was set into oscillation manually and the damped oscillations were recorded directly by the software. By means of an FFT and Gaussian fit run in IGOR 6.36, the force constants and resonance frequencies of the graphite platelet were determined and averaged to: $k_{graphite} = 0.03 \pm 0.007\ N/m$ and $f_{graphite} = 4.94 \pm 0.057$ Hz.

The magnetic unit and the graphite platelet were transferred to the AFM (Asylum Research®, MFP, Great Britain). To calibrate the reference cantilever (μ-Mash, HQ:NSC36/AL BS, Bulgaria), the axial spring constant was first determined as described in the previous paragraph:

$k_{cantilever,axial} = 1.58 \pm 0.007$ N/m and sensitivity $_{cantilever,axial} = 78.50$ nm/V. Then, the cantilever was approached to the graphite surface as shown in figure 4.3 **B** and a scan in contact mode was performed for a series of 68 lines. Based on the scan results and the D-LFC software, the lateral sensitivity of the cantilever was determined to: sensitivity $_{cantilever,lateral} = 1.15 \pm 0.0056$ mN/V (crosstalk$_{cantilever} = 8.13 \cdot 10^{-12}$ N/V). In the following, the D-LFC calibration unit was exchanged by the sensor plates and the sensitivity was set in the calibration software. Here, the three representatives of the same sensor element types as for the axial spring constant determinations were analyzed. The cantilever was approached to the sensor centre plate and the lateral displacement of the sensors was initialized by scans in contact mode. The resulting voltage-to-displacement curves were then analyzed in Origin$^{®}$ to determine the average lateral spring constants for each sensor element type.
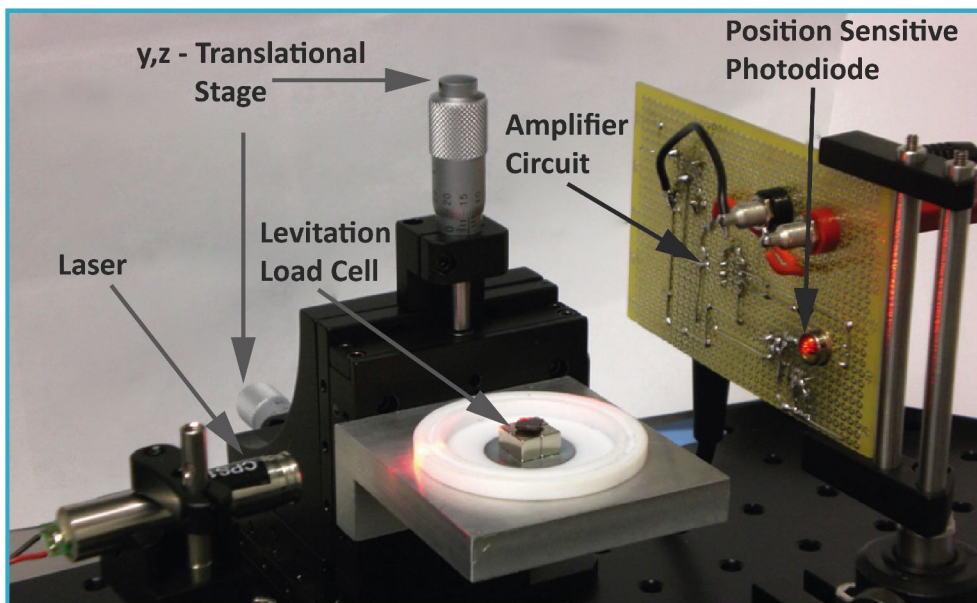
Figure 4.4: Picture of the real laser-displacement-tracer setting used for the calibration of the pyrolytic graphite plate (PGP) with all components as indicated. A red laser diode beam (600 nm) is directed on one edge of the levitation load cell, which blocks the beam until its set into oscillation. The alternating intensity of the beam is then recorded via the position sensitive photodiode (PSPD), converted into an electrical signal that was amplified by an amplifier circuit before being recorded by a LabView based computer software. The correct positioning of the D-LFC setting towards the laser beam is ensured by a y,z- translational stage (image modified from L. Wiegleb, *Kalibration eines Rasterkraftmikroskops für Reibungsmessnungen*, Bachelorarbeit, TU München, Zentralinstitut für Medizintechnik, July, the 11th, **2011** with kind permission of Prof. Hugel).

4.4 Results and Discussion

Three different sensor elements of each of the nine designs (see table 4.1) were calibrated out-of-plane by the axial cantilever to element and in-plane by the D-LFC method. Two exemplary, processed AFM results for axial spring constant calibrations of the two sensor element types 4-FE and 4-FR are presented in figure 4.5. In figure 4.5 **A**, the AFM cantilever deflection-distance curves of the membrane based 4-FE NiTi sensor element with an edge length of 170 μm are shown. As described above, the high elasticity of the element causes a small jump into contact at about 5 nm as seen in the approach curve and higher deflection values at small distances when retracting the cantilever due to deformations of the sensor element out-of-plane. After a travel path of the piezo of 450 nm, the cantilever loses contact to the element centre plate and jumps back to its original position. With regard to sensor element 4-FR with an edge length of 45 μm, the same observation like for element type 4-FE are made. In addition, there are vibrations in the curves, which could be caused by stresses within the material. Another, more suitable reason is the similarity of the spring constants between the reference cantilever and the sensor element. To determine the stiffness of the sensor elements, a slope was plotted to the linear region of the retraction curves (red line). By considering the spring constant of the reference cantilever with a spring constant of 0.0149 N/m, the spring constant of the sensor element could be determined to 0.012 N/m. In consequence, the reference cantilever experiences a higher counterforce than by sensor element type 4-FE, which has spring constant of 0.004$\pm$0.0004 N/m.

The slopes of the AFM curves for element type 4-FR are three times higher than for 4-FE. A difference in stiffness has already been observed within the FEA results with numerically determined axial spring constants of 0.098 N/M for element type 4-FR and 0.0065 N/m vor 4-FE. This is caused by the sensor element design.

Lateral spring constants were determined via the D-LFC method. Here, the calibrated cantilever is approached to the middle of the sensor element centre plate and then run in scan mode to displace the the sensor element from its origin in a defined scan range. The procedure is exemplarily shown in figure 4.6 for a 4-FE NiTi sensor element. The cantilever is moved along the blue arrow by 700 nm (figure 4.5 **A**). This movement can directly be observed via the deformation of the upper spring
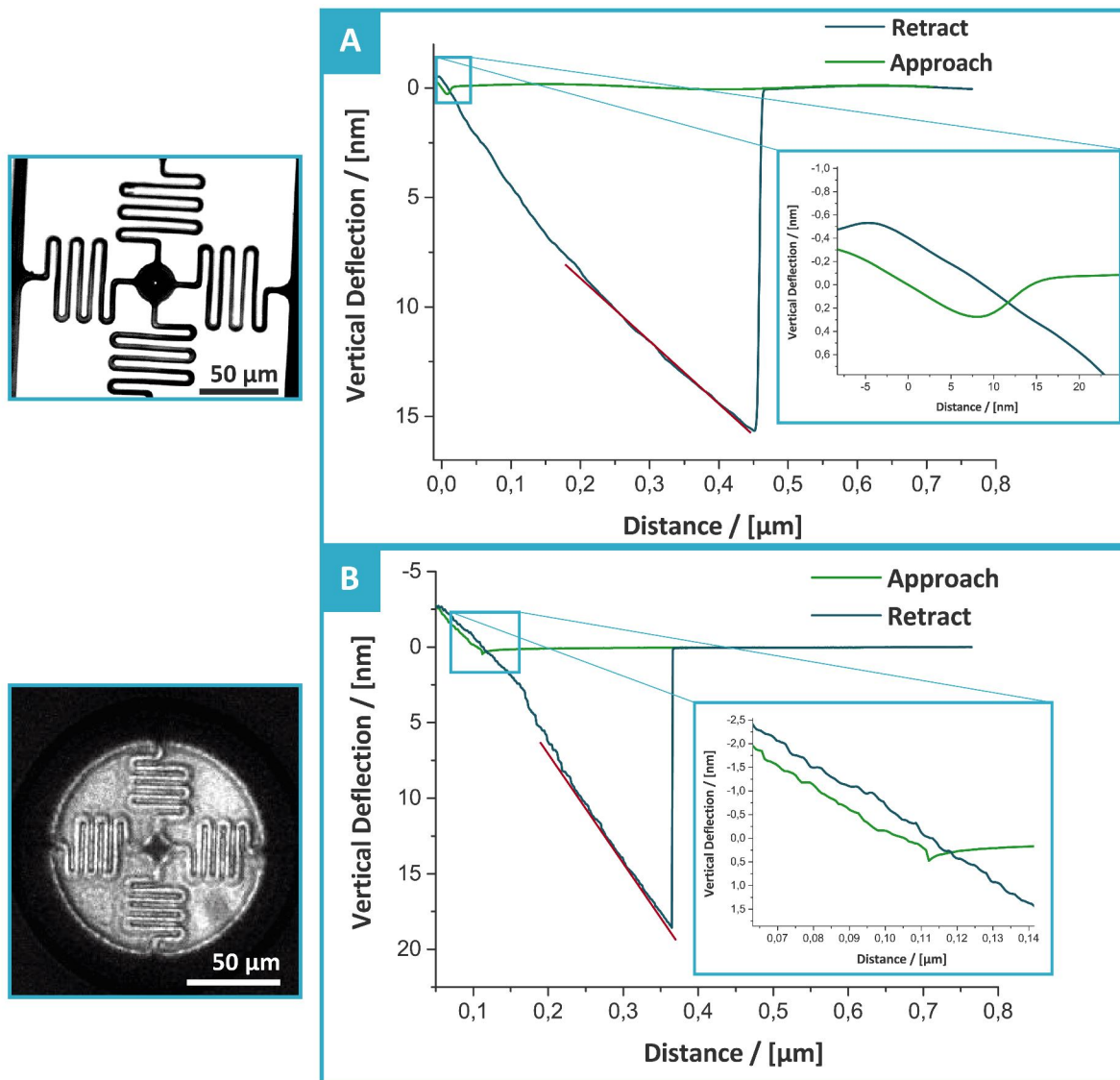
Figure 4.5: Exemplary processed AFM curves to calibrate the spring constant of: **A** Membrane based NiTi 4-FE sensor element with an edge length of 170 μm and **B** an a-Si 4-FR sensor structure with an edge length of 45 μm. Both curves show a small jump into contact (see inset boxes) due to the deformability of the elements out-of-plane. The slope of the retract curve (blue line) for 4-FE is three times higher than for 4-FR, which is directly proportional to its spring constant. Note the difference of the scales for **A** and **B**.

arm as marked by the opening tilt between the two orange lines lengthening the two spring slopes. The result of 20 scans is presented in figure 4.6 **A2**. The scans are entirely reproducible, wherefore

the slopes of the different scans are nearly the same. The slope is directly proportional to the spring constant considering the spring constant of the cantilever. Here, $k_{x,y}$ is 0.087$\pm$0.0008 N/m, which corresponds to an uncertainty of 0.9 % based on the fitting analysis of the scan results. Due to the imprecision in the determination of the spring constant of the levitation spring of 0.007 N/m, of the sensitivity of the reference cantilever of $5.6 \cdot 10^{-6}$ N/V and of the fitting deviation for the determination of the sensor element spring constant, the overall Gaussian distribution width Δk_x is $1.04 \cdot 10^{-6}$ N/m, which is 0.001 %. However, this method is based on the assumption that the scan range or rather the cantilever displacement in-plane is several orders higher than the tilt of the cantilever during the scan process according to Li et al.

Within these experiments, the scan range had to be reduced to displacements below 1 μm to ensure the friction between the cantilever and the sensor element surface, while avoiding sliding. Hence, all data were analyzed regarding the influence of a cantilever tilt that was determined by scanning the cantilever on a rigid surface.
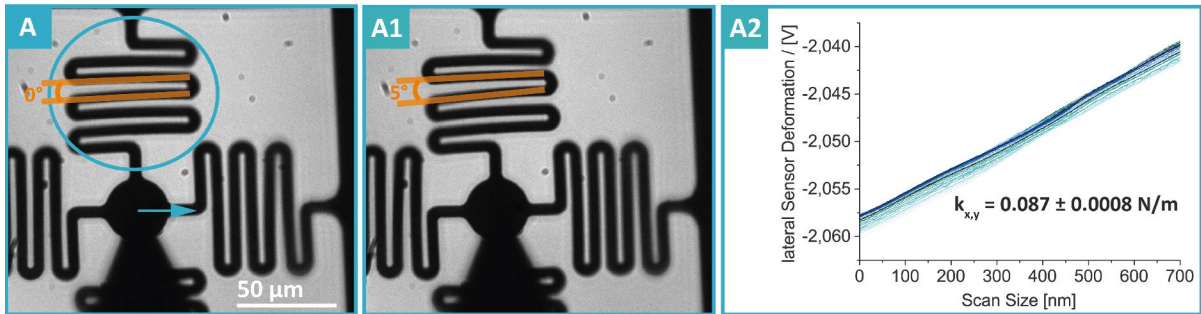
Figure 4.6: Determination of the lateral spring constant of a 4-SE sensor element by lateral displacement of the centre plate via a rectangular cantilever with a tip. The displacement was 700 nm along the blue arrow as indicated in image **A**. The displacement of the sensor element can be observed via the upper spring as marked by the blue circle. Here, the opening angle (see two orange lines) was increased from a parallel positioning to about 5 degree (see **A1**). In **A2**, the result over 20 scans is presented. Via the slope of the scan lines, the lateral spring constant could be calculated to 0.087 N/m. The standard deviation of 0.0008 N/m just reflects the error caused by the fitting analysis over 20 scans.

To find the maximum possible tilt, a high force and small scan range between 10 and 50 nm was chosen in the software, so the cantilever was tilted and not moved. The tilt was then extracted via

the slope of the scan results and the corresponding voltage range. In this experiment, the slope is 3.43 mV/nm and the voltage range is 17,5 mV. Hence, the tilt was 5.10 nm. Based on the results, all displacement signals were corrected by the corresponding tilt and a final average deviation of the spring constant of about 1 % caused by the tilt has been determined. So in general, an overall inaccuracy of 1.001 % has to be considered for all results in this calibration method before the determination of the final spring constant of the sensor elements by the fitting procedure.

In the following table 4.1, the results for nine sensor elements regarding the experimentally determined lateral and axial spring constants k_x and k_z as well as the corresponding FEA results are summarized. Each of the experimental results corresponds to the average over three different sensor elements of the same type with twenty scans on each element. The deviation just includes the standard deviation due to the fitting procedure to calculate the spring constant.

In first part of table 4.1, the smallest and biggest fully producible a-Si based 4-FE sensor elements are summarized (see figure 3.14 as well). The lateral spring constant of the 4-FR-1B element is in the order of the theoretically simulated results with 1.95 N/m. While for 4-FR-1E, k_x is 28.9 N/m and by this, varies by a factor of about 5 compared to the FEA results. As already described in chapter 3, this sensor element design suffered from a lack of space between the spring arm slopes, wherefore residues of the sacrificial Si layer remained between the slopes and hence, the movability of the sensor in-plane appears to be rather arbitrary. The axial spring constant was again in good agreement with the theoretically expected value of 0.048 (experimental) to 0.017 N/m (FEA). On the opposite, the experimentally determined value of k_x of the smallest favoured design 4-FR-2A is in very good agreement with the simulated data of about 4.7 to 4.9 N/m, while the experimentally determined value of k_z proves to be in the same magnitude like the corresponding FEA results. For the bigger design version 4-FR-2E, the in-plane spring constant was found to be slightly higher than for 4-FR-2A as supposed by the FEA data. The experimentally determined axial spring constant is the same like for the smaller 4-FR design 2A, although it should be about ten times lower according to the simulation results. Hence, these elements seem to be modified in their mechanical behavior by residues of the sacrificial layer just like the 4-FR-1E sensor elements.

In the second part of table 4.1, three more sensor element types and their corresponding lateral and axial stiffness are presented. The design types DSR and 3-AR are representatives of two and

Table 4.1: Experimental and linear static FEA spring constant results in N/m for two different sensor element types of the smallest and the biggest fabricated element size. Regarding the experimental data, the standard deviation just includes the error caused by the fitting procedure over 20 scans. The lateral spring constant is given only in x-direction as the element is fully symmetric. To determine the lateral spring constants, the direction and the target point for displacements are shown exemplarily for sensor element 4-FR-1B. They are the same for all following sensor designs.
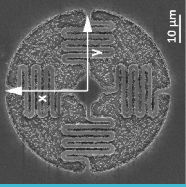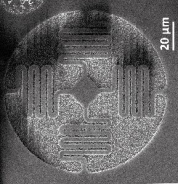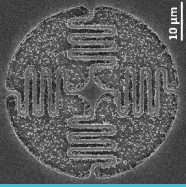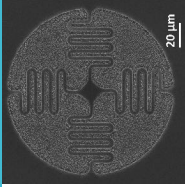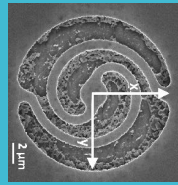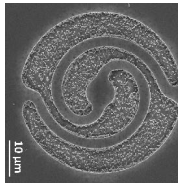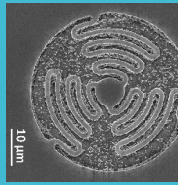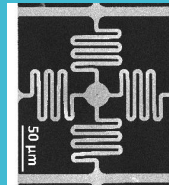
Material	Sensor Type	SEM	Experimental Results/[N/m]		FEA Results/[N/m]			Sensor Size /[μm]
			k_x	k_z	k_x	k_y	k_z	
a-Si	4-FR-1B		1.95±0.035	not measurable	6.30	6.30	0.068	56.8
a-Si	4-FR-1E		28.9±0.001	0.048±0.013	6.14	6.14	0.017	114
a-Si	4-FR-2A		4.66±0.022	0.012±0.001	4.93	4.89	0.098	45
a-Si	4-FR-2E		5.07±0.001	0.013±0.001	4.77	4.77	0.011	136

Table 4.1, Part 2: To determine the lateral spring constants, the direction and the target point for displacements are shown exemplarily for sensor element DSR-4A. They are the same for all following sensor designs.

Material	Sensor Type	SEM	Experimental Results/[N/m]		FEA Results/[N/m]			Sensor Size /[μm]
			k_x	k_z	k_x	k_y	k_z	
a-Si	DSR-4A		0.73	0.016±0.003	0.88	1.46	0.13	15
a-Si	DSR-4E		6.64	0.021±0.008	8.78	14.35	0.009	45.5
a-Si	3-AR-5A		0.26±0.002	0.027±0.004	3.52	3.73	0.104	29.6
a-Si	3-AR-5E		0.13±0.017	0.026±0.008	0.35	3.7	0.012	89.9
NiTi	4-FE		0.087±0.008	0.004±0.0004	0.054	0.054	0.0065	168

three armed sensor element types that were chosen to analyze the strength or weaknesses of the mechanical calibration methods for sensor types that possess a lower symmetry than the four armed designs, which are fully symmetrical. Regarding the smaller element type DSR-4A with a diameter of 15 μm the in-plane spring constant is in good agreement with the FEA data, but the axial stiffness is ten times lower than expected with 0.016 N/m instead of 0.13 N/m. The same result can be found for the three times bigger design DSR-4E, whose in-plane spring constant is about ten times higher than for DSR-4A with 6.64 N/m and differs from the theoretical result by a factor of 1.3. However, the out-of-plane stiffness is about double the amount that was expected via FEA with 0.021 N/m instead of 0.009 N/m. These deviations between FEA simulation and experiment are even more obvious for the three armed design 3-AR. For 3-AR-5A with a diameter of about 30 μm, k_x is 0.26 N/m instead of the FEA based result of 3.52 N/m. This might be most possibly due to a slight difference in the displacement direction caused by the setting. Especially for the small designs, it was a challenging task to accurately position the sensor element along the x, y-axis as indicated in table 4.1 for design 4-FR-1B. Consequently, the lower symmetric design is strongly prone for small variations of in-plane deformation directions. The out-of-plane spring constant is five times smaller than expected. For 3-AR-5E, the theoretical and experimental lateral spring constant match, while the axial spring constant is twice as high as the value predicted by FEA. As the out-of-plane spring constants are in the same range, it appears to be highly probable that here again, residues of the sacrificial layer are left that strongly influence the mechanical element behavior in this direction.

Finally, the above mentioned NiTi design 4-FE was calibrated. In this case, all spring constants are in very good agreement with the theoretically predicted data. So, the lateral spring constant was determined to 0.087 N/m instead of the expected value of 0.054 N/m, while of out-of-plane the lowest spring constant was sensed with 0.004 N/m compared to a theoretical constant of 0.0065 N/m.

Overall, these results point out that the theoretical assumption of a linear elastic behavior of the elements in this displacement range is suitable. In consequence, the FEA results proved to be reliable. Furthermore, the in-plane calibration via a reference cantilever is suitable for fully symmetric designs, but would need to be optimized for less symmetric designs like shown for the three armed 3-AR element type. Regarding the axial spring constant determination, the choice of a suitable reference cantilever is fundamental to the reliability of the spring constant determination. This method holds

some inaccuracies by the exact positioning of the reference cantilever or a high difference in spring constants between the cantilever and the sensor element. Here, especially the remaining grinds of the sacrificial layer caused the biggest influence in an accurate determination of k_z. Nevertheless, the AFM based calibration technique is the simplest on the calibration market and currently the only possible method for the calibration of the sensor elements. For future applications, the sensor elements should be implemented in a surrounding which is compatible to commercial vibrometer settings to calculate the spring constants via non-contact methods such as thermal noise.

Within this thesis, the D-LFC based calibration method was for the first time successfully used to calibrate MEMS like structures. The results are most promising with a captivating precision of about 1 % for the determination of the reference cantilever spring constant. Regarding a future application of the sensor system conceptualized within this project, the overall effort for this three step lateral calibration of the sensor elements is however high and also depends on the accuracy of additional calibration settings like the laser-displacement-tracer setting.

In the future, another simple method for the determination of the spring constants that was not available in the course of this thesis might be useful. This method was first published by Dziekonski et al. in 2017. Since 2018, it is a patented, commercially available, precise and direct method based on MEMS micro-force sensors used for the determination of in-plane spring constants, which has an inaccuracy of about 2 %.[312][313] By this, the overall calibration time and effort could be reduced significantly for future high-throughput measurements.

5 Optical Readout

The concept of the cell force sensing method based on the sensor elements fabricated, characterized and calibrated as described in chapters 2 to 4 uses the three dimensional displacement detection of the element centre plate to sense the cell traction forces. In this project part of the microsensor system prototyping, an optical readout approach has been conceptualized and realized for optical non-contact displacement sensing in three dimensions. The displacement is measured via changes in light properties, recorded as electrical signals, digitally processed to then directly be correlated to the effecting cell force via the determined spring constant of the sensor element. Here, a minimum traction force resolution out-of-plane of down to 0.8 nN and in-plane of 17 nN were succesfully determined within the applied settings.

To determine the most suitable methods that are both 1. sensitive to forces in the nanonewton range i.e. nanometer displacements, 2. cost-efficient, 3. cell compatible, 4. easy in handling and 5. usable to measure forces in three dimensions, different techniques were taken into consideration. Their fulfillment of the above listed requirements are analyzed and the most important methods are summarized within this chapter.

The theoretical background regarding the chosen methods is furthermore presented, followed by the materials and settings that were used and the final data for optical displacement detections in x-, y- and z-direction are analyzed and discussed.

5.1 Optical Methods for Displacement Sensing

Ever since the application of LiDAR (light detection and ranging) during the Apollo 13 mission in the 1970s, the accuracy [314] and power of non-contact optical sensing methods has been shown and established in a wide field of different everyday applications such as in 1. agriculture for plant growth and structure development analysis, [315] 2. geophysics for the determination of topographies and geo-spatial information [316], 3. urban traffic for parking assistance [317] and velocity control of vehicles as well as 4. the alternative energy industry for the control of wind turbines [318] or 5. the fast growing market of autonomous cars for obstacle detection. [319]

Besides of the rather long distance laser time-of-flight measurement technique in LiDAR ranging between 0.2 to several hundreds of meters, [316] there is a number of additional methods that are applied for shorter distances and precise displacement measurements, which are presented in several reviews and are selectively and shortly introduced within this chapter. [320] [316] [321] [322] [323]

In general, optical displacement sensors are systems that sense the distance change between a fixed sensor part and a moving object or between a fixed and a movable part of the same sensor via a change in transmission, diffraction, scattering, reflection or absorption of a light beam. [321] By this, further information like displacements can be determined. In the majority of optical displacement sensors, a displaced sensor part is compared to a reference position detecting the variation of reflection or transmission. Established techniques for distance and displacement sensing are: intensity-based sensors, triangulation, time-of-flight sensors, confocal methods and interferometry. [322] The most important techniques are summarized in table 5.1. regarding their resolution, accuracy, handling and price region.

Intensity-based sensors were one of the first types of contact-free distance measurement methods and are rather simple and cheap. [322] Here, a point light source illuminates the object and the light intensity of the reflected light is then detected as a function of the distance between the object and the detector. The light source and the detector are mostly fibre-optic based cost-efficient components. [324] In some settings, the transmission is measured instead of the reflection intensity. Today, very high resolutions of down to 0.01 μm for shiny objects can be measured, but intensity changes caused by outer impacts are also detected as displacements, wherefore this method is very

inaccurate.[325] [321]

Table 5.1: Overview on established non-contact optical displacement measurement methods, their corresponding sensitivities, resolution, a rating of the setting, the dimensions that can be recorded simultaneously and the price region based on the cited literature. The techniques listed beyond the double line are relevant for this work.

Method	Resolution	Accuracy	Dimension	Handling	Price	Literature
Confocal Laser Scanning Microscopy (CLSM)	lower nm region	high	3D	simple, software needed, time-intense	high	[220] [219] [215] [237] [238] [239]
Triangulation	several μm	high	1D, 2D, 3D	fast, simple	low cost	[326] [327] [328]
Intensity-Based	$> 0.001\ \mu$m	very inaccurate	1D	simple	cheap	[329] [330] [325]
Time-of-Flight	0.1 x <400 m	high	2D, 3D	simple (commercial)	high	[320] [331] [332]
Displacement Measuring Interferometry	pm to 1 m	high	1D, 2D, 3D	complex	high	[333] [334]
DHM	experimental: nm range (commercial: > 150 pm)	experimental: > 5 nm (commercial: > 300 pm)	3D	simple, intense computational processing	low	[335] [336] [337]
IC	nm range (sub-pixel)	nm	2D, 3D	very simple, easy implementation in various settings	low	[338] [339] [340] [341]

Triangulation is a technique first used by the Greek mathematician Thales in 600 BC to calculate the height of pyramides and the distance to ships on the ocean.[342] In this method, a laser spot is directed on the sample surface and the scattered light is then focused on a position sensitive detector (PSD). The known angle of incidence of the incoming beam, the angle of reflection or rather the collection angle on the PSD and a baseline, which is the distance between the incoming

beam and the focus of the scattered light, define a triangle. Finally, the coordinate of a certain point on the sample surface can be calculated. The displacement of this point is correlated to a change in the collecting angle equivalently detected via a shift on the PSD, wherefore this method is also suitable for dynamic 3D measurements.[316][321][322] Commercial settings allow for distance measurements between 100 mm to 1 m.[343] The resolution is depending on the laser beam size, the pixel size of the PSD as well as the distance to the sample and can be as high as a few micrometer. The handling is simple although sensitive to the setting parameters and the commercial settings are low-cost.[327][322]

Time-of-flight (tof) sensors are based on the emission of electromagnetic waves like light or acoustic waves to an object and measuring the entire travel time of the wave during this procedure. The distance is then determined by the one-way time-of-flight and the speed of light or rather the speed of sound.[320] Current tof sensors use pulsed laser sources. To measure distances below 50 m, the temporal pulse shape is measured to determine the pulse shift of the incoming and returned laser pulses. This principle is e.g. used within radar and LiDAR sensors and allow for dynamic distance measurements between 0.1 m and several hundreds of meters.[316][344]

Confocal sensing was already describes in detail in section 3.3 (chapter 3). In general, the confocal setups offer high resolution in the nanometer range in all three spatial directions. Commercial setups are easy to use and offer powerful image processing software tools to increase the precision of the recorded data. Due to the scanning procedure that is used to reconstruct three dimensional sample information via z stacking, and due to their processing time of at least a minute at a given resolution for confocal white light microscopy and laser scanning microscopy, this 3D method is suitable especially for static measurements. However, the sensitivity of the microsensor elements developed in the course of this project and their displacement range in the nanometer region during cell traction force sensing and their displacements need to be recorded dynamically, wherefore the above described methods are not suitable.

In contrast, **laser interferometry** is the most powerful static and dynamic principle to determine displacements in the sub-micron region. In literature, a variety of different techniques are known to measure distances and displacements interferometrically.[345]

The most well-known prototype of displacement measuring interferometers is the Michelson inter-

ferometer. Here, a coherent light beam partly passes through a beam splitter, while the other part is reflected by 90°.[346][347]

Both beams encounter on the reflective surfaces of two mirrors and are reflected back to the beam splitter, where the beams are superimposed in time and space. By installing one of the two mirrors on a translational stage, one beam path length can be varied against the other. By this, the phases of the two electromagnetic waves are delayed against each other: If they are in phase, the amplitudes of the waves sum and constructive interference can be observed. If they are out of phase, then destructive interference cause the extinguishing of the two waves. These constructive and destructive interferences can be observed as fringes with high intensity (in phase) or as dark spots (out of phase). By measuring the intensity changes, even very small optical and geometrical path differences of the waves can be determined. The path difference in z-direction then corresponds to half of the wavelength λ multiplied with the amount of occuring interference fringes N:

$$\Delta z = \frac{\lambda}{2} \cdot N \tag{5.1}$$

The resolution of the Michelson interferometer therefore is directly proportional to half of the wavelength of the laser. Today, subnanometer accuracies can be obtained using digital data processing and acusto-optical light modulators.[348] However, these interferometers are cost-intensive and sensitive towards outer impacts like temperature changes which influence the behavior of the optical components, vibrations as well as pressure dependence of the medium.[346][347]

In the course of the years, a diversity of other interferometric techniques that shall be just named here has been developed such as multiple wavelength and scanning interferometry,[349][350] optical coherence tomography,[351][352] speckle interferometry[353] or self-mixing interferometry.[354]

However, these interferometric settings are both very complex, highly interference-prone, too cost-intensive, suffer from a lack of resolution and sensitivity to sub-micron displacements or do not open the possibility for three dimensional displacement measurements.

A comparably simple setting based on the Michelson interferometric approach that offers the possibility of sub-second fast, highly precise measurements of 3D geometries and displacements at low costs was found to be digital holography that will be presented in the following.

5.2 Digital Holography

In 1948, Dennis Gabor developed a method to record the entire field information consisting of amplitude and phase or electron microscopy at once, for which he received the Nobel Prize in 1971.[355] This new principle of microscopy in terms of light today is known as holography, in which the object beam wavefront first interferes with the reference beam wavefront creating an interference pattern based on Fresnel diffraction, which is recorded on a photosensitive film.[356] The setting here is comparable to the Michelson interferometer. In a second step, the so-called hologram is read by illuminating it with the initial reference wavefront and by this, a three dimensional image of the object is reconstructed.[357]

A major drawback of this technique was the time-consuming processing of the holograms recorded analogously on photographic films or holography plates, wherefore holography stayed an inconvenient method for most applications for several years. With the development of the first laser as a highly coherent light source in the 1950s[358] and the production of chips and photosensitive sensors like the charge coupled device (CCD) in the late 1960s,[359] holography experienced a scientific boost.

In 1967, Goodman et al. exchanged the photographic film by a CCD camera and used digital filters to extract the complex information of amplitude and phase digitally for reconstruction of the image instead of using a reference beam.[360] In 1994, Schnars et al. were able for the first time to directly record digital holograms via a CCD sensor.[361] From now on, it was possible to directly compare two or more wavefronts that were recorded at different times and meant the starting point for today's digital holography - a fast, scanning-free 3D microscopic imaging method suitable for non-fluorescent, label-free samples. With the upcoming mass production of high-resolution CCD and Complementary Metal Oxide Semiconductor (CMOS) sensors, a diversity of different digital reconstruction methods were developed.[362] [363] [364] [365] [366] Nowadays, hologram reconstruction can be run in real time due to constantly improved, powerful image processing algorithms in Graphics Processing Units (GPU).[367] [368] [369] Hence, digital holography has developed to a distinct, independent category in modern optics[370] and became an important tool in a variety of scientific and industrial fields such as in biomedical and live cell imaging[371] [372] [373] [374] [375] [376] [357] [377], fluid mechanics[378] [379] [380] [381], information security in optical data transmission[382], mechanical vibration anal-

ysis[383][384][385], shape of MEMS[386][387][388][389][337] or displacement measurements.[390][391][392] Due to its compact design, stability even in case of long working distances and high resolution, Pedrini et al. recently implemented digital holography for long-term erosion measurements within the International Thermonuclear Experimental Reactor (ITER) in southern France.[393]
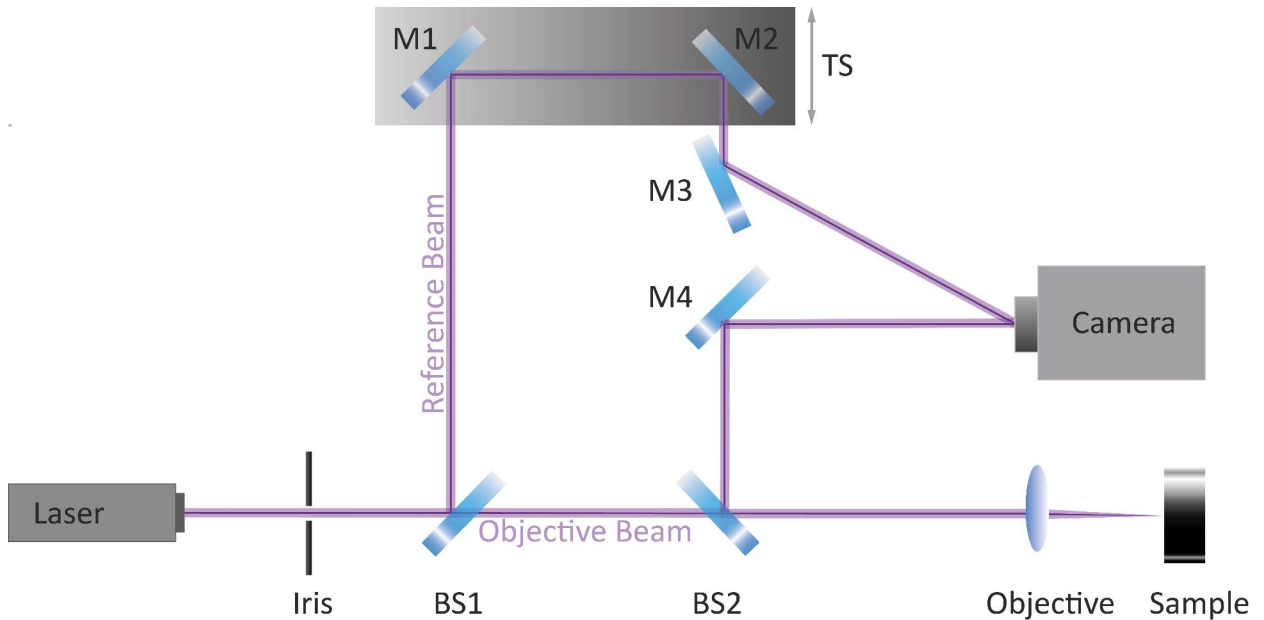

Figure 5.1: Schematic beam path in an off-axis digital holography microscope (DHM). The setting was used for recording out-of–plane as well as in-plane displacements by blocking the reference beam. The laser light first passes through an iris to eliminate scattered light and further shape the laser beam. The beam is then splitted into an objective and a reference beam via a beam splitter (BS1). The objective beam is then focused on the sample surface via the objective lens. The reflected light passes through the objective lens once again, is then redirected via a second beam splitter (BS2) and a mirror (M4) to a camera. The reference beam is set to a spatial and temporal overlap with the objective beam via mirrors M1 and M2 positioned on a translational stage. The reference beam is then launched with an angle to the objective beam directed on the camera via mirror M3.

Here, the working distance between the inner reactor surface and the DHM objective is more than 13 m and the researchers were able to ensure a depth accuracy of $\pm$ 10 μm. Hence, the DHM has the potential for high stability at variable working distances with high accuracies, which is of significance for future applications of the setting conceptualized in the course of this work. In general,

the lateral resolution of DHM is comparable to this of light microscopy, but the axial resolution in experimental settings was reported to be down to 5 nm. [336] [394] Current commercially available, but expensive settings with very powerful algorithms in the reconstruction process allow for resolutions in the subnanometer range with an accuracy of about 150 pm. [335]

A schematic illustration of a digital holography microscopic setup is presented in figure 5.1. A coherent laser beam is divided via a beam splitter (BS1) into an objective and a reference beam. The objective beam is focused via an objective lens with a well chosen numerical aperture (NA) on the reflective sample surface. The reflected light is focused by the lens and redirected via a semitransparent mirror (BS2) and the mirror M4 to the CCD camera. The reference beam is overlapped in time and space via a mirror M3 with the objective beam on the camera chip surface. To ensure temporal overlap, the reference wavefront can be delayed via a translational stage (TS). Due to the entrance angle between the reference and the objective beam, this setting is a so-called off-axis digital holography microscope (DHM), which was first proposed by Leith and Upatnieks in 1962. [395] It overcomes the general problems of in-line holography settings of an overlap between the real image, a twin, virtual image, which corresponds to the reconstruction of an object field behind the detector film, and the zero order diffraction distribution. By spatial modulations like adding so-called carrier frequencies, these two images and the zero order diffraction can be separated in space. [396] As the mathematical analysis of the holograms via algorithms is fundamental for digital holography, the most important equations are introduced in the following, which are basis for writing suitable algorithms. These equations are not discussed in all detail and not wished to be understood by the reader in detail, but used to outline the complexity of the processes solved in the background throughout all digital holography measurements.

The recorded hologram is digitally reconstructed as presented exemplarily for a NiTi 4-FE sensor element in figure 5.2. First, the object is focused (figure 5.2.1). Then, the object and the reference beam are overlapped in space and time till optimized to maximum contrast within the interference pattern as shown within the inset box in figure 5.2.2. The intensity of the interference pattern $I(x, y)$ can then be described as: [397]

$$I(x, y) = |R(x, y)|^2 + |O(x, y)|^2 + O^*(x, y) \cdot R(x, y) + O(x, y) \cdot R^*(x, y) \qquad (5.2)$$

Here, $O(x,y)$ and $R(x,y)$ describe the optical fields of the object beam (O) and the reference beam (R). The terms $|R(x,y)|^2$ and $|O(x,y)|^2$ are autocorrelations and correspond to the zero order distribution with the highest spatial frequencies of the object. The holographic interferogram, which consists of N x N real pixels, is transferred to the spatial-frequency domain using a fast Fourier transform.
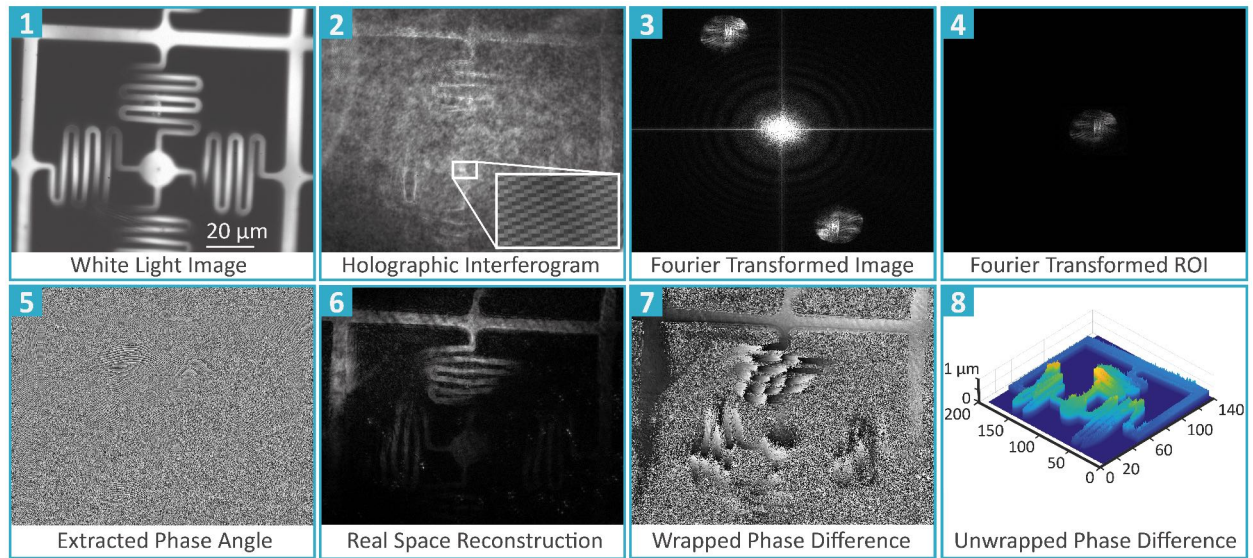

Figure 5.2: Image recording and processing procedure in digital holography. **1** Laser light image of a 4-FE NiTi sensor element **2** Holographic interferogram of the 4-FE sensor element with optimized contrast of the interfering objective and reference beam. **3** Fourier transformed image extracted via digital processing containing the real and virtual image of the sensor element as well as the zero order diffraction in the centre of the image. Each part of the image contains all information of the objective like phase or intensity. **4** Choice of region of interest (ROI) for further processing. **5** Phase angles for the chosen ROI image. **6** Reconstruction of the real space of the phase angle image. **7** Phase difference image calculated by the difference between an original image and a second image after slight displacement of the sensor element in z-direction. **8** 3D reconstructed image of the displaced sensor element after phase correcting the phase difference image via an unwrapping algorithm. To reduce computational time, the bottom spring has been excluded from analysis as it does not influence the overall displacement result.

By this, the hologram is set to the complex space with a N x N complex matrix. $O^*(x,y) \cdot R(x,y)$ then contains all information about the real image, while $O(x,y) \cdot R^*(x,y)$ describes the virtual image. The functions marked with an asterisk are complex conjugate values of the object and

reference optical fields. These two terms are half the amount of the zero order distribution, which disturbs a proper reconstruction and therefore needs to be excluded in further processing. In figure 5.2.3, the spatial separation of the real image (upper right spot), the zero order diffraction (bright spot in the centre of the image) and the virtual image are observable. For further analysis and optimization of the reconstruction process, the real image is then cropped via a spatial filter choosing the region of interest (ROI).

The hologram is directly proportional to the intensity of the interference pattern, with $h(x,y) = \alpha \cdot I(x,y)$. For its reconstruction, its amplitude h(x,y) has to be multiplied with the complex amplitude of the reference wavefront:

$$h(x,y) \cdot R(x,y) = R(x,y) \cdot \alpha \cdot |R(x,y)|^2 + R(x,y) \cdot \alpha \cdot |O(x,y)|^2$$
$$+\alpha \cdot O^*(x,y) \cdot R^2(x,y) + \alpha \cdot O(x,y) \cdot |R(x,y)|^2$$

(5.3)

The first term is the attenuated reference wave front, the second a cloud surrounding the wavefront, which both together describe the zeroth order diffraction The third term corresponds to the conjugate image of the original wavefront defined as the real image. The last term describes the virtual image. The reconstruction then corresponds to a propagation of $h(x,y) \cdot R(x,y)$ from the holographic to the image plane.[386] The reconstructed wavefront in the image plane $E(\xi,\eta)$ with distance r to the holographic plane is then determined by the Sommerfeld-Rayleigh diffraction equation:[361]

$$E(\xi,\eta) = \frac{exp(\frac{j2\pi r}{\lambda})}{j\lambda r} exp(\frac{j\pi(\xi^2 + \eta^2)}{\lambda r}) \times \iint h(x,y) \cdot R(x,y) \cdot exp(\frac{j\pi(x^2 + y^2)}{\lambda r})$$
$$\times exp(-\frac{2j\pi(x\xi + y\eta)}{\lambda r})dxdy$$

(5.4)

x,y are spatial coordinates in the hologram, j is the fringe number, ξ and η are the corresponding coordinates in the reconstruction plane. Here, the Fresnel approximation is used, in which λ is expected to be several magnitudes smaller than the physical dimensions, with: $z^3 >> \frac{1}{8\kappa}[(x-\xi)^2 + (y-\eta)^2]^2$. The distance is therefore defined as:

$$r = \sqrt{z^2 + (x-\xi)^2 + (y-\eta)^2}$$
$$= z[1 + \frac{1}{2}(\frac{x-\xi}{z})^2 + \frac{1}{2}(\frac{y-\eta}{z})^2]$$

(5.5)

By substitution of $\mu = \eta/(d\lambda)$ and $\nu = \xi/(d\lambda)$ and use of the spatial Fourier transform FT definition, equation 5.4 finally is:[386]

$$E(\xi, \eta) = \frac{exp(\frac{j2\pi r}{\lambda})}{j\lambda r} exp(j\pi\lambda r(\nu^2 + \mu^2)) \times FT\{h(x,y) \cdot R(x,y) \cdot exp(\frac{j\pi(x^2 + y^2)}{\lambda r})\} \quad (5.6)$$

In digital holography, the hologram is recorded on a CCD chip, consisting of an N x M matrix of pixels, which have pitches of Δx and Δy. These pitches are recording intervals on the image plane and define the resolution of the reconstructed hologram. With $x = n \cdot \Delta x$ and $y = m \cdot \Delta y$, the sensed intensity then is defined as::[386]

$$I(n \cdot \Delta x, m \cdot \Delta y) = I(x,y)rect(\frac{x}{N\Delta x}, \frac{y}{M\Delta y}) \times \sum_{n=1}^{N}\sum_{m=1}^{M} \delta(x - n \cdot \Delta x, y - m \cdot \Delta y) \quad (5.7)$$

with: $rect(x,y)$ - function that is a constant amplitude value, if the point defined by x,y is inside the hologram and zero on all other points of the image, $N\Delta x \times M\Delta y$ - area of the recorded hologram, n, m - integers, $\delta(x,y)$ - two dimensional Dirac delta function. The intensity based record of the hologram and the digital multiplication of intensity of the hologram and the reference wavefront finally leads to a diffraction field in the image plane by which the intensity and the phase distribution of the reconstructed real image can be determined. Here, the spatial Fourier transformation algorithm is replaced by a discrete Fourier transformation via a fast Fourier algorithm:[386]

$$\begin{aligned}
E(m,n) &= \frac{exp(\frac{j2\pi r}{\lambda})}{j\lambda r} \exp(\frac{j\pi\lambda r}{N \cdot M}(\frac{n^2}{\Delta x^2} + \frac{m^2}{\Delta y^2})) \\
&\times \sum_{k=0}^{N-1}\sum_{l=0}^{M-1} h(k \cdot \Delta x, l \cdot \Delta y) \cdot R(\Delta x, l \cdot \Delta y) \\
&\times \exp(\frac{j\pi(k^2 \cdot \Delta x^2 + l^2 \cdot \Delta y^2}{\lambda r} \exp(-2j\pi(\frac{kn}{N} + \frac{lm}{M})) \\
&= \frac{\exp(\frac{j2\pi r}{\lambda})}{j\pi r} \exp(\frac{j\pi\lambda r}{N \cdot M}(\frac{n^2}{\Delta x^2} + \frac{m^2}{\Delta y^2})) \\
&\times DF\{h(k,l) \cdot R(k,l) \cdot \exp(\frac{j\pi}{\lambda r}(k^2 \cdot \Delta x^2 + l^2 \cdot y^2)\}
\end{aligned} \quad (5.8)$$

with: k, l - discrete sample indexes within the frequency and time domain.

The fast Fourier algorithm is basis to current digital holography algorithms. This algorithm then creates a digital real image consisting of an N x M matrix that contains n, m elements and step sizes in ξ, ν direction that are defined as:[386]

$\Delta\xi = \frac{d\lambda}{N \cdot \Delta x}$ and $\Delta\nu = \frac{d\lambda}{M \cdot \Delta y}$.

The extracted phase as well as the corresponding reconstruction of the real image considering the reference beam are presented in figure 5.2.5 and 5.2.6. For deformation analysis, a reference hologram of the sensor element was recorded without any displacement. Then the element is displaced out-of plane and a second hologram is recorded. Both interference patterns are then digitally reconstructed independently. The extracted phases of the two waves are then subtracted, which results in the so-called phase-difference which is shown in figure 5.2.7. The displacement d of a single point of the sensor element can be determined via:[398]

$$dS = \lambda N = \frac{\lambda \Delta\delta}{2\pi} \tag{5.9}$$

with: S - sensitivity vector, which depends on the geometry of the setup, N - order of interference, $\Delta\delta$ - phase difference, which is caused by the difference in beam path length due to the deformation.

To extract the displacement information for the entire reconstructed real image (see figure 5.2.8) via the phase difference, so-called phase unwrapping algorithms are used within digital holography. In general, a central problem in digital data processing and interferometric setups is the restriction of the acquisition systems like Fourier transformations to measurements of 2π-modulo. These modulo are called phase principle values or wrapped phases, which restrict the phase to a range of $\pm\pi$ radiants, and cause a misinterpretation of the physical properties like the quantitative displacement information. Due to its high relevance for precise data analysis via accurate reconstruction, a broad spectrum of various unwrapping algorithms have been developed, which are e.g. presented in the book of Ghiglia et al.[399] and there is further development still in progress.[400][401][402][403][404] In the course of this project, a modified, meanwhile established and competitive open-source algorithm for digital holography called PUMA (phase unwrapping-max-flow/min-cut) developed by Goncalo Valadao and José Bioucas-Dias has been applied.[405] To optimize the PU process, a mask is first designed to block unwanted interference patterns outside the region of interest. Then, PUMA

was applied. This exact algorithmic solver is based on the so-called minimum L^P norm class of phase unwrapping tasks, in which iterative binary optimizations are exchanged by clique potentials and graph cuts using efficient max-flow/min-cut algorithms, which are well-known in combinatorial optimizations. For further information see[406][407]. Having applied this reconstruction procedure, the displacement can then be depicted in pseudo 3D plots of the unwrapped phase image (figure 5.2.8), in which yellow areas represent element parts that are displaced out-of plane, while blueish areas are non-deformed parts.

The nano-meter resolution of the DHM setting is restricted to out-of-plane displacement measurements, while in-plane measurements needed a different setup that is directly compatible with the DHM setting for simultaneous x,y,z-measurements. In consequence, more complex settings like the combination of digital holographic and speckle interferometry published by Pedrini et al. in 2011 for lateral displacement measurements in the nano-newton region were not suitable.[337] Here, the only compatible, fast and easy to handle solution is the use of image correlation based on a time-dependend image-to-image comparison during in-plane displacements, which is presented in the following.

5.3 Digital Image Correlation

In 1957, Gilbert Hobrough set the starting point for digital image correlation (DIC) by analog comparison of photographs for mapping of features of the same object from different points of view.[408] In the course of the upcoming development of robotics and artificial intelligence as well as the digitalization of the photography and data processing in the 1960s and 1970s, vision-based algorithms and stereovision techniques underwent an explosive growth that paved the way for an increasing and broad interest in image correlation processes.[409] Due to its simple implementation and use, this technique today is widespread within nano- and micro-mechanical testing in the fields of science, engineering and industry such as automotive,[410][411] aerospace,[412][413][414] government and military,[415][416] bio-[417][418][419][420] and solid mechanics[421][422][423][424][425] or electronics.[426][427][428]

In general, DIC is a non-contact image based measurement method that can be run in static and dynamic mode and includes three central process steps: 1. the acquisition of grey value images of a

sample, 2. the digital image storage and 3. the numerical analysis of the images to extract shape, motion or deformations via powerful algorithms. [429] For displacement and deformation measurements, the movement of the naturally or artificially patterned sample surfaces is first tracked. Here, the starting point with zero displacement is set as the reference image. To maintain high accuracy, the sample surface needs to be flat and kept in the same plane parallel to the CCD detector surface.

The principle of DIC is schematically depicted in figure 5.3. The reference image is subdivided into discretized elements, so-called subsets of the image, and the centre points $O(x_0, y_0)$ of each subset are defined. The position of the subset centre points in the pattern of the displaced sample are then compared to those of the reference image. This procedure is called cross-correlation. [430] The displacement of this centre point is then analyzed by a similarity degree between the reference and the displaced sample image. Here, the cross correlation coefficient maximum is determined via a equation of the type: [338] [430]

$$S(x, y, \xi, \nu, \frac{\varphi\xi}{\varphi x}, \frac{\varphi\xi}{\varphi y}, \frac{\varphi\nu}{\varphi x}, \frac{\varphi\nu}{\varphi y})] = \sum \sum F(x, y) G(x*, y*) \qquad (5.10)$$

S(x,y) is the so-called correlation coefficient. F(x,y) then is the function of gray level values at the spatial coordinates P(x,y) in the reference image and G(x*,y*) is the corresponding function of gray level values at point P*(x*,y*) of the displaced object image. The coordinates of the displaced sample image for an in-plane displacement parallel to the CCD sensor surface can be defined as: [338]

$$
\begin{aligned}
x* &= x + \xi + \frac{\varphi\xi}{\varphi x}\Delta x + \frac{\varphi\xi}{\varphi y}\Delta y \\
y* &= y + \nu + \frac{\varphi\nu}{\varphi x}\Delta x + \frac{\varphi\nu}{\varphi y}\Delta y
\end{aligned}
\qquad (5.11)
$$

Here, ξ corresponds to the displacements of the subset centres O(x,y) to O*(x*,y*) in x direction, and ν to corresponding displacements in y direction. Δx and Δy are distances from point P(x,y) to the subset centre. Finally, the parameters $\xi, \nu, \frac{\varphi\xi}{\varphi x}, \frac{\varphi\xi}{\varphi y}, \frac{\varphi\nu}{\varphi x}, \frac{\varphi\nu}{\varphi y}$ are determined via image correlation to find the minimum correlation coefficient S, which then also determines the displacement in x and y direction. For template matching applications, in which a small part of an image shall be found based on a predefined template image - as used within this project -, the cross correlation cannot
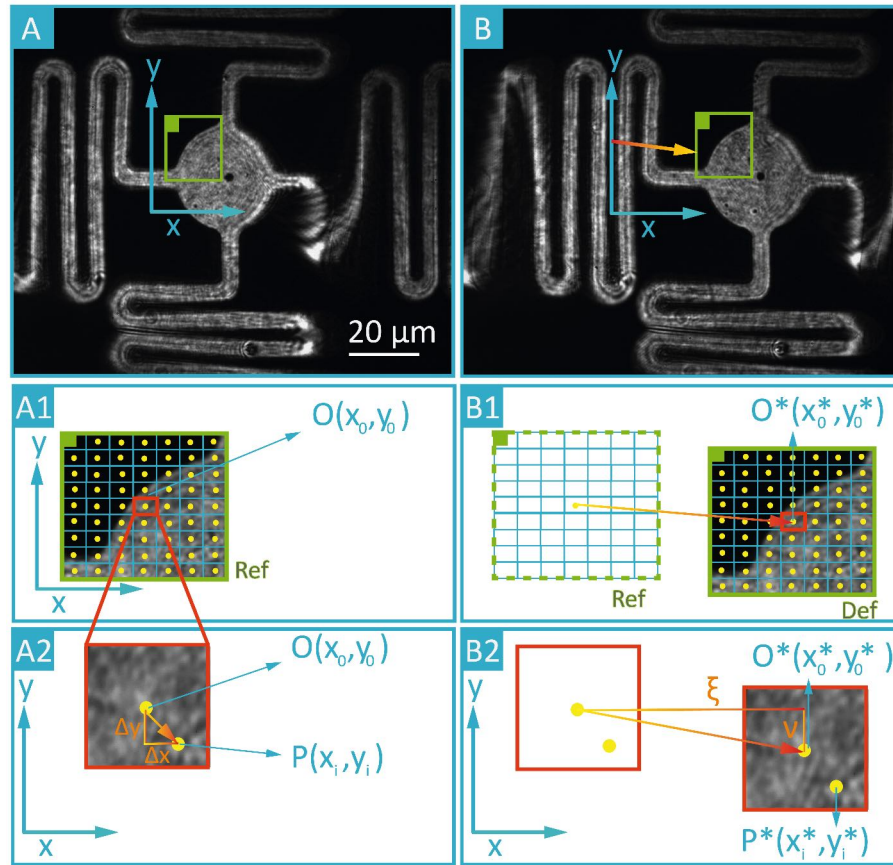
Figure 5.3: Schematic illustration of a lateral displacement measurement by DIC along the x- and y-axis. **A** Reference image without any displacement of the sensor element centre plate. The green box corresponds to a chosen landmark, which is subdivided in subsets as shown in **A1**. Each subset contains a centre point $O(x_0,y_0)$ (yellow dots in the centre of the subset boxes), in which gray value functions are defined representative by a random $P(x_i, y_i)$ (see **A2**). Within the correlation procedure, the gray value functions of $P(x_i, y_i)$ are correlated with the gray value functions of $P^*(x_i^*, y_i^*)$ after the displacement of the sensor element to find the minimum correlation coefficient S and by this, determine the x-displacement ξ and the y-displacement ν of the subset centres (see **B2**). **B**, **B1** Image after x- and y-displacement of the centre plate.

be applied properly. Here, disturbed images contain e.g. bright spots, which are directly cross correlated with the reference image instead of the chosen area of interest. In this case, normalized cross correlation is used, in which the global and local intensities within the images are normalized in the frequency domain before correlation. The normalized cross correlation function then is: [430]

$$S(x, y, \xi, \nu, \frac{\varphi\xi}{\varphi x}, \frac{\varphi\xi}{\varphi y}, \frac{\varphi\nu}{\varphi x}, \frac{\varphi\nu}{\varphi y})] = \sum\sum[\frac{F(x, y)G(x*, y*)}{\sqrt{\sum\sum F(x, y)^2}\sqrt{\sum\sum G(x*, y*)^2}}] \qquad (5.12)$$

and basis of the used open-source image correlation software. A detailed description of this procedure was published by Lewis et al. and shall not be presented in more detail here. [339]

Due to the discretized nature of digital sensor surfaces, which are subdivided into pixels, no gray level information is available between the pixels. If the coordinates x, y, x*, y* of the pixel centers could be determined only, the displacement values therefore would depend on the gray value of an entire pixel. Here, the signal within one pixel is created by the integration of spatial continuous signals of the entire pixel area. [431]

This is directly run by the imaging sensor, for which reason this integration process cannot be manipulated from the outside. By this, the resolution of this method would be then also limited by the amount of pixels. To overcome this limitation, the reconstruction of the continuous signal is realized via the spatially discrete image. Here, algorithms have been developed to approximate the gray values between the pixels, which is realized by interpolations such as the so-called bilinear interpolation, bicubic spline interpolation as supposed by Bruck et al. [338] or similarity interpolations applied by Debrella-Gilo et al. [431] According to Pan et al., the errors of the setting or rather the accuracy of this displacement measurement method is limited by various parameters such as:

1. a lack of contrast between the background and the sample that is to say the speckle pattern by which the accuracy of the algorithm is reduced, 2. lacking parallelism between the CCD sensor surface and the sample surface, 3. disturbances by noises during the acquisition and digitization process, 4. distortions of the image by lens distortions, 5. the subset size chosen by the user, which needs to contain a sufficiently distinctive intensity pattern, 6. an adequate correlation criterion and 7. the type of sub-pixel interpolation. [430]

Applying an optimized setting, sub-pixel image correlations in combination with short wavelengths and optimum magnification, today allow for resolutions down to the nanometer range. [430] [432] [341]

In the course of this work, an open-source ImageJ plugin published by Tseng et al. [418] [433] was applied, which is based on the normalized cross correlation of a template matching procedure described

by Lewis et al.,[339] which allows for sub-pixel resolved displacement determinations.

5.4 Materials and Methods

In-plane (x, y) and out-of-plane (z) sensor displacements were measured by a combination of digital holography and image correlation. These methods were carried out on the same homebuilt off-axis digital holography microscope (DHM) with kind introduction into the field of DHM, providing and supervision by Dr. Pedrini in the working group of Prof. Dr. Osten at the Institute for Technical Optics at the University of Stuttgart. The setup was modified by me in accordance to the requirements of this project by conceptualization, building and pre-testing of a micromanipulator setting for the mechanical manipulation of the microsensor elements in the laboratories of our working group in Kiel and precise implementation of the setting into the DHM/DIC setup in the laboratories of Stuttgart. All measurements were run and analyzed by me. The setting and the real course of the beam path are shown in figure 5.3 **A**.

Out-of–plane Displacement measurements: DHM   The setup was positioned vibration damped on an optical table (Microplan® Schwingungstechnik, Saarbrücken, Germany). All optical components were screwed to a home-built optical plate and implemented in an optical cage system (Thorlabs®) for maximum vibration-free stability. Based on pre-tests in the laboratories in Stuttgart run by me, the setting described in the following was optimized to a compact design at lowest possible costs, minimum installation height in order to reduce external vibrational movements influencing the DHM measurements, but guarantee optimum sample adjustment. The DHM setting is shown in figure 5.3 **A**. A continuous wave LED laser beam (**1**) ($\lambda = 405$ nm, 20 mW, short coherence length: 1 m) was focused by a convex thin lens **3** on a beamsplitter (BS1, **4**), and thus, divided into an object beam (**OJ**) and a reference beam (**REF**). The object beam passed this BS1 and a second BS2 (**9**) before being focused on the sample surface (**10**) by an objective (**10**) (20 x, Nikon® LU Plan FLUO, 0.45 Apertur, WD 4.5). The scattered light then passed the objective and was reflected by the beam splitter to the CCD chip of the fast camera (**13**) (SVS-VISTEK®, Evo2050MFHCPC, 2/3" sensor size, 1600 x 1200 pixel, 106 fps,). The reference beam was diffracted by $90°$ by BS1 to
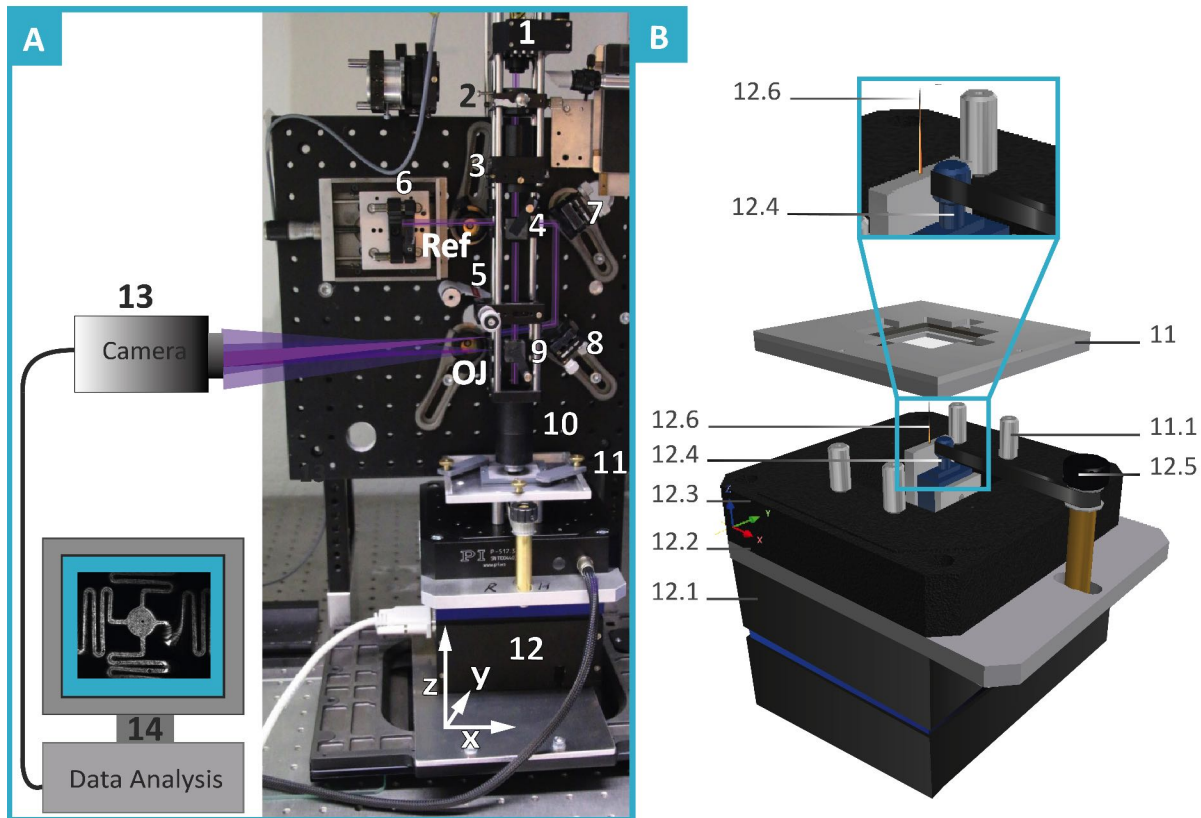
Figure 5.4: **A** DHM setting and its different components: **1** Continuous laser light source with a short coherence length, **2** iris, **3** lens, **4** prism to split the laser beam into the reference (**Ref**) and the objective (**OJ**) beam, **5** lens to collimate the objective lens, **6** mirror on a translational stage for adaptation to the beam path length of the objective beam. **7,8** mirrors to direct the reference beam to the CCD camera and spatially overlap the reference beam with the objective beam under a defined angle, **9** second prism, **10** objective lens with an adapter, **11** sample holder with fixed sensor array sample, **12** electrically driven micromanipulator, **13** SVS Vistek CCD camera, **14** computer to control the camera program. For lateral displacement measurements, the same setting was used by blocking the reference beam after prism **4**. **B** Detailed CAD image of the manipulator unit shown in **A**(12) (from bottom to top): **12.1** micrometer z-translational stage, **12.2.** adapter plate, **12.3** x-, y-, z-piezo nano-positioner, **12.4** mechanical micro-translational stage, **12.5** home-built belt-drive to adjust the adjust tungsten tip position in z-direction, **12.6** tungsten needle with a tip diameter of 2 μm (see also inset box), **11** Stainless steel posts to ensure assembly space for the tungsten needle unit. **11.1** plastic sample holder that is fixed via screws after adjustment (see **A 11** as well).[1]

---

[1]11, 11.1, 12.5, 12.4, 12.3, 12.2 reproduced from B. Neumann, Project Work, Workshop of the Faculty of Engineering, CAU, 2017 with kind permission of B. Neumann.

a mirror on a mechanically translational stage (**6**). Here, it was reflected and optically guided to the camera sensor. Reference and object beam were spatially overlapped on the sensor chip via mirrors (**7** and **8**). For a better alignment and ensured stability against outer impacts, components 1, 2, 3, 5 and 10 were installed in a vertical axis cage system. The sensor signal was recorded by an ITO-written LabView program. To ensure a corresponding beam path lengths of the object and the reference beam, the path of the reference beam was adjusted via the translational stage to a maximum contrast within the interference fringes recorded by the camera (see figure 5.2.2).

For positioning of the sample, a home-build micromanipulator setting shown in figure 5.3 **B** was conceptualized, optimized, tested in the labories in Kiel and implemented into the DHM setting by me in the course of this sub-project. The positioning unit consisted of a micrometer z-translational stage (**12.1**) (PI$^{®}$ M501.1PD: $\delta(z) = 12.50$ mm, resolution: 0.024 μm; controller C-863 Mercury Servo Controller), an x-, y-, z-piezo nanopositioner (**12.3**) (PI$^{®}$ 517.3CL: $\delta(x,y)_{max} = 100$ μm; $\delta(z) = 20$ μm, resolution: x,y: 1 nm, z: 0.1 nm and controller E-517), a sample holder (**11, 11.1**) and a manipulator unit (**12.4-12.6**). This unit consisted of a mechanical micro-translational stage (**12.4**) (THORLABS$^{®}$ 1/2" (12mm) Dovetail Translation Stage) screwed in the centre of the positioning unit and was mechanically driven by a home-built belt-drive (**12.5**). A tungsten needle (**12.6**) (American Probe & Technologies, 71T Tungsten Wire Probe, r $=$ 2 μm, length: 1") was fixed on top of the stage and used to deform the tested sensor structures in x-,y-, and z-direction. The entire positioning unit could be moved in x- and y-direction by a lockable microscope co-axial object table (Olympus) for a simple and precise lateral first positioning of the needle relative to the DHM objective.

Before starting a measurement, the sample was clamped to the sample holder on the positioning unit and the tungsten tip adjusted and approached to the sensor centre plate. Here, NiTi sensor structures (170 μm edge length, 200 nm thickness, fabricated by ACQUANDAS$^{®}$, Kiel) were analyzed. The contrast of the resulting interference fringes was optimized by adjusting the beam paths via the mirror (**6**) on the translational stage. Then the software was started. Different sensor deformations in the nanometer up to the micrometer range were adjusted via the manipulator (**12**) and holograms were then recorded. Based on a standard MATLAB program provided by the working group of Prof. Dr. Osten, the holographic interference images were first transformed into

their undiffracted reconstruction waves. Then the digital holograms were generated and numerically reconstructed by a fast Fourier transformation. A non-commercial, free, state-of-the-art phase unwrapping algorithm called PUMA (p̲ase u̲nwrapping-m̲ax-f̲low analysis) developed by G. Valadao and J. Bioucas-Dias[407] and modified by Pedrini et al., was partly rewritten and adapted to the requirements of these measurements in our working group in Kiel by MSc Huth and me, three-dimensional images of the temporal sensor deformation were then reconstructed. Finally, the set position and each measured position were compared as displacement profiles via Origin®.

In-plane Displacement measurements: DIC In-plane deformations were recorded by blocking the reference beam within the DHM setup after the first prism. The sensor centre plate was manipulated like described in the previous paragraph, but deformed in-plane by running the x-, that is to say y-piezo of the nanopositioner. The images were stored via the MATLAB software and the deformation analyzed by an sub-pixel image correlation algorithm developed by Tseng et al.[418][433][434] implemented in the non-commercial open-source software Fuji®.

5.5 Results and Discussion

DHM and DIC were initially tested for the first time in combination with the fabricated sensor elements to validate the suitability of these precise, but simple and low-cost methods for future 3D traction force sensing.

The applied settings were based on a pre-installed already published setup by Prof. Osten et al. that was used with additional modifications regarding the additionally needed equipment for sensor manipulation to ensure minimum possible sources of error within the arrangement of the components and the data processing. To validate the sensitivity of these settings, DHM and DIC were run separately.

5.5.1 DHM

In Figure 5.5, the results of the out-of-plane displacement recording for a NiTi 4-FE sensor element (see figure 5.5**A**) are exemplarily presented. As described in section 5.4, the axial deformation was
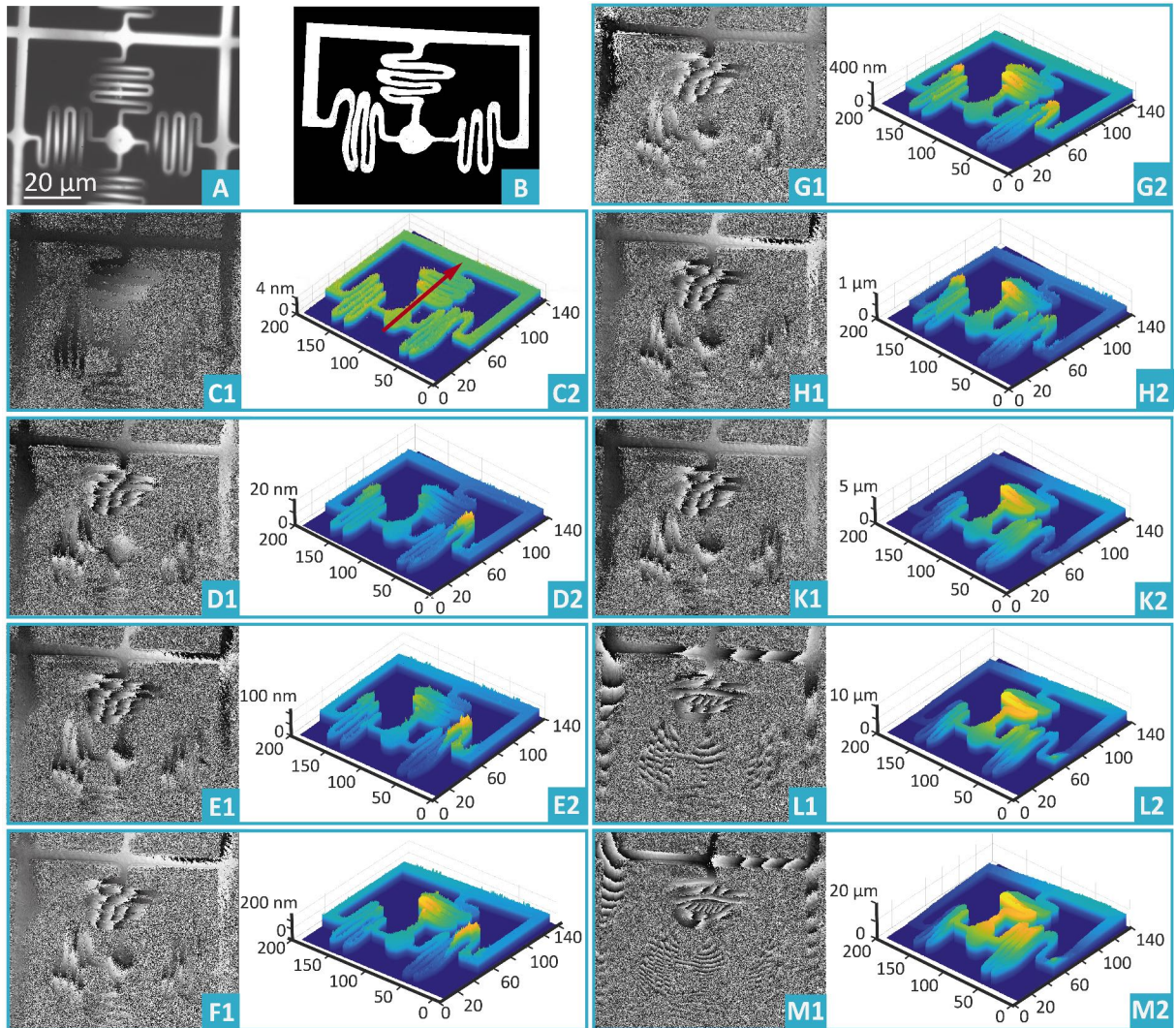
Figure 5.5: **A** Laser-light microscopic image of the 4-FE NiTi sensor, **B** Mask design used to mask the background noise during phase unwrapping, **C1**-**K1** Wrapped difference phase images after reconstruction of the sensor element at a deformation in z direction of: **C1** 4 nm, **D1** 20 nm, **E1** 100 nm, **F1** 200 nm, **G1** 400 nm, **H1** 1 μm, **K1** 5 μm, **L1** 10 μm, **M1** 20 μm. **C2**-**M2** corresponding pseudo 3D images after phase unwrapping.

simulated by use of a tungsten tip that was positioned under the sensor element, while the DHM recorded from top view. The tip was moved in defined steps from 0 nm to 20 μm via a micromanipulator setup and interference patterns were then recorded via the CCD camera. By means of the reconstruction algorithm, the phase information was extracted and by subtraction of

the reference (see figure 5.5 **C1**) and the displaced sensor element images, the phase difference images (see figure 5.5 **D1** to **K1**) were calculated.

The alternating black and white stripes are the above described interference fringes that contain all information about the axial displacement. Due to the noise in the background, a mask is needed to run the phase unwrapping algorithm for the displacement extraction accurately. To reduce the computational time, but keep the interference information, the template must consist of a closed path along the silhouette of the sensor element including the sensor centre plate. As a result, a template shown in figure 5.5 **B** has been used, in which the element was reduced to three spring arms and the centre plate and used to mask all phase difference images. By means of the phase unwrapping algorithm PUMA and additional processing in MATLAB, pseudo 3D displacement images could be extracted as presented in figures 5.5 **C2** to **K2**. Here, the color coding indicates the topography of the sensor element surface and its deformation, in which blue is a non-deformed part of the sensor or even a material free area within the surface (dark blue), while yellow areas represent out-of-plane displaced element parts. The color coding is a relative topography illustration with its own scaling for each image.

In figure **C2**, the sensor element was slightly deformed by 1 nm. The DHM is not sensitive for accurate deformation measurements in this scale range due to its limitation via the chosen wavelength, which was 400 nm. However, a phase difference image could be reconstructed due to slight differences between the reference phase image and the second image. According to the regularity of the green surface color of the frame and the element structure, the sensor is not deformed axially. In **D2**, the element is displaced by 20 nm, which corresponds to a traction force of 3.2 pN when considering the spring constant of this element of 0.004 N/m. Here, a displacement was sensed obviously, in which the right spring slope is deformed by 5 nm and the upper spring arm shows some tilt. This deformation region is still outside the resolution limits of this DHM setting wherefore the displacement value is not reliable. The presented deformations can be caused via a misinterpretation of the interference pattern within the phase unwrapping algorithm, and slight vibrational disturbances within the element. This inaccuracy is also contained in **E2**, with a displacement of 100 nm. However, a change within the element surface is observable, in which the upper spring arm is displaced slightly out-of-plane, while the right spring slope is still deformed the same way like in **D2**. This spring slope

is not of further interest as its not manipulated and not relevant for future readout processes. In **F2**, an out-of-plane displacement of 200 nm is depicted, which would correspond to a traction force of 0.8 nN. Here, the upper spring arm is displaced instead of the element centre plate, which is due to a slight mechanical offset of the tungsten tip, when manually adjusting the tip position via the mechanical microscopic table. This was not directly observable via the microscope or the recorded holograms. The phase unwrapping algorithm was implemented independently and was not available at the time of the measurements. However, the proof of the sensitivity of the DHM is not influenced by this offset. In future applications, a tip based mechanical manipulation will be exchanged by the impact of an axial cell traction force. The positioning of this force impact will be controlled chemically as described in the following chapter 6.

In figures **G2** to **M2**, high displacements of 1 μm, 5 μm, 10 μm and 20 μm are presented to analyze the sensitivity with regard to strong out-of-plane deformations that correspond to traction forces of 4 nN, 20 nN, 40 nN and 80 nN, respectively. The height development of the impact area of the upper spring arm can be well observed. Regarding the extensive displacements of 10 and 20 μm, the entire sensor element and the frame experience an increasing displacement. Consequently, the calibrated spring constant of this NiTi 4-FE sensor element would not be usable anymore as it just includes the mechanical behavior of the element itself, while the frame was set to be rigid during calibration. Hence, these displacements can be well observed via DHM, but will not be of further relevance for future traction force sensing.

The accurate analysis of the axial displacement was ensured by topographic line profiles extracted via MATLAB along a pre-defined vector. The line profiles along the vector marked in the used mask shown in figure 5.6 **C** for sixteen different out-of-plane displacement of the NiTi 4-FE element, are summarized in figure 5.6 **A**. Here, six pillars are observable: the broad pillar on the left corresponds to the cross section of the upper frame, the four lean pillars are the slopes of the upper sensor element spring arm, in which the fourth slope was directly displaced by the tungsten tip. The sixth broad pillar corresponds to the element sensor plate. Regarding the frame, a curved surface can be observed at 20 μm due to the displacement of the entire sensor element including the frame. The surface of the centre plate and partly of the fourth slope boast reproducible surface noise, which is due to some external noise influencing the image reconstruction. This phenomenon could be
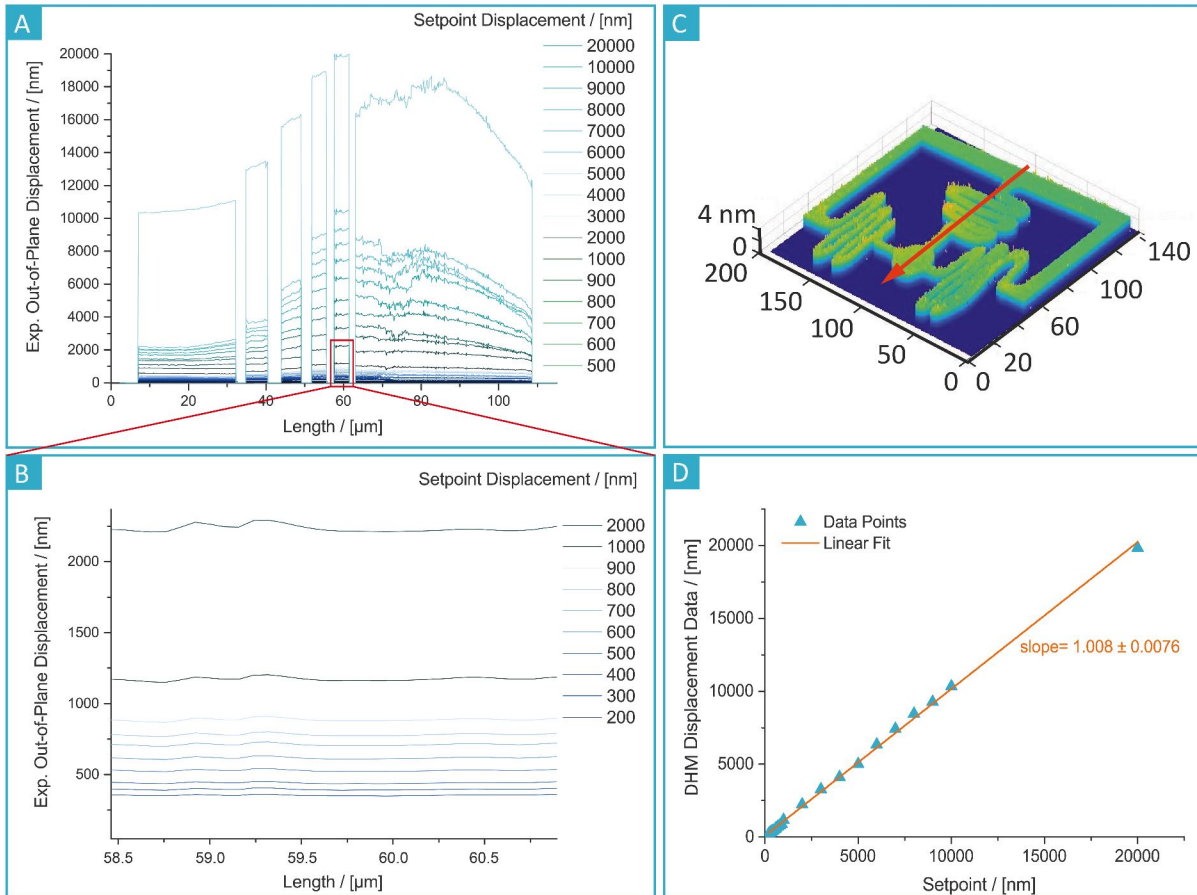
smoothed via filters

Figure 5.6: **A** and **B** Line profiles extracted from the different displacement pseudo 3D images presented in figure 5.6 along the orange arrow inscribed in the 3D plot in **C** or 4-FE NiTi sensor element. **A** Line profiles in the range of 0 nm to 20 μm along the vector marked in **C**. The left pillar corresponds to the cross section of the upper frame, the four thin pillars represent the four slopes of the upper spring arm and the right broad pillar shows the displacement of the sensor element centre plate. As the element is manipulated off-centre via the fourth slope, the centre plate has a sloping right edge. **B** Blowup of the displacement profiles shown in **A** in the range of 200 nm to 2 μm. **D** Direct comparison of the manually set displacements (set point) and the corresponding experimentally determined displacement data (DIC) plotted as blue triangles. In case of a direct matching between these two data sets, a linear fit with a slope of 1 would be identified, which is the case regarding this setting. Hence, a good quality of the experimentally determined displacement data between 200 nm and 20 μm could be shown.

in future applications. The increasing negative slope on the right side of the sensor centre plate line

profiles is due to the increase of the plate tilt at higher displacements. In consequence, inaccuracies in the determination of the sensed force due to slight tilts of the centre plate can directly be recorded and corrected via this axial force sensing method. However, this correction would only be needed for non-centered and very high out-of-plane displacements, which will not be the case in this future sensor application. With regard to the fourth pillar, the measured axial displacement and the displacement set mechanically via the micromanipulator as listed on the left side are in good agreement. In figure 5.6 **B**, an inset of the fourth pillar is shown containing displacement measurements between 200 nm and 2 μm. Here, the measured out-of-plane displacements are slightly higher by about $10\,\%$ than the expected values, which can have several reasons as already described within the general information about DHM in section 5.2. Noise could have occured during the measurement due to the arrangement of the optical components and the sensitivity of the sensor elements to small impacts. This slightly changes the interference information due to vibrations of the sensor element. This could then cause changes in the phase reconstruction. Moreover, the phase unwrapping algorithm might need more detailed adaptation to this task for future tests like the definition of the masked area.

However, the results are promising with regard to the reached resolution and accuracy based on a simple, low-cost and just slightly modified DHM, which was originally optimized for the characterization of MEMS surface topographies. By use of the 4-FE NiTi sensor element , which has a lateral spring constant of 0.087 N/M and an axial spring constant of 0.004 N/m, traction forces down to 800 pN and up to 20 nN can be sensed limited considering the lateral resolution of the DHM of 200 nm. This force range of the sensor system is in the range of cell adhesion forces exerted by focal adhesion clusters.

By using shorter wavelengths, adapting the optical components to a more compact design and realizing an even more vibration-free setting by installing the off-axis DHM from a vertical to a horizontal arrangement on an optic table, the resolution can even be increased below 10 nm as already shown by Pedrini et al.[337] Due to the dimensions of the necessary external mechanical manipulator, which was used for the manipulation of the sensor elements, the more compact setting developed by Pedrini et al. could unfortunately not be taken into consideration in the course of this project. Consequently, a next step for further experiments would be the very cost-intensive miniaturization of the three axis micromanipulator with smaller components for installation within a

more compact DHM setting.

5.5.2 DIC

In-plane displacements were recorded with the same setup like for DHM by blocking the reference beam. Lateral displacements between 0 nm and 20 μm were again realized via the micromanipulator and recorded for further cross correlation of the reference and images of the displaced sensor element centre plates.

To verify the resolution of this setting by excluding incertainties like possible vibrations of the sensor, first the lateral displacement in (+x)-direction was just simulated by in-plane translation via the piezo nano-positioner without the tungsten tip of the micromanipulator.

In figure 5.7 **B**, the experimentally determined displacements (bright blue bars) and the corresponding displacements (dark blue bars) set via the manipulator for a 4-FE PDMS sensor element (see figure 5.7 **A**) are plotted.

Here, every experimental data point corresponds to an average over three different measurements for the same displacement values. The standard deviation for each data point within the three experiments is indicated by the orange bars and ranges randomly between 4 nm and up to 18 nm. Consequently, the overall percentage error for small displacements is comparably high than for displacements above 200 nm. When comparing the matching between the set and the experimentally determined values, the values are in good agreement with each other for displacements between 200 nm (step No 28) and 20 μm (step No 50), with a percentage deviation between 0.05 % (for 20 μm) and 7 % (200 nm). Here again, the deviation is the higher, the smaller the displacement. For lateral displacements beyond 200 nm, the percentage deviation in comparison to the set displacement values varies between 10 % and over 100 %, the smaller the in-plane displacement. For set displacements smaller than 18 nm, the experimental data are even negative, indicating that there is a misinterpretation of the algorithm showing drifts in (-x)-direction.

This might be due to difficulties in the analysis of the gray values for such small displacements based on a pixel size of the CCD camera and magnification via the objective that do not support displacement resolutions in this range. Hence, this simple, low-cost setting in combination with the algorithm developed by Tseng et al. is just sensitive for displacements above 200 nm.
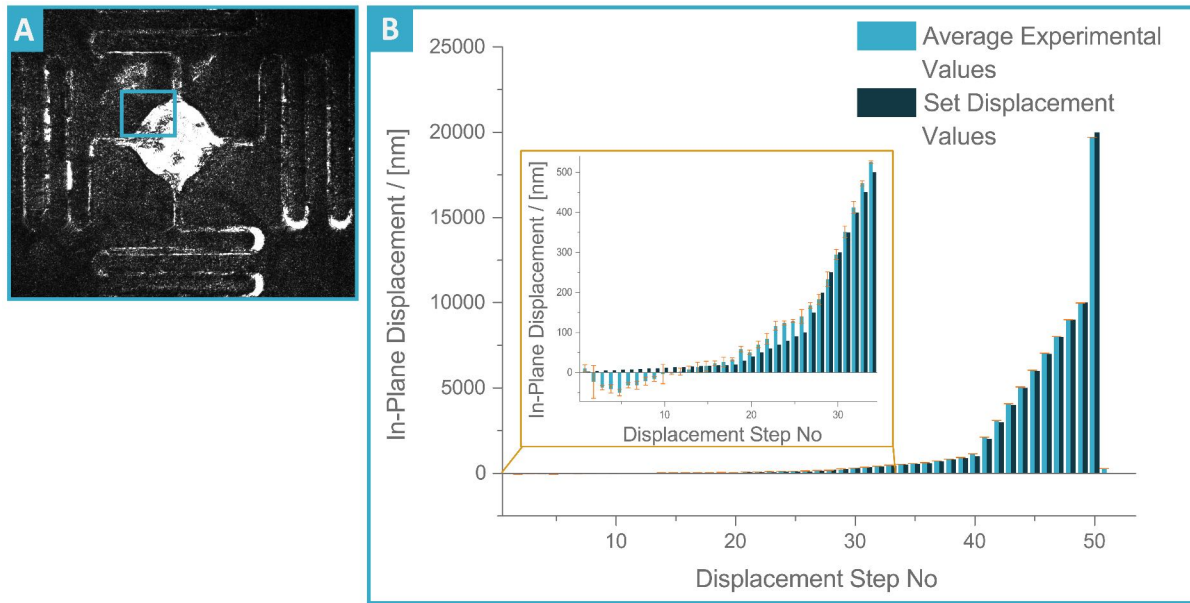
Figure 5.7: Comparison of the in-plane displacement set manually along the x-axis via the piezo-electric nano-positioner (dark blue bars) and the experimental displacement values determined via normalized cross correlation (bright blue bars) for **A**) a 4-FE PDMS sensor element. The blue inset box in **A** shows the chosen template area for normalized cross correlation of the images. **B** The experimental data correspond to the average over three independent displacement measurements, in which the orange brackets present the standard deviation within these measurements. As can be seen within the inset box in **B**, the two data sets are in good agreement up to step No 28, which corresponds to a in-plane displacement of 200 nm. Beyond 200 nm, the experimental data vary clearly from the manually set displacements and differ by more than 100 %. Hence, the limitation of the resolution of this setting and the chosen algorithm is 200 nm.

To validate the resolution in combination with a free-standing sensor element, type NiTi 4-FE sensor elements, which were also used for DHM, were displaced in-plane along the x-axis by means of the tungsten tip based manipulator. The results are presented in figure 5.8. The chosen template image for image correlation is indicated in the laser microscopic images of the sensor elements **A** and **B** via the blue box. To outline the differences in measurement results, a properly working sensor element **A** and a slightly defect element with strong in-plane deformations and a ruptured sensor arm **B** were installed. In figure **A1**, the experimentally determined lateral displacement (blue bars) is compared to the manually set displacement values (green bars). Displacements in the range of 900 nm to 20 μm are in good agreement with the set points. Here, the experimental and the
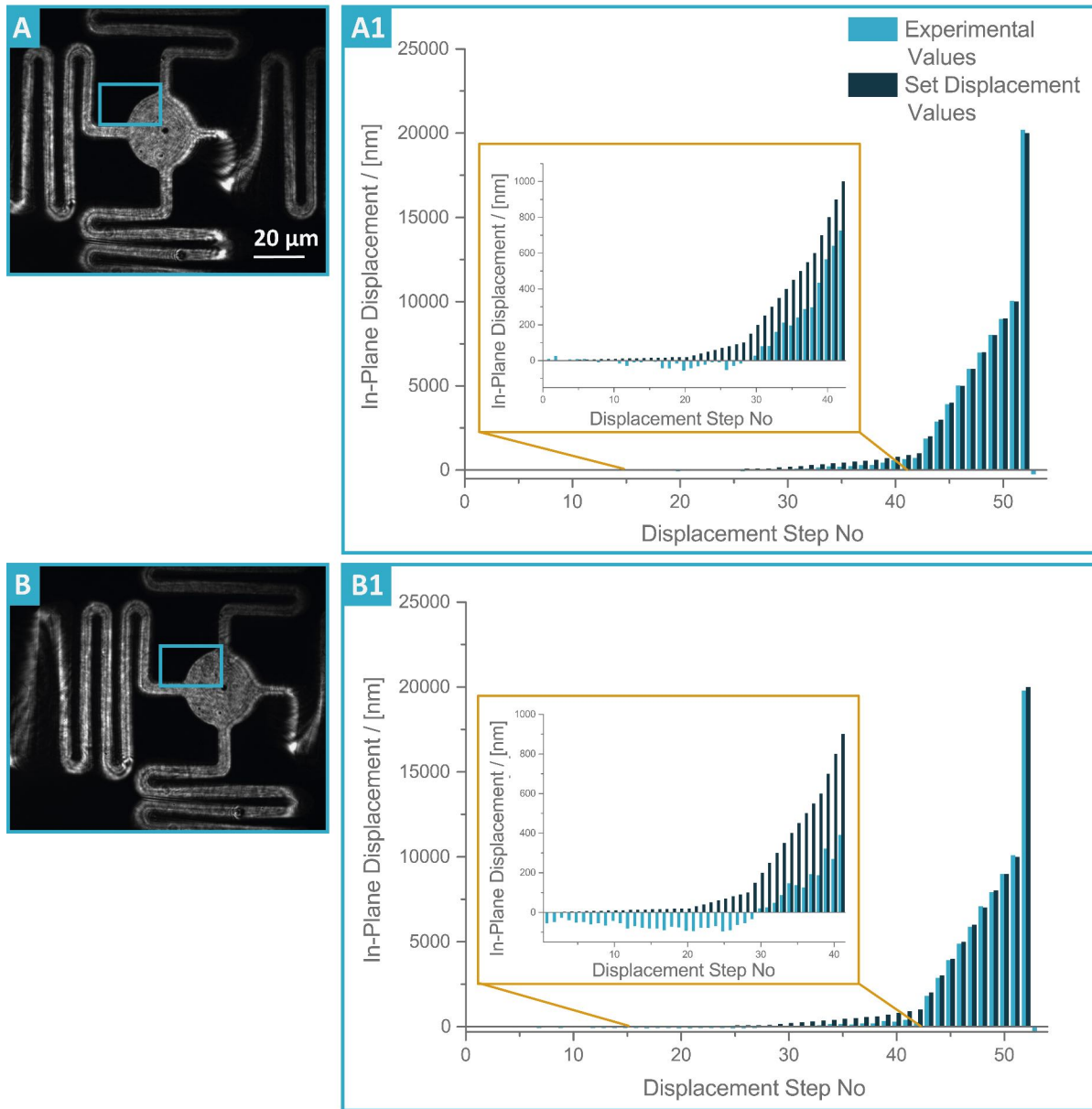
Figure 5.8: Comparison of the accuracy regarding in-plane displacement sensing via of a fully working NiTi sensor element type 4-FE (**A**) and a defect sensor element of the same type (**B**). **A1** Experimentally determined displacements via image correlation (bright blue bars) are compared with the manually set lateral displacements by means of the nano-positioner (dark blue bars) for the fully working sensor element. Good agreement between the experimental and theoretical set points are given for displacements in the range of 700 nm and 20 μm. Beyond 600 nm, the error increases to at least 100 %. **B1** Corresponding diagram for a defect sensor element of the same sensor element type. Here, the experimental data deviate by more than 60 % for displacements smaller than 1 μm. In consequence, defect elements can be detected easily via this method.

theoretical values vary by 0.2 % to 8 %. Regarding values beyond 900 nm, the deviation increases dramatically with decreasing displacement as can be observed in the blue inset box for displacements between 1 nm and 800 nm. Here, the error increases to at least 100 % for displacements smaller than 600 nm. For set displacements below 100 nm and beyond the limit of resolution of the setting, the values turn even to negative displacements as already observed for the PDMS sensor element. As the method was entirely transferred from the first experiment with the PDMS sensor element to the free-standing NiTi element, the decrease in resolution is due to changes in the mechanical and optical properties and behavior of the NiTi structures. First, the NiTi surface is smoother than the gold-coated PDMS surface wherefore bright spots can be observed in the microscopic image that might influence the matching procedure within the correlation process. Second and more important, the NiTi elements are very sensitive to outer impacts like noises, which is why slight vibrations after displacement and during the image recording can cause disturbances or rather imaging errors during the data processing via correlation.

An additional source for misrepresentations is the determination of the exact object dimensions in combination with the corresponding number of pixels regarding the defined template image dimension. The factor is relevant for the translation of the pixel-to-pixel displacement into a spatial displacement. Here, 60 nm correspond to one pixel. In consequence, the resolution can be optimized by a CCD sensor chip with a high pixel density.

For optimum matching of the images or more specifically maximum correlation results, a high contrast regarding the analyzed structure is needed. This is ensured by high reflectivity of the sensor element, maximum absorbance of the background and by this, a clear definition of a sharp edge between the element and the background. Further optimization is in accordance to the parameters described in section 5.3.

Consistent observations are possible for the defect sensor element as shown in figure 5.8 **B1**. At first glance, a good matching is found for values between 2 μm and 20 μm. However, the experimental and theoretical data for this displacement range already differ by 4 % to 10 %. The error for displacements below 2 μm are at least 200 % as can be seen within the blue inset box in **B2**. In consequence, a defect sensor element can clearly be identified in future applications.

Finally, DIC has shown to be a suitable, simple, low-cost and comparably precise technique for

lateral displacement measurements. Here, the setting allowed for measurements down to 200 nm. With regard to the determined lateral spring constant of 0.087 N/m for a 4-FE sensor element with an edge length of 170 μm, lateral traction forces down to 17 nN can be sensed.

To improve the overall resolution of this DIC setting, three major components can be optimized, which are image acquisition, image analysis, and the interference pattern of the image. Regarding, image acquisition CCD chips with smaller pixels and hence, a higher pixel density can be used. Furthermore, the entire measurement is highly sensitive to vibrations and outer impacts on the sensor elements wherefore a strong vibrational damping needs to be ensured in future applications. Hence, the entire setup design needs to be arranged more compact as already mentioned for DHM. The high sensitivity of DIC to slight ouf-of-plane displacements can be overcome via a telecentric imaging system as described by Sutton et al. [435] [436] With respect to the image analysis, the results are dependent on a fully suitable and rigid correlation algorithm, which needs to be verified in more detail. Considering the current development of new, more powerful algorithms, an increase in accuracy and resolution to even lower forces will be supported. [437] Finally, the interference pattern that is recorded can be optimized via adequate algorithms before the correlation procedure is run as shown by Bomarito et al. [438] In consequence, the above presented data outline the suitability of this method for the analysis of lateral displacements in order to measure lateral cell traction forces in the nano-newton range and can be optimized via various parameters to open a resolution down to piconewton scale.

5.6 Conclusion

In the course of this sub-project, measurements with a modified, simple, low-cost combined DHM/DIC setting to record in- and out-of-plane displacements of a sensor element proved the suitability of these methods for cell traction force sensing. Hence, in- and out-of-plane displacement measurements down to 200 nm offer an axial force resolution of 800 pN via DHM and 17 nN for in-plane traction force determinations sensed by a 4-FE sensor element. By this, the force range of confocal clusters is succesfully reached as targeted within this project. So far, the modified setting was still highly sensitive to outer impacts and vibrations, which is why the deviation between the experimental data and

the set displacement points was at least 7 to 10 % for higher displacements up to 20 μm and more than 40 % for displacements smaller than 200 nm (DHM) and 600 nm (DIC). A first improvement is the modification to more compact setup design with shorter beam paths, directly installed on an optical table instead of the top-vied setting used within this project. Further optimizations for future applications to improve the resolution in all three spatial directions have been described in detail for DHM and DIC above. In this testing, the in-and out-of-plane measurements were run separately and

static to validate the resolution limits. For future measurements, a fast-rotating optical chopper will be installed in the path of the reference beam that triggers the CCD camera. By means of rotating frequencies up 100 kHz for commercially available low-cost choppers, the reference beam is shortly blocked and DHM and DIC can be run pseudo simultaneously. The application of high-resolution fast CCD cameras then allow for continuous records for dynamic displacement measurements. However, this combined technique offers a broad range of sensitivity modifications via various hardware and software components while being cost-effective and simple both in setup and handling wherefore it is most promising for future applications in 3D low-force traction sensing.

6 Surface Functionalization

The precise measurement of defined cell traction forces is influenced by the sensor element surface and requires both, the biocompatibility of the sensor material and the control of adhesion sites on the sensor element centre plate. Regarding the chosen biocompatible element materials, PDMS shows appropriate cell adhesion properties,[439] while the spreading of cells on structured NiTi was proved to be adequate[154] and pronounced on silicon and amorphous silicon surfaces.[440] Hence, a surface functionalization is needed by which cell adhesion can be controlled with respect to the amount of adhesion sides in the nanometer range, the density of these nano-functionalizations and the adhesion position on the sensitive, free-standing sensor element in the micrometer region. Several techniques of surface micro-and nanopatterning are already established. However, these methods are both cost- and time-intense or cannot be used for spatially restricted or non-contact patterning. In this chapter, a non-contact method is presented that was conceptualized and tested for the first time in the course of this project to generate locally defined micro-and nanostructures within a few seconds by means of inkjet printing. This will allow for high-throughput user defined surface micropatternings including quasi-hexagonal arranged gold nanodot structures that can be further biologically functionalized for cell testing. The results and modified images presented in this chapter are part of the paper "High-throughput micro-nanostructuring by microdroplet inkjet printing" written by Selhuber-Unkel and me and published in the Beilstein Journal of Nanotechnology in 2018.[441]

6.1 Surface Micro-Nanopatterning Methods

As already shown in various previous studies, cells are able to sense the physical and biochemical properties of their nanoscopic and microscopic surrounding with high sensitivity.[442] Hence, changes in cellular adhesion, migration, actin organization, force generation or differentiation behavior can be observed as a result of changes in substrate stiffness[74][443][444][445] and the response of adhered cells is controllable by a distinct choice of adhesion ligand distributions and grouping in micro- and nanostructures.[446][447][433][448]

The substrate surface modifications and corresponding effects on cell behavior are highly relevant e.g. in the fields of 1. implants to improve the physiological compatibility for bone healing,[449] 2. biosensors to introduce functional or organic groups, enhance the hydrophilicity and bioactivity by attaching biomolecules or adding ligands,[450] 3. tissue engineering applications and mechanobiological investigations for mimicking the extracellular matrix,[442] or 4. biomaterials, in general.[451]

Due to the versatile importance of micro-and nanopatterns, various methods were developed to design distinct structures on soft and solid substrate surfaces within the last years, such as photolithography based mask designs,[452] soft lithography based on contact ink printing via elastomeric micro-stamps,[453] the more space selective micro-contact printing method,[454] dip pen lithography, in which an ink loaded AFM cantilever tip is applied to create defined nanopatterns via contacting the substrate surface,[455] or the mask-less, non-contact methods electron beam, for high-resolution patternings, and focused electron beam induced deposition (FEBID), in which even three dimensional nano-structures can be designed.[456] However, these techniques are either highly time-and cost-intense as they have to be run in clean room atmosphere or under vacuum like the lithography and electron beam based methods, just allow for very small patterns beyond 50 nm (electron beam and FEBID), or work only in contact mode (dip pen lithography, soft lithography, photolithography based masks).

Another well established bottom-up method is block-copolymer micelle nanolithography (BCML) first suggested by Spatz et al.[457] to produce periodic and aperiodic nanoparticle arrays. Here, polymeric, glass or silicon surfaces are nanopatterned via a micelle solution, in which amphiphilic block-copolymer consisting of polystyrene and polyvinylpyridine based ligands with adjustable length

are loaded with gold nanodots and dissolved in toluene based solvents. When coating a substrate surface via dip coating[19] or spin coating[103] of the BCM solution, the micelles self-assemble via microphase segregation during the evaporation process in quasi hexagonal patterned monolayers on the surface. After plasma treatment, a pattern of gold nanodots with distinct inter-particle distances remains. The distance between the nanoparticles can be controlled via the molecular weight that is to say the length of the micellar ligands, the BCM concentration and the spinning or dipping speed during the coating procedure. [458] [459] For biological testing and further control of the cell adhesion binding sites linked to the pattern, the inter-particle space is passivated by polyethylenglycole (PEG), while the gold nanodots are functionalized via pentapeptides consisting of arginine (R), glycine (G) and asparagine (D) sequences. These RGD based peptides are then bond via thiol linkers to the gold nanodot surface. For more detailed information, please also see [460] [446]regular pmicropatterns of 4x 4 dro[19] [461] [39] [462] [103].

Using BCML, Spatz et al. were able to show that cell adhesion on nanopatterned surfaces with an inter-particle distance above 73 nm decreases drastically due to a reduced formation of actin stress fibers and focal adhesion. [446] A major drawback of this method is its lack in spatial selectivity, for which reason coating of the entire substrate surface is only possible, while micropatterns are not feasible.

Hence, there was no no cost-and time-efficient established non-contact method available to micro- and nanopattern a defined area of a sample surface with quasi-hexagonal nanodot patterns at once.

A solution approach was successfully been tested in the course of this project. Here, BCML was combined with the well-established and fast technique of inkjet printing to overcome the restriction to a comprehensive nanopatterning, which will be presented in the following section.

6.2 Ink-jet Printing

Ink-jet technology summarizes all methods where liquid is pumped through a nozzle on a substrate in a defined structure to create patterns or graphics.[463] The starting point of this con-contact printing method was set by William Thomson in 1858 by the invention and construction of the so-called Siphon recorder, an electromechanical receiver for submarine telegraphy, already working like a rudimentary continuous ink-jet printer.[464] It took another 100 years of intense research work by various scientists until Elmquist of the Siemens-Elema company patented the first practical continuous ink-jet device in 1951.[465] With ongoing developments like the invention of piezoelectric nozzles by IBM in the 1970s[466], the first drop-on-demand (DOD) ink-jet setups allowed for drop-wise printing processes and should prevail throughout the years on the world market due to their high speed application and very high reliability.[467] Today, ink-jet printing is not only an established printing method for everyday media reproduction, but the most versatile and reproducible dispensing technique in a broad spectrum of fields like rapid prototyping[468] or surface functionalizations.

In general, DOD ink-jet printers expel a few μm sized droplets of fL to μL volumes of liquid ink on material surfaces via a nozzle one at a time while it is moved in two dimensions with a defined distance to the substrate surface.[469] Based on 1. a short pressure impulse generated by a heater, which evaporates the ink, or 2. volume changes of piezo-crystals in a chamber that is attached to the nozzle, the droplet then takes a ballistic trajectory to the substrate surface. By this, a pattern of droplets is created on the substrate depicting the desired printing object.[469] The droplet size is manipulable via the nozzle opening diameter, the impulse, which defines the velocity of the droplet and the nozzle opening time as well as the viscosity and chemical properties of the ink and typically ranges between 10 to 100 μm in diameter.[470][471] Finally, the dried droplet diameter on the substrate surface depends on the droplet volume, its impact velocity, and its general spreading behavior with regard to the chemical and physical substrate surface properties like roughness and wettability.[472][473]

Based on this comprehensive amount of variable parameters and operating principle, besides its cost-efficient setting, ink-jet printing offers several advantages over other more complex or multi-step, established methods like lithography and electron beam processes. First, it can be performed contact-

free and under ambient conditions, which makes it most attractive to biological applications. [463] Hence, it used in tissue engineering in the field of bio-printing to directly imprint live cells containing ink, [474] proteins, [475] or bacterial colonies. [476] Second, multiple liquids are printable at once by use of multiple printer heads and nozzles. Furthermore, it proved to be a highly position accurate method by which means defined structures can be printed on computer-defined positions. These features and the contact-less mode even open the possibility of three dimensional prints via layer-by-layer material deposition. [469] Last but not least, precise high-throughput patterning over large surface areas are possible by means of robotic automation. [463]

Besides the use of biological inks, metallic, semiconducting, or insulating material can be printed via precursor stabilized inorganic nanoparticle inks. These inks are increasingly used in the field of general functional nanostructures [477] and printable microelectronics [478] [479] [480] such as the low-cost, high-throughput fabrication solutions for protein immunosensor devices used for the detection of clinically relevant proteins , [481] [482] gas sensors, [483] MEMS [469], bus lines, [480] conductors, [484] electrodes. [485] thin film transistors [486] or solar cells. [487] [488] Hence, inorganic printed electronics is a research field of tremendous commercial potential and progress. [489]

Regarding conductive inks, metallic nanoparticles based on copper, gold, palladium or silver are well understood and widely used. [489] Here, gold-nanodot solutions are most interesting to fabricate inert electronic structures on various material substrates like glass, [490] silicone, [480] plastic [491] [481] or paper [492] due to their high stability against outer influences like water or air.

Based on the above described features and advantages of ink-jet printing, a micellar solution of dissolved gold salt was prepared to produce microstructures consisting of mono-layers of quasi-hexagonal particle patterns by combination of this solution with a highly-accurate commercial ink-jet printing system.

6.3 Materials and Methods

6.3.1 Gold-nanodot Inkjet Printing

Block-copolymer micelle solution (BCM)   Gold nanoparticle solutions for further ink-jet printing were prepared by dissolving poly(styrene-b-2-vinylpyridine) (PS(79000)- P2VP(36500), 4 mg/mL, Polymer Source, Canada) in o-xylene (p.A., Merck$^®$, Germany) and loading with hydrogen tetra-chloroaurate(III) (Sigma Aldrich, Germany) in a molecular ratio of 0.4. After cleaning of the substrates in an acetone ultrasonic bath for 15 min and drying, the reference sample was prepared by spin-coated of 20 μL of the gold-loaded BCM solution on the poly-silicon substrate at 7000 rpm (WS-650Mz-23NPP, Laurell, USA). Afterwards, inkjet printing was run with the same BCM solution. Finally, the dried substrates were plasma treated by a mixture of hydrogen and argon gas (10 % hydrogen, 90 % argon) in a plasma etcher (TePla 100 plasma system, PVA, Germany) at 0.4 mbar and 300 W for 1 h to remove the micellar ligands.

Inkjet printing   Ink-jet printing was carried out kindly supported and supervised by MSc Marjan Goudari in the working group of Prof. Dr. Al-Shamery at the Institute for Physical Chemistry (Carl-von-Ossetzky University of Oldenburg) at their ink-jet printer setup in their laboratories. Micropatterns of the BCM solution were created by means of a commercial piezoelectric, laboratory scale inkjet printer (Dimatix$^®$ Materials Printer DMP-2850). Eight piezo-electric driven orifices were embedded in a row with the removable printer head (DMC-11600), which all had a channel-type connection to the refillable cartridge ink storage unit. The entire cartridge was composed of epoxy, polypropylene, silicone and silicon dioxide based components and hence, chemically resistant. By means of a glass-based syring, a volume of 4 mL BCM solution was transferred into the polypropylene bag of the cartridge storage unit. Then, the cartridge was installed in the printer head and a first cleaning cycle was run before the first print to ensure optimum printing results. Here, the jetting part of the cartridge was brought into contact for a few seconds with a cleaning pad for blotting, purging and jetting, which was repeated after each printing process. The substrates were positioned on the in-plane moveable sample plate, which included equally distanced, small holes to create local vacuum for optimum sample fixation throughout the printing procedure. BCM droplets were then

generated by automatically apply electric impulses to the jetting module of the printer head. The nozzle voltage and opening frequency was then iteratively tuned until

optimum sized droplets at regular dropping rates and maximum homogenous micro-patterns were achieved. Regarding the different substrates, nozzle voltages between 16 to 20 V and frequencies between 6 to 12 kHZ were applied The droplet size was set to a minimum of 10 μm within the printer software. Then, automated micro-patterns of 4 x 4 BCM droplets were printed on:

1. a poly-silicon wafer, 2. amorphous silicon thin films of 200 nm and 400 nm thickness deposited on glass wafers kindly prepared by Fraunhofer ISIT, Itzehoe, 3. 200 nm thin nickel-titanium films sputtered on 4 μm thick copper layer and a glass substrate, 4. as well as a 50 μm thick free-standing NiTi foil, both kindly fabricated by Acquandas®, Kiel.

After drying of the droplets, all substrates were plasma treated as described above.

6.3.2 Characterization

Scanning electron microscopy (SEM) and image analysis   To characterize the quality of the printing results, SEM (Supra 55VP, Zeiss®, Germany) images were recorded via an in-lens detector at a gun voltage of 5 kV and at a working distance of 5 mm. All SEM images were further processed by means of ImageJ. Here, the nanodots were highlighted in each image and then automatically set as maxima. Afterwards, each image was transferred to a binary image to analyze the coordinates of all nanoparticles by means of the particle analyzer implemented in ImageJ. Finally, the inter-particle distances of the nanodots was auotomatically determined for all images via an open-source nearest-neighbor distance (NND) algorithm written by Mao.[493]

Atomic force microscopy (AFM) imaging and image processing   Atomic force microscopy (AFM) surface scanning was applied to determine the average roughness of the different sample surfaces. Here, a commercial JPK NanoWizard® 3 (JPK Instruments AG) AFM head in combination with an inverse microscope was used in oscillating mode using ACTA cantilevers ($k_z = 40$ N/m, resonance frequency = 300 kHz; Applied NanoStructuresInc.). Afterwards, the images were all processed via the JPK SPM Data Processing software and hence, the average roughness was automatically determined within the scanning area.

6.4 Results and Discussion

The o-xylene based BCM solution was first spin-coated on a cleaned 10 x 10 mm poly-silicon wafer to validate the quality of the solution as well as the range of expectable inter-particle distances and define a reference sample for further comparison.

According to pertinent publications, [460] [446] [19] [461] [39] [103] a regular pattern of 5 nm sized gold particles defining slightly distorted hexagonal structures was created as shown in figure 6.1 **A**. The mean inter-particle distance of the nano-particles within these quasi hexagonal patterns were determined to 32.6 ± 3.2 nm based on the analysis of about thirty SEM images.
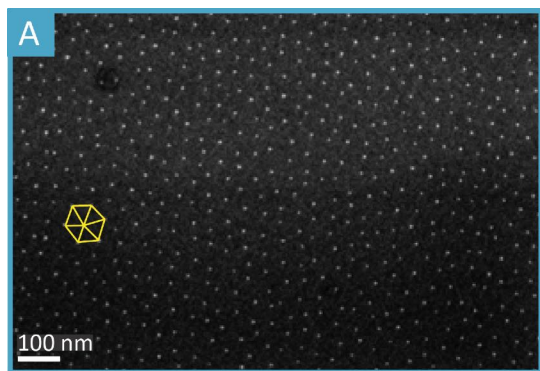
Figure 6.1: Scanning electron microscopic image of an inset of a nano-patterned poly-silicon wafer surface. Quasi hexagonal patterns of gold-nanodots (see imprinted yellow hexagon) with a mean inter-particle distance of about 33 nm have been created by spin-coating and subsequent plasma etching. (modified from H. Neumann et al., Beilstein J. Nanotechnol., 2018, 9, 2372-2380.)

To micro-pattern the four different substrates via printing, a volume of 4 mL of this BCM solution was then transferred to the cartridge storage unit of the Fuji Dimatix ink-jet printer head as schematically presented in figure 6.2 **A**. By iterative optimization of the voltage and opening time of one nozzle of the cartridge head, homogenous droplets of about 10 pL of BCM were applied to the different sample surfaces. Optimum sample positioning was ensured by a movable translational sample plate. Patterns of 4 x 4 droplets were created by automatic movement of the printer head in accordance to the software template designed before the experiment. The droplet size was set to a minimum of 10 μm and the droplet-to-droplet distance to 200 μm. Regular micropatterns were obtained as shown in the upper SEM image of figure 6.2 **B**. Each droplet contained the diluted micelles, which formed self-assembled monolayers on the substrate surfaces. After plasma treatment to etch the organic micellar ligands, patterns of gold-nanodots remained. In the bottom right image in figure 6.2 **B**, the resulting quasi

hexagonal nanopattern on smooth poly-silicon is shown. To evaluate the homogenity of the droplet size on the different substrate material surfaces, the droplet diameter for up to 50 droplets pe material was determined. In figure 6.3, SEM images of representative droplets printed on: **A** poly silicon (poly-Si), **B** amorphous silicon of 400 nm
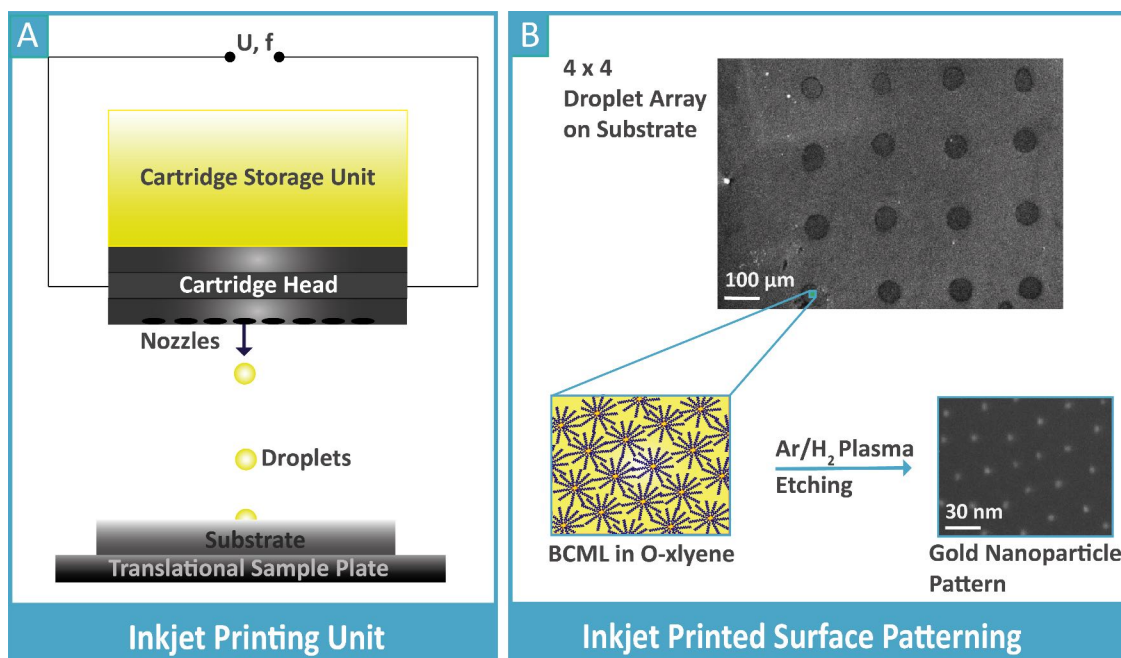
Figure 6.2: Schematic presentation of the Fuji Dimatix DMP-2800 ink-jet printer: (**A**) 4 mL of the o-xylene based BCM solution was filled in the cartridge storage unit and applied to the different substrates through piezo-driven nozzles installed in the cartridge head. By variation of the nozzle voltage and opening times, the droplet size was controlled. Regarding possible in-plane misalignment of the samples, the exact positioning of the sample with regard to the nozzles could be controlled via the translational sample plate. By in-plane movement of the head, user-defined 4 x 4 patterns of single droplets were created as shown in **B**. Here, the micelles formed quasi hexagonal micelle arrangements as depicted in the drawn inset, which were then plasma treated. By this, the organic ligand spacers were etched and the gold-nanodot pattern remained. (modified from H. Neumann et al., Beilstein J. Nanotechnol., 2018, 9, 2372-2380.)

thickness sputtered on a 400 μm thick glass wafer (a-Si 400), **C** amorphous silicon of 200 nm thickness sputtered on a 400 μm thick glass wafer (a-Si 200) **D** a free-standing nickel-titanium foil of 50 μm thickness and **E** a nickel-titanium (NiTi) thin film layer of 200 nm thickness sputtered on a 4 μm copper buffer layer deposited on a 400 μm thick glass wafer are presented. All of the droplets
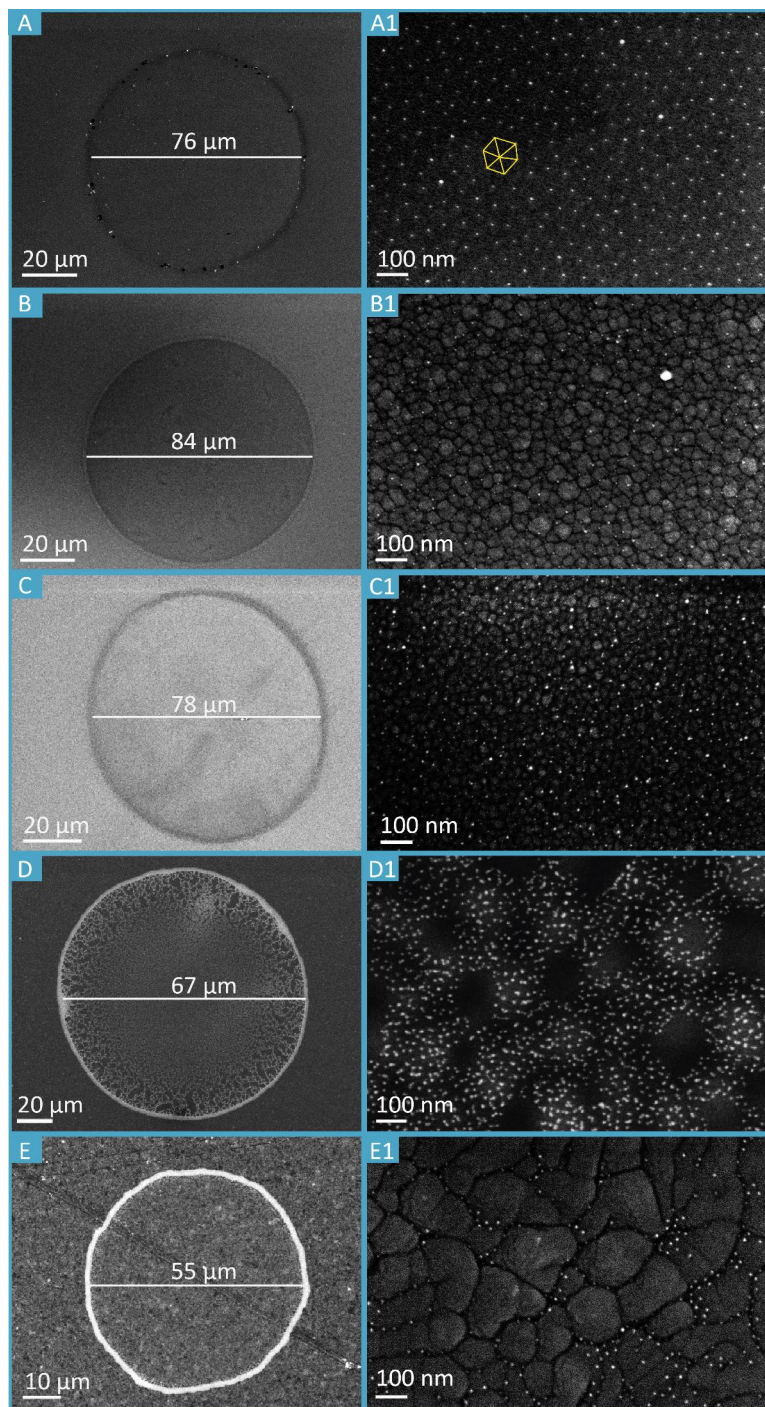
Figure 6.3: Scanning electron microscopic images of a single representative BCM droplet on each of the different device materials surfaces (**A** to **E**) and the corresponding nano-dot distributions in the droplet centre for each material (**A1** to **E1**) after plasma treatment. The substrates are: **A** poly-crystalline silicon (poly-Si) **B** amorphous silicon of 400 nm thickness sputtered on a 400 μm thick glass wafer (a-Si 400) **C** amorphous silicon of 200 nm thickness sputtered on a 400 μm thick glass wafer (a-Si 200) **D** a free-standing nickel-titanium foil of 50 μm thickness, **E** a nickel-titanium (NiTi) thin film layer of 200 nm thickness sputtered on a 4 μm copper buffer layer deposited on a 400 μm thick glass wafer.(modified from H. Neumann et al., Beilstein J. Nanotechnol., 2018, 9, 2372-2380.)

possess a more or less intense outer hem, which is a well-known phenomenon within ink-jet printing of nanoparticle solutions named coffee ring effect, which was first explained in 1997 by Deegan et al.[494][495] Here, the evaporation process within the droplet causes an internal flow, which radially develops in the droplet center toward the outer contact line. Due to this convective flow, the micellar particles are transported to the outer contact line and begin to agglomerate, which finally ends in the formation of a ring.[496][497] The characteristics of the ring such as the ring thickness depend on the outward flow, which can be manipulated by the evaporation rate of the solvent on the respective material surface as well as on the spreading behavior of the solvent on this substrate.[472] Within the printing of microelectronics, this phenomenon is tried to be excluded to ensure homogenous printing results. For this, two parameters can be used. First, the pinning of the contact line must be eliminated, which is e.g. realized by electrowetting via the insertion of an additional electrode during the printing process.[498][499] Second, the evaporation at the outer contact line needs to be reduced. For this, the evaporation in the centre of the droplet needs to be increased, which is e.g. possible in a closed environment, in which there is a hole directly above the droplet apex that shifts the evaporation rate of the droplet centre towards the contact line.[472] Moreover, a gradient along the interface between the droplet surface and the vapor can be used to equalize the inner and outer convective flow, which is possible by adding surfactants.[500][501] Finally, the convective flow can be overcome by minimum times of evaporation, which is possible for droplets of diameters $< 10 \ \mu$m as proved by Shen et al in 2010.[502]

Due to the sensitivity of the micelles especially with regard to concentration changes within the solution, manipulation like adding of surfactants and electrowetting could not be applied. The two other approaches based on convective flow equalization via evaporation shifting through a hole above the droplet centre or minimum droplet size could not be realized by means of the commercial setting used in this project. This could be can be implemented in future studies. Moreover, the use of other gold-nanoparticle based inks as suggested by Wu et al.,[486] Cui et al.,[478] Määtänen et al.,[492] Anto et al.,[503] Jensen et al.,[481], Hu et al.[483] or Chung et al.[504] are useful for multilayer gold depositions in order to generate homogenously covering micro-structures, but do not support the assembly of gold nanodots with distinct interparticle distances within monolayers, for which reason the used ink is the only possible solution to micro-and nanopattern the substrate surfaces at once.

Within this project, the droplet diameter and the coffee ring properties on silicon based substrates vary from those on NiTi based sample surfaces. Hence, the droplet diameter on poly-Si and both a-Si samples ranges between 76 μm for poly-Si and 84 μm for a-Si 400 showing a slight outer contact line. The droplets on the NiTi foil and a 200 nm thin film are 10 μm - regarding the NiTi foil - to 20 μm -
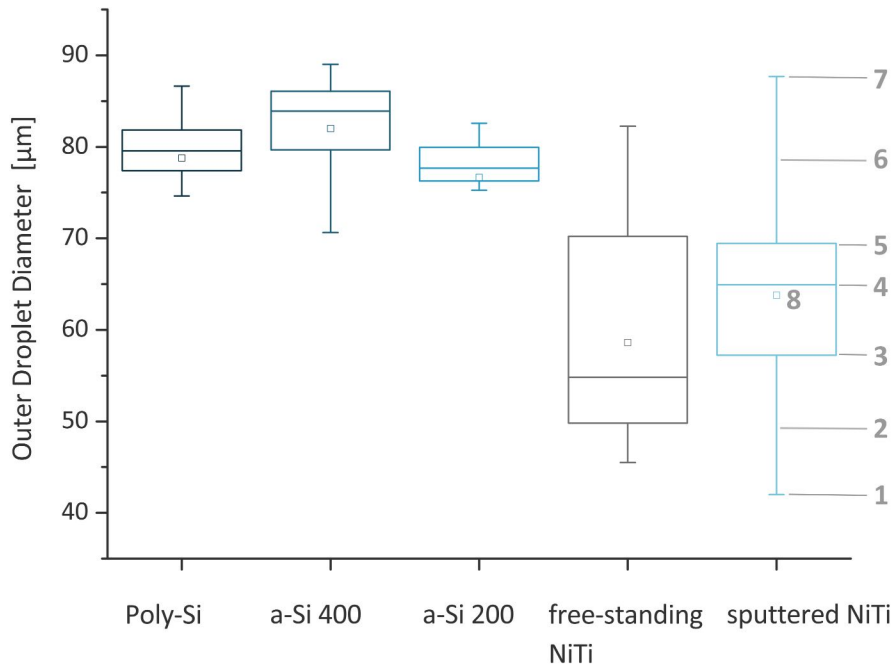
Figure 6.4: Distribution of the outer droplet diameter for each device material shown as boxplot based on about 50 droplets per substrate. For better understanding of the structure of a box plot, the different components are marked for the distribution of the 200 nm thin film of NiTi sputtered on copper: **1** lower extreme, **2** lower whisker, **3** lower quantile, **4** median, **5** upper quartile, **6** upper whisker, **7** upper extreme, **8** mean value.
The average droplet diameters on poly-Si, a-Si 200 and a-Si 400 are comparable and range at about 80 μm. In difference, the NiTi based samples allow for droplet diameters around 60 μm, but possess a very broad distribution between 45 and 88 μm of droplet diameter. (modified from H. Neumann et al., Beilstein J. Nanotechnol., 2018, 9, 2372-2380.)

with respect to the NiTi thin film - smaller than those on the silicon based surfaces and additionally, possess a prominent coffee ring. When analyzing the outer droplet diameters statistically over up to 50 droplet measurements per material, this difference is even more distinct as can be seen in figure

6.4. Here, the size distribution is summarized by means of boxplots for each sample material. For better understanding, the structure of one plot is exemplarily marked for the boxplot of the 200 nm thin NiTi film. **1** and **7** indicate the lower (**1**) and upper (**7**) extreme, which mark droplet diameter values, which are by $1.5 \cdot$ IQR lower (**1**) or higher than the diameter value at the lower (**3**) that is to say the upper (**5**) quartile. In symmetric distributions like Gaussian distributions this corresponds to 0.35 % of the data. The quartiles describe the droplet diameter at which 25 % (**3**) that is to say 75 % (**5**) of all datasets are included. Hence, the lower quartile depicts the middle diameter between the smallest diameter and the median of the dataset, while the upper quartile corresponds to the average diameter value between the highest and the median value. The range between **3** and **5** is called interquartile range (IQR) or box, which consequently summarizes 50 % of all measurements. Within the box, the median (**4**) represents the middle value of the considered datasets, while **8** corresponds to the average value over all diameters. The connecting lines **2** and **6** are so-called whiskers, in which range 24.65 % of all data with diameteres lower (**2**) than for the lower quartile or rather bigger (**6**) than the upper quartile are included. The size of the box or more specifically the entire boxplot contains the information about the width of the diameter distribution for each material. Hence, the IQR of the outer droplet diameter for poly-Si, a-Si 400 and a-Si 200 are comparably tight, for which reason 50 % of the considered datasets range between 77 and 81 μm for poly-Si, 80 and 86 μm for a-Si 400 and 76 to 80 μm for a-Si 200. In consequence, the mean droplet diameter for silicon based substrates here varies between 78 μm for a-Si 200 and 84 μm for a-Si 400. With regard to datasets with diameters above or below these values, a-Si 400 has a prominent lower whisker with a lower extremum at 71 μm, in which range the diameter distribution of poly-Si and a-Si 200 are covered. In result, the droplet sizes of these three sample materials are in the same region and relatively homogenous. In contrast, the droplet diameter distribution on NiTi based substrate surfaces show a very broad and asymmetric distribution. By this, 50 % of the measured data range between 50 and 70 μm on 50 μm thick NiTi foils and 57 to 69 μm on NiTi thin film. The median values are here 54 μm on the foil and 65 μm on the 200 nm NiTi thin layer. With regard to the whiskers, the NiTi foil substrate data are skewed to the right in direction of the diameter data of the thin film sample, while this sample possess a symmetric distribution in this range. Overall, 99 % of the measurements result in droplet diameters between 46 and 82 μm for the NiTi foil, and even broader between 42

and 88 μm on the NiTi thin film, which results in a size variation of about 40 μm under the same conditions as for the fabrication of the a-Si samples with a maximum diameter range between 71 and 89 μm. Obviously, additional effects besides the evaporation time and wetting behavior of the surfaces influence the droplet shape on the NiTi substrates.

This observation regarding e.g. evaporation time, surface and wetting behaviour, can also be transferred to the nanometer scale as shown in figure 6.4 **A1** to **E1**. Here, insets to the SEM images of the corresponding droplet centre of each substrate shown in **A** to **E** present the resulting nanodot pattern. For more precise insights in the quality and homogenity of these patterns, boxplots were additionally compiled for each substrate to summarize the inter-particle distance distribution based on the analysis of up to 35 images per substrate material with an overall amount of 60,000 scored particles. The analysis was run via an open source nearest neighbor distance (NND) algorithm written by Mao.[493]

On poly-Si, an almost regular pattern of quasi hexagonal arranged gold nano-particles is observable, which is in good agreement with the pattern of the reference sample shown in figure 6.1. However, the distribution of inter-particle distances is broad compared to the spin-coated reference sample. Hence, 99 % of the NND data for spin-coated poly-Si range between 27 to 36 nm at an average NND of 33 nm $\pm$ 3 nm. The distribution is slightly left skewed to higher inter-particle distances., but in general comparably tight. For ink-jet printed BCM coating on poly-Si, 99 % of the NND data are distributed between 26 to 57 nm and 50 % within the range of 28 to 44 nm, while the average NND is 38 $\pm$ 11 nm. In comparison, the majority of the data are slightly shifted by about 5 nm to bigger inter-particle distances compared to spin coating results. In contrast to the controllable rotation speed during the spin coating process, the NND of ink-jet nano-coating is only controlled via the convective flow within the droplet during evaporation. This phenomenon hence causes the comparably broad NND distribution.

With an average NND of 37 $\pm$ 4 nm for a-Si 400 and 42 $\pm$ 6 nm for a-Si 200, the inter-particle distances on amorphous silicon are in the same region like these on poly-crystalline silicon. However, the distributions are notably tighter by over 10 nm than for poly-Si, for which reason 99 % of the NND measurements range between 29 and 45 nm for a-Si 400 and 31 to 52 nm for a-Si 200. Although these distributions are leaner than for poly-Si, the SEM image insets **B1** and **C1** in figure 6.3 reveal

a gold nanodot distribution that does not contain any kind of regular pattern like on poly.-Si. This is even more obvious, when analyzing the nanodot arrangement on the NiTi based substrates shown in figure 6.3 **D1** and **E1**. The gold particles create small islands of grouped or even agglomerated nanodots on the NiTi foil surface (**D1**), wherefore very small inter-particle distances can be found
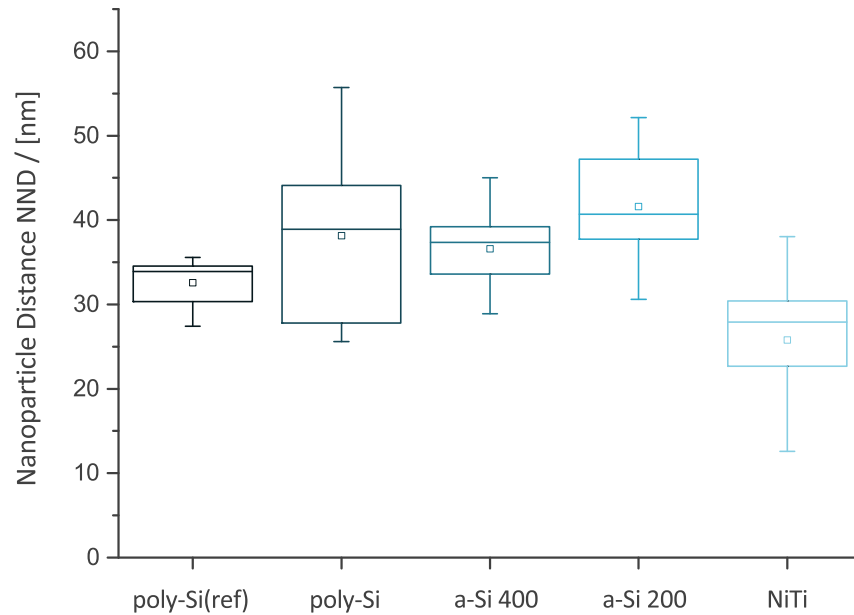
Figure 6.5: Boxplot chart of the the average inter-particle distances for each device material. The inter-particle spacing was determined via the open-source nearest-neighbor distance (NND) algorithm written by Mao. Here, a poly-silicon substrate spin-coated with the same BCM solution was set as the reference sample poly-Si(ref), which presents the tightest NND distribution compared to the samples functionalized via ink-jet printing. In total, up to 35 images per substrate and the inter-particle distance over 60 000 nanodots were analyzed for the determination of each box. (modified from H. Neumann et al., Beilstein J. Nanotechnol., 2018, 9, 2372-2380.)

within the islands, while there are also areas without any gold nanodots. On the 200 nm thin NiTi layer (**E1**), this appears to be more dominant as the gold nano-dots assemble very lean along the trenches within the substrate surface. For NiTi foils, a meaningful distribution of NND could not be determined as the inter-particle distances were partly not measurable due to local agglomerations.

Regarding, the NND boxplot for gold nanoparticles on the NiTi thin film (see figure 6.5, bright blue boxplot on the right), a broad distribution, which is slightly left skewed to higher NND values is observable. Here, 99 % of all measurements along the trench lines vary over 25 nm between 13 to 38 nm inter-particle distances. These observations again confirm the results already stated for the micro-droplet size distribution, in which not only the evaporation process seem to be responsible for the size and inter-particle distance distributions, but also the substrate surface topography. Therefore, atomic force microscopic surface scans were run, which are presented in figure 6.6. Here, 10 x 10 μm sized topographies of the five different substrates namely: **A** poly-Si, **B** a-Si 400, **C** a-Si 200, **D** 50 μm thick NiTi foil and **E** a 200 nm thin NitTi layer deposited on a 4 μm copper buffer layer and a glass wafer are shown. For better overview, magnified records depicting 1 x 1 μm of each substrate surface are presented within the corresponding inset boxes. According to each color scale bar, dark red regions correspond to flat areas, while yellow to white regions illustrate elevations. Based on the AFM topography scans, the average surface roughnesses were then determined automatically via the processing software. As supposed, poly-Si possesses a very smooth surface of 48 pm roughness, while the amorphous silicon surfaces are 0.85 nm for a-Si 400 and 1.23 nm for a-Si 200. These values range in comparable roughness regions, which is in accordance to the similarities within the mean values for the droplet diameter and inter-particle distances of these three silicon based surfaces. In contrast, the NiTi foil shows an average roughness of 2.35 nm, which is twice that of a-Si 200 and additionally, boasts surface waviness as can be seen in the inset box of figure **D**. These topographic particularities are caused during the fabrication process.

The NiTi thin film has the highest roughness with about 8 nm, consisting of islands of NiTi separated by trenches. These materials textures are created by thermal cracks of the copper buffer layer during the fabrication procedure. In accordance with the broad distributions of the outer droplet diamater and the NND, on the one hand, and the smaller mean values compared to the a-Si samples, on the other hand, the droplet diameter and the NND seem to be the smaller the rougher the substrate surface. This was also found by Chen et al. investigating the evaporation behavior of droplets on superhydrophic surfaces of different roughness. [505] The spreading of the droplet seems to be limited by energetical effects, which were presented by Kadem et al., in which the micelles particularly preferred to concentrate in lower surface regions. [506]
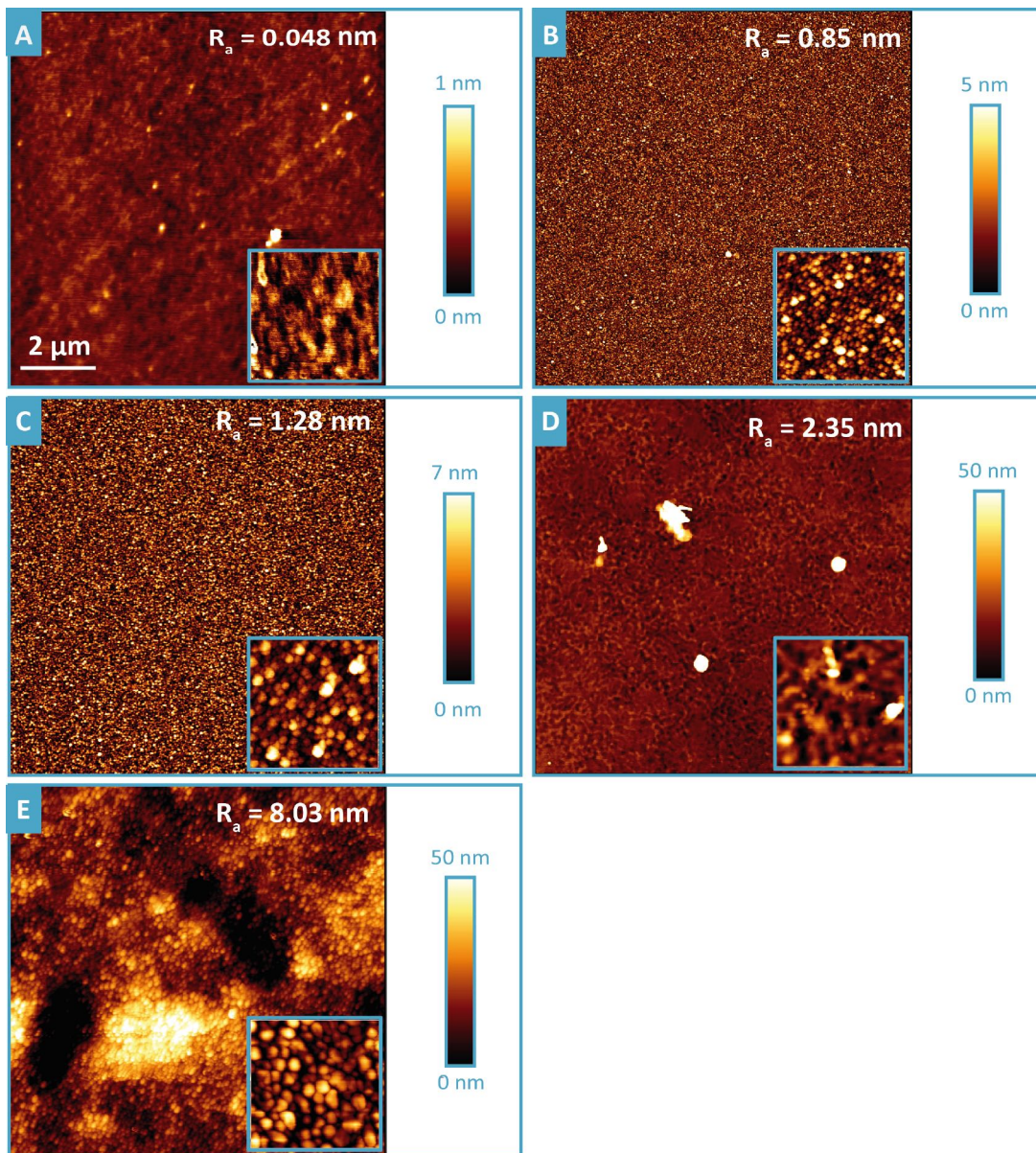
Figure 6.6: Atomic force microscopic scans to determine the topographic quality and roughness of the different sample surfaces, which were: **A** poly silicon (poly-Si) **B** amorphous silicon of 400 nm thickness sputtered on a 400 μm thick glass wafer (a-Si 400) **C** amorphous silicon of 200 nm thickness sputtered on a 400 μm thick glass wafer (a-Si 200) **D** a free-standing nickel-titanium foil of 50 μm thickness, **E** a nickel-titanium (NiTi) thin film layer of 200 nm thickness sputtered on a 4 μm copper buffer layer deposited on a 400 μm thick glass wafer. The inset boxes show enlarged areas of a 1 x 1 μm sample surface area. The average roughnesses R_a was automatically determined by the JPK processing software for the depicted surface area. Here, poly-Si is the smoothest sample, while the sputtered NiTi on Cu possesses the roughest sample surface. The bright spots on the surface of the free-standing NiTi foil correspond to dirt due to the long-term storage before imaging and were not included on the roughness determination. (modified from H. Neumann et al., Beilstein J. Nanotechnol., 2018, 9, 2372-2380.)[157]

6.5 Conclusion and Outlook

In the course of this subproject, ink-jet printing has been successfully combined for the first time with BCML to micro- and nanopattern different substrate surfaces simultaneously within about 16 s per 4 x 4 droplet matrix. By this, quasi hexagonal patterns with gold inter-particle distances of about 38 nm can be achieved on very smooth surfaces with lower picometer surface roughness in high-throughput and without additional sample preparations, which are in good agreement with patterns fabricated via the established spin-coating process. Hence, a simple and fast method has been tested, which can be used for the locally selective surface nanopatterning via automated printing processes and additionally opens the possibility of user-defined contact-less surface micro-patternings of any programmable shape.
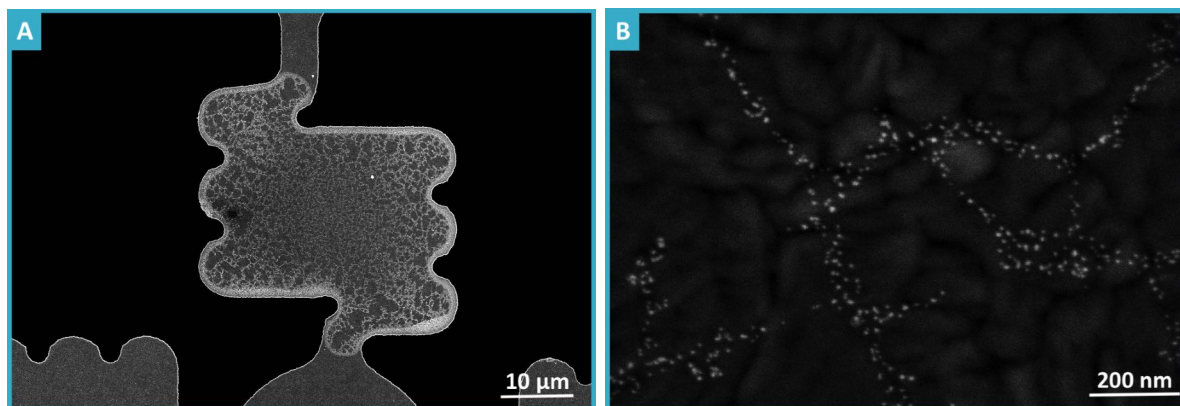
Figure 6.7: **A** SEM images of a surface treated spring arm of a 4-FE NiTi sensor element after ink-jet printing of the BCM solution and plasma etching. On the edges, a continuous hem of agglomerated gold is created, while groups of gold nanodots are formed within the functionalized area. As already shown in figure 6.3 **D1**, the particles tend to arrange in dependence of the surface topography and roughness. Hence, paths of gold nanodots are observable when imaging the surface at higher magnification as presented in figure **B**.

In general, the droplet size and inter-particle distance depends on the evaporation rate of the droplet and the surface roughness, for which reason the rougher the surface, the smaller the droplet diameter and the NND along the material texture structures. For future applications, this non-contact printing method shall be used for the locally defined surface treatment of the sensitive free-standing sensor element centre plates. Here, the gold nano-dots will be used to control the

cell adhesion sites via additional biological functionalization by RGD-thiol-based linkers bond to the nanodots as described in section 6.1.

The result of the first trials is presented in figure 6.7 for an untreated 200 nm thin NiTi 4-FE sensor element. Here, a BCM droplet was exemplarily printed on one sensor element arm spring. As can be seen, the droplet spreaded properly along the structure and a well-defined coffee ring was generated along the edges of the spring arm. Within the droplet area, single gold nanodots as well as their agglomerations are observable. Within the magnified SEM image in figure 6.7 **B**, nano-particle paths along the trenches within the material surfaces are visible, according to the observations described above. Here, the NND again is in the region of 30 nm, which is a suitable inter-particle distance for proper cell adhesion. Here, a next step would be the locally targeted coating of smoother free-standing sensor element centre plates like those made of a-Si.

7 Conclusion and Outlook

In the course of this project, the prototyping of a novel 3D mechano-optical microsensor system to measure traction forces in the pN to nN region in three dimensions at once was successfully designed, fabricated, planned, characterized and tested from scratch.

First, a suitable design for a surface-integrated microsensor element was determined by means of topology optimization and FEA fulfilling a list of defined requirements (see chapter 2). Here, the element design 4-FR showed the most promising overall results regarding: comparable sensitivities in-plane and out-of-plane, stability regarding uncentered force impact, producibility and compact design as well as minimum producible sensor element dimensions.

The sensor element arrays where then fabricated using suitable materials, which have low Young's moduli, are fully biocompatible and can be fabricated by well-established micromachining processes. In consequence, NiTi, a-Si and PDMS were chosen, characterized and tested regarding their bio-compatibility where needed (see chapter 3). NiTi foils of 50 μm and structures of 200 nm thickness were prepared via photolithography and wet etching and offered good mechanical and biocompatible properties. However, they were limited regarding their producible minimum element edge length of 170 μm at a feature size of 2 μm and are sensitive to outer impacts.

Hence, a-Si elements were fabricated via dry etching on glass substrates. Minimum feature sizes of 1 μm were achieved with sensor element diameters of down to 45 μm. The elements showed adequate mechanical deformation properties, an easy handling and stability against outer impacts as well as biocompatibility. By a size reduction of the sensor arrays of 70 % compared to NiTi arrays, these sensor elements meet the central aspects defined within the sensor requirements list (see section 2.2.2.) best and are therefore the most promising for regular future application in 3D cell traction force measurements.

According to the International Roadmap of Systems and Devices (IRDS) forecasting the improvements in CMOS and electronics miniaturization, the producible device feature sizes shall be significantly reduced within the next 10 years.[507] This might allow for the further reduction of the overall sensor element array size in future applications.

Moreover, a process has successfully been developed to produce thin membrane based gold coated PDMS sensor arrays to reduce overall product costs, on the one hand. On the other hand, the material opens the possibility of tuneable spring constants by variable material elasticities controlled via the cross-linking within the polymer. Hereby, the PDMS elements can be adapted to various application requirements and broaden the field of sensor element force sensing applications. In this project, first well-defined structures were achieved by ICP-RIE, in which an edge length of 1 mm was reproducibly fabricated.

To ensure a high accuracy of the sensor elements regarding low force sensing, calibration methods had to be conceptualized to determine the lateral and axial spring constants for each sensor element considering the element size, the accuracy of established calibration techniques and the complexity of the handling (see chapter 4). Here, the cantilever to cantilever method has been chosen for out-of-plane calibrations due to its easy handling, simple implementation in the AFM setting and suitability to the geometrical dimensions of the sensor elements and arrays. Regarding the favoured a-Si sensor element design 4-FR and NiTi 4-FE type, the results were in good agreement with the theoretical determined values via linear elastic FEA. Hence, the smallest 4-FR element with a diameter of 45 μm has an out-of-plane spring constant of 0.012$\pm$0.001 N/m and the four times bigger NiTi 4-FE element with an edge length of 170 μm has a lower constant of 0.004$\pm$0.0004 N/m. In this thesis, the diamagnetic lateral force calibrator (D-LFC) method developed by Li et al. has succesfully been used for the first time to calibrate MEMS sensor structures (cooperation work with the working group of Prof.Dr. Hugel/ University of Freiburg). With an accuracy of about 1 %, a high precision of the calibration procedure for the reference cantilever can be ensured. The spring constants were again in very good agreement with the simulated data. Here, the lateral spring constant of the 4-FR a-Si element could be determined to 4.66$\pm$0.022 N/m and of the 4-FE NiTi element to 0.087$\pm$0.008 N/m.

Based on the developed sensor elements and their properties, a combination of digital holography

and digital image correlation has been applied for the first time in first measurements to record in- (DIC) and out-of-plane (DHM) displacements as small as 200 nm for traction force sensing within the sub-project for the development of a suitable optical readout system (see chapter 5). Using the before fabricated NiTi 4-FE sensor element, traction forces as low as 800 pN up to 20 nN ($\pm$ 10 %) out-of-plane and between 17 nN ($\pm$ 40 %) and 0.8 μN ($\pm$ 2 %) in-plane can be resolved via this simple, cost-efficient, easy manageable, and comprehensively modifiable setup. In consequence, the target force range of this sensor system has successfully been reached for future adhesion force sensing via this combined DHM/DIC detection method.

To ensure the control of cell adhesion binding sites on the sensor element for future applications, a method has been conceptualized to functionalize the sensitive sensor element centre plates in the course of the sub-project. Here, simultaneous micro- and nanopatterning of different substrate surfaces by combining ink-jet printing with the established gold-nanodot patterning method of BCML has been succesfully tested, for the first time (see chapter 6). By means of the highly accurate technology of ink-jet printing, user-defined micropatterns of 4 x 4 droplets with a dried droplet diameter of about 80 μm for silicon based and about 60 μm for NiTi based surfaces will allow for variable micro-shapes in future applications. On smooth surfaces, quasi hexagonal patterns of gold nano-particles with inter-particle distances of about 30 nm are printable within one second and are in very good qualitative agreement with nanopatternings created via the established spin-coating method. By this, a contact-less, easy, fast, high-throughput, cost-efficient and reproducible technique is available, which can be used to print variable and user-defined micropatterns that are nanopatterned at the same time.

Based on the conceptualization, design, fabrication and setting up of this novel 3D adhesion force microsensor system and the proof of its principle by first measurement results in the course of this project work, the entire sensor setting can now be optimized within ongoing projects for future routine measurements as a commercial add-on application.

In the following, the different future optimization steps for a preparation of the setup to its final market maturity are described that define six different work packages:

1. Timing of DHM and DIC and compact setup design

The technical improvement of the DHM and DIC coupling by introduction of a chopper within the reference beam path triggering a fast camera and finding the correct timing between the components (see figure 7.1 A). By this, the sensor displacement in lateral and axial direction shall be recorded with a slight time shift nearly simultaneously and at a chopper rotation high frequency. In consequence, more information about the deformation during the cell rupture procedure can be monitored. Additionally, the resolution could be improved by testing other laser sources of shorter wavelengths and an adequate choice of corresponding optical components. Furthermore, the entire setting will be reduced in size for a more compact, less vibration sensitive design. Here, optical components of minimum possible dimensions will be chosen.

2. Opimization of the digital data processing

In DHM and DIC well established algorithms were used for the data processing. The results of this processes depend on the suitability of the algorithms concerning the stated physical problem. As there is a fast development regarding new, more powerful algorithms, first, a general analysis of the most sufficient algorithm type should be run, followed by the testing of different new algorithms to finally adapt these algorithms to the setting or the development self-written algorithms to create maximum data precision and high resolutions. Moreover, a program needs to be developed to automate the image data processing and direct presentation of the correlated 3D forces. By this, the analysis and process time is reduced and the simplicity of the data handling for the end user is increased.

3. Multisensor element readout

Within this project, the 3D displacement optical readout was realized for one sensor element. For simultaneous force distribution measurements, the developed technique needs to be transferred to an entire sensor element array. Here, microlens arrays that are used in laser collimators and are already of central interest in modern 3D imaging systems, [508] could replace the single objective lens. By this, each sensor element of the array has a corresponding microlens. Here, a suitable compact readout solution for multiple DHM and DIC processes would be the bottleneck of this project.

4. PDMS sensor miniaturization

To miniaturize the PDMS structures for future applications and by this, increase the force resolution of this sensor system for future force distribution measurements, the membrane should be first optimized regarding its thickness for optimum handling and mechanical properties such as stability against outer impacts or deformability. As Moreover, the sensor element structure could be reduced from the presented meander based designs with a centre plate to simple gold or silicon circular plates printed or sputtered in arrays on the bottom side of the PDMS membrane. To control the adhesion sites, gold nanodots could be printed on the top side by inkjet printing, in case of high densities of cell binding sites on PDMS or by FEBID, if even just a few nanodots should be positioned on PDMS. Hence, the force induced displacement of the gold circles could be recorded via the optical readout in case of a force impact. Furthermore, this solution offers not only a comparably cheap material and fabrication process, but also the tuning of the membrane elasticity, which was already shown by Palchenko et al.[258] In consequence, the measurable force range could be enhanced and adapted to particular scientific matters apart from cell testing.

To design these PDMS based membranes more precisely, FEA simulations would be needed. For that reason, accurate material parameters are indispensable including precise stress-strain-data and load-displacement curves for different PDMS Young's moduli that are currently not available in literature. Hence, first discussions were already lead concerning suitable uniaxial and biaxial testing settings with experts in the field of mechanical engineering. This sub-project would contribute to a more comprehensive insight into the mechanical properties of stiffness tunable PDMS.

5. DHM/DIC microsensor system for testing in liquids

The DHM/DIC microsensor system needs to be optimized for measurements in solution. Here, the optical components might need to be adopted to different parameters like a different refractive index of the medium. Next, more cell force measurements of well-known cell types like REF52 fibroblast cells need to be run to verify the reproducability of the measurements. Here, calibration routines might be defined and afterwards, the application can be extended to characterize biomimetic material and biomaterial for the validation of their adhesion behavior and adhesion forces compared to cells.
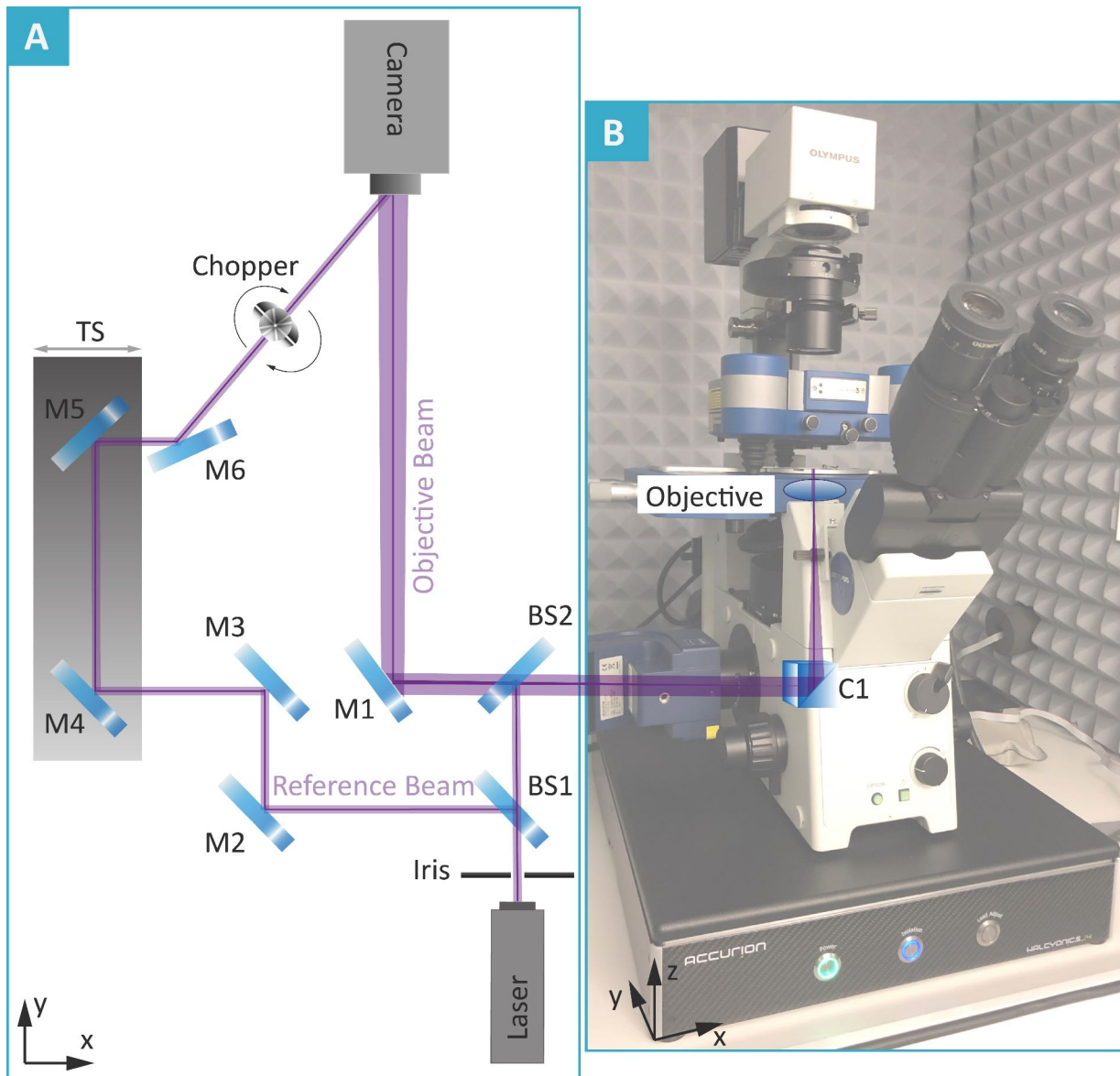
Figure 7.1: Schematic overview on a combination of an off-axis DHM (**A**) as described in chapter 5 with an commercial AFM in use of an inverted Olympus microscope IX81 (**B**): **BS1** and **BS2** Beam splitter, **M1**-**M6** Dichroic mirrors, **C1** optical cubic. The reference and object beams are coupled to the inverted microscope via an additionally installed optical cube to record the displacement of the sensor elements positioned on the sample holder of the microscope. The AFM head is used to record the global forces during the cell rupture process, while the sensor elements allow for the determination of the local force distribution during this cell rupturing.

6. Coupling of the DHM/DIC microsensor system with an AFM

The AFM-DHM/DIC setting presented in figure 7.1. is a new approach, combining AFM spectroscopy with dynamic DHM and DIC to be able to measure global forces (AFM) and 3D local forces (DHM/DIC) in real-time. Here, a 365 nm laser beam is adjusted via an external beamsplitter (BS2) on a microsope inherent UV compatible cube (C1) and focused via an objective on the sensor array. The reflected light again passes the reflective cube C1, then a beam splitter BS2 to finally be recorded on the CCD camera. The reference beam is reflected by the dichroic mirrors M2 to M5 and finally overlapped with the object beam by mirror M6 on the fast CCD camera. To record in-plane deformation by image correlation at once, an optical chopper will be used to trigger the fast camera and block the reference beam for recording of an interference-free image. By means of a set time delay, DHM images and simple laser microscopic images can then be recorded in real-time and afterwards analyzed via a combined software. The cell test is started by adhesion of the cell to the biofunctionalized sensor surface on bottom and the functionalized AFM canilever on top of the cell matrix. To record the force development during the cell rupture process, the cantilever is then retracted as already described in chapter 3 and the corresponding 3D displacement of the sensor elements is recorded on bottom of the sample.

The group of Mohanty et al. developed a comparable setting to image fluorescent polystyrene microspheres, two-photon polymerized microstructures and red blood cells from top and bottom at once.[509] In contrast, they analyzed the samples using a 670 nm laser diode and therefore had a low maximum resolution of 335 nm. The setting was optimized for static fluoresence measurements. So, the AFM was not used in spectroscopy mode, but imaged the top of the samples in scanning mode. Furthermore, a significant time shift between the AFM image scan and the DHM measurements disturbed the measurement, on the one hand. On the other hand, the movement of the AFM cantilever and light reflection of the AFM laser caused pertubations within the DHM fringes.

Commercially available high-resolution DHM settings provided by Lyncée Tec were used by research groups in combination with fluorescence microscopes for 3D imaging of cells.[510] [511] [512] However, the settings are cost-intensive and not simply modifiable by the user for 3D force displacement measurements like home-built DHM/DIC settings.[513] [335] For that reason, my attempt would be different from techniques already known in literature.

Overall, the challenging realization of this 3D adhesion force sensing setting and its proof of principle for forces as low as piconewton in the course of this project now is the initial point for a compact powerful force sensing system. Based on further comprehensive, versatile hardware and software development with final market maturity, it could then be used as add-on application in different imaging settings for biomedical, medical, biological or material development applications.

8 Acknowledgement

In four and a half years of intense research work in a challenging project and in a totally new discipline for me, a lot of different people accompanied me - shall they be supervisors, collegues, family, old or new friends - to whom I would like to dedicate this chapter.

First of all, I would like to express my deepest gratitude to my doctoral supervisor Prof.Dr. Christine Selhuber-Unkel for her support within and next to this thesis project, her trust in my work, the offered working freedom and advice. She gave me the chance to experience a free development in scientific research and gave me back again my believe in scientific work. Here, I also thank the ERC and by this, the European Commission under the European Union's Horizon Seventh Framework Programme for Research and Development according to the grant agreement No 336104 for financial support, which enabled this project as part of the grant CellInspired.

My deepest thanks go to my parents for their unlimited mental support, unconditional love, always listening, their motivation, their passion, and believe in me throughout my life and especially in my PhD time in bright, but also very dark moments. You are the best and I cannot thank you enough for what you gave to me. And dad: I miss you and wish you all my best of wishes for your journey and your long race to find the freedom and peace that you were always looking for.

And to my sister, who supported me in rough times by listening, supporting, taking over and solving difficult and exhausting burdens and struggles for our family especially at the end of my PhD time, that gave me the chance to finish my thesis. To my grandmother Marion Schneider for being an inspiring, positive, reliable and always supportive family member.

Moreover, I would like to thank Prof.Dr.-Ing. Eckhard Quandt, Dr.-Ing Rodrigo Lima de Miranda (Acquandas), Prof.Dr. Bernhard Wagner and Björn Jensen (Fraunhofer ISIT) for fruitful discussions, providing and optimizing the NiTi and a-Si samples in our cooperative work.

like that.

Furthermore, I would like to thank my brothers in mind inside and outside our office times:

- my good old friend Dr. Laith Kadem, "captain nasty", for our great talks, divers discussions about cultures, religion, sports, science, cameras, etc., our awesome Berlin trip, awesome times during our two-years spokesperson period in the graduate school of the SFB677, for introducing me to the world of the production of micellar goldnanodots and for his support in difficult times, so for being a really good friend.

- Dr. Sören Gutekunst, "Dr. G.", who shared not only the same educational background as a chemist, but also his appartement as a roommate and his PostDoc position as an assistant in the appraisal process for the DFG funded graduate school "Materials for Brain" with me. Thanks for creating such a great working atmosphere especially at the beginning of my MaWi PhD time, for our nice talks about cameras, cars, motorcycles, tyres, science and chemistry in special, the great trip in Mannheim with your family as well as in Boston. Let's keep it racin', bro!

- Dr.-Ing. Mohammadreza Taale, "Mr. Myterious", for introducing me to the Persian culture and their diversity, the entertaining road trip to Darmstadt, the nice talks, great parties, the lovely MTT tests and support in not so happy times.

- Steven, "Steve-Oh", the most relaxed dude I might know, with whom I share the love for philosophy, French and a critical view on social developments. Thanks a lot for your reliable, creative support during the big holography data combat and the creation of a solution channel, the creative discussions, critical hints, the awesome food and authentic statements! Vive le savoir vivre, Steve, n'est-ce pas?

Thanks bros, for our photography super sessions, the breaking time table-tennis combats and tennis appointments.

And on the female side of our +30 cycle, I would like to thank Katharina Siemsen, "Kasi", for introducing me to the world of Kiels City setting the milestone for my bodybuilding adventure, the divers, relieving and entertaining chats beyond the scientific world, ensuring my nutrition during the rough times of writing.

I would like to thank the entire Bnano group including the once already mentioned above starting with Manuela Lieb, who was always open for a little, nice, controvers and supportive chat, while keeping the labs in top condition. Christine Arndt, Dr.Thorsten Grabosch, Galina Haidarschin, Dr.-Ing. Julia Jedtberg, Dr. Tina Kerby, Ali Khaheshi, Nils Lukat, Dr. Qian Li, Sandra Sinth, Dr. Tobias Tellkamp, Dr.-Ing. Michael Timmermann, Huu Chanh Trinh, Dr. Saskia Viebig, Dr. Wei Wang and Hannes Westerhaus for the family atmosphere and nice surrounding that meant a significant point in my life and my second family who I will honestly miss in the future.

Moreover, I thank my sports buddies: Jörg, Inga and Torben Gröndahl for giving me the chance to compete one more time within the German Motorsports Championship on their BMW "Beast" and being a real good motorsports family to me; my bodybuilding family for the great bodybuilding fun sessions apart of all PhD stress times and Bernd and Hella Schwartinsky for their longterm support and friendship throughout my 10 years in slalom championships in Schleswig-Holstein, Northern Germany and Germany. You all opened some time of free breath for me during the big project.

Last but not least, great thanks go to my very old and good friends:

- Jürgen Falb for the supportive and entertaining physics and IT inputs not only during Formula Student Austria and the entertaining times "im Schwabenländle",

- Dr. Ina and Claus Gernert for our longterm friendship, your mental support during my writing time of the PhD thesis, our nice trips and long discussions during and after our chemistry study time,

- Dr. Andrea Hahn for our social, political and cultural journeys in harsh and very nice times,

- Johannes Kratzel ("Herr Kratzl"), for the long and cultivated calls with a broad spectrum of nearly every possible topic, the flexibility for short-term decisions like karting in Stuttgart and the awesome time in Formula Student Germany and

- Dr. Katharina Richter ("the little black one") for your friendship, your sometimes critical voice and our philosophical and sociopolitical discourses in the last years since our A-level.

Thanks for the awesome moments that we shared being the best friends one could wish for.

I wish you all the very best. Let's keep us moved and go on trying to change the world to its best. And do not you ever forget: Never give up!

List of Figures

List of Tables

Bibliography

[1] M. Wolfgang, V. Lukic, A. Sander, J. Martin, and D. Küpper, *Gaining robotics advantage, 2017*.
https://www.bcg.com/de-de/publications/2017/strategy-technology-digital-gaining-robotics-advantage.aspx on 2019-06-16.

[2] M. Intelligence, *Robotics market - growth, trends, and forecast (2019 - 2024), 2018*.
https://www.mordorintelligence.com/industry-reports/robotics-market on 2019-06-16.

[3] C. Strathearn and M. Ma, "Biomimetic pupils for augmenting eye emulation in humanoid robots," *Artificial Life and Robotics*, vol. 23, no. 4, pp. 540–546, 2018.

[4] J. O. Winter, M. Gokhale, R. J. Jensen, S. F. Cogan, and J. F. Rizzo III, "Tissue engineering applied to the retinal prosthesis: Neurotrophin-eluting polymeric hydrogel coatings," *Mater Sci Eng C Mater Biol Appl.*, vol. 28, no. 3, pp. 448–453, 2011.

[5] F. Russell, Y. Zhu, W. Hey, R. Vaidyanathan, and P. Ellison, "A biomimicking design for mechanical knee joints A biomimicking design for mechanical knee joints," *Bioinspir. Biomim.*, vol. 13, pp. 1–12, 2018.

[6] L. Ma, J. Barkerb, C. Zhoua, W. Li, J. Zhangc, B. Linc, G. Foltzc, J. KuÌĹblbecke, and P. Honkakoski, "Towards personalized medicine with a three-dimensional micro-scale perfusion-based two-chamber tissue model system," *Biomaterials.*, vol. 33, no. 17, pp. 4353–4361, 2013.

[7] K. Dzobo, N. E. Thomford, D. A. Senthebane, H. Shipanga, A. Rowe, C. Dandara, M. Pillay, K. Shirley, and C. M. Motaung, "Review article advances in regenerative medicine and tissue engineering: Innovation and transformation of medicine," *Stem Cells International*, vol. 2018, pp. 1–25, 2018.

[8] E. Stratakis, "Novel biomaterials for tissue engineering 2018," *Int. J. Mol. Sci.*, vol. 19, no. 3960, pp. 19–22, 2018.

[9] T. Ahsan, "Bioengineered tissues: the science, the technology, and the industry," *Orthod Craniofacial Res*, vol. 8, pp. 134–140, 2005.

[10] A. Aijaz, M. Li, D. Smith, D. Khong, C. LeBlon, O. S. Fenton, R. M. Olabisi, S. Libutti, J. Tischfield, M. V. Maus, R. Deans, R. N. Barcia, D. G. Anderson, J. Ritz, R. Preti, and B. Parekkadan, "Biomanufacturing for clinically advanced cell therapies," *Nature Biomedical Engineering*, vol. 2, no. 6, pp. 362–376, 2018.

[11] A. W. Johnson and B. A. C. Harley, eds., *Mechanobiology of Cell-Cell and Cell-Matrix Interactions*, New York: Springer Science+Business Media, LLC 2011, 2011.

[12] M. L. Rodriguez and P. J. Mcgarry, "Review on cell mechanics: Experimental and modeling approaches," *Applied Mechanics Reviews*, vol. 65, no. 6, pp. 060801–41, 2013.

[13] E. Moeendarbary and A. R. Harris, "Cell mechanics: principles, practices, and prospects," *WIREs Syst Biol Med*, vol. 6, pp. 371–388, 2014.

[14] F. Martino, A. R. Perestrelo, V. Vinarský, S. Pagliari, G. Forte, and L. A. Peyré-Tartaruga, "Cellular mechanotransduction: From tension to function," *Frontiers in Physiology*, vol. 9, pp. 1–21, 2018.

[15] J. Sapp, "The prokaryote-eukaryote dichotomy: meanings and mythology," vol. 69, no. 2, pp. 292–305, 2005.

[16] W. B. Whitman, D. C. Coleman, and W. J. Wiebe, "Perspective prokaryotes: The unseen majority," *Proc. Natl. Acad. Sci. USA*, vol. 95, pp. 6578–6583, 1998.

[17] M. Yamaguchi and C. O. D. Worman, "Deep - sea microorganisms and the origin of the eukaryotic cell," *Jpn. J. Protozool.*, vol. 47, no. 1,2, pp. 29–48, 2014.

[18] B. Alberts, A. Johnson, J. Lewis, M. Raff, K. Roberts, and P. Walter, *Molecular biology of the cell*, New York: Garland Science, 4th ed., 2002.

[19] C. Selhuber-Unkel, *Biological adhesion on nanopatterned substrates studied with force spectroscopy and microinterferometry*, PhD thesis, Ruperto-Carola University of Heidelberg, 2006.

[20] H. M. McBride, M. Neuspiel, and S. Wasiak, "Mitochondria: More than just a powerhouse," *Current Biology*, vol. 16, pp. R551–R560, 2006.

[21] B. N. Kholodenko, "Review four-dimensional organization of protein kinase signaling cascades: the roles of diffusion, endocytosis and molecular motors nuclear targets," *The Journal of Experimental Biology*, vol. 206, pp. 2073–2082, 2003.

[22] M. Winey, C. L. Mamay, E. T. O'Toole, D. N. Mastronarde, J. Thomas H. Giddings, K. L. McDonald, and J. R. McIntosh, "Three-dimensional ultrastructural analysis of the saccharomyces cerevisiae mitotic spindle," *The Journal of Cell Biology*, vol. 129, no. 6, pp. 1601–1615, 1995.

[23] A. S. Verkman, "Solute and macromolecule diffusion in cellular aqueous compartments," *Trends Biochem. Sci.*, vol. 27, no. 1, pp. P27–33, 2002.

[24] D. A. Fletcher and R. D. Mullins, "Cell mechanics and the cytoskeleton," *Nature*, vol. 463, pp. 485–492, jan 2010.

[25] K. C. Holmes, D. Popp, W. Gebhard, and W. Kabsch, "Atomic model of the actin filament," *Nature*, vol. 347, pp. 44–49, 1990.

[26] T. D. Pollard, G. G. Borisy, and N. Haven, "Cellular Motility Driven by Assembly and Disassembly of Actin Filaments," *Cell*, vol. 112, pp. 453–465, 2003.

[27] H. Herrmann, H. Bär, L. Kreplak, S. V. Strelkov, and U. Aebi, "Intermediate filaments: From cell architecture to nanomechanics," *Nature Reviews Molecular Cell Biology*, vol. 8, p. 562, jul 2007.

[28] K. Saladin, *Anatomy & Physiology: The unity of form and function*, McGraw Hill, 5th ed., 2010.

[29] R. J. Petrie and K. M. Yamada, "Fibroblasts Lead the Way: A Unified View of 3D Cell Motility," *Trends in Cell Biology*, vol. 25, no. 11, pp. P666–674, 2015.

[30] D. Campion, "The muscle satellite cell: a review," *Int Rev Cytol.*, vol. 87, pp. 225–251, 1984.

[31] A. R. Gillies and R. L. Lieber, "Structure and function of the skeletal muscle extracellular matrix," *Muscle & nerve*, vol. 44, pp. 318–331, sep 2011.

[32] M. Benoit and C. Selhuber-unkel, "Atomic Force Microscopy in Biomedical Research," *Methods Mol. Biol.*, vol. 736, pp. 355–377, 2011.

[33] T. Matsunaga, T. Iyoda, and F. Fukai, "Adhesion-dependent cell regulation via adhesion molecule, integrin: Therapeutic application of integrin activation-modulating factors," in *Colloid and Interface Science in Pharmaceutical Research and Development* (H. Ohshima and K. Makino, eds.), pp. 243–260, Elsevier B.V., 2014.

[34] N. Wang, J. P. Butler, and D. E. Ingber, "Mechanotransduction across the cell surface and through the cytoskeleton," *Science*, vol. 260, pp. 1124–1127, 1993.

[35] F. Guilak, L. Alexopoulos, I. Y. M.L. Upton, J. Choi, L. Cao, L. Setton, and M. Haider, "The pericellular matrix as a transducer of biomechanical and biochemical signals in articular cartilage," *Ann. N. Y. Acad. Sci.*, vol. 1068, pp. 498–512, 2006.

[36] M. Chiquet, L. Gelman, R. Lutz, and S. Maier, "From mechanotransduction to extracellular matrix gene expression in fibroblasts," *BBA - Molecular Cell Research*, vol. 1793, no. 5, pp. 911–920, 2009.

[37] V. W. Wong, M. T. Longaker, and G. C. Gurtner, "Seminars in cell & developmental biology soft tissue mechanotransduction in wound healing and fibrosis," *Seminars in Cell and Developmental Biology*, vol. 23, no. 9, pp. 981–986, 2012.

[38] L. A. Barnes, C. D. Marshall, T. Leavitt, M. S. Hu, A. L. Moore, J. G. Gonzalez, M. T. Longaker, and G. C. Gurtner, "Mechanical forces in cutaneous wound healing: Emerging therapies to minimize scar formation," *Advances in Wound Care*, vol. 7, no. 2, pp. 47–56, 2018.

[39] C. Selhuber-Unkel, M. Lopez-Garcia, H. Kessler, and J. P. Spatz, "Cooperativity in adhesion cluster formation during initial cell adhesion," vol. 95, pp. 5424–5431, 2008.

[40] C. Selhuber-Unkel, P. Yde, K. Berg-Sørensen, and L. B. Oddershede, "Variety in intracellular diffusion during the cell cycle," *Physical Biology*, vol. 6, no. 2, p. 25015, 2009.

[41] D. MacKenna, S. Summerour, and F. Villarreal, "Role of mechanical factors in modulating cardiac fibroblast function and extracellular matrix synthesis," *Cardiovasc. Res.*, vol. 49, pp. 257–263, 2000.

[42] P. Davies, K. Barbee, M. Volin, A. Robotewskyj, J. Chen, L. Joseph, M. Griem, M. Wernick, E. Jacobs, D. Polacek, N. DePaola, and A. Barakat, "Spatial relationships in early signaling events of flow-mediated endothelial mechanotransduction," *Annu. Rev. Physiol.*, vol. 59, pp. 527–549, 1997.

[43] B. Geiger and A. Bershadsky, "Exploring the neighborhood: Adhesion-coupled cell mechanosensors," *Cell*, vol. 110, pp. 139–142, 2002.

[44] A. del Rio, R. Perez-Jimenez, R. Liu, P. Roca-Cusachs, J. M. Fernandez, and M. P. Sheetz, "Stretching single talin rod molecules activates vinculin binding," *Science*, vol. 323, no. 5914, pp. 638–641, 2009.

[45] Y. Sun and B. J. Nelson, "MEMS capacitive force sensors for cellular and flight biomechanics," *Biomed. Mater.*, vol. 2, pp. 16–22, 2007.

[46] J. Rajagopalan and M. T. A. Saif, "MEMS sensors and microsystems for cell mechanobiology," *J. Micromech Microeng.*, vol. 21, no. 5, pp. 054002–054012, 2011.

[47] X. R. Zheng and X. Zhang, "Microsystems for cellular force measurement: a review," *J. Micromech. Microeng.*, vol. 21, pp. 1–13, 2011.

[48] W. J. Polacheck and C. S. Chen, "Measuring cell-generated forces: a guide to the available tools," *Nature Methods*, vol. 13, no. 5, pp. 415–423, 2016.

[49] M. Goktas and K. G. Blank, "Molecular force sensors: From fundamental concepts toward applications in cell biology," *Adv. Mater. Interfaces*, vol. 4, pp. 1–16, 2017.

[50] B. Li, "Application of sensing techniques to cellular force measurement," *Sensors*, vol. 10, pp. 9948–9962, 2010.

[51] P. Roca-cusachs, V. Conte, and X. Trepat, "Quantifying forces in cell biology," *Nature Cell Biology*, vol. 19, no. 7, pp. 742–751, 2017.

[52] J. Fraden, *Handbook of modern sensors*, San Diego: Springer Science+Business Media, LLC 2010, 4th ed., 2010.

[53] M. Madou, *Fundamentals of microfabrication: The science of miniaturization*, Boca Raton: Taylor & Francis Ltd., 3rd ed., 2011.

[54] M. Marelli, N. Gadhari, G. Boero, M. Chiquet, and J. Brugger, "Cell force measurements in 3D microfabricated environments based on compliant cantilevers," *The Royal Society of Chemistry, Lab on a Chip*, vol. 0, no. 2, p. 8, 2013.

[55] K. A. Beningo, M. Dembo, I. Kaverina, J. V. Small, and Y. L. Wang, "Nascent focal adhesions are responsible for the generation of strong propulsive forces in migrating fibroblasts," *Journal of Cell Biology*, vol. 153, no. 4, pp. 881–888, 2001.

[56] O. du Roure, A. Saez, A. Buguin, R. H. Austin, P. Chavrier, P. Silberzan, and B. Ladoux, "Force mapping in epithelial cell migration," *Proceedings of the National Academy of Sciences*, vol. 102, no. 7, pp. 2390–2395, 2005.

[57] W. R. Leganta, C. K. Choia, J. S. Millera, L. Shaob, L. Gaob, E. Betzigb, and C. S. Chen, "Multidimensional traction force microscopy reveals out-of-plane rotational moments about focal adhesions," *PNAS*, vol. 110, no. 3, pp. 881–886, 2013.

[58] C. G. Galbraith and M. P. Sheetz, "A micromachined device provides a new bend on fibroblast traction forces," *Proceedings of the National Academy of Sciences*, vol. 94, pp. 9114–9118, 1997.

[59] J. L. Tan, J. Tien, D. M. Pirone, D. S. Gray, K. Bhadriraju, and C. S. Chen, "Cells lying on a bed of microneedles: An approach to isolate mechanical force," *PNAS*, vol. 100, no. 4, pp. 1484–1489, 2002.

[60] S. R. Polio, K. E. Rothenberg, D. StamenovicİĄ, and M. L. Smith, "A micropatterning and image processing approach to simplify measurement of cellular traction forces," *Acta Biomater.*, vol. 8, no. 1, pp. 82–88, 2012.

[61] E. Bell, B. Ivarsson, and C. Merrill, "Production of a tissue-like structure by contraction of collagen lattices by human fibroblasts of different proliferative potential in vitro," *Proc. Natl. Acad. Sci.*, vol. 76, no. 3, pp. 1274–1278, 1979.

[62] P. Delvoye, P. Wiliquet, J.-L. Leveque, B. Nusgens, and C. Lapiere, "Measurement of mechanical forces generated by skin fibroblasts embedded in a three-dimensional collagen gel," *J. Invest. Dermatol.*, vol. 97, pp. 898–902, 1991.

[63] W. H. Zimmermann, C. Fink, D. Kralisch, U. Remmers, J. Weil, and T. Eschenhagen, "Three-dimensional engineered heart tissue from neonatal rat cardiac myocytes," in *Biotechnology and Bioengineering* (D. S. Clark, ed.), vol. 68, pp. 106–114, Wiley Periodicals, Inc., 2000.

[64] H. Vandenburgh, J. Shansky, F. Benesch-Lee, V. Barbata, J. Reid, L. Thorrez, R. Valentini, and G. Crawford, "Drug-screening platform based on the contractility of tissue-engineered muscle," *Muscle Nerve*, vol. 37, pp. 438–447, 2008.

[65] A. Hansen, A. Eder, M. B. İĹnstrup, M. Flato, M. Mewe, S. Schaaf, B. Aksehirlioglu, A. Schwoerer, J. Uebeler, and T. Eschenhagen, "Development of a drug screening platform based on engineered heart tissue," *Circ. Res.*, vol. 107, pp. 35–44, 2010.

[66] W. Legant, A. Pathak, M. T. Yang, V. S. Deshpande, R. M. McMeeking, and C. S. Chena, "Microfabricated tissue gauges to measure and manipulate forces from 3D microtissues," *Proc. Natl. Acad. Sci. USA*, vol. 106, pp. 10097–10102, 2009.

[67] T. Boudou, W. R. Legant, A. Mu, M. A. Borochin, N. Thavandiran, M. Radisic, P. W. Zandstra, J. A. Epstein, K. B. Margulies, and C. S. Chen, "A microfabricated platform to measure and manipulate the mechanics of engineered cardiac microtissues," *Tissue Eng. Part A*, vol. 18, pp. 910–919, 2012.

[68] J. Lee, M. Leonard, T. Oliver, A. Ishihara, and K. Jacobson, "Traction Forces Generated by Locomoting Keratocytes," *The Journal of Cell Biology*, vol. 127, no. 6, pp. 1957–1964, 1994.

[69] S. A. Maskarinec, C. Franck, D. A. Tirrell, and G. Ravichandran, "Quantifying cellular traction forces in three dimensions," *PNAS*, vol. 106, no. 52, pp. 1–6, 2009.

[70] N. Q. Balaban, U. S. Schwarz, D. Riveline, P. Goichberg, G. Tzur, I. Sabanay, D. Mahalu, S. Safran, A. Bershadsky, L. Addadi, and B. Geiger, "Force and focal adhesion assembly: a close relationship studied using elastic micropatterned substrates," *Nature Cell Biology*, vol. 358, pp. 35–41, 2001.

[71] C. Franck, S. A. Maskarinec, D. A. Tirrell, and G. Ravichandran, "Three-dimensional traction force microscopy: A new tool for quantifying cell-matrix interactions," *PLoS ONE*, vol. 6, no. 3, 2011.

[72] J. P. Butler, I. V. A. M. Tolic, B. E. N. Fabry, and J. J. Fredberg, "Traction fields, moments, and strain energy that cells exert on their surroundings," *Am J Physiol Cell Physiol*, vol. 282, pp. 595–605, 2002.

[73] J. Chen, N. Wang, I. V. A. M. Tolic, S. M. Mijailovich, J. P. Butler, J. J. Fredberg, I. M. Tolic, S. M. Mijailovich, J. P. Butler, J. Fredberg, and D. Stamenovic, "Cell prestress. I. Stiffness and prestress are closely associated in adherent contractile cells," *Am. J .Physiol. Cell. Physiol.*, vol. 282, pp. 606–616, 2001.

[74] R. J. J. Pelham and Y.-L. Wang, "Cell locomotion and focal adhesions are regulated by substrate flexibility," *Proc. Natl. Acad Sci. USA*, vol. 94, pp. 13661–13665, 1997.

[75] J. Fu, Y.-k. Wang, M. T. Yang, R. A. Desai, X. Yu, Z. Liu, and C. S. Chen, "Mechanical regulation of cell function with geometrically modulated elastomeric substrates," *Nat. Methods*, vol. 7, no. 9, pp. 733–736, 2010.

[76] L. Trichet, J. Le, R. J. Hawkins, S. Ram, K. Vedula, M. Gupta, and C. Ribrault, "Evidence of a large-scale mechanosensing mechanism for cellular adaptation to substrate stiffness," *PNAS*, vol. 109, no. 18, pp. 6933–6938, 2012.

[77] M. Zuendel, A. E. Ehret, and E. Mazza, "Factors influencing the determination of cell traction forces," *PLoS ONE*, pp. 1–18, 2017.

[78] F. Klein, T. Striebel, J. Fischer, Z. Jiang, C. M. Franz, G. von Freymann, Martin Wegener, and M. Bastmeyer, "Elastic fully three-dimensional microstructure scaffolds for cell force measurements," *Adv. Mater.*, vol. 22, pp. 868–871, 2010.

[79] W. R. Legant, J. S. Miller, B. L. Blakely, D. M. Cohen, G. M. Genin, and C. S. Chen, "Measurement of mechanical tractions exerted by cells within three-dimensional matrices," *Nat. Methods.*, vol. 7, no. 12, pp. 969–971, 2010.

[80] Y. Zhang, C. Ge, C. Zhu, and K. Salaita, "DNA-based digital tension probes reveal integrin forces during early cell adhesion," *Nature Communications*, vol. 5, pp. 1–10, 2014.

[81] B. L. Blakely, C. E. Dumelin, B. Trappmann, L. M. Mcgregor, C. K. Choi, P. C. Anthony, V. K. Duesterberg, B. M. Baker, M. Steven, D. R. Liu, and C. S. Chen, "A DNA-based molecular probe for optically reporting cellular traction forces Brandon," *Nat Methods.*, vol. 11, no. 12, pp. 1229–1232, 2014.

[82] J. Rodríguez-Hernández and C. M. González-Henríquez, *Wirnkled polymer surfaces: Strategies, methods and applications.*
Santiago: Springer Nature Switzerland, 2019.

[83] J. le Digabel, M. Ghibaudo, L. Trichet, A. Richert, and B. Ladoux, "Microfabricated substrates as a tool to study cell mechanotransduction," *Med. Biol. Eng. Comput.*, vol. 48, no. 10, pp. 965–976, 2010.

[84] S. Yokoyama, T. S. Matsui, and S. Deguchi, "New wrinkling substrate assay reveals traction force fields of leader and follower cells undergoing collective migration," *Biochemical and Biophysical Research Communications*, vol. 482, no. 4, pp. 975–979, 2016.

[85] K. Burton and D. L. Taylor, "Traction forces of cytokinesis measured with optically modified elastic substrata," *Nature*, vol. 385, pp. 450–454, 1997.

[86] M. E. Fauver, D. L. Dunaway, D. H. Lilienfeld, H. G. Craighead, and G. H. Pollack, "Microfabricated cantilevers for measurement of subcellular and molecular forces," *IEEE Transactions on Biomedical Engineering*, vol. 45, no. 7, pp. 891–898, 1998.

[87] G. Lin, K. S. J. Pister, and K. P. Roos, "Surface micromachined polysilicon heart cell force transducer," *JOURNAL OF MICROELECTROMECHANICAL SYSTEMS*, vol. 9, no. 1, pp. 9–17, 2000.

[88] S.-J. Park, M. B. Goodman, and B. L. Pruitt, "Analysis of nematode mechanics by piezoresistive displacement clamp," *PNAS*, vol. 104, no. 44, pp. 17376–17381, 2007.

[89] U. G. Jung, H. Takahashi, T. Kan, K. Matsumoto, and I. Shimoyama, "A piezoresistive cellular traction force sensor," in *IEEE 26th International Conference on Micro Electro Mechanical Systems (MEMS)*, 2013.

[90] E. T. Enikov and B. J. Nelson, "Three-dimensional microfabrication for a multi-degree-of-freedom capacitive force sensor using fibre-chip coupling," *J. Micromech. Microeng.*, vol. 10, pp. 492–497, 2000.

[91] Y. Sun, B. J. Nelson, D. P. Potasek, and E. Enikov, "A bulk microfabricated multi-axis capacitive cellular force sensor using transverse comb drives," *J. Micromesh. Microeng.*, vol. 12, pp. 832–840, 2002.

[92] Y. Sun, K.-T. Wan, K. P. Roberts, J. C. Bischof, and B. J. Nelson, "Mechanical property characterization of mouse zona pellucida," *IEEE Transactions on Nanobioscience*, vol. 2, no. 4, pp. 279–286, 2003.

[93] Y. Sun and B. J. Nelson, "MEMS for cellular force measurements and molecular detection," *International Journal of Informatio Acquisition*, vol. 1, no. 1, pp. 23–32, 2004.

[94] G. Charras, P. Lehenkari, and M. Horton, "Atomic force microscopy can be used to mechanically stimulate osteoblasts and evaluate cellular strain distributions," *Ultramicroscopy*, vol. 85, pp. 85–95, 2001.

[95] K. Haase and A. E. Pelling, "Investigating cell mechanics with atomic force microscopy," *J. R. Soc. Interface*, vol. 12, pp. 1–16, 2015.

[96] F. Battistona, J.-P. Ramseyera, H. Langa, M. Ballera, C. Gerberb, J. Gimzewskib, E. Meyera, and H.-J. Guèntherodta, "A chemical sensor based on a microfabricated cantilever array with simultaneous resonance-frequency and bending readout," *Sensors and Actuators B*, vol. 77, pp. 122–131, 2001.

[97] C. Wang, D. Wang, Y. Mao, and X. Hu, "Ultrasensitive biochemical sensors based on microcantilevers of atomic force microscope," *Analytical Biochemistry*, vol. 363, pp. 1–11, 2007.

[98] K. M. Hansen and T. Thundat, "Microcantilever biosensors," *Methods*, vol. 37, pp. 57–64, 2005.

[99] H. P. Lang, M. Hegnerand, and C. Gerber, "Cantilever array sensors," *Materials Today*, vol. 8, no. 4, pp. 30–36, 2005.

[100] A. Moulin, S. O'Shea, and M. Welland, "Microcantilever-based biosensors," *Ultramicroscopy*, vol. 82, pp. 23–31, 2000.

[101] JPK, "A practical guide to AFM force spectroscopy and data analysis," *Manual*, pp. 1–8, 2019.

[102] J. Helenius, C.-P. Heisenberg, H. E. Gaub, and D. J. Muller., "Single-cell force spectroscopy," *Journal of cell science*, vol. 121, no. 11, pp. 1785–1791, 2008.

[103] L. F. Kadem, *Nanostructured and photoswitchable biointerfaces for controlling cell adhesion*, PhD thesis, University of Kiel, 2016.

[104] Y. Wang, F. Meng, and F. Sachs, "Genetically encoded force sensors for measuring mechanical forces in proteins," *Communicative & Integrative Biology*, vol. 4, no. 4, pp. 385–390, 2011.

[105] A. Sarkar, Y. Zhao, Y. Wang, and X. Wang, "Force-activatable coating enables high-resolution cellular force imaging directly on regular cell culture surfaces," *Phys. Biol.*, vol. 15, pp. 1–9, 2018.

[106] C. Soon, K. Tee, M. Youseffi, and M. Denyer, "Tracking traction force changes of single cells on the liquid crystal surface," *Biosensors*, vol. 5, pp. 13–24, 2015.

[107] P. Mehrotra, "Biosensors and their applications - A review," *J. Oral. Biol. Craniofac. Res.*, vol. 6, no. 12, pp. 153–159, 2016.

[108] J. Arlett, E. Myers, and M. Roukes, "Comparative advantages of mechanical biosensors," vol. 6, no. 4, pp. 1–28, 2013.

[109] N. M. Kronenberg, P. Liehm, A. Steude, J. A. Knipper, J. G. Borger, G. Scarcelli, K. Franze, S. J. Powis, and M. C. Gather, "Long-term imaging of cellular forces with high precision by elastic resonator interference stress microscopy," *Nature Cell Biology*, vol. 19, no. 7, pp. 864–872, 2017.

[110] P. Liehm, N. M. Kronenberg, and M. C. Gather, "Analysis of the precision, robustness , and speed of elastic resonator interference stress microscopy," *Biophysical Journal*, vol. 114, no. 9, pp. 2180–2193, 2018.

[111] P. Ringer, A. Weißl, A. Cost, A. Freikamp, B. Sabass, A. Mehlich, M. Tramier, M. Rief, and C. Grashoff, "Multiplexing molecular tension sensors reveals piconewton force gradient across talin-1," *Nature Methods*, vol. 14, no. 11, pp. 1090–1096, 2017.

[112] M. L. Sin, K. E. Mach, P. K. Wong, and J. C. Liao, "Advances and challenges in biosensor-based diagnosis of infectious diseases," *Expert Rev Mol Diagn.*, vol. 14, no. 2, pp. 225–244, 2014.

[113] A.-L. Cost, P. RIinger, A. Chrostek-Grashoff, and C. Grashoff, "How to measure molecular forces in cells : A guide to evaluating genetically-encoded FRET-based tension sensors," *Bioengineering, Cellular and Molecular*, vol. 8, no. 1, pp. 96–105, 2015.

[114] D. Logan, "Introduction to the stiffness (displacement) method," 2013. http://www.ce.memphis.edu/7117/notes/presentations/chapter-02.pdf on 2019-06-16.

[115] X. Chen and Y. Liu, *Finite Element Modeling and Simulation with ANSYS Workbench*. Boca Raton: CRC Press, 2015.

[116] I. A. Karnovsky and O. Lebed, "Matrix stiffness method," in *Advanced Methods of Structural Analysis*, pp. 369–420, Springer Science+Business Media, LLC 2010, 2009.

[117] M. J. Turner, R. W. Clough, H. C. Martin, and L. J. Topp, "Stiffness and deflection analysis of complex structures," *Journal of the Aeronautical Sciences*, vol. 23, no. 9, pp. 805–823, 1956.

[118] S. Johansson and D. Sätterman, *Simulation driven product development: How it can be combined with lean philosophy to achieve increased*, Master thesis, Chalmers University of Technology, 2012.

[119] R. W. Clough, "Areas of application of the finite element method," *Computers and Structures*, vol. 4, no. 1, pp. 17–40, 1974.

[120] K. E. Kurrer, *The history of the theory of structures: From arch analysis to computational mechanics.*
John Wiley & Sons Inc., 2012.

[121] S. K. Parashar and J. K. Sharma, "A review on application of finite element modelling in bone biomechanics," *Perspectives in Science*, vol. 8, pp. 696–698, 2016.

[122] P. Groth, *FEM Anwendungen - Statik-, Dynamik- und Potenzialprobleme mit professioneller Software lösen*, Heidelberg, Berlin: Springer-Verlag, 2002.

[123] Performance Engineered Solutions (PES) LTD, "Finite element analysis," 2019.
https://www.pes-performance.com/news/category/finite-element-analysis/ on 2019-06-16.

[124] J. E. Akin, *Finite element analysis with error estimators*, Oxford: Elsevier Butterworth-Heinemann, 2005.

[125] The Open University, "Introduction to finite element analysis." 2016.
https://www.open.edu/openlearn/science-maths-technology/introduction-finite-element-analysis/content-section-0?active-tab=description-tab on 2019-06-16.

[126] M. Okereke and S. Keates, *Finite element applications*, Cham: Springer International Publishing AG, 2018.

[127] P. M. Knupp, "Remarks on mesh quality," in *45th AIAA Aerospace Sciences Meeting and Exhibit*, (Reno), p. 10, American Institute of Aeronautics and Astronautics Paper 2007, 2007.

[128] A. Schmidt, "Finite-elemente-analyse - aus der Sicht des Anwenders," Tech. Rep., IMW - Tu Clausthal, 1995.

[129] M. P. Bendsøe, "Opitimal shape design as a material distribution problem," *Structural Optimization*, vol. 1, no. 2, pp. 193–202, 1989.

[130] H. R. Hörnlein and K. Schnittkowski, *Software systems for structural optimization*, Basel: Birkhäuser Verlag, 1 ed., 1993.

[131] M. Beckers, "Topology optimization using a dual method with discret variables," *Structural Otimization*, vol. 17, pp. 14–24, 1999.

[132] M. P. Bendsøe and N. Kikuchi, "Generating optimal topologies in structural design using a homogenization method," *Computer Methods in Applied Mechanics and Engineering 71*, vol. 71, pp. 197–224, 1989.

[133] M. P. Bendsøe, *Optimization of structural topology, shape and material*.
Berlin, Heidelberg, New York: Springer Verlag, 1995.

[134] M. A. O. Montes, *Topology optimization algorithms for the solution of compliance and volume problems in 2D*, PhD thesis, Centro de Investigacion en Matematicas A.C., 2016.

[135] J. Brownlee, *Clever algorithms: Nature-inspired programming recipes*, 2 ed., Melbourne, 2012.

[136] O. Sigmund and J. Petersson, "Numerical instabilities in topology optimization: A survey on procedures dealing with checkerboards, mesh-dependencies and local minima," *Structural optimization*, vol. 16, no. 1, pp. 68–75, 1998.

[137] A. Dadalau, A. Hafla, and A. Verla, "A new adaptive penalization scheme for topology optimization," tech. rep., Institute for Control Engineering of Machine Tools and Manufacturing Units, Stuttgart, 2008.

[138] W. J. Buehler and R. C. Wiley, "Nickel-based alloys technical report," US Patent 3,174,851, 1965.

[139] S. K. Bhaumik, "Progress in the understanding of NiTi shape memory alloys," *Transactions of the Indian Institute of Metals*, vol. 61, no. 5, pp. 435–445, 2008.

[140] A. Greninger and V. Mooradian, "Strain transformation in metastable beta copperzinc and beta copper-tin alloys," *Trans. Met. Soc. AIME*, vol. 128, pp. 337–368, 1938.

[141] T. Saburi, "Shape Memory Materials," in *Shape memory materials* (K. Otsuka and M. C. Wayman, eds.), p. 147, London: Cambridge University Press, 1 ed., 1998.

[142] W. Tang and R. Sandstrom, "Some aspects on NiTi SMA properties based on the calculation of Ti-Ni phase diagram," in *Proc. SMST-97* (A. R. Pelton, D. Hodgson, S. Russel, and T. Durieg, eds.), pp. 1–6, 1997.

[143] K. Otsuka and X. Ren, "Physical metallurgy of Ti-Ni-based shape memory alloys," *Progress in Materials Science*, vol. 50, pp. 511–678, 2005.

[144] L. Delaey, R. V. Krishnan, H. Tas, and H. Warlimont, "Thermoelasticity, pseudoelasticity and the memory effects associated with martensitic transformations," *Journal of Materials Science*, vol. 9, no. 9, pp. 1521–1535, 1974.

[145] K. Otsuka and C. M. Wayman, *Shape memory materials*, London: Cambridge University Press, 1998.

[146] C. Chluba, W. Ge, R. Lima de Miranda, J. Strobel, L. Kienle, E. Quandt, and M. Wuttig, "Ultralow-fatigue shape memory alloy films," *Science*, vol. 46, no. 34, pp. 1004–1007, 2015.

[147] T. Duerig, A. Pelton, and D. Stöckel, "An overview of nitinol medical applications," *Materials Science and Engineering: A*, vol. 273-275, pp. 149–160, 1999.

[148] J. Humbeeck van, "Shape memory alloys: A material and a technology," *Advanced Engineering Materials*, vol. 3, no. 11, pp. 837–850, 2001.

[149] D. König, *Fabrication and characterization of nanoscale shape memory alloy objects*, PhD thesis, Ruhr-University of Bochum, 2013.

[150] T. W. Duerig and R. Zadno, "Engineering aspects of shape memory alloys," in *Engineering aspects of shape memory alloys* (T. W. Duerig, K. N. Melton, D. Stockel, and C. M. Wayman, eds.), p. 550, London: Butterworth-Heinemann Ltd., 1990.

[151] S. A. Shabalovskaya and J. W. Anderegg, "Surface spectroscopic characterization of TiNi nearly equiatomic shape memory alloys for implants," *Journal of Vacuum Science & Technology A: Vacuum, Surfaces, and Films*, vol. 13, no. 5, pp. 2624–2632, 2002.

[152] M. F. Chen, X. J. Yang, R. X. Hu, Z. D. Cui, and H. C. Man, "Bioactive NiTi shape memory alloy used as bone bonding implants," *Materials Science and Engineering C*, vol. 24, no. 4, pp. 497–502, 2004.

[153] S. Barcikowski, A. Hahn, M. Guggenheim, K. Reimers, and A. Ostendorf, "Biocompatibility of nanoactuators: stem cell growth on laser-generated nickel-titanium shape memory alloy nanoparticles," *J. Nanopart. Res.*, vol. 12, pp. 1733–1742, 2010.

[154] K. Loger, A. Engel, J. Haupt, Q. Li, C. Lamprecht, R. Lima de Miranda, E. Quandt, G. Lutter, and C. Selhuber-Unkel, "Cell adhesion on NiTi thin film sputter deposited meshes," *Materials Science and Engineering C*, vol. 59, pp. 611–616, 2016.

[155] A. Ishida and V. Martynov, "Sputter-deposited shape-memory alloy thin films: Properties and applications," in *MRS Bulletin/February 2002*, pp. 111–114, 2002.

[156] M. Bahraminasab and B. B. Sahari, "NiTi shape memory alloys, promising materials in orthopedic applications," in *Shape Memory Alloys - Processing, Characterization and Applications*, ch. 10, pp. 261–278, InTech, 2013.

[157] D. Stöckel, "Nitinol medical devices and implants," *Minimally Invasive Therapy and Allied Technologies*, vol. 9, no. 2, pp. 81–88, 2000.

[158] D. Kapoor, "Nitinol for medical applications: A brief introduction to the properties and processing of nickel titanium shape memory alloys and their use in stents," *Johnson Matthey Technology Review*, vol. 61, no. 1, pp. 66–76, 2017.

[159] E. Quandt, C. Zamponi, and R. Lima de Miranda, "Method for producing medical functional element comprising a self-supporting lattice structure," 2010.

[160] R. Lima de Miranda, C. Zamponi, and E. Quandt, "Micropatterned freestanding superelastic TiNi films," *Advanced Engineering Materials*, vol. 15, pp. 1–2, 2013.

[161] R. L. de Miranda, "Material Parameter NiTi-Datasheet," *Technical Datasheet*, p. 1, 2015.

[162] M. Fujiki and G. Kwak, "Amorphous and crystalline silicon films from soluble Si-Si network polymers," in *Crystalline Silicon* (S. Basu, ed.), ch. 1, pp. 1–22, IntectOpen, 1 ed., 2011.

[163] T. O'Keeffe and R. Handy, "Fabrication of planar silicon transistors without photoresist," *Solid-State Electronics*, vol. 11, no. 2, pp. 261–266, 2002.

[164] L. Kergoat, B. Piro, M. Berggren, G. Horowitz, and M. C. Pham, "Advances in organic transistor-based biosensors: From organic electrochemical transistors to electrolyte-gated organic field-effect transistors," *Analytical and Bioanalytical Chemistry*, vol. 402, no. 5, pp. 1813–1826, 2012.

[165] L. Kricka, "Microchips, microarrays, biochips and nanochips - lersonal Laboratories for the 21st century," *EJIFCC*, vol. 12, no. 4, pp. 105–108, 2000.

[166] R. Won, O. Graydon, D. Pile, N. Horiuchi, "The lure of silicon," *Nature Photonics*, vol. 1, no. 4, pp. 187–187, 2007.

[167] W. G. J. H. M. van Sark, L. Korte, and F. Roca, *Physics and technology of amorphous-crystalline heterostructure silicon solar cells*, Berlin, Heidelberg: Springer-Verlag Berlin Heidelberg, 1 ed., 2012.

[168] M. H. Irfan, "Silicones in the construction industry," in *Chemistry and Technology of Thermosetting Polymers in Construction Applications*, pp. 170–202, Dordrecht: Springer, 1998.

[169] F. Alshmri, "Lightweight material: Aluminium high silicon alloys in the automotive industry," *Advanced Materials Research*, vol. 1, pp. 1271–1276, 2013.

[170] B. Roe and X. Zhang, "Durable hydrophobic textile fabric finishing using silica nanoparticles and mixed silanes," *Textile Research Journal*, vol. 79, no. 12, pp. 1115–1122, 2009.

[171] M. J. Whitford, "The chemistry of silicone materials for biomedical devices and contact lenses," *Biomaterials*, vol. 5, no. 5, pp. 298–300, 1984.

[172] M. Vallet-Regí and F. Balas, "Silica Materials for Medical Applications," *Open Biomed Eng J.*, vol. 2, pp. 1–9, 2008.

[173] X. Wang, X. Li, Q. Lei, Y. Wu, and W. Li, "Fabrication of superhydrophobic composite coating based on fluorosilicone resin and silica nanoparticles," *Royal Society Open Science*, vol. 5, no. 7, p. 180598, 2019.

[174] W. Gao, M. Rigout, and H. Owens, "The structural coloration of textile materials using self-assembled silica nanoparticles," *Journal of Nanoparticle Research*, vol. 19, no. 9, 2017.

[175] N. M. Julkapli and S. Bagheri, "Developments in nano-additives for paper industry," *Journal of Wood Science*, vol. 62, no. 2, pp. 117–130, 2016.

[176] J. M. Courtney and T. Gilchrist, "Silicone rubber and natural rubber as biomaterials," *Medical & Biological Engineering & Computing*, vol. 18, pp. 538–540, 1980.

[177] S. Nafisi and M. Maibach, "Silica Nanoparticles for Increased Cosmetic Ingredient Efficacy," *Cosmetics & Toiletries*, no. December, pp. 4–7, 2015.

[178] N. Spomer, *Synthese, Charakterisierung und Reaktivität von amorphem, schwarzem Silicium*, PhD thesis, Johann Wolfgang von Goethe-University, 2007.

[179] M. Narisawa, "Silicone resin applications for ceramic precursors and composites," *Materials*, pp. 3518–3536, 2010.

[180] L. J. Gay-Lussac and L. J. Thenard, *Recherches physico-chimiques, Bd. 2*, vol. 2, Paris: Deterville, 1 ed., 1811.

[181] H. Davis, *The collected works of Humphry Davy*, vol. 9, London: Smith, Elder & Co., 1 ed., 1839.

[182] K. Morigaki and C. Ogihara, "Amorphous semiconductors: Structure, optical, and electrical properties," in *Handbook of Electronic and Photonic Materials* (S. Kasap and P. Capper, eds.), ch. 24, pp. 557–571, Cham: Springer International Publishing, 2017.

[183] W. Fuhs, "Amorphous hydrogenated silicon, a-Si:H," in *Silicon* (P. Siffert and E. Krimmel, eds.), pp. 123–137, Berlin, Heidelberg: Springer, 2004.

[184] W. Guangyu, *Technology, manufacturing and grid connection of photovoltaic colar Cells*, John Wiley & Sons, 2018.

[185] W. Qarony, M. I. Hossain, M. K. Hossain, U. M. Jalal, A. Haque, A. R. Saad, and Y. H. Tsang, "Efficient amorphous silicon solar cells: characterization, optimization, and optical loss analysis," *Results in Physics*, vol. 7, pp. 4287–4293, 2017.

[186] P. Hart, "Crystalline vs. amorphous silicon - a comparison of their respective properties and their significance in photovoltaic applications," in *Seventh E.C. Photovoltaic Solar Energy Conference.* (A. Goetzberger, W. Palz, and G. Willeke, eds.), pp. 521–527, Dordrecht: Springer, 1987.

[187] J. P. Conde, J. Gaspar, and V. Chu, "Low-temperature thin-film silicon MEMS vol 427, pp. 181-186, 2003," *Thin Solid Films*, vol. 427, pp. 181–186, 2003.

[188] S. Polach, D. Horst, G. Maier, and E. LuederErnst, "Matrix of light sensors addressed by aSi:H TFTs on a flexible plastic substrate," in *The International Society for Optical Engineering 3649*, pp. 31–39, 1999.

[189] H. Lee, J. S. Yoo, C. D. Kim, I. B. Kang, and J. Kanicki, "Hexagonal a-Si:H TFTs: A new advanced technology for flat-paneld displays," *IEEE Transactions on Electron Devices*, vol. 55, no. 1, pp. 329–336, 2008.

[190] M. Pagliaro, G. Palmisano, and R. Ciriminna, "Flexible solar cells," *ChemSusChem*, vol. 1, pp. 880 − 891, 2018.

[191] G. De Cesare, A. Nascetti, and D. Caputo, "Amorphous silicon p-i-n structure acting as light and temperature sensor," *Sensors (Switzerland)*, vol. 15, no. 6, pp. 12260–12272, 2015.

[192] Y. Vygranenko, J. H. Chang, and A. Nathan, "Two-dimensional a-Si:H n-i-p photodiode array for low-level light detection," *IEEE Journal of Quantum Electronics*, vol. 41, no. 5, pp. 697–703, 2005.

[193] U. Rizal, B. S. Swain, N. Rameshbabu, and B. P. Swain, "Biocompatibility of hydrogen-diluted amorphous silicon carbide thin films for artificial heart valve coating," *Journal of Materials Engineering and Performance*, vol. 27, no. 6, pp. 2679–2686, 2018.

[194] L. Freund and S. Suresh, *Thin film materials*, Cambridge University Press, 2003.

[195] G. McGuire, *Semiconductor materials and process technology handbook*, Noyes: William Andrew Publishing, 1988.

[196] R. Street, *Technology and application of amorphous silicon*, Berlin, Heidelberg, New York: Springer Verlag, 2000.

[197] C. Selhuber-Unkel, "Mechanotransduction mediating cell adhesion - towards cell-inspired adaptive materials CELLINSPIRED," Reserach Proposal, 2013.

[198] C. Selhuber-Unkel, "ERC starting grant 2013: Research proposal," *ERC Grant*, vol. Part B2, pp. 1–17, 2013.

[199] M. J. Madou, *Fundamentals of microfabrication*, Boca Raton: CRC Press LLC, 2nd ed., 2002.

[200] S. Zur Verth, *Entwicklung der Halbleiterindustrie 2018*, 2018.
München: https://www.zvei.org/fileadmin/user_upload/Presse_und_Medien/Pressebereich/2018-89_Deutscher_Halbleitermarkt/2018-12_Pressekonferenz_Fachgruppe_Halbleiter_ZVEI.pdf on 2019-16-06.

[201] J. Elders, , V. Spiering, and S. Walsh, "Microsystems technology (MST) and MEMS applications: An overview," *MRS Bulletin*, vol. 26, no. 4, pp. 312–315, 2001.

[202] W. Menz, J. Mohr, and O. Paul, *Microsystem technology*.
Weinheim: Wiley-VCH Verlag GmbH, 1 ed., 2001.

[203] Bundesministerium für Bildung und Forschung, "Trends in der Weiterentwicklung und Anwendung der Mikrosystemtechnik," tech. rep., Bundesministerium für Bildung und Forschung, Berlin, 2007.

[204] A. Quabili, "Bulk and surface micromachining," Tech. Rep., A. James Clark School of Engineering, 2009.

[205] C. Linder, L. Paratta, M.-A. Gretillat, V. P. Jaecklin, and N. F. de Rooij, "Surface micromachining," *Journal of Micromechniaics and Microengineering,*, vol. 2, no. 3, p. 122, 1992.

[206] P. J. French and P. M. Sarro, "Surface versus bulk micromachining: the contest for suitable applications," *Journal of Micromechanical Microengineering*, vol. 8, pp. 45–53, 1998.

[207] Southwest Centre for Microsystems Education, "MEMS micromachining overview," Tech. Rep., Southwest Centre for Microsystems Education, 2017.

[208] R. Kohli and K. Mittal, eds., *Developments in surface contamination and cleaning: Methods for surface cleaning*, Cambridge, Oxford: Elsevier Inc., 2017.

[209] N.-T. Ngyuen, *Micromixers - Fundamentals, design and fabrication*, Elsevier Inc., 2012.

[210] U. of Florida, *Wet and Dry Etching Theory*, 2019. http://ww2.che.ufl.edu/unit-ops-lab/experiments/semiconductors/etching/Etching-theory.pdf on 2019-03-21.

[211] D. Moore and R. R. A. Syms, "Recent development in micromachined silicon," tech. rep., Department of Electronic and Electrical Engineering / Imperial College, Cambridge, 2002.

[212] H.-J. Butt and M. Kapl, "Normal capillary forces," *Advances in Colloid and Interface Science*, vol. 146, pp. 48–60, 2008.

[213] G. S. May and S. M. Sze, *Fundamentals of seminconductor fabrication*, John Wiley & Sons, Inc, 2003.

[214] J. W. Bartha, "Jahresbericht," Tech. Rep., TU Dresden/Institut fuÌr Halbleiter- und Mikrosystemtechnik, 2012.

[215] S. W. Paddock and K. W. Eliceiri, *Laser scanning confocal microscopy: History, applications, and related optical sectioning techniques*, vol. 1075, New York: Springer Science+Business Media, 2013.

[216] P. H. Winston, "Marvin L. Minsky," *Nature Communications*, vol. 530, p. 282, 2016.

[217] M. Misky, "Memoir on inventing the confocal scanning microscope," *Scanning*, vol. 10, pp. 128–138, 1988.

[218] M. Minsky, "Microscope apparatus," *US Patent 3013467A*, p. 5, 1957.

[219] N. S. Claxton, T. J. Fellers, and M. W. Davidson, "Confocal microscopy," in *Encyclopedia of Medical Devices and Instrumentation* (J. G. Webster, ed.), pp. 449–475, John Wiley & Sons, Inc., 2nd ed., 2006.

[220] B. Matsumoto, *Methods in cell biology*, Santa Barbara: Academic Press Inc., 83 ed., 1993.

[221] H. Beyer, *Handbuch der Mikroskopie*, Berlin: VEB Verlag Technik, 3nd ed., 1988.

[222] S. Wilhelm, B. Gröbler, M. Gluch, and H. Heinz, "Carl Zeiss principles," Tech. Rep., ZEISS GmbH, 1997.

[223] R. W. Cole, T. Jinadasa, and C. M. Brown, "Measuring and interpreting point spread functions to determine confocal microscope resolution and ensure quality control," *Nature Protocols*, vol. 6, no. 12, pp. 1929–1941, 2011.

[224] K. R. Spring, T. J. Fellers, and M. W. Davidson, *Electronic imaging detectors, 2019*. Tallhassy, Lusby: https://www.olympus-lifescience.com/en/microscope-resource/primer/techniques/confocal/detectorsintro/ on 2019-16-06.

[225] D. K. Toomre, M. F. Langhorst, and M. W. Davidson, *Introduction to spinning disk confocal microscopy*, 2019. http://zeiss-campus.magnet.fsu.edu/articles/spinningdisk/introduction.html on 2019-16-06.

[226] L. M. Higgins, M. Zevon, V. Ganapathy, Y. Sheng, R. E. Riman, M. C. Tan, C. M. Roth, P. V. Moghe, and M. C. Pierce, "Line-scanning confocal microscopy for high-resolution imaging of upconverting rare-earth-based contrast agents," *Journal of Biomedical Optics*, vol. 20, no. 11, pp. 1105061–1105064, 2015.

[227] P. J. Dwyer, C. A. DiMarzio, J. M. Zavislan, W. J. Fox, and M. Rajadhyaksha, "Confocal reflectance theta line scanning microscope for imaging human skin in vivo," *Optics letters*, vol. 31, pp. 942–944, 2006.

[228] B. Kagerer, R. Brodmann, J. Valent, J. Filze, and U. Popp, "3D-confocal microscopy for surface analysis of micro-structured materials," in *Optical Scanning 2002* (L. B. Stephen F. Sagan, Gerald F. Marshall, ed.), pp. 52–63, SPIE, 2002.

[229] T. Wilson, "Confocal microscopy," in *Microanalysis of Solids* (B. Yacobi, D. Holt, and K. L.L., eds.), pp. 219–232, New York: Springer Science+Business Media, 1994.

[230] S. W.D., "Overview of confocal microscopy," in *Immunocytochemical Methods and Protocols. Methods in Molecular Biology,* (C. Oliver and M. Jamur, eds.), p. 588, Human Press, 2010.

[231] A. Nwaneshiudu, C. Kuschal, F. H. Sakamoto, R. R. Anderson, K. Schwarzenberger, and R. C. Young, "Introduction to confocal microscopy," *Journal of Investigative Dermatology*, vol. 132, pp. 1–5, 2012.

[232] P. V. Belichenko and A. Dahlström, "Confocal laser scanning microscopy and 3-D reconstructions of neuronal structures in human brain cortex," *Neuroimage*, vol. 2, pp. 201–207, 1995.

[233] W. B. Amos and J. White, "How the confocal laser scanning microscope entered biological research," *Biology of the Cell*, vol. 95, pp. 335–342, 2003.

[234] W. Hoheisel, W. Jacobsen, B. Lüttge, and W. Weiner, "Confocal microscopy: Applications in materials science," *Macromol. Mater. Eng.*, vol. 286, no. 11, pp. 663–668, 2001.

[235] W. Schrof, J. Klinler, W. Heckmann, and D. Hoern, "Confocal fluorescence and Raman microscopy in industrial research," *Colloid Polym. Sci*, vol. 276, no. 7, pp. 577–588, 1998.

[236] A. R. Clarke, G. Archenhold, and N. C. Davidson, "A novel technique for determining the 3D spatial distribution of glass fibres in polymer composites," *Composites Science and Technology*, vol. 55, pp. 75–91, 1995.

[237] D. B. Hovis and A. H. Heuer, "The use of laser scanning confocal microscopy (LSCM) in materials science," *Journal of Microscopy*, vol. 240, no. 3, pp. 173–180, 2010.

[238] E. Merson, A. V. Kudryab, V. A. Trachenkob, D. Merson, V. Danilova, and A. Vinogradov, "The use of confocal laser scanning microscopy for the 3D quantitative characterization of fracture surfaces and cleavage facets," *Procedia Structural Integrity*, vol. 2, pp. 533–540, 2016.

[239] V. Panchal, Y. Yang, G. Cheng, J. Hu, M. Kruskopf, C.-I. Liu, A. F. Rigosi, C. Melios, A. R. H. Walker, B. D. Newell, O. Kazakova, and R. E. Elmquist, "Confocal laser scanning microscopy for rapid optical characterization of graphene," *Nature Communications Physics*, vol. 1, no. 83, pp. 1–7, 2018.

[240] B. Tata and B. Raj, "Confocal laser scanning microscopy: Applications in material science and technology," *Bull. Mater. Sci.*, vol. 21, pp. 263–278, 1998.

[241] J. Black, *Biological performance of materials - fundamentals of biocompatibility*, Boca Raton: CRC Press Taylor & Friends, 2005.

[242] D. Williams, *The Williams dictionary of biomaterials*, Liverpool University Press, 1999.

[243] D. F. Williams, "On the mechanisms of biocompatbility," *Biomaterials*, vol. 29, pp. 2941–2953, 2008.

[244] L. Mertz, "What is Biocompatibility ?: A new definition based on the latest Technology," *IEEE Pulse*, vol. 4, no. 4, pp. 14–15, 2013.

[245] B. D. Ratner, "The biocompatibility manifesto: Biocompatibility for the twenty-first century," *J. Cardiovasc. Transl. Res.*, vol. 4, no. 5, pp. 523–527, 2011.

[246] ISO, "Biological evaluation of medical devices," 2018.

[247] T. L. Riss, R. A. Moravec, and A. L. Niles, "Cytotoxicity testing: measuring viable cells, dead cells, and detecting mechanism of cell death," in *Mammalian Cell Viability: Methods and Protocols* (M. J. Stoddart, ed.), vol. 740, ch. 12, pp. 103–114, Springer Science+Business Media, LCC, 2011.

[248] T. Mosmann, "Rapid colorimetric assay for cellular growth and survival: Application to proliferation and cytotoxicity assays," *J. Immunol. Meth.*, vol. 65, no. Rapi, pp. 55–63, 1983.

[249] P. Podulka, P. Pawlus, P. Dobrzanski, and A. Lenart, "Spikes removal in surface measurement," *Journal of Physics*, vol. 483, pp. 1–10, 2014.

[250] Keyence, "3D Laser Scanning Microscope-VK-X100K/X200K User's Manual," Manual, 2012.

[251] V. M. Donnelly and A. Kornblit, "Plasma Etching: Yesterday, today, and tomorrow," *Journal of Vacuum Science & Technology A*, vol. 31, pp. 1–44, 2013.

[252] J. Ryhänen, *Biocompatibility evaluation of nickel-titanium shape memory metal alloy*, PhD thesis, University of Oulu, 1999.

[253] L. M. Gaetke, H. S. Chow-Johnson, and C. K. Chow, "Copper: toxicological relevance and mechanisms," *Archives of Toxicology*, vol. 88, no. 11, pp. 1929–1938, 2014.

[254] S. Foglia, M. Ledda, D. Fioretti, G. Iucci, M. Papi, G. Capellini, M. G. Lolli, S. Grimaldi, M. Rinaldi, and A. Lisi, "In vitro biocompatibility study of sub-5 nm silica-coated magnetic iron oxide fluorescent nanoparticles for potential biomedical application," *Nature Scientific Reports*, vol. 7, p. 13, 2017.

[255] S. Avestan, L. A. Naseri, A. Hassanzade, S. M. Sokri, and A. V. Barker, "Effects of nanosilicon dioxide application on in vitro proliferation of apple rootstock," *Journal of Plant Nutrition*, vol. 39, no. 6, 2015.

[256] P.-J. Wipff, H. Majd, C. Acharya, L. Buscemi, J.-J. Meister, and B. Hinz, "The covalent attachment of adhesion molecules to silicone membranes for cell stretching applications," vol. 30, pp. 1781–1789, 2009.

[257] Viktor Heinrichs, S. Dieluweit, J. Stellbrink, W. Pyckhout-Hintzen, N. Hersch, D. Richter, and R. Merkel, "Chemically defined, ultrasoft PDMS elastomers with selectable elasticity for mechanobiology," *PLoS ONE*, vol. 13, no. 4, pp. 1–22, 2018.

[258] R. N. Palchesko, L. Zhang, Y. Sun, and A. W. Feinberg, "Development of polydimethylsiloxane substrates with tunable elastic modulus to study cell mechanobiology in muscle and nerve," *PLOS ONE*, vol. 7, no. 12, pp. 1–14, 2012.

[259] K. Zhang, J. W. Wong, T. H. Begley, D. G. Hayward, and W. Limm, "Determination of siloxanes in silicone products and potential migration to milk, formula and liquid simulants," *Food Additives & Contaminants: Part A*, vol. 29, no. 8, pp. 1311–1321, 2012.

[260] V. Bergeron, P. Cooper, C. Fischer, J. Giermanska-Kahn, D. Langevin, and A. Pouchelon, "Polydimethylsiloxane (PDMS)-based antifoams," *Colloids and Surfaces A:Physicochem. Eng. Aspects*, vol. 122, pp. 103–120, 1997.

[261] D. V. McAllister, P. M. Wang, S. P. Davis, J.-H. Park, P. J. Canatella, M. G. Allen, and M. R. Prausnitz, "Microfabricated needles for transdermal delivery of macromolecules and nanoparticles: Fabrication methods and transport studies," *PNAS*, vol. 100, no. 24, pp. 13755–13760, 2003.

[262] E. S. Bennett and B. A. Weissmann, *Clinical contact lens practice*, Philadelphia: Lippincott Williams & Wilkins, 2005.

[263] J. Friend and L. Yeo, "Fabrication of microfluidic devices using polydimethylsiloxane," *Biomicrofluidics*, vol. 4, p. 6, 2010.

[264] T. James, M. S. Mannoor, and D. V. Ivanov, "BioMEMS âĂŞAdvancing the frontiers of medicine," *Sensors*, vol. 8, pp. 6077–6107, 2008.

[265] W. Chen, R. H. W. Lam, and J. Fu, "Photolithographic surface micromachining of poly-dimethylsiloxane," *Lab Chip*, vol. 12, pp. 391–395, 2012.

[266] Clariant, *Product data sheet -AZ520D*, Technical Datasheet, 2019. https://www.microchemicals.com/micro/tds_az_520d_protective_coating.pdf on 2019-16-06.

[267] MicroChemicals, *Resist, Developers and Removers, Technical Datasheet, 2013*. Ulm: https://www.microchemicals.com/technical_information/resists_developers_removers.pdf on 2019-16-06.

[268] A. L. Thangawng, R. S. Ruoff, M. A. Swartz, and M. R. Glucksberg, "Bond-detach lithography: a method for micro/nanolithography by precision PDMS patterning.," *Biomed. Microdevices*, vol. 9, pp. 587–595, 2007.

[269] H. T. Kim and O. C. Jeong, "PDMS surface modification using atmospheric pressure plasma," *Microelectronic Engineering*, vol. 88, pp. 2281–2285, 2011.

[270] S. Lopera and R. D. Mansano, "Plasma-based surface modification of polydimethylsiloxane for PDMS-PDMS molding," *ISRN Polymer Science*, vol. 2012, p. 6, 2012.

[271] D. Maji and S. Das, "Analysis of plasma-induced morphological changes in sputtered thin films over compliant elastomer," *J. Phys. D: Appl. Phys.*, vol. 47, pp. 1–15, 2014.

[272] T. A. Green, "Gold etching for microfabrication," *Gold bulletin*, vol. 47, no. 3, pp. 205–216, 2014.

[273] U. Cvelbar, S. Pejovnik, M. Mozetiè, and A. Zalar, "Increased surface roughness by oxygen plasma treatment of graphite/polymer composite," *Applied Surface Science*, vol. 210, no. 3-4, pp. 255–261, 2003.

[274] JCMG, *JCGM 200: 2008 International vocabulary of metrology - Basic and general concepts and associated terms (VIM)*, No. 200, BIPM, 3rd ed., 2008.

[275] The Editors of the Encyclopaedia of Britannica, *Mohs hardness*, 2019. https://www.britannica.com/science/Mohs-hardness on 2019-16-06.

[276] M. Göken and M. Kempf, "Pop-ins in nanoindentations - the initial yield point," *Zeitschrift fuer Metallkunde*, vol. 92, no. 9, pp. 1061–1067, 2001.

[277] D. Tabor, *The hardness of metals*, Oxford: Oxford University Press, 2000.

[278] Z. C. Ying, M. G. Reitsma, R. S. Gates, M. G. Reitsma, and R. S. Gates, "Direct measurement of cantilever spring constants and correction for cantilever irregularities using an instrumented indenter," *Rev. Sci. Instrum.*, vol. 78, no. 063708, pp. 1–8, 2007.

[279] R. S. Gates, W. A. Osborn, J. R. Pratt, R. S. Gates, W. A. Osborn, G. A. Shaw, A. D. Slattery, A. J. Blanch, and F. J. Flores-ruiz, "Accurate and precise calibration of AFM cantilever spring constants using laser Doppler vibrometry," *Nanontechnology*, vol. 23, pp. 1–12, 2012.

[280] D. A. Mendels, M. Lowe, A. Cuenat, M. G. Cain, E. Vallejo, and D. Ellis, "Dynamic properties of AFM cantilevers and the calibration of their spring constants," *J. Micromech. Microeng.*, vol. 16, pp. 1720–1733, 2006.

[281] G. Binnig, C. F. Quate, and C. Gerber, "Atomicforce microscope," *Phys. Rev. Lett.*, vol. 56, pp. 930–933, 1986.

[282] B. Cappella and G. Dietler, "Force-distance curves by atomic force microscopy," *Surface Science Reports*, vol. 34, no. 1, pp. 1–104, 1999.

[283] R. García and R. Pérez, "Dynamic atomic force microscopy methods," *Surface Science Reports*, vol. 47, no. 6, pp. 197–301, 2002.

[284] F. J. Giessibl, "Advances in atomic force microscopy," *Reviews of Modern Physics*, vol. 75, pp. 949–983, 2003.

[285] Y. Seo and W. Jhe, "Atomic force microscopy and spectroscopy," *Reports on Progress in Physics*, vol. 71, no. 1, p. 16101, 2007.

[286] M. L. B. Palacio and B. Bhushan, "Normal and Lateral Force Calibration Techniques for AFM Cantilevers," *Critical Reviews in Solid State and Materials Sciences*, vol. 35, pp. 73–104, 2010.

[287] T. J. Senden and W. A. Ducker, "Experimental determination of spring constants in atomic force microscopy," *Langmuir*, vol. 10, pp. 1003–1004, 1994.

[288] J. P. Cleveland, S. Manne, D. Bocek, and P. K.Hansma, "A nondestructive method for determining the spring constant of cantilevers for scanning force microscopy," *Rev. Sci. Instrum.*, vol. 64, pp. 403–405, 1993.

[289] H. J.Butt, P.Siedle, K.Seifert, K.Fendler, T.Seeger, E.Bamberg, A. L. Weisenhorn, K. Goldie, and A. Engel, "Scan speed limit in atomic force microscopy," *J. Microsc.*, vol. 169, pp. 75–84, 1993.

[290] J.E. Sader, "Parallel beam approximation for V-shaped atomic force microscope cantilevers," *Rev. Sci. Instrum.*, vol. 75, pp. 4583–4586, 1995.

[291] J. E. Sader, "Frequency response of cantilever beams immersed in various fluids with applications to the atomic force microscope," *J. Appl. Phys.*, vol. 84, pp. 64–76, 1998.

[292] J. L. Hutter and J. Beckhoefer, "Calibration of atomic-force microscope tips," *Rev. Sci. Instrum.*, vol. 64, pp. 1868–1873, 1993.

[293] G. A. Matei, E. J. Thoreson, J. R. Pratt, D. B. Newell, and N. A. Burnham, "Precision and accuracy of thermal calibration of atomic force microscopy cantilevers," *Review of Scientific Instruments*, vol. 77, no. 083703, 2006.

[294] J. Ruan and B. Bhushan, "Atomic-scale friction measurements using friction force microscopy: Part I-General principles and new measurement techniques," *ASME J. of Tribol.*, vol. 116, no. 2, pp. 378–388, 1994.

[295] C. A. Clifford and M. P. Seah, "Improved methods and uncertainty analysis in the calibration of the spring constant of an atomic force microscope cantilever using static experimental methods," *Measurement Science and Technology*, vol. 20, no. 125501, pp. 1–11, 2009.

[296] R. W. Carpick and M. Salmeron, "Scratching the surface: Fundamental investigations of tribology with atomic force microscopy," *Chemical Reviews*, vol. 97, pp. 1163–1194, jun 1997.

[297] H. Wang, "Lateral force calibration in atomic force microscopy: Minireview," *Sci. Adv. Mater.*, vol. 9, no. 1, pp. 56–64, 2017.

[298] C. P. Green, J. P. Cleveland, R. Proksch, and P. Mulvaney, "Normal and torsional spring constants of atomic force microscope cantilevers," *Review of Scientific Instruments*, vol. 75, no. 6, pp. 1988–1996, 2004.

[299] S. Jeon, Y. Braiman, and T. Thundat, "Torsional spring constant obtained for an atomic force microscope cantilever," *Appl. Phys. Lett.*, vol. 84, pp. 1795–1797, 2004.

[300] M. G. Reitsma, "Lateral force calibration using a modified atomic force microscope cantilever," *Rev. Sci. Instrum.*, vol. 78, no. 106102, 2007.

[301] S. Ecke, R. Raiteri, E. Bonaccurso, C. Reiner, H. J. Deiseroth, and H. J. Butt, "Measuring normal and friction forces acting on individual fine particles," *Rev. Sci. Instrum.*, vol. 72, pp. 4164–4170, 2001.

[302] A. Feiler, P. Attard, and I. Larson, "Calibration of the tor- sional spring constant and the lateral photodiode response of frictional force microscopes," *Rev. Sci. Instrum.*, vol. 71, pp. 2746–2750, 2000.

[303] J. Stiernstedt, M. W. Rutland, and P. Attard, "A novel technique for the in situ calibration and measurement of friction with the atomic force microscope," *Rev. Sci. Instrum.*, vol. 76, no. 083710, pp. 1–9, 2005.

[304] E. V. Anderson, S. Chakraborty, T. Esformes, D. Eggiman, C. Degraf, K. M. Stevens, D. Liu, and N. A. Burnham, "Shape-independent lateral force calibration," *ACS Appl. Mater. Interfaces*, vol. 3, pp. 3256–3260, 2011.

[305] Q. Gao, G. Wu, K. Wai, and C. Lai, "Calibration of lateral force of AFM measurement calibration of lateral force of AFM measurement," in *Proceedings of the 17th IEEE International Conference on Nanotechnology*, pp. 121–126, 2017.

[306] D. F. Ogletree, R. W. Carpick, and M. Salmeron, "Calibration of frictional forces in atomic force microscopy," *Rev. Sci. Instrum.*, vol. 67, pp. 3298–3306, 1996.

[307] M. Varenberg, I. Etsion, and G. Halperin, "An improved wedge calibra- tion method for lateral force in atomic force microscopy," *Rev. Sci. Instrum.*, vol. 74, pp. 3362–3367, 2003.

[308] H. Wang and M. L. Gee, "Ultramicroscopy AFM lateral force calibration for an integrated probe using a calibration grating," *Ultramicroscopy*, vol. 136, pp. 193–200, 2014.

[309] H. S. Khare and D. L. Burris, "The extended wedge method : Atomic force microscope friction calibration for improved tolerance to instrument misalignments, tip offset, and blunt probes," *Rev. Sci. Instrum.*, vol. 84, no. 055108, pp. 1–9, 2013.

[310] Q. Li, K. S. Kim, and A. Rydberg, "Lateral force calibration of an atomic force microscope with a diamagnetic levitation spring system," *Review of Scientific Instruments*, vol. 77, no. 065105, pp. 1–13, 2006.

[311] L. Wiegleb, *Kalibration eines Rasterkraftmikroskops für Reibungsmessungen*, Master thesis, TU Munich, 2011.

[312] C. Dziekoński, W. Dera, and D. M. Jarząbek, "Method for lateral force calibration in atomic force microscope using MEMS microforce sensor," *Ultramicroscopy*, vol. 182, pp. 1–9, 2017.

[313] D. Jarzabek, W. Dera, and C. Dziekonski, "Method of lateral force calibration in an AFM microscope," 2018.

[314] T. E. Laux and C.-I. Chen, "3D flash lidar visiton systems for imaging in degraded visual environments.," in *Proceedings of SPIE*, vol. 9087, pp. 1–12, 2014.

[315] K. Omasa, F. Hosoi, and A. Konishi, "3D Lidar imaging for detecting and understanding plant responses and canopy structure," *Journal of Experimental Botany*, vol. 58, no. 4, pp. 881–898, 2007.

[316] G. Vosselman and H.-G. Maas, *Airborne and terrestrial laser scanning*, Dunbeath: Whittles Publishing, 2010.

[317] A. Ibisch, S. Stümper, H. Altinger, M. Neuhausen, M. Tschentscher, M. Schlipsing, J. Salmen, and A. Knoll, "Towards autonomous driving in a parking garage: Vehicle localization and tracking using environment-embedded LIDAR sensors," in *IEEE Intelligent Vehicles Symposium*, (Gold Coast), pp. 1–6, 2013.

[318] M. Mirzaei and J. Mann, "Lidar configurations for wind turbine control," *J. Phys.: Conf. Ser.*, vol. 753, no. 032019, pp. 1–8, 2016.

[319] J. Levinson, J. Askeland, J. Becker, J. Dolson, D. Held, S. Kammel, J. Z. Kolter, D. Langer, O. Pink, V. Pratt, M. Sokolsky, G. Stanek, D. Stavens, A. Teichman, M. Werling, and S. Thrun, "Towards fully autonomous driving: systems and algorithms," pp. 3–8, 2011.

[320] M.-C. Amann, T. Bosch, M. Lescure, R. Myllyla, I. Oulu, and M. Rioux, "Laser ranging: a critical review of usual techniques for distance measurement," *Opt. Eng.*, vol. 40, no. 1, pp. 10–19, 2001.

[321] P. P. L. Regtien, "Optical sensors," in *Sensors for Mechatronics*, pp. 161–217, 2012.

[322] G. Berkovic and E. Shafir, "Optical methods for distance and displacement measurements," *Advances in Optics and Photonics*, vol. 4, pp. 441–471, 2012.

[323] J. António, S. Dias, A. Baptista, M. J. Martins, and J. P. N. Torres, "Distance measurement systems using lasers and their applications," *Applied Physics Research*, vol. 9, no. 4, pp. 33–43, 2017.

[324] H. Wang, "Reflective fibre optical displacement sensors for the inspection of tilted objects," *Opt. Quantum Electron.*, vol. 28, no. 11, pp. 1655–1668, 1996.

[325] W. Ko, K. Chang, and G.J. Hwang, "A fibre-optic reflective displacement micrometer," *Sens. Actuators A*, vol. 49, pp. 51–55, 1995.

[326] Z. Ji and M. C. Leu, "Design of optical triangulation devices," *Opt. Laser Technol.*, vol. 21, no. 5, pp. 339–341, 1989.

[327] R. G. Dorsch, G. Häusler, and J. M. Herrmann, "Laser triangulation: fundamental uncertainty in distance measurement," *Appl. Opt.*, vol. 33, pp. 1306–1314, 1994.

[328] G. Fu, A. Menciassi, and P. Dario, "Development of a low-cost active 3D triangulation laser scanner for indoor navigation of miniature mobile robots," *Robotics and Autonomous Systems*, vol. 60, no. 10, pp. 1317–1326, 2012.

[329] M.Johnson, "Fiber displacement sensors for metrology and control," *Opt. Eng.*, vol. 24, pp. 961–965, 1985.

[330] G. Berkovic, S. Zilberman, and E. Shafir, "Size effect in fiber optic displacement sensors," in *Optical Sensors, OSA Technical Digest*, vol. SM4F.6, 2012.

[331] A.D. Payne, A.A. Dorrington, M.J. Cree, and D.A. Carnegie, "Improved measurement linearity and precision for AMCW time-of-flight range imaging cameras," *Appl. Opt.*, vol. 49, no. 23, pp. 4392–4403, 2010.

[332] Y. Cui, S. Schuon, D. Chan, S. Thrun, and C. Theobalt, "3D shape scanning with a time-of-flight camera," in *2010 IEEE Conference on Computer Vision and Pattern Recognition (CVPR)*, pp. 1173–1180, 2010.

[333] V. G. Badami and P. J. D. Groot, "Displacement measuring interferometry," in *Handbook of optical dimensional metrology* (K. Harding, ed.), p. 506, Boca Raton: CRC Press Taylor & Friends, 2013.

[334] N. Bobroff, "Recent advances in displacement measuring interferometry," *Measurement Science and Technology*, vol. 4, no. 9, pp. 907–926, 1993.

[335] LyncéeTec, "DHM® - R series", Technical Datasheet, 2014.

[336] B. Kemper, P. Langehanenberg, and G. von Bally, "Digital holographic microscopy: a new method for surface analysis and marker-free dynamic life cell imaging," *Optik & Photonik*, vol. 2, pp. 41–44, 2007.

[337] J. Gaspar, "Measurement of nano/micro out-of-plane and in-plane displacements of micromechanical components by using digital holography and speckle interferometry," *Optical Engineering*, vol. 50, no. 10, pp. 1–10, 2011.

[338] H. A. Bruck, S. R. Mcneill, M. A. Sutton, and W. H. Peters III, "Digital image correlation using newton-raphson method of partial differential correction," *Experimental Mechanics*, pp. 261–267, 1989.

[339] J.P. Lewis, "Fast normalized cross-correlation," in *Vision Interface 95, Canadian Image Processing and Pattern Recognition Society,*, no. 1, (Quebec), pp. 120–123, 1995.

[340] J. Blaber, B. Adair, and A. Antoniou, "Ncorr: Open-source 2D digital image correlation Matlab software," *Experimental Mechanics*, vol. 55, pp. 1105–1122, 2015.

[341] J. Williamson, H. Martin, and X. Jiang, "High resolution position measurement from dispersed reference interferometry using template matching," *Optics Express*, vol. 24, no. 9, pp. 10103–10114, 2016.

[342] D. Laërtius, "Life of Thales of Miletus," in *The Lives and Opinions of Eminent Philosophers - Book I*, p. 576, 220.

[343] F. Chen, G. M. Brown, and M. Song, "Overview of 3-D shape measurement using optical methods," *Optical Engineering*, vol. 39, pp. 10–22, jan 2000.

[344] A. W. Burner, G. A. Fleming, J. C. Hoppe, and J. Reno, "Comparison of three optical methods for measuring model deformation," in *38th Aerospace Sciences Meeting & Exhibit*, no. January, pp. 1–16, 2000.

[345] B. E. A. Saleh and M. C. Teich, *Fundamentals of photonics*, New York: Wiley, 1991.

[346] D. Meschede, *Gerthsen Physik*, Heidelberg: Springer-Verlag, 24th ed., 2010.

[347] W. Demtroeder, *Elektrizitaet und Optik*, Heidelberg: Springer-Verlag, 17th ed., 2017.

[348] J. Lawall and E. Kessler, "Michelson interferometry with 10 pm accuracy," *Review of Scientific Instruments*, vol. 71, no. 2669, pp. 2669–2676, 2000.

[349] D. Xiaoli and S. Katuo, "High-accuracy absolute distance measurement by means of wavelength scanning heterodyne interferometry," *Meas. Sci. Technol.*, vol. 9, no. 7, pp. 1031–1035, 1998.

[350] P. A. Coe, D. F. Howell, and R. B. Nickerson, "Frequency scanning interferometry in ATLAS: remote, multiple, simultaneous and precise distance measurements in a hostile environment," *Meas. Sci. Technol.*, vol. 15, no. 11, pp. 2175–2187, 2004.

[351] A. F. Fercher, "Optical coherence tomography," *J. Biomed. Opt.*, vol. 1, no. 2, pp. 157–173, 1996.

[352] W. Drexler, "Ultrahigh-resolution optical coherence tomography," *J.Biomed. Opt.*, vol. 9, no. 1, pp. 47–74, 2004.

[353] Z. Gao, X. Wang, and S. Yang, "Three-dimensional continuous displacement measurement with temporal speckle," *Sensors*, vol. 16, no. 2020, pp. 1–13, 2016.

[354] F. P. Mezzapesa, L. Columbo, M. Brambilla, M. Dabbicco, A. Ancona, T. Sibillano, F. De Lucia, P. M. Lugarà, and G. Scamarcio, "Simultaneous measurement of multiple target displacements by self-mixing interferometry in a single laser diode," *Optics Express*, vol. 19, no. 17, p. 16160, 2011.

[355] D. Gabor, "A new microscopic principle," *Nature*, vol. 161, p. 777, 1948.

[356] P. Hariharan, *Basics of holography*, Cambridge: Cambridge University Press, 1 ed., 2002.

[357] A. Faridian, G. Pedrini, and W. Osten, "High-contrast multilayer imaging of biological organisms through dark-field digital refocusing through dark-field digital refocusing," *Journal of Biomedical Optics*, vol. 18, no. 8, pp. 1–7, 2019.

[358] T. Maiman, "Stimulated optical radiation in ruby," *Nature*, vol. 187, no. 4736, pp. 493–494, 1960.

[359] W. S. Boyle and G. E. Smith, "This week's citation classic," *Bell Syst. Tech. J.*, vol. 49, no. 1970, pp. 593–600, 1982.

[360] J. W. Goodman and R. W. Lawrence, "Digital image formation from electronically detected holograms," *Applied Physics Letters*, vol. 11, pp. 77–79, 1967.

[361] U. Schnars and W. JuÌĹptner, "Direct recording of holograms by a CCD target and numerical reconstruction," *Appl. Opt.*, vol. 33, pp. 179–181, 1994.

[362] I. Yamaguchi, K. Yamamoto, G. Mills, and M. Yokota, "Image reconstruction only by phase data in phase-shifting holography," *Appl. Opt.*, vol. 45, pp. 975–983, 2006.

[363] K. Matsushima, "Shifted angular spectrum method for off-axis numerical propagation," *Opt. Express*, vol. 18, pp. 18453–18463, 2010.

[364] D. Lebrun, A. Benkouider, S. CoeÌĹtmellec, and M. Malek, "Particle field digital holographic recon- struction in arbitrary tilted planes," *Opt. Express*, vol. 11, pp. 224–229, 2003.

[365] S. De Nicola, A. Finizio, G. Pierattini, P. Ferraro, and D. Alfieri, "Angular spectrum method with correction of anamorphism for numerical reconstruction on tilted planes," *Opt. Express*, vol. 13, pp. 9935–9940, 2005.

[366] N. Verrier, S. CoeÌLtmellec, M. Brunel, D. L. Brun, and A. Janssen, "Digital in-line holography with an elliptical, astigmatic, Gaussian beam: wide angle reconstruction," *J. Opt. Soc. Am. A*, vol. 25, pp. 1459–1466, 2008.

[367] T. Shimobaba, J. M. Y. Sato, M. Takenouchi, and T. Ito, "Real-time digital holographic microscopy using the graphic processing unit," *Opt. Express*, vol. 16, pp. 11776–11781, 2008.

[368] L. Ahrenberg, A. Page, B. Hennelly, J. McDonald, and T. Naughton, "Using commodity graphics hardware for real-time digital hologram view-reconstruction," *IEEE J. Display Technol.*, vol. 60, no. 5, pp. 111–119, 2009.

[369] T. Shimobaba, N. Masuda, Y. Ichihashi, and T. Ito, "Real-time digital holographic microscopy ob- servable in multi-view and multi-resolution," *J. Opt.*, vol. 12, no. 065402, 2010.

[370] W. Osten, A. Faridian, P. Gao, K. Körner, D. Naik, G. Pedrini, A. K. Singh, M. Takeda, and M. Wilke, "Recent advances in digital holography," *Applied Optics*, vol. 53, no. 27, pp. 44–64, 2014.

[371] E. Bruckheimer, C. Rotschild, T. Dagan, G. Amir, A. Kaufman, S. Gelman, and E. Birk, "Computer-generated real-time digital holography: first time use in clinical medical imaging," *European Heart Journal âĂŞ Cardiovascular Imaging*, vol. 17, pp. 845–849, 2016.

[372] S. Schedin, G. Pedrini, and H. Tiziani, "Pulsed digital holography for deformation measurements on biological tissues," *Appl. Opt.*, vol. 39, pp. 2853–2857, 2000.

[373] M. Kim, "Tomographic three-dimensional imaging of a biological specimen using wavelength-scanning digital interference holography," *Opt. Express*, vol. 7, pp. 305–310, 2000.

[374] F. Charriere, N. Pavillon, T. Colomb, C. Depeursinge, T. Heger, E. Mitchell, P. Marquet, and B. Rappaz, "Living specimen tomography by digital holographic microscopy: morphometry of testate amoeba," *Opt. Express 1*, vol. 4, pp. 7005–7013, 2006.

[375] W. Xu, M. H. Jericho, I. A. Meinertzhagen, and H. J. Kreuzer, "Digital in-line holography for biological applications," *PNAS*, no. 98, pp. 11301–11305, 2001.

[376] M.-K. Kim, "Applications of Digital Holography in Biomedical Microscopy," *Journal of the Optical Society of Korea*, vol. 14, no. 2, pp. 77–89, 2010.

[377] B. Kemper, A. Bauwens, A. Vollmer, S. Ketelhut, and P. Langehanenberg, "Label-free quantitative cell division monitoring of endothelial cells by digital holographic microscopy," *J. Biomed. Opt.*, vol. 15, no. 3, pp. 90–96, 2010.

[378] A. Lozano, J. Kostas, and J. Soria, "Use of holography in particle image velocimetry measurements of a swirling flow," *Exp. Fluids*, vol. 27, pp. 251– 261, 1999.

[379] F. Dubois, N. Callens, C. Yourassowsky, M. Hoyos, P. Kurowski, and O. Monnom, "Digital holographic microscopy with reduced spatial coherence for three-dimensional particle flow analysis," *Appl. Opt.*, vol. 45, pp. 864–871, 2006.

[380] N. Verrier, C. Remacha, M. Brunel, D. Lebrun, and S. CoeÏĹtmellec, "Micropipe flow visualization using digital in-line holographic microscopy," *Opt. Express*, vol. 18, pp. 7807–7819, 2010.

[381] J. Katz and J. Sheng, "Applications of holography in fluid mechanics and particle dynamics," *Annual Review of Fluid Mechanics*, vol. 42, pp. 531–555, 2010.

[382] T. Nomura, E. Tajahuerce, O. Matoba, and B. Javidi, "Applications of digital holography for information security," in *Optical and Digital Techniques for Information Security. Advanced Sciences and Technologies for Security Applications* (J. B., ed.), pp. 241–260, New York, NY: Springer Science+Business Media, 1st ed., 2005.

[383] R. Powell and K. Stetson, "Interferometric vibration analysis by wavefront reconstruction," *J. Opt. Soc. Am.*, vol. 55, pp. 1593–1597, 1965.

[384] D. Borza, "Mechanical vibration measurement by high-resolution time-averaged digital holography," *Meas. Sci. Technol.*, vol. 16, pp. 1853–1864, 2005.

[385] F. Joud, F. LanoeÏĹL, M. Atlan, J. Hare, and M. Gross, "Imaging a vibrating object by sideband digital holography," *Opt. Express*, vol. 17, pp. 2774–2779, 2009.

[386] G. Coppola, P. Ferraro, M. Iodice, S. De Nicola, A. Finizio, and S. Grilli, "A digital holographic microscope for complete characterization of microelectromechanical systems," *Meas. Sci. Technol.*, vol. 15, pp. 529–539, 2004.

[387] Y. W. Lai, N. Koukourakis, N. C. Gerhardt, M. R. Hofmann, R. Meyer, S. Hamann, M. Ehmann, K. Hackl, E. Darakis, and A. Ludwig, "Integrity of micro-hotplates during high-temperature operation monitored by digital holographic microscopy," *Journal of Micromechanical Systems*, vol. 19, no. 5, pp. 1175–1180, 2010.

[388] Y. W. Lai, S. Hamann, M. Ehmann, and A. Ludwig, "High-throughput characterization of stresses in thin film materials libraries using Si cantilever array wafers and digital holographic microscopy," *Review of Scientific Instruments*, vol. 82, no. 6, pp. 1–5, 2011.

[389] M. Dekiff, P. Berssenbrügge, B. Kemper, C. Denz, and D. Dirksen, "Simultaneous acquisition of 3D shape and deformation by combination of interferometric and correlation-based laser speckle metrology," *Biomedical Optics Express*, vol. 6, no. 12, pp. 465–472, 2015.

[390] B. Gombkoeto, J. Kornis, and Z. Füzessy, "Difference displacement measurement using digital holography," *Optics Communications*, vol. 214, no. 1âĂŞ6, pp. 115–121, 2002.

[391] M. Paturzo, V. Pagliarulo, V. Bianco, P. Memmolo, L. Miccio, F. Merola, and P. Ferraro, "Digital holography, a metrological tool for quantitative analysis: Trends and future applications," *Optics and Lasers in Engineering*, vol. 104, pp. 32–47, 2018.

[392] Y. Morimoto, M. Toru, M. Fujigaki, and N. Kawagishi, "Subnanometer displacement measurement by averaging of phase difference in windowed digital holographic interferometry," *Optical Engineering*, vol. 46, no. 2, pp. 1–8, 2007.

[393] G. Pedrini, I. Alekseenko, G. Jagannathan, M. Kempenaars, G. Vayakis, and W. Osten, "Digital holography for erosion monitoring inside the ITER Tokamak," in *Unconventional Optical Imaging, Proc. SPIE 10677*, vol. 10677, 2018.

[394] B. Kemper and G. von Bally, "Digital holographic microscopy for live cell applications and technical inspection ," *Appl. Opt.*, vol. 47, pp. 52–61, 2008.

[395] E. N. Leith and J. Upatnieks, "Reconstructed wavefronts and communication theory," *J. Opt. Soc. Am.*, vol. 52, pp. 1123–1130, 1962.

[396] N. Verrier and M. Atlan, "Off-axis digital hologram reconstruction: Some practical considerations," *Applied Optics*, vol. 50, no. 34, pp. 136–146, 2011.

[397] J. Goodman, *Introduction to fourier optics*, Greenwood Village: Roberts and Company, 2005.

[398] S. Seebacher, "Measuring shape and deformation of small objects using digital holography," *Optical Engineering*, vol. 50, no. 10, pp. 1–10, 1998.

[399] D. C. Ghiglia and M. D. Pritt, *Two-dimensional phase unwrapping: theory, algorithms, and software*, New York: Wiley-Interscience, 1998.

[400] X. Zhang, X. Zhang, H. Zhang, and M. Xu, "Phase unwrapping in digital holography based on non-subsampled contourlet transform," *Optics Communications ·*, vol. 407, p. 367, 2018.

[401] G. C. Antonopoulos, B. Steltner, A. Heisterkamp, T. Ripken, and H. Meyer, "Tile-based two-dimensional phase unwrapping for digital holography using a modular framework," *PLoS ONE*, vol. 10, no. 11, pp. 1–18, 2015.

[402] P. Girshovitz and N. T. Shaked, "Fast phase processing in off-axis holography using multiplexing with complex encoding and live-cell fluctuation map calculation in real-time," *Optics Express*, vol. 23, no. 7, pp. 1–6, 2015.

[403] I. Shevkunov, "A new phase unwrapping method," *J. Phys.: Conf. Ser*, vol. 737, no. 012065, pp. 1–5, 2016.

[404] G. Dardikman, G. Singh, and N. T. Shaked, "Four dimensional phase unwrapping of dynamic objects in digital holography," *Opt. Express*, vol. 26, pp. 3772–3778, 2018.

[405] J. Bioucas-Dias and G. Valadao, "Discontinuity preserving phase unwrapping using graph cuts," *Energy Minimization Methods in Computer Vision and Pattern Recognition-EMMCVPR'05*, vol. 3757, pp. 268–284, 2005.

[406] J. Bioucas-Dias and G. Valadao, "Phase unwrapping: A new max- flow/min-cut based approach," in *Proceedings of the IEEE International Conference on Image Processing - ICIP 05*, pp. 1–4, 2005.

[407] G. Valadao and J. Bioucas-Dias, "PUMA: Phase unwrapping via MAX flows," *IEEE*, pp. 1–4, 2005.

[408] Z. Li, J. Chen, and E. Baltsavias, eds., *Advances in photgrammetry, remote sensing and spatial information sciences: 2008 ISPRS Congress Book*, Boca Raton: CRC Press Taylor & Francis Group, 1st ed., 2008.

[409] J. S. Weszka, C. R. Dyer, and A. Rosenfeld, "A comparative study of texture measures for terrain classification," *IEEE Transactions on Systems, Man, and Cybernetics*, vol. SMC-6, no. 4, pp. 41–46, 1976.

[410] T. R. Botha, *Digital image correlation: Applications in vehicle dynamics*, PhD thesis, University of Pretoria, 2015.

[411] D. Reagan, A. Sabato, and C. Niezrecki, "Feasibility of using digital image correlation for unmanned aerial vehicle structural health monitoring of bridges," *Structural Health Monitoring,*, vol. 17, no. 5, pp. 1056–1072., 2018.

[412] S. H. Daly, "Digital image correlation in experimental mechanics for aerospace materials and structures," in *Encyclopedia of Aerospace Engineering*, pp. 1–12, Wiley, 2010.

[413] T. P. Chu and A. Poudel, "Digital image correlation techniques for aerospace applications," in *ASNT Fall Conference*, (Charleston), p. 9, 2014.

[414] T. Beberniss, M. Spottswood, and T. Eason, "High-speed digital image correlation measurements of random nonlinear dynamic response," *Experimental and Applied Mechanics*, vol. 6, pp. 171–186, 2011.

[415] S. Shoop, A. Sopher, J. Stanley, T. Botha, C. Becker, and S. Ells, "Digital immage correlation for off-road mobility," in *India Ground Vehicle Ssystems Engineering and Technology Symposium*, (Michigan), p. 11, 2016.

[416] R. Hunady, M. Stamborska, M. Hagara, and M. Binda, "The application of digital image correlation method under the search of facilities of materials and mechanical systems," in *International Conference on Military Technologies 2011*, (Brno), p. 11, 2011.

[417] D. Zhang, C. Eggleton, and D. Arola, "Evaluating the mechanical behavior of arterial tissue using digital image correlation," *Exp. Mech.*, vol. 42, no. 4, pp. 409–416, 2002.

[418] Q. Tseng, *Etude d ' architecture multicellulaire avec le microenvironnement contrôlé*, Phd thesis, University of Grenoble, 2011.

[419] H. Wang, W. Lai, A. Antoniou, and A. Bastawros, "Application of digital image correlation for multiscale biomechanics," in *Handbook of imaging in biological mechanics* (C. P. Neu and G. M. Genin, eds.), pp. 141–151, CRC Press, Oxfords, 2014.

[420] M. Palanca, G. Tozzi, and L. Cristofolini, "The use of digital image correlation in the biomechanical area: a review," *International Biomechanics*, vol. 5432, pp. 1–21, 2016.

[421] G. Stoilov and V. Kavardzhikov, "Application of digital image correlation method to solid mechanics," in *12th National Congress on Theoretical and Applied Mechanics*, (Varna), pp. 1–13, 2013.

[422] F. Hild, A. Bouterf, P. Forquin, and S. Roux, "On the use of digital image correlation for the analysis of the dynamic behavior of materials," in *The Micro-World Observed by Ultra High-Speed Cameras* (Kinko Tsuji, ed.), pp. 185–206, Springer, 2018.

[423] W. Tong, "Detection of plastic deformation patterns in a binary aluminum alloy," *Exp Mech*, vol. 37, no. 4, pp. 452–459, 1997.

[424] S. Daly, G. Ravichandran, and K. Bhattacharya, "Stress-induced martensitic phase transformation in thin sheets of Nitinol," *Acta Mater*, vol. 55, no. 10, pp. 3593–3600, 2007.

[425] M. Jerabek, Z. Major, and R. Lang, "Strain determination of polymeric materials using digital image correlation," *Polym Test*, vol. 29, no. 3, pp. 407–416, 2010.

[426] S. Yaofeng, T. Y. Meng, J. Pang, and S. Fei, "Digital image correlation and its applications in electronics packaging," in *2005 7th Electronic Packaging Technology Conference*, (Singapore), pp. 129–134, IEEE, 2005.

[427] P. Lall, D. Panchagade, D. Iyengar, S. Shantaram, J. Suhling, and H. Schrier, "High speed digital image correlation for transient-shock reliability of electronics," in *2007 Proceedings 57th Electronic Components and Technology Conference*, (Reno), pp. 924–939, IEEE, 2007.

[428] P. Lall, S. Shantaram, A. Angral, and M. Kulkarni, "Explicit submodeling and digital image correlation based life-prediction of leadfree electronics under shock-impact," in *Electronic Components and Technology Conference*, pp. 542–555, 2009.

[429] M. A. Sutton, J.-J. Ortens, and H. W. Schreier, *Image correlation for shape, motion and deformation measurements: Basic concepts, theory and applications*.
New York, NY: Springer Science+Business Media, LCC 2009, 2009.

[430] B. Pan, K. Qian, H. Xie, and A. Asundi, "Two-dimensional digital image correlation for in-plane displacement and strain measurement: a review," *Meas. Sci. Technol.*, vol. 20, no. 062001, pp. 1–17, 2009.

[431] M. Debella-Gilo and A. Kääb, "Remote sensing of environment sub-pixel precision image matching for measuring surface displacements on mass movements using normalized cross-correlation," *Remote Sensing of Environment*, vol. 115, no. 1, pp. 130–142, 2011.

[432] A. W. Scrivens, Y. Luo, M. A. Sutton, S. A. Collette, M. L. Myrick, P. Miney, P. E. Colavita, and A. P. Reynolds, "Development of patterns for digital image correlation measurements at reduced length scales," *Experimental Mechanics*, vol. 47, no. 1, pp. 63–77, 2006.

[433] Q. Tseng, E. Duchemin-pelletier, A. Deshiere, M. Balland, H. Guillou, and O. Filhol, "Spatial organization of the extracellular matrix regulates cell - cell junction positioning," *PNAS*, vol. 109, no. 5, pp. 1506–1511, 2012.

[434] Q. Tseng, *Template matching and slice alignment - imageJ plugins*, 2011. https://sites.google.com/site/qingzongtseng/template-matching-ij-plugin on 2019-06-01.

[435] M. A. Sutton, S. R. McNeill, J. D. Helm, and Y. J. Chao, "Advances in two-dimensional and three-dimensional computer vision topics," in *Applied Physics* (P. K. Rastogi, ed.), pp. 323–372, Berlin: Springer, 77 ed., 2000.

[436] M. A. Sutton, J. H. Yan, V. Tiwari, W. H. Schreier, and J. J. Orteu, "The effect of out-of-plane motion on 2D and 3D digital image correlation measurements," *Opt. Lasers Eng.*, vol. 46, pp. 746–57, 2008.

[437] S. R. J. Ramson, K. L. Raju, S. Vishnu, and T. Anagnostopoulos, "Nature inspired optimization techniques for image processing - A short review," in *Intelligent Systems Reference Library* (J. Hemanth and V. E. Balas, eds.), ch. 5, p. 150, Springer International Publishing, 2019.

[438] G. F. Bomarito, J. D. Hochhaltera, T. J. Rugglesb, and A. H. Cannon, "Increasing accuracy and precision of digital image correlation through pattern optimization," *Optics and Lasers in Engineering*, vol. 91, pp. 73–85, 2017.

[439] L. Wang, B. Sun, K. S. Ziemer, G. A. Barabino, and R. L. Carrier, "Chemical and physical modifications to poly(dimethylsiloxane) surfaces affect adhesion of Caco-2 cells," *Journal of Biomedical Materials Research Part A*, vol. 93, no. 4, pp. 1260–71, 2010.

[440] F. Mussano, T. Genova, M. Laurenti, L. Munaron, C. F. Pirri, P. Rivolo, S. Carossa, and P. Mandracci, "Applied surface science hydrogenated amorphous silicon coatings may modulate gingival cell response," *Applied Surface Science*, vol. 436, pp. 603–612, 2018.

[441] H. R. Neumann and C. Selhuber-Unkel, "High-throughput micro-nanostructuring by micro-droplet inkjet printing," *Beilstein Journal of Nanotechnology*, vol. 9, no. 1, pp. 2372–2380, 2018.

[442] R. Alameddine, A. Wahl, F. Pi, K. Bouzalmate, A. Charrier, K. Sengupta, R. Alameddine, A. Wahl, F. Pi, K. Bouzalmate, and L. Limozin, "Printing functional protein nano-dots on soft elastomers: from transfer mechanism to cell mechanosensing," *Nano Letters, American Chemical Society*, vol. 17, no. 7, pp. 4284–4290, 2017.

[443] J. Solon, I. Levental, K. Sengupta, P. C. Georges, and P. A. Janmey, "Fibroblast adaptation and stiffness matching to soft elastic substrates," *Biophysical Journal*, vol. 93, pp. 4453–4461, 2007.

[444] D. E. Discher, P. Janmey, and Y.-l. Wang, "Tissue cells feel and respond to the stiffness of their substrate," *Science*, vol. 310, pp. 1139–1144, 2005.

[445] L. A. Flanagan, Y.-E. Ju, B. Marg, M. Osterfield, and A. Paul, "Neurite branching on deformable substrates," *Neuroreport*, vol. 13, no. 18, pp. 2411–2415, 2008.

[446] M. Arnold, E. A. Cavalcanti-Adam, R. Glass, and W. Eck, "Activation of integrin function by nanopatterned adhesive interfaces," *ChemPhysChem*, vol. 5, pp. 383–388, 2004.

[447] E. A. Cavalcanti-Adam, T. Volberg, A. Micoulet, H. Kessler, B. Geiger, and J. P. Spatz, "Cell spreading and focal adhesion dynamics are regulated by spacing of integrin ligands," *Biophysical Journal*, vol. 92, no. 8, pp. 2964–2974, 2007.

[448] P. Dillard, F. Pi, A. Lellouch, L. Limozin, P. Dillard, F. Pi, A. Lellouch, L. Limozin, and K. S. Nano-clustering, "Nano-clustering of ligands on surrogate antigen presenting cells modulates T cell membrane adhesion and organization," *Royal Society of Chemistry, Integrative Biology*, vol. 8, no. 3, pp. 287–301, 2016.

[449] V. Varanasi, M. Velten, T. Odatsu, A. Ilyas, S. Iqbal, and P. Aswath, "Surface modifications and surface characterization of biomaterials used in bone healing," in *Disorders, Materials for Bone* (S. Bose and A. Bandyopadhyay, eds.), pp. 405–452, Academic Press Inc., 2017.

[450] B. D. Malhotra and M. A. Ali, "Bioconjugated nanostructured metals and metal oxides for biosensors," in *Nanomaterials for Biosensors - Fundamentals and Applications*, ch. 3, pp. 105–125, Elsevier, 2018.

[451] O. Sahin, M. Ashokkumar, and P. M. Ajayan, "Micro- and nanopatterning of biomaterial surfaces," in *Fundamental Biomaterials: Metals* (P. Balakrishnan, S. M. S., and S. Thomas, eds.), ch. 3, pp. 67–78, Elsevier Ltd, 2018.

[452] A. Revzin, R. G. Tompkins, and M. Toner, "Surface engineering with poly(ethylene glycol) photolithography to create high-density cell arrays on glass," *Langmuir*, vol. 19, no. 23, pp. 9855–62, 2003.

[453] R. S. Kane, S. Takayama, E. Ostuni, D. E. Ingber, and George M. Whitesides, "Patterning proteins and cells using soft lithography," *Biomaterials*, vol. 20, no. 23, pp. 2363–76, 1999.

[454] Z. Wang, P. Zhang, B. Kirkland, Y. Liu, and J. Guan, "Microcontact printing of polyelectrolytes on PEG using an unmodified," *Soft Matter*, vol. 8, pp. 7630–7637, 2012.

[455] D. S. Ginger, H. Zhang, and C. A. Mirkin, "The Evolution of Dip-Pen Nanolithography Angewandte," *Angewandte Chemie Int. Ed.*, vol. 43, pp. 30–45, 2004.

[456] M. M. Shawrav, P. Taus, H. D. Wanzenboeck, M. Schinnerl, M. Stöger-Pollach, S. Schwarz, A. Steiger-Thirsfeld, and E. Bertagnolli, "Highly conductive and pure gold nanostructures grown by electron beam induced deposition," *Nature Scientific Reports*, vol. 6, no. 34003, pp. 1–10, 2016.

[457] J. P. Spatz, S. Modmer, and M. Moiler, "Mineralization of gold nanoparticles in a block copolymer microemulsion," *Chem. Eur. J.*, vol. 2, no. 12, pp. 1552–1555, 1996.

[458] M. Arnold, V. C. Jakubick, T. Lohmüller, P. Heil, E. A. Cavalcanti-Adam, M. López-García, P. Walther, B. Geiger, and J. P. Spatz, "Induction of Cell Polarization and Migration by a Gradient of Nanoscale Variations in Adhesive Ligand Spacing," *Nano Lett.*, vol. 8, no. 7, pp. 1–10, 2008.

[459] I. Platzman, K. M. Gadomska, J.-w. Janiesch, I. Louban, E. A. Cavalcanti-adam, and J. P. Spatz, "Soft/elastic nanopatterned biointerfaces in the service of cell biology," in *Micropatterning in Cell Biology Part A*, vol. 119, pp. 237–260, Elsevier Inc., 1 ed., 2014.

[460] J. P. Spatz, S. Mo, C. Hartmann, M. Mo, D. Ulm, T. Herzog, M. Krieger, H.-g. Boyen, P. Ziemann, and F. Ju, "Ordered deposition of inorganic clusters from micellar block copolymer films," *Langmuir*, vol. 16, pp. 407–415, 2000.

[461] S. V. Graeter, J. Huang, and N. Perschmann, "Mimicking cellular environments by nanostructured soft interfaces," *Nano Letters, American Chemical Society*, vol. 7, no. 5, pp. 1413–1418, 2007.

[462] D. Aydin, I. Louban, N. Perschmann, J. Blümmel, T. Lohmüller, E. A. Cavalcanti-Adam, T. L. Haas, H. Walczak, H. Kessler, R. Fiammengo, and J. P. Spatz, "Polymeric substrates with tunable elasticity and nanoscopically controlled biomolecule presentation," *Langmuir*, vol. 26, no. 14, pp. 15472–15480, 2010.

[463] R. T. Hill and A. Chilkoti, "Surface patterning," in *Biomaterials Science: An Introduction to Materials in Medicine* (B. D. Ratner, F. J. Schoen, A. S. Hoffman, and Jack E. Lemons, eds.), ch. I.2.13, pp. 276–301, Elsevier, third edit ed., 2013.

[464] W. Thomson, "Electric telegraphs," *US92228, US156897*, p. 9, 1867.

[465] R. Elmqvist, "Measuring instrument of the recording type," *US2566443A*, pp. 21–23, 1951.

[466] J. P. Arndt, "Pulsed droplet ejecting system," *US3832579A*, no. 19, 1974.

[467] JetXpert, *The history of (and differences between) piezo, thermal, and continuous inkjet printing, 2018.*
https://jetxpert.com/the-history-of-and-differences-between-piezo-thermal-and-continuous-inkjet-printing/ on 2019-16-06.

[468] A. J. Killard, "Screen printing and other scalable point of care (POC) biosensor processing technologies," in *Medical Biosensors for Point of Care (POC) Applications* (R. J. Narayan, ed.), ch. 4, pp. 67–98, Woodhead Publishing, Elsevier Ltd, 2017.

[469] S. B. Fuller, E. J. Wilhelm, and J. M. Jacobson, "Ink-jet printed nanoparticle microelectromechanical systems," *Journal of Microelectromechanical Systems*, vol. 11, no. 1, pp. 54–60, 2002.

[470] T. Driessen and R. Jeurissen, "Drop formation in inkjet printing," in *Fundamentals of Inkjet Printing* (S. D. Hoath, ed.), ch. 4, pp. 93–116, Weinheim: Wiley VCH Verlag GmbH & Co, 2016.

[471] M. R. Mackley, D. C. Vadillo, and T. R. Tuladhar, "Inkjet fluid characterization," in *Fundamentals of Inkjet Printing* (S. D. Hoath, ed.), ch. 13, pp. 339–364, Weinheim: Wiley-VCH Verlag, 2016.

[472] E. Talbot, C. Bain, R. D. Dier, W. Sempels, and J. Vermant, "Droplets drying on surfaces," in *Fundamentals of Inkjet Printing* (S. D. Hoath, ed.), ch. 10, pp. 251–279, Weinheim: Wiley-VCH Verlag, 2016.

[473] S. Jung, H. J. Hwang, and S. H. Hong, "Drops on Substrates," in *Fundamentals of Inkjet Printing* (S. D. Hoath, ed.), vol. 1, ch. 8, pp. 199–218, Weinheim: Wiley-VCH Verlag, 2016.

[474] T. Xu, J. Jin, C. A. Gregory, J. J. Hickman, and T. Boland, "Inkjet printing of viable mammalian cells," *Biomaterials*, vol. 26, no. 1, pp. 93–99, 2005.

[475] L. Pardo, W. C. Wilson, and T. Boland, "Characterization of patterned self-assembled monolayers and protein arrays generated by the inkjet method," *Langmuir*, vol. 19, no. 5, pp. 1462–1466, 2003.

[476] T. Xu, S. Petridou, E. H. Lee, E. A. Roth, and N. R. Vyavahare, "Construction of high-density bacterial colony arrays and patterns by the ink-jet method," *Biotechnol. Bioeng.*, vol. 85, no. 1, pp. 29–33, 2004.

[477] M. Brust and C. J. Kiely, "Some recent advances in nanostructure preparation from gold and silver particles : a short topical review," *Colloids and Surfaces A: Physicochemical and Engineering Aspects*, vol. 202, pp. 175–186, 2002.

[478] W. Cui, W. Lu, Y. Zhang, G. Lin, T. Wei, and L. Jiang, "Gold nanoparticle ink suitable for electric-conductive pattern fabrication using in ink-jet printing technology," *Colloids and Surfaces A: Physicochemical and Engineering Aspects*, vol. 358, no. 1-3, pp. 35–41, 2010.

[479] S. H. Ko, J. Chung, H. Pan, C. P. Grigoropoulos, and D. Poulikakos, "Fabrication of multilayer passive and active electric components on polymer using inkjet printing and low temperature laser processing," *Sensors and Actuators A*, vol. 134, pp. 161–168, 2007.

[480] S. R. Samarasinghe, I. Pastoriza-santos, M. J. Edirisinghe, M. J. Reece, L. Liz-marzán, M. R. Nangrejo, and Z. Ahmad, "Electric-jet assisted layer-by-layer deposition of gold nanoparticles to prepare conducting tracks," *Natural Science*, vol. 1, no. 2, pp. 142–150, 2009.

[481] G. C. Jensen, C. E. Krause, A. Sotzing, and J. F. Rusling, "Inkjet-printed gold nanoparticle electrochemical arrays on plastic. Application to immunodetection of a cancer biomarker protein," *Phys. Chem. Chem. Phys.*, vol. 13, pp. 4888–4894, 2011.

[482] S. Kubitschko, J. Spinke, T. Bru, S. Pohl, and N. Oranth, "Sensitivity enhancement of optical immunosensors with nanoparticles," *Aanalytical Biochemistry*, vol. 253, pp. 112–122, 1997.

[483] C. Hu, X. Bai, Y. Wang, W. Jin, X. Zhang, and S. Hu, "Inkjet printing of nanoporous gold electrode arrays on cellulose membranes for high-sensitive paper-like electrochemical oxygen sensors using ionic liquid electrolytes," *Anal. Chem.*, vol. 84, pp. 3745–3750, 2012.

[484] D. Huang, F. Liao, S. Molesa, and D. Redinger, "Plastic-compatible low resistance printable gold nanoparticle conductors for flexible electronics," *Journal of The Electrochemical Society*, vol. 150, no. 7, pp. 412–417, 2003.

[485] B. S. Gamerith, A. Klug, H. Scheiber, U. Scherf, E. Moderegger, and E. J. W. List, "Direct ink-jet printing of Ag-Cu nanoparticle and Ag-precursor based electrodes for OFET applications," *Adv. Funct. Mater.*, vol. 17, pp. 3111–3118, 2007.

[486] Y. Wu, Y. Li, P. Liu, S. Gardner, S. Ong, and O. Lk, "Studies of gold nanoparticles as precursors to printed conductive features for thin-film transistors," *Chem. Mater.*, vol. 18, pp. 4627–4632, 2006.

[487] J. Barbé, J. Eid, E. Ahlswede, S. Spiering, M. Powalla, R. Agrawal, and S. D. Gobbo, "Inkjet printed Cu (In, Ga) S2 nanoparticles for low-cost solar cells," *Journal of Nanoparticle Research*, vol. 18, no. 379, pp. 1–9, 2016.

[488] J. Hermans, P. Papet, K. Pacheco, Y. Yao, W. Brok, and B. Strahm, "Inkjet printing of Ag nanoparticle inks for heterojunction solar cell metallization," in *SNEC PV Power Expo*, (Shanghai), pp. 1–8, 2015.

[489] N. C. Raut and K. Al-Shamery, "Inkjet printing metals on flexible materials for plastic and paper electronics," *Journal of Materials Chemistry C*, vol. 0, no. 7, pp. 1–22, 2018.

[490] N. R. Bieri, J. Chung, S. E. Haferl, D. Poulikakos, and C. P. Grigoropoulos, "Microstructuring by printing and laser curing of nanoparticle solutions," *Appl. Phys. Lett.*, vol. 82, no. 20, pp. 3529–3531, 2007.

[491] U. S. Schubert, R. Abbel, and J. Perelaer, "Progress of alternative sintering approaches of inkjet-printed metal inks and their application for manufacturing of flexible electronic devices," *J. Mater. Chem. C*, vol. 2, pp. 10232–10261, 2014.

[492] A. Määtänen, P. Ihalainen, P. Pulkkinen, S. Wang, H. Tenhu, and J. Peltonen, "Inkjet-printed gold electrodes on paper: characterization and functionalization," *ACS Appl. Mater. Interfaces*, vol. 4, pp. 955–965, 2012.

[493] Y. Mao, "Nearest neighbor distances calculation with ImageJ," 2016. https://icme.hpc.msstate.edu/mediawiki/index.php/Nearest-Neighbor-Distances-Calculation-with-ImageJ on 2019-16-06.

[494] R. Deegan, O. Bakajin, T. Dupont, G. Huber, S. Nagel, and T. Witten, "Capillary flow as the cause of ring stains from dried liquid drops.," *Nature*, vol. 389, pp. 827–829, 1997.

[495] R. Deegan, O. Bakajin, T. Dupont, G. Huber, S. Nagel, and T. Witten, "Contact line deposits in an evaporating drop," *Phys. Rev. E*, vol. 62, no. 1, pp. 756 – 765, 2000.

[496] B. Fischer, "Particle convection in an evaporating colloidal droplet," *Langmuir*, vol. 18, pp. 60–67, 2002.

[497] H. Hu and R. Larson, "Analysis of the microfluid flow in an evaporating sessile droplet," *Langmuir*, vol. 21, no. 9, pp. 3963 – 3971, 2005.

[498] V. Vancauwenberghe, P. Di Marco, and D. Brutin, "Wetting and evaporation of a sessile drop under an external electrical field: a review," *Colloids Surf. A: Physicochem. Eng. Aspects*, vol. 432, pp. 50–56, 2013.

[499] H. Eral, M. Augustine, M. D., Duits, and F. Mugele, "Suppressing the coffee stain effect: how to control colloidal self-assembly in evaporating drops using electrowetting," *Soft Matter*, vol. 7, pp. 4954–4958, 2011.

[500] T. Kajiya, W. Kobayashi, T. Okuzono, and M. Doi, "Controlling the drying and film formation processes of polymer solution droplets with addition of small amount of surfactants," *J. Phys. Chem. B*, vol. 113, pp. 15460 – 15466, 2009.

[501] E. Talbot, A. Berson, and C. Bain, "Internal flows and particle trans- port inside picoliter droplets of binary solvent mixtures.," in *NIP29: 29th International Conference on Digital Printing Technologies, and Digital Fabrication 2013*, (Springfield), pp. 307 – 312, IS&T, 2013.

[502] X. Shen, C.-M. Ho, and T.-S. Wong, "Minimal size of coffee ring structure," *J. Phys. Chem. B*, vol. 114, pp. 5269 – 5274, 2010.

[503] B. B. T. Anto, S. Sivaramakrishnan, L.-l. Chua, and P. K. H. Ho, "Hydrophilic sparse ionic monolayer-protected metal nanoparticles: Highly concentrated nano-Au and nano-Ag 'inks' that can be sintered to near-bulk conductivity at 150 °C," *Adv. Funct. Mater.*, vol. 20, pp. 296–303, 2010.

[504] J. W. Chung, S. W. Ko, N. R. Bieri, C. P. Grigoropoulos, and D. Poulikakos, "Conductor microstructures by laser curing of printed gold nanoparticle ink," *Appl. Phys. Lett.*, vol. 84, no. 5, pp. 801–803, 2004.

[505] X. Chen, R. Ma, J. Li, C. Hao, W. Guo, B. L. Luk, S. C. Li, S. Yao, and Z. Wang, "Evaporation of droplets on superhydrophobic surfaces: Surface roughness and small droplet size effects," *Physical Review Letters*, vol. 109, no. 11, pp. 1–6, 2012.

[506] L. F. Kadem, C. Lamprecht, J. Purtov, and C. Selhuber-Unkel, "Controlled self-assembly of hexagonal nanoparticle patterns on nanotopographies," *Langmuir*, vol. 31, no. 34, pp. 9261–9265, 2015.

[507] IRDS, *International roadmap for devices and systems*, 2017. https://irds.ieee.org/editions/2017 on 2019-16-06.

[508] W. Yuan, L. Li, W. Lee, and C. Chan, "Fabrication of Microlens Array and Its Application: A Review," *J. Mech. Eng.*, vol. 31, no. 16, pp. 1–9, 2018.

[509] N. Cardenas, N. Ingle, L. Yu, and S. Mohanty, "Development of a digital holographic microscopy system integrated with atomic force microscopy," in *Three-Dimensional and Multidimensional Microscopy: Image Acquisition and Processing XVIII* (J.-A. Conchello, C. J. Cogswell, T. Wilson, and T. G. Brown, eds.), pp. 7904091–7904097, Proc. of SPIE, 2011.

[510] B. Rappaz, P. Marquet, E. Cuche, Y. Emery, C. Depeursinge, and P. J. Magistretti, "Measurement of the integral refractive index and dynamic cell morphometry of living cells with digital holographic microscopy," *Opt. Express*, vol. 13, pp. 9361–9373, 2006.

[511] P. Marquet, B. Rappaz, P. J. Magistretti, E. Cuche, Y. Emery, T. Colomb, and Christian Depeursinge, "Digital holographic microscopy: a noninvasive contrast imaging technique allowing quantitative visualization of living cells with subwavelength axial accuracy," *Opt. Lett.*, vol. 30, pp. 468–470, 2005.

[512] I. Moon, E. Ahmadzadeh, K. Jaferzadeh, and N. Kim, "Automated quantification study of human cardiomyocyte synchronization using holographic imaging," *Biomedical Optics Express*, vol. 10, no. 2, p. 610, 2019.

[513] LynceeTec, "DHMTM T1000 Living cells analysis: shape and structure measurements," *Manual*, pp. 1–2, 2006.

In times of humanoids and new demanding protheses technologies, self-healing materials mimicking the human tissue are of growing scientific, medical and industrial interest. Here, recent studies showed that a comprehensive understanding of tissue cell mechanical behavior and intercellular forces is needed.

In consequence, recording quantitative cell traction forces at different positions of the cell surface in three dimensions at once is the ultimate goal to gain a deeper understanding of the force distribution during a cell rupture process. Here, methods based on established techniques did not offer comprehensive solutions so far.

In this monograph, a novel surface-integrated optical microsensor system is presented that has been developed within the course of this project. It allows for 3D measurements of cell forces in the pico- to nanonewton range by combining the optical methods of image correlation with digital holography.

The reader is introduced and lead through the six different sub-projects of this prototyping:

• Sensor Element Design and Optimization

• Sensor Element Fabrication

• Sensor Element Characterization

• Sensor Element Calibration

• Optical Readout and

• Sensor Material Surface Micro-and Nanopatterning

that were autonomously developed, conceptualized and run within this work in interaction with scientific partners all over Germany.

Bnano